

Fatigue crack growth behavior in weld-repaired high-strength low-alloy steel

Chunguo Zhang ^{a,b}, Stefan van der Vyver ^a, Xiaozhi Hu ^{a,*}, Pengmin Lu ^b

^a School of Mechanical and Chemical Engineering, The University of Western Australia, Perth 6009, Australia

^b Construction Machinery School, Chang'an University, Xi'an 710064, PR China

ARTICLE INFO

Article history:

Received 29 October 2010

Received in revised form 1 February 2011

Accepted 17 March 2011

Available online 22 March 2011

Keywords:

Fatigue crack growth

Weld

Buffer layer

High-strength low-alloy (HSLA)

Heat affected zone (HAZ)

ABSTRACT

Fatigue crack growth properties and Vickers micro-hardness of a weld-repaired high-strength low-alloy steel, known for high strength, low carbon, excellent notch toughness and good weldability and formability, have been studied under the following conditions: as-received high-strength low-alloy, weld-repaired high-strength low-alloy without buffer layer, and weld-repaired high-strength low-alloy with various thickness buffer layers. Those conditions are examined to determine the respective fatigue crack growth behaviors and Vickers hardness distribution, and the effects of different weld-repaired conditions on fatigue characterizations and microscopic features of the fracture and fatigue surface. The extended-compact tension specimen geometry is adopted in this study for all tests. Paris fatigue crack growth curves and the hardness distribution across weld metal, buffer layer and parent metal has been measured together with the relevant scanning electron microscope observations along the fatigue crack growth path, with special attention at and around the interfaces between the weld metal, buffer layer and parent metal. The results show the presence of the BL of a moderate thickness has a significant influence on the fatigue crack growth behavior in the heat-affected zone and around the interface between buffer layer and parent metal. The fatigue resistance of the selected high-strength low-alloy + buffer layer + weld metal tri-metal system is higher than that of the high-strength low-alloy + weld metal bi-metal system.

Crown Copyright © 2011 Published by Elsevier Ltd. All rights reserved.

1. Introduction

High-strength low-alloy (HSLA) steels are known for their excellent mechanical and structural properties such as high strength, low carbon, excellent notch toughness and good weldability and formability. Because of those excellent properties, HSLA has been used in various applications including car components, transport equipments, mining equipments, lifting equipments, storage tanks, excavator buckets, high rise buildings and induced draft fans [1,2]. Utilizing the high strength property of HSLA allows reduction in section thickness, without loss of structural integrity [2]. It is noted that wear damaged sections of supporting structures manufactured from HSLA are often weld-repaired or filled by similar metals through welding [3]. The objective of the present study is to investigate an extensively weld-repaired HSLA steel of either a tri- or bi-metal system (with or without a buffer layer), which has not been systematically studied as shown in previous literatures.

Due to their high strength, HSLA steels can be difficult to repair through welding and special care is needed [4,5]. Furthermore, when these steels are welded they are often prone to softening in the weld HAZ, which exhibits low strength and

* Corresponding author. Tel.: +61 8 6488 2812; fax: +61 8 6488 1024.

E-mail addresses: zcguo2008@163.com (C. Zhang), dynamic.engineering@bigpond.com (S. van der Vyver), xhu@mech.uwa.edu.au (X. Hu), lpmin@chd.edu.cn (P. Lu).

Nomenclature

HSLA	high-strength low-alloy
PM	parent metal
WM	weld metal
BL(s)	buffer layer(s)
E-CT	extended-compact tension
K	stress intensity factor (MPa \sqrt{m})
P	applied load (kN)
B	thickness of specimen (mm)
W	width of specimen (mm)
a	crack length from loading line (mm)
d	distance from specimen (mm)
SEM	scanning electron microscopy

hence is a weak link in mechanical testing indicating poor fatigue properties [6]. To avoid any detrimental effect on fatigue behavior of weld-repaired component, a number of studies have been carried out to assess the effects of the strength on fatigue properties of weld-repaired HSLA steels [7–13], the effects of welding current and speed on the fracture toughness, microstructure and hardness [14], and other relevant issues such as surface finish [15], microstructure manufacturing processes [16]. The effects of post weld heat treatments have also been discussed in [17,18]. An abnormally high fatigue crack growth rate in the WM and HAZ of a welded HSLA has been observed without any post weld heat treatment. However, with either laser multiple-temping or post weld heat treatment at 525 °C for 1 h, the fatigue performance is improved to similar to that of the base metal. It has also been shown that there is no need for post weld heat treatment if laser welding is adopted as shown in Ref. [19]. In this case, the yield strength of WM is similar to that of PM, the fatigue crack growth rates in the WM and HAZ were even lower than that in the PM for similar K range.

For thermo-mechanical control process steel weldments, the fatigue crack growth rate in the heat-affected zone is lower than that of the parent metal regardless of the post weld heat treatment [20]. A bi-metal system with strength gradient welded together [21] was also studied to investigate the fatigue crack growth characteristics through the soft parent steel and ultra strong weld of a maraging steel, which shows the high strength gradient across the weld interface has a strong influence on fatigue crack growth rate.

With different emphases to those aforementioned studies on HSLA steels, the primary objective of the present investigation is to study fatigue characteristics of an extensively weld-repaired HSLA, Bisplate, known for high strength, good toughness and weldability, and the influence of a soft buffer layer between the weld metal and parent metal on the overall fatigue crack growth behavior of the tri-metal system. This study is relevant since wear damaged sections of supporting structures manufactured from HSLA are often repaired or filled by similar metals through welding [3]. The incorporation of a soft buffer layer can assist welding of two hard metals, and can also change the characteristics of a heat-affected zone around the welded area, and thus will have a profound influence on the overall fatigue behavior of a welded structure.

2. Experimental procedure

2.1. Material and specimen

A HSLA steel widely used for earth moving and mining equipments was selected in this study. Flux cored arc welding was employed to perform the extensive welding repair, e.g. filling the section removed by erosion wear, while CO₂ was used as the shielding gas. The HSLA parent metal (PM), together with a weld metal (WM) and a thin buffer layer (BL) between PM and WM form a tri-metal system with different compositions and strength characteristics.

The chemical compositions and mechanical properties of PM, WM and BL are listed in Tables 1 and 2. The welding conditions and process parameters used in the welding repair including WM and BL are listed in Table 3. extended-compact

Table 1

Chemical compositions of tri-metal system.

Series	Element (wt.%)								
	C	Si	Mn	Cr	B	Mo	Ni	P	S
Parent metal (PM)	0.16	0.2	1.1	—	0.2	—	0.01	0.003	0.02
Weld metal (WM)	0.06	0.30	1.4	0.22	0.44	2.29	—	—	—
Buffer layer (BL)	0.03	0.59	1.66	—	—	—	—	—	—

Table 2

Mechanical properties of tri-metal system (typical value*).

Series	Tensile properties			
	Tensile strength, yield (Mpa)	Tensile strength energy at break (Mpa)	Elongation at break Min (%)	Impact Min (J)
PM	690 min (750°)	790–930 (830°)	18 (26°)	40 (160°)
WM	690 min	760–840	17	30
BL	410 min	490–600	22	27

Table 3

Welding procedure.

Welding process	Flux cored arc welding	Flux cored arc welding
Series	Weld metal	Buffer layer
Electrode diameter (mm)	1.2	1.2
Welding consumable	100% CO ₂	100% CO ₂
Welding current (A)	230	230
Arc voltage (V)	27	27
Electrode stick-out (mm)	20	20

tension (E-CT, since CT is well-known and commonly used) specimens with machined through-the-thickness notches have been prepared following the specifications of ASTM E647 (23). The specimens were divided into four groups, i.e. as-received HSLA, weld-repaired HSLA without BL, and weld-repaired HSLA with 4 or 10 mm BLs. The soft BL is introduced to assist welding of two hard metals, and to neutralize the adverse influence of the HAZ around the extensively weld-repaired region. The metal blocks were then sliced and machined into the required dimensions (as shown in Fig. 1) to produce the extended-compact tension (E-CT) specimens for fatigue testing.

2.2. Vickers hardness test at 20 kilogram-force

Micro-Vickers hardness tests were carried out using a Mitutoyo AVK-C2 Hardness Tester (Akashi Corporation). Around 35 indentations near fatigue crack growth path were made across the weld metal, buffer layer and parent metal of each specimen. The distance between the centers of two adjacent indentations is about 0.9 mm. All the hardness readings were obtained using 2 kg-force load, and the full load was held for 15 s. The hardness measurements are presented in Figs. 2a–4b together with the sketches indicating their positions, and the corresponding Paris fatigue measurements.

2.3. Measurement of fatigue crack propagation

Four groups of E-CT specimens, (1) as-received HSLA specimens, (2) weld-repaired specimens without BL between the WM and PM, (3) weld-repaired specimens with 4 mm BL, and (4) weld-repaired specimens with 10 mm BL, were tested under the same fatigue loading condition. The Paris fatigue curves for each group were measured twice with two identical specimens, and the results are quite consistent.

The E-CT specimens were tested at the ambient condition using Instron 8501. Constant amplitude loading with haversine waveform at a frequency of 5 Hz was used, and the R ratio was set at 0 throughout the test. The fatigue pre-crack of about 1 mm was introduced with gradual increasing ΔK in each specimen from the machined notch so that the initial crack size after fatigue pre-cracking is about 5.8 mm from the loading line. Paris fatigue curves were measured starting at around ΔK_{th} , and a traveling optical microscope with 250 \times magnification was used to monitor and measure the crack length during fatigue test. The accuracy of the measurement of crack length was close to ± 0.01 mm. Number of fatigue cycles, N, required for incremental crack growth was recorded, and the fatigue crack propagation rate, da/dN , was calculated directly by dividing the increment of crack length, Δa , by the elapsed number of fatigue cycles. The fatigue crack growth surface in various regions, especially around the interfaces between the PM, WM and BL was examined using SEM.

The stress intensity factor K and its variation during fatigue for E-CT specimens can be calculated following the standard equation in [22]:

$$K = (P/B\sqrt{W}) \times (2 + \alpha) / [(1 - \alpha)^{3/2} \times (1 - d/W)^{1/2}] \times (1.15 + 0.94\alpha - 2.48\alpha^2 + 2.95\alpha^3 - 1.24\alpha^4) \quad (1)$$

where P = the applied load, B = thickness, W = width of specimen, $\alpha = a/(W - d)$, a = crack length from load line, d = distance from specimen edge to loading line, and $0.1 \leq (a + d)/W < 1$.

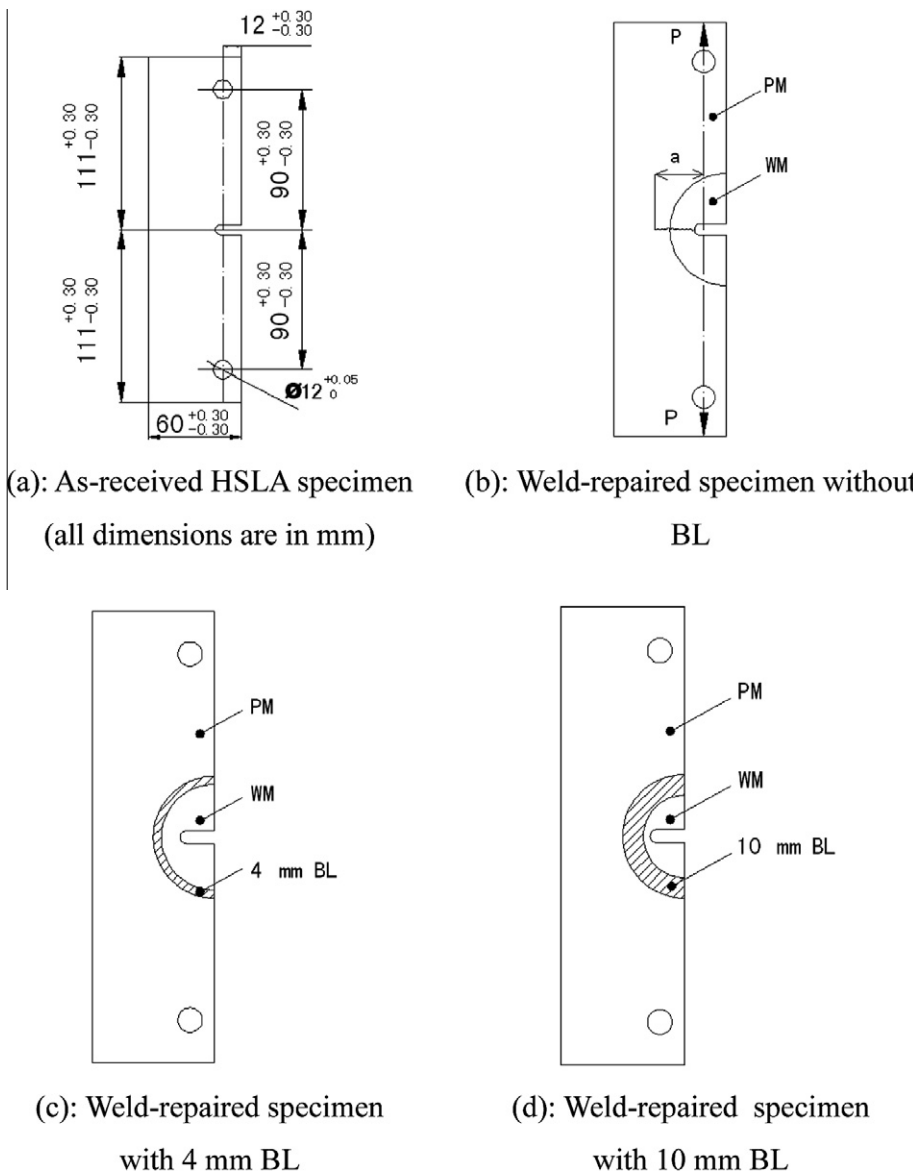


Fig. 1. E-CT specimens of different welding conditions, and the crack length is measured from the loading line as indicated in (b).

3. Results and discussion

3.1. Comparison of as-received HSLA with weld-repaired bi- and tri- metals systems

Vickers hardness (VH) measurements and Paris fatigue curves from the as-received HSLA, are shown in Figs. 2a and 2b. It is clear that the results from two separate tests are very consistent, which therefore provide a good reference base so that the effects of welding, incorporating of BL and BL thickness can be studied. The comparisons with the as-received HSLA are thus shown in Figs. 3a–5b following the reference properties of as-received HSLA in Figs. 2a and 2b.

As shown in Figs. 3a and 3b, both VH and da/dN vs ΔK from the weld-repaired HSLA without BL, fluctuate around the interface between the WM and PM, and have a larger scatter comparing with the as-received HSLA, and there is obvious reduction in VH close to the WM and PM interface and within the HAZ. The soft region around the interface and in the HAZ adjacent to the PM, and the sharp rebounding high-hardness region in the weld HAZ have also been reported in Ref. [23]. It should be mentioned that the lowest hardness at the interface shown in Figs. 3a and 3b is also corresponding to the sudden jump of da/dN at the interface shown in Fig. 3b. Furthermore, a dip of da/dN in Fig. 3b occurred at about 3 mm away from the interface, which maybe resulted from the formation of localized high-hardness weld region in the weld

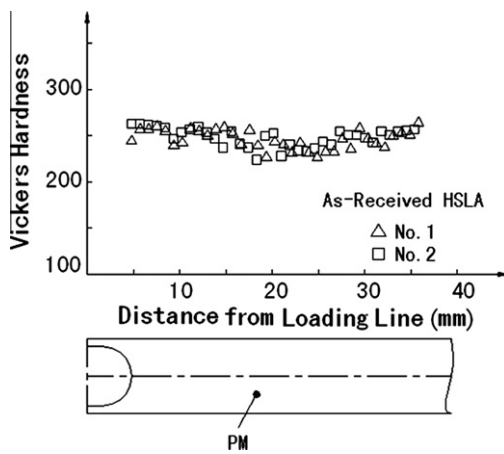


Fig. 2a. Vickers hardness in as-received HSLA.

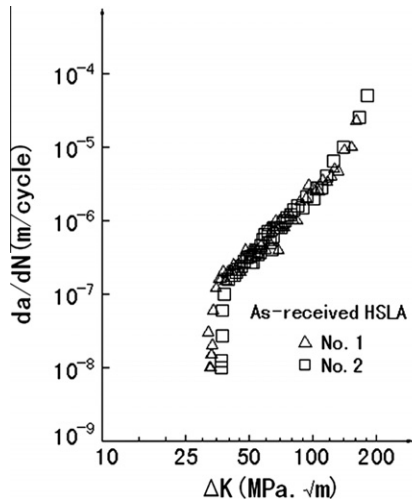


Fig. 2b. Fatigue behavior in as-received HSLA.

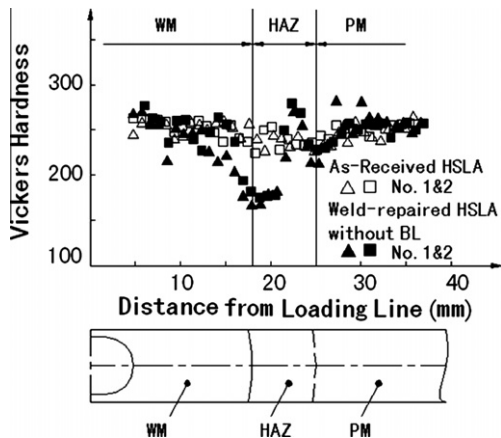


Fig. 3a. Vickers hardness in as-received HSLA and weld-repaired HSLA without BL.

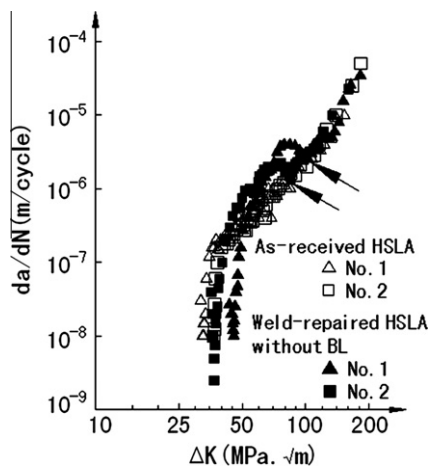


Fig. 3b. Fatigue behavior in as-received HSLA and weld-repaired HSLA without BL.

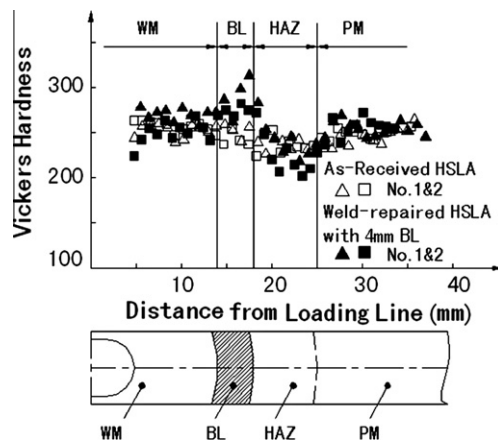


Fig. 4a. Vickers hardness in as-received HSLA and weld-repaired HSLA with 4 mm BL.

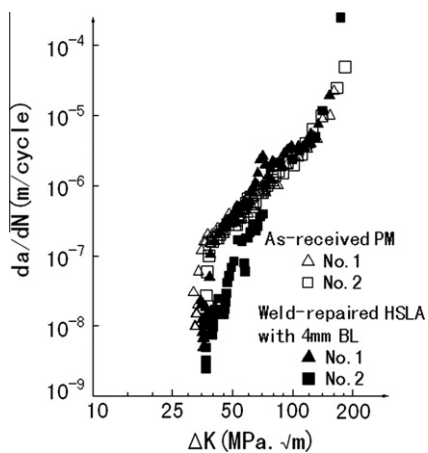


Fig. 4b. Fatigue behavior in as-received HSLA and weld-repaired HSLA with 4 mm BL.

HAZ shown in Fig. 3a. While the soft region exhibits poor fatigue resistance as it corresponds to higher da/dN in the 2nd stage of fatigue, it seems that the localized high-hardness region in HAZ, improves the fatigue resistance with lower da/dN .

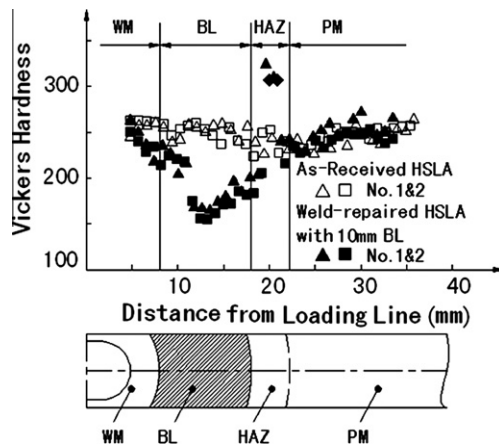


Fig. 5a. Vickers hardness in as-received HSLA and weld-repaired HSLA with 10 mm BL.

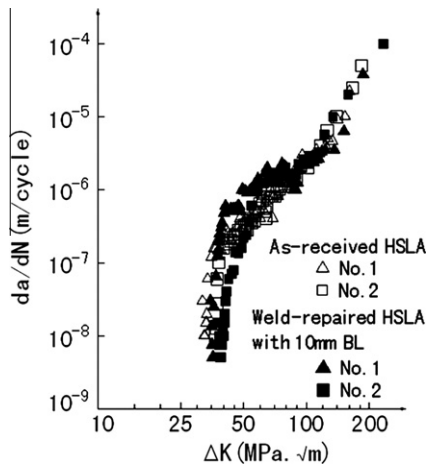


Fig. 5b. Fatigue behavior in as-received HSLA and weld-repaired HSLA with 10 mm BL.

As shown in Fig. 4a, the sharp reduction in VH around the WM and PM boundary and within the HAZ shown in Fig. 3a has been removed with the incorporation of a 4 mm BL. Although the BL has a lower yield strength than those of PM and WM, the micro-VH within the BL is higher than those of PM and WM. The corresponding reduction in da/dN in the 2nd stage of fatigue is also very obvious, indicating the incorporation of BL is not only beneficial to the welding process, but also improves the fatigue resistance.

In the case of 10 mm BL, VH drops substantially within the relatively thick BL as shown in Fig. 5a, but VH is increased in the HAZ. As shown in Fig. 5b, da/dN in the 2nd stage fatigue is increased within the BL, and fluctuates especially around the interface between the BL and the PM. It can be concluded from the results in Figs. 4a, 4b and 5a, 5b that the soft BL selected for this study should not be too thick as the BL by itself does not have better fatigue resistance in comparison with the PM.

Comparing the da/dN results in Figs. 3a–5b, particularly those around the interfaces between the WM and PM, WM and BL, and BL and PM, it seems that the WM and PM interface is the least fatigue resistant due to the formation of HAZ. Comparing the Figs. 3a and 4a, it can be found that the incorporation of 4 mm BL has limited the soft zone around the WM and PM interface, and the weld HAZ indicating the higher Vickers hardness as comparison with weld-repaired HSLA without BL. By incorporating a BL, the original properties at the WM and PM interface region have been positively modified in two ways. First, there is no longer a direct interface between WM and PM. Second, the HAZ properties in the PM are also modified. For the tri-metal system selected in the current study, incorporation of 4 mm BL achieves the best result. It is also noted that the interface between the WM and BL does not have much influence on da/dN and the total fatigue life. Those results indicate that the selection of WM and BL are adequate for the HSLA.

3.2. Influence of buffer layer and its thickness on material properties

To emphasize the influence of BL among those weld-repaired HSLA specimens, VH and Paris fatigue curves from the bi-metal system (WM and PM) are chosen as the reference properties and compared with the properties of the tri-metal system

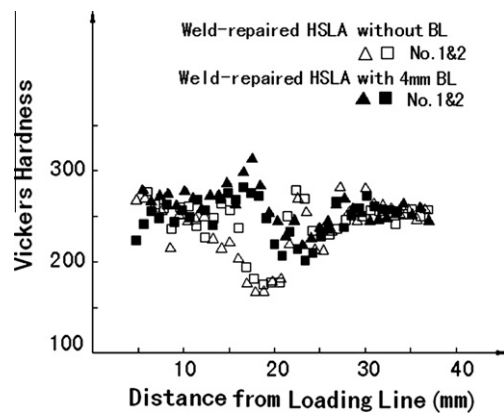


Fig. 6a. Vickers hardness in weld-repaired HSLA without and with 4 mm BL.

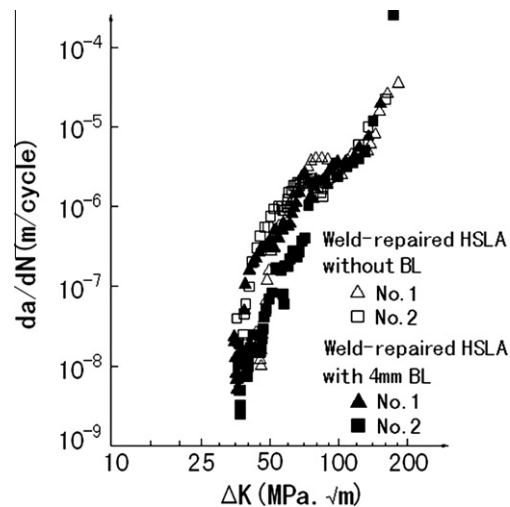


Fig. 6b. Fatigue behavior in weld-repaired HSLA without and with 4 mm BL.

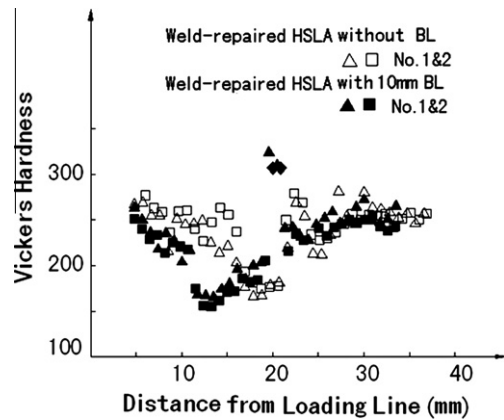


Fig. 7a. Vickers hardness in Weld-repaired HSLA without and with 10 mm BL.

(WM, BL and PM) as shown in Figs. 6a, 6b and 7a, 7b. To emphasize the BL thickness influence, the tri-metal systems with the 4 and 10 mm BLs are further compared in Figs. 8a and 8b.

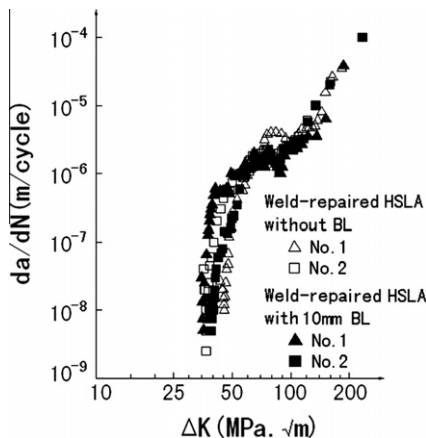


Fig. 7b. Fatigue behavior in weld-repaired HSLA without and with 10 mm BL.

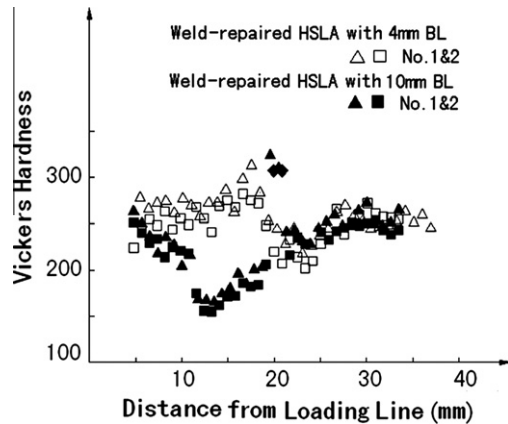


Fig. 8a. Vickers hardness in Weld-repaired HSLA with 4 mm and with 10 mm BL.

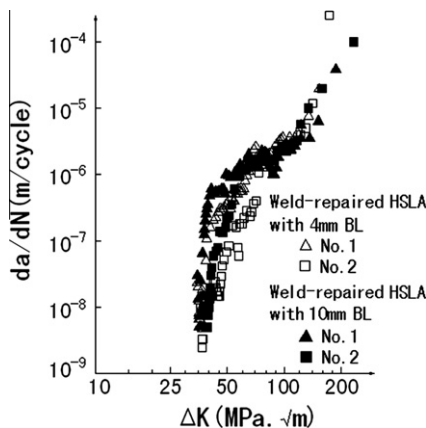


Fig. 8b. Fatigue behavior in weld-repaired HSLA with 4 mm and 10 mm BL.

VH of the bi-metal (WM and PM) and tri-metal (WM, 4-mm-BL, PM) systems exhibits the opposite trends within the HAZ and 4 mm BL region as shown in Fig. 6a. It is clear that the higher VH of the tri-metal in this region has resulted in slower fatigue crack growth and thus increased fatigue resistance. However, the tri-metal system (WM, 10-mm-BL, PM) with a relatively thick BL of 10 mm exhibits a substantial reduction in VH within the BL due to its low yield strength and a sudden

increase in VH within the HAZ. As a result, the overall improvement in fatigue life is not as significant as the 4-mm-BL system. The direct comparisons of two tri-metal systems (WM, 4-mm-BL or 10-mm-BL, PM) in Figs. 8a and 8b further suggest BL cannot be too thick, and incorporation of a thin BL is sufficient to alter the fatigue properties of HAZ.

3.3. SEM details at bi- and tri- metal interface regions

Fatigue fracture surfaces have been examined using SEM with special emphasis on the regions around the bi- and tri-metal interfaces. To correlate the microscopic observations to the relevant locations and corresponding VH and da/dN measurements, sketches for the boundary regions and da/dN curves have been numbered accordingly for the bi- and tri-metal systems.

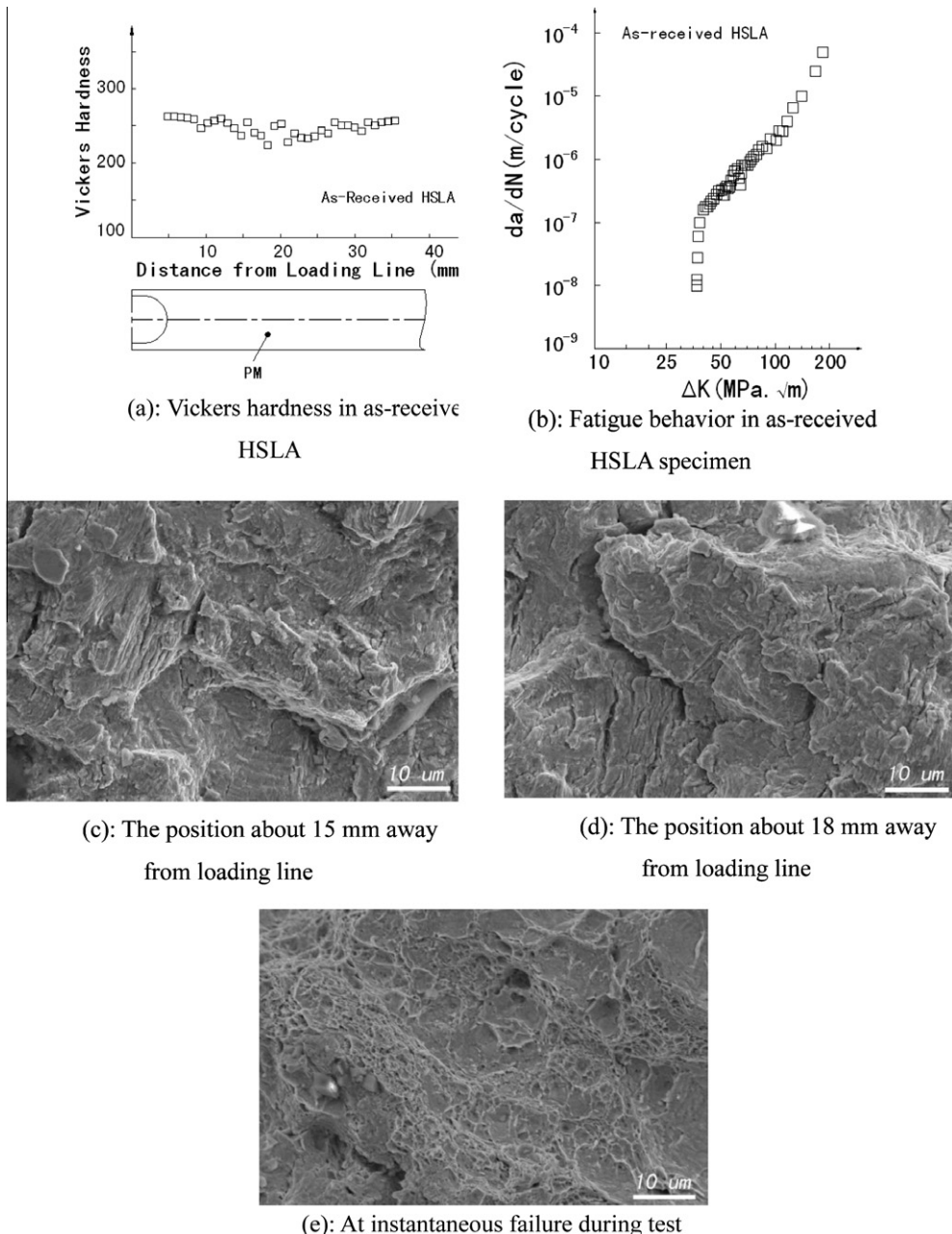


Fig. 9. Vickers hardness, fatigue behavior and SEM micrographs in stable and unstable crack propagation regions of as-received HSLA specimen.

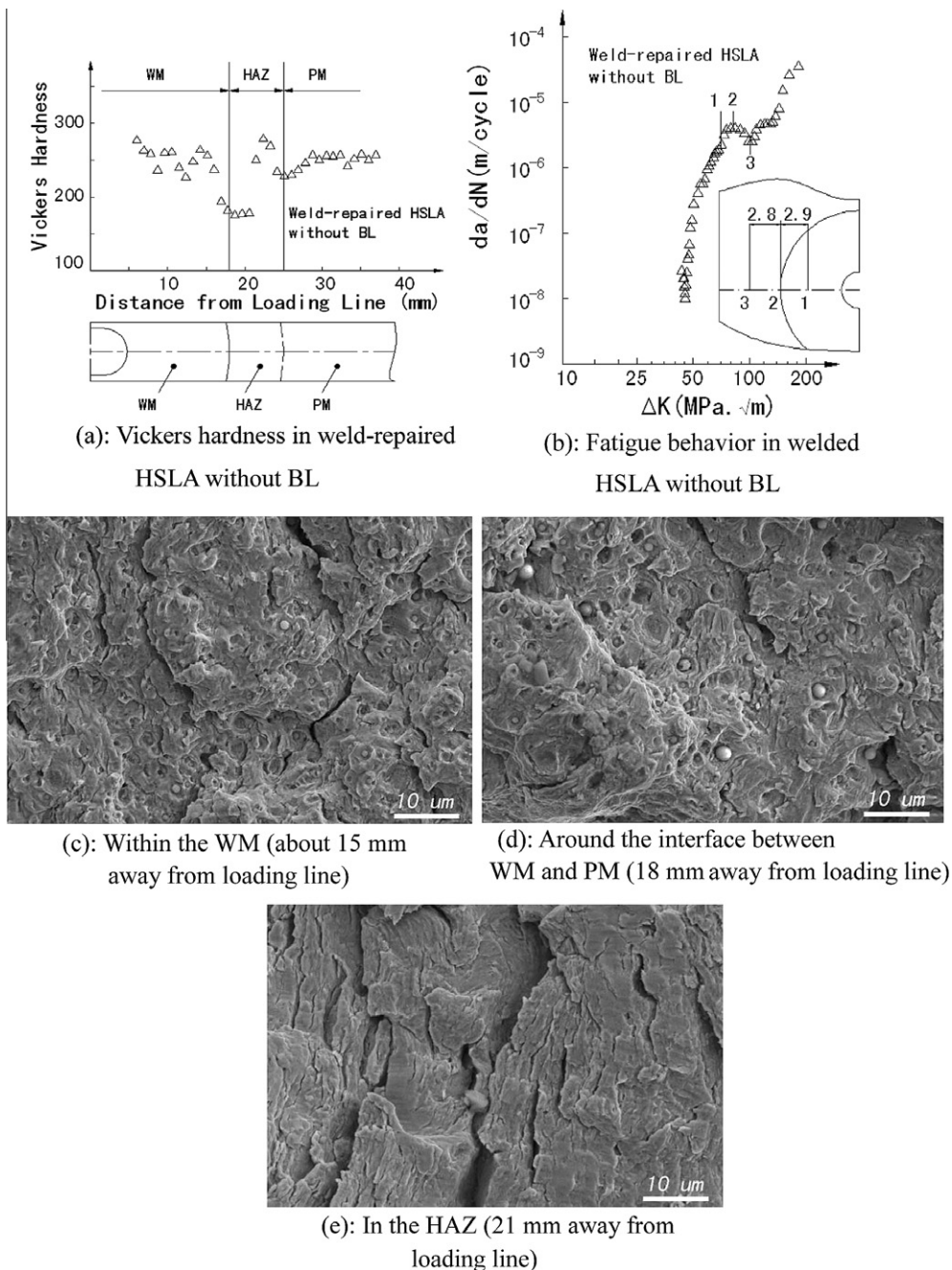


Fig. 10. Vickers hardness, fatigue behavior and SEM micrographs in stable crack propagation region of weld-repaired HSLA specimen without BL.

Following the above descriptions, Fig. 9 displays the details for PM, Fig. 10 displays the property, position and SEM details for the bi-metal system (WM and PM), Fig. 11 displays the details for the tri-metal system (WM, 4-mm-BL, PM), and Fig. 12 displays the details for the tri-metal system (WM, 10-mm-BL, PM).

The SEM micrographs in Fig. 9c–e for PM and Fig. 10c–e for the bi-metal system (WM and PM) show that multiple micro-cracking occurred in both systems, and it became more severe in the HAZ indicating the change in material properties. Fig. 10c and d display some spherical shaped non metallic particles from the welding process. Micro-plastic failure through micro void coalescence is evident in Fig. 9e for the PM at the final stage of unstable fracture.

The SEM micrographs, VH and fatigue crack growth measurements at comparable locations for the two tri-metal systems are shown and compared in Fig. 11 (WM, 4-mm-BL, PM), and Fig. 12 (WM, 10-mm-BL, PM). As can be seen, both VH and da/dN fluctuate within the BL and HAZ, especially around the interface between the BL and PM. Interestingly, VH within the thin

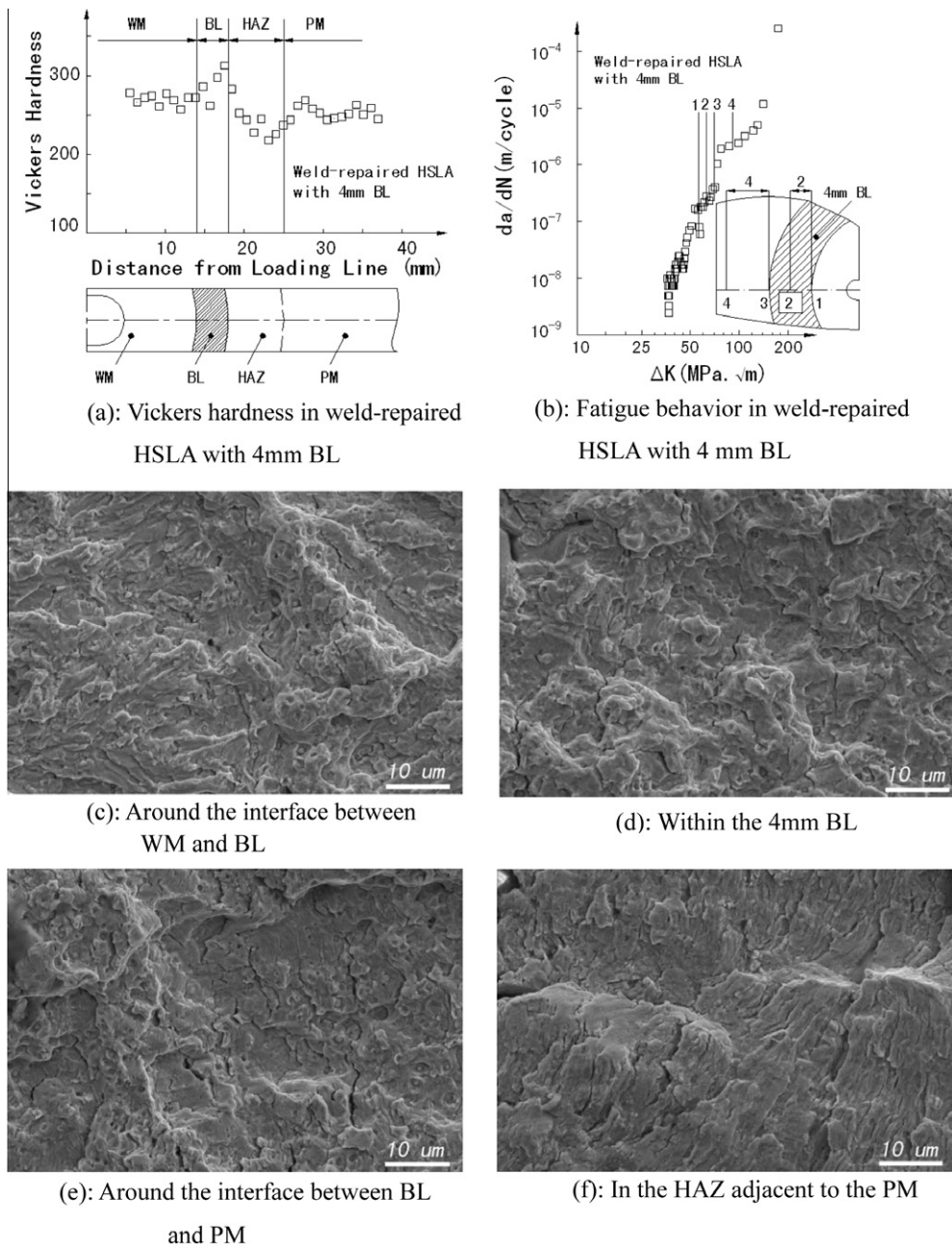


Fig. 11. Vickers hardness, fatigue behavior and SEM micrographs in stable crack propagation region of welded HSLA specimen with 4 mm BL.

4-mm-BL is the highest although BL has lower yield strength in comparison with WM and PM, indicating both BL and HAZ have been altered by the welding process, which has resulted in better fatigue performance for the tri-metal system (WM, 4-mm-BL, PM). While the thick 10-mm-BL displays the lowest VH, the highest VH is within the HAZ.

The SEM micrographs in Fig. 11c–f and in Fig. 12c–f provide direct comparisons for the two tri-metal systems at the WM and BL interface (c), within the BL (d), at the BL and PM interface (e), and in HAZ (f). In all those locations, the fatigue/fracture surfaces of the tri-metal system with the 10-mm-BL appear to be rougher than their counterparts of the tri-metal systems with the 4-mm-BL. This finding appears to be consistent with the relatively rough fatigue surfaces within the HAZ of the bi-metal system as both the relatively rough fatigue surfaces are corresponding to lower fatigue resistance as shown by the Paris fatigue measurements.

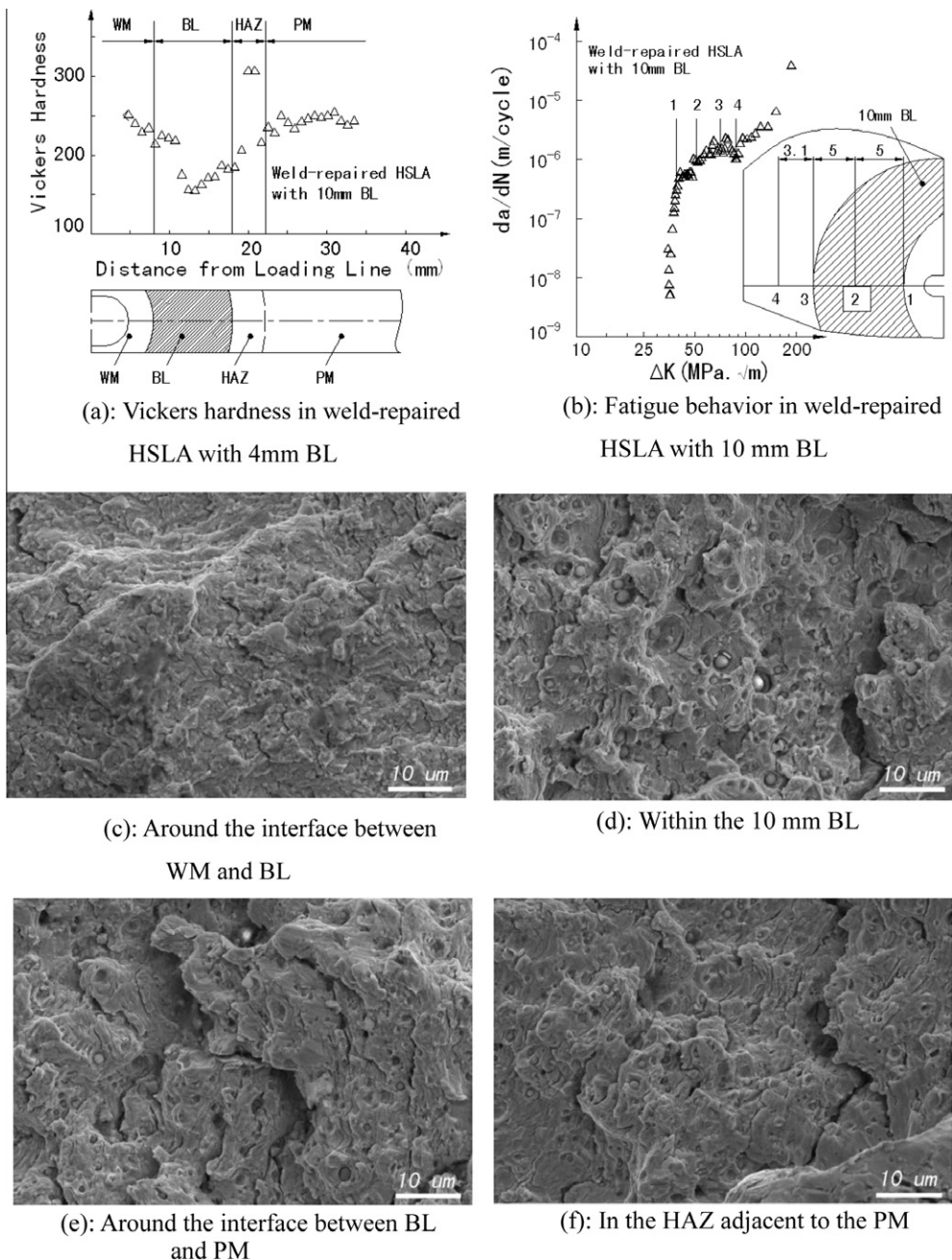


Fig. 12. Vickers hardness, fatigue behavior and SEM micrographs of stable crack propagation region of welded HSLA specimen with 10 mm BL.

4. Conclusions

An extensively weld-repaired HSLA steel has been studied using bi- and tri- metal systems with a BL (buffer layer) as the third phase between the PM (parent metal) and WM (weld metal). For the selected tri-metal (PM, WM and BL) with the specified material compositions and properties, the thin 4-mm-BL works well by virtually removing the adverse influence of HAZ present in the bi-metal system (WM and PM) although BL has the lowest yielding strength among the three materials. The micro-VH within the BL and HAZ has been increased and the variation in VH has also been reduced leading to a substantial improvement in the fatigue resistance. However, the improvement in fatigue resistance is less significant for the tri-metal system with the thick 10-mm-BL as micro-VH drops within the thick BL and so does the overall fatigue resistance.

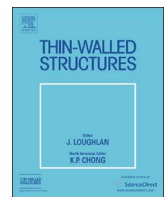
The comparable SEM micrographs of the tri-metal systems with 4-mm and 10-mm BLs at similar locations show increasing micro-fracture activities on the fatigue/fracture surface of the tri-metal system (WM, 10-mm-BL, PM), which should be related to the reduction in the fatigue resistance. The resultant “rougher” fatigue also corresponds to the lower VH region.

In summary, a soft buffer layer of a moderate thickness is beneficial as far as the fatigue life of HSLA is concerned according to the test results of the current study. This is because a thin soft buffer layer with a low carbon wt.% can effectively reduce the influence of the HAZ around the weld-repaired region. However, excessive usage of a soft buffer layer can weaken a welded structure because of its low strength. For the selected tri-metal system in this investigation, it seems the 4 mm thick buffer layer offers a promising compromising solution.

It should also be mentioned that the influence of residual stresses due to welding has not been considered in the current study. Although the micro-hardness measurements emphasized in this paper are not influenced by the residual stresses, the fatigue crack growth will be influenced. As residual stresses are structure/specimen geometry dependent, this complicated issue is beyond scope of the current paper, and can only be dealt with in the future in a separate paper.

References

- [1] Mohan S, Prakash V, Pathak JP. Wear characteristics of HSLA steel. *Wear* 2002;252:16–25.
- [2] http://www.bisalloy.com.au/files/Bisplate_Pdfs/Bisplate_80.pdf.
- [3] Scholl M, Devanathan R, Clayton P. Abrasive and dry sliding wear resistance of Fe–Mo–Ni–Si and Fe–Mo–Ni–S–C weld hardfacing alloys. *Wear* 1990;135:355–68.
- [4] Bisalloy steels. Bisplate technical manual. P48, <www.bisalloy.com.au>.
- [5] A.V. Borozdin, A.A. Pavlov, V.A. Kroskin. Experience with the use of high strength low alloy steels. Translated from Khimicheskoe i Neftyanoe Mashinostroenie; 1991. p. 31–2.
- [6] Mohandas T, Reddy GM, Kumar BS. Heat-affected zone softening in high-strength low alloy steels. *J Mater Process Technol* 1999;88:284–94.
- [7] Yamasaki T, Kawai Y, Maeda Y. Fatigue life of welded and bolted repair parts. *J Struct Eng* 1984;10:2499–512.
- [8] Mutoh Y, Sakamoto I. Fatigue crack propagation in the weld bond region of a type 304 stainless steel weldment. *Advances in fracture research*. Oxford: Pergamon Press; 1984. p. 1695–702.
- [9] Ravi S, Balasubramanian V, Nasser SN. Fatigue life prediction of strength mis-matched high strength low alloy steel welds. *Mater Des* 2006;27:278–86.
- [10] Ravi S, Balasubramanian V, Nasser SN. Assessment of some factors influencing the fatigue life of strength mis-matched HSLA steel weldments. *Mater Des* 2004;25:125–35.
- [11] Smith C, Pistorius PG, Wannenburg J. The effect of a long post weld heat treatment on the integrity of a welded joint in a pressure vessel steel. *Int J Press Vess Pip* 1997;70:183–95.
- [12] Ravi S, Balasubramanian V, Nasser SN. Effect of mis-matched ratio (MMR) on fatigue crack growth behavior of HSLA steel welds. *Eng Fail Anal* 2004;11:413–28.
- [13] Singh V, Raju PVSS, Namboodhiri TKG, Rao PR. Low-cycle fatigue behavior of a low-alloy high-strength steel. *Int J Fatigue* 1990;12:289–92.
- [14] Prasad K, Dwivedi DK. Some investigations on microstructure and mechanical properties of submerged arc welded HSLA steel joints. *Int J Adv Manuf Technol* 2008;36:475–83.
- [15] Liu J, Yue ZF, Liu YS. Surface finish of open holes on fatigue life. *Theor Appl Fract Mech* 2007;47:35–45.
- [16] Yu MT, Topper TH, Wang L. The effect of microstructure on the mechanical behavior of a low carbon. *Int J Fatigue* 1988;10:249–55.
- [17] Tsay LW, Li YM, Chen C, Cheng SW. Mechanical properties and fatigue crack growth rate of laser-welded 4130 steel. *Int J Fatigue* 1992;14:239–47.
- [18] Ohta A, Sasaki E, Niher M, Kosuge M, Kanao M, Inagaki M. Fatigue crack propagation rates and threshold stress intensity factors for welded joints of HT80 steel at several stress ratios. *Int J Fatigue* 1982;233–7.
- [19] Tsay LW, Chung CS, Chent C. Fatigue crack propagation of D6AC laser welds. *Int J Fatigue* 1997;19:25–31.
- [20] Tsay LW, Chern TS, Gau CY, Yang JR. Microstructure and fatigue crack growth of EH36 TMCP steel weldments. *Int J Fatigue* 1999;21:857–64.
- [21] Ukadgaonker VG, Bhat S, Jha M, Desai PB. Fatigue crack growth towards the weld interface of alloy and maraging steels. *Int J Fatigue* 2008;30:689–705.
- [22] Piascik RS, Newman Jr JC. An extended compact tension specimen for fatigue crack growth and fracture testing. *Int J Fracture* 1995;76:43–8.
- [23] Omweg GM, Frankel GS, Bruce WA, Ramirez JE, Koch G. Performance of welded high-strength low-alloy steels in sour environments. *Corrosion* 2003;59:640–53.



Full length article

Fatigue improvements of cracked rectangular hollow section steel beams strengthened with CFRP plates



Tao Chen*, Xian Wang, Ming Qi

Department of Structural Engineering, Tongji University, Shanghai 200092, China

ARTICLE INFO

Keywords:

Rectangular hollow section steel beam
Fatigue crack propagation life
Prestressed carbon fiber reinforced polymers plate
Finite element modeling
Parametric study

ABSTRACT

Concerns over means to improve fatigue behavior of cracked rectangular hollow section (RHS) steel beams exist. This paper presents the details of strengthening schemes that was carried out using prestressed or high modulus carbon fiber reinforced polymer (CFRP) plates. A set of fatigue tests were conducted and results indicated that prestressed CFRP technique could increase fatigue crack propagation life 35.57 times longer than that of un-repaired one. The results also indicated that high modulus CFRP is effective at increasing fatigue life. Following crack propagation lives were calculated based on finite element models and close agreement with test results were observed. Thereafter, a parametric study was conducted considering the influence of various parameters such as the CFRP prestressing level, plate width and modulus on the fatigue life of the strengthened specimens. The findings of this paper can be employed to formulate design guidance for RHS beams under fatigue loading.

1. Introduction

Hollow section steel members have been adopted as structural members in bridges, civil buildings, offshore structures and even cranes. These members are often subjected to bending under external actions during service, and they may have structural deficiencies due to fabrication or harsh environments [1–4]. Fatigue cracking is a predominant problem for structures subject to repeated loading [3,5]. Thus, a critical need exists for repair techniques that allow convenient rehabilitation. However, traditional welding or bolting methods involve additional heavy plates and other applications that lead to fatigue sensitive defects [6,7]. In recent decades, carbon fiber reinforced polymer (CFRP) materials have been adopted as a popular repairing material for steel members [8–11]. Previous investigations showed the fatigue lives of repaired specimens can be greatly extended by non-prestressed CFRP repair methods [1,12–16] and even increased 21.5 times over that of control specimens using prestressed CFRP repair method [12]. Extensive research has focused on prestressed CFRP patched elements subjected to uniaxial loading [13,15,17,18].

A great deal of attention has also been paid to structural elements subjected to bending moments. Most of them have been conducted on the "I" section steel beams [16,19–21] and circular hollow section (CHS) beams [4,8,22] strengthened with CFRP materials. Linghoff et al. [23,24] conducted four-point bending tests on steel beams with I cross-sections strengthened with various configurations of CFRP laminates. Increased moment capacity was found. Finite element analyses of steel

beams were also performed as a parametric study to capture the behavior of the strengthened specimens. Experimental research has also shown the effectiveness of CFRP rehabilitation on damaged CHS members under three-point bending [22]. Fatigue performance of the CFRP strengthening system has been reported. Colombi and Fava [25] carried out fatigue tests on nine cracked steel beams, each with an I cross section strengthened with a CFRP plate. Fatigue crack growth was retarded and fatigue life was prolonged. Jiao et al. [26] investigated eight notched steel beams strengthened with strand CFRP sheets. The specimens were subjected to fatigue loadings and fatigue life enhancement was achieved. CFRP strengthening was confirmed as an ideal way to rehabilitate cracked steel beams after comparing fatigue performance with traditional strengthening methods [27]. In the aforementioned studies, artificial slot was employed to simulate the initial damage degree instead of welded details. The purpose is to eliminate scatter of fatigue results due to welding that can introduce residual stress, kinds of imperfections such as pores, blowholes, under cuts and heat affected zone.

The prestressing technique is often used to strengthen steel beams by CFRP plates to exploit its high strength. Walbridge et al. [28] carried out fatigue tests on strengthened I-beams with welded cover plates. The results indicated that a significant fatigue life enhancement can be achieved by applying prestressed CFRP strips to the cover plates. Numerical analysis with a fracture mechanics model were performed to predict fatigue life with reasonable results. Due to the complexity of weld details, artificial notched steel elements were introduced.

* Corresponding author.

E-mail address: t.chen@tongji.edu.cn (T. Chen).

Ghafoori et al. [16] investigated notched steel I-beams strengthened with prestressed CFRP and developed a theoretical method to calculate the prestressing levels in CFRP by controlling the stress intensity factor at the crack tip. The prestressed CFRPs were further employed to increase the buckling strength of steel I-beams with experimental and numerical approaches [29]. In regards to the strengthening of a rectangular hollow section (RHS) structural members, research focused on monotonic loadings [30,31], but limited research dealt with fatigue problems [32,33]. Field application with prestressed CFRP laminates were reported by Koller et al. [33]. A cracked steel pendulum was monitored and fatigue cracks ceased to propagate for nine years. In summary, the prestressed CFRP strengthening method is effective for steel members with open and closed sections.

Previous research indicates the fatigue performance improvement with hollow section steel members. However, to further explore the application of prestressed CFRP in this area, systematic experimental and numerical efforts are required. The aim of this paper is to examine and compare the fatigue life improvements of CFRP-strengthened RHS steel beams with different CFRP moduli and prestressing levels with un-strengthened ones. Firstly, six strengthened specimens were tested under four-point fatigue bending. The results were compared to that of the un-strengthened control specimens. Subsequently, a numerical simulation technique for studying the cracking behavior of RHS steel beams subjected to fatigue loading was developed and validated against experimental testing data. A study was then carried out on the effects of several strengthening related parameters as they relate to the response of the cracked beams using validated numerical models.

2. Experimental investigation of fatigue crack propagation life

2.1. Experimental program

The specimens were fabricated by patching CFRP plates to the bottom notched steel beams. Fig. 1 shows the basic geometry of the strengthened cracked RHS steel beams considered in this study. They were 700 mm long with an RHS cross section, which measured 100 mm × 50 mm × 6 mm. Initial damage was simulated by a notch on the bottom of the steel beam. It was cut by wire electrical discharge machining. The width of the notch was 0.18 mm and the crack depths were 10 mm or 30 mm. The lower surface was sandblasted and cleaned with acetone before applying adhesive and patching with a CFRP plate. Two types of CFRP plates with normal or high modulus were used and they had dimensions of 500 mm long and 20 mm wide. As for the prestressed CFRP plate, they were tensioned with a hydraulic jack.

Four series of tests, with a total of eight specimens, involving different combinations of CFRP types, prestressing levels and initial damage levels were considered. The test matrix are presented in Table 1. Series A consists of two un-retrofitted beams with a 10 mm or 30 mm initial crack as the control ones. Series B and C includes specimens repaired with normal modulus CFRP plates that are designated by NC followed by either N or P, indicating non-prestressed or prestressed CFRP plates, respectively. Series D is two specimens repaired with non-prestressed CFRP plates of high modulus. HC refers to the used type of

Table 1
Test matrix.

Series	No.	Initial crack depth (mm)	CFRP prestressing level (%)	CFRP modulus ($\times 10^5$ MPa)	Loading ranges 2 P (kN)	Fatigue life (Cycles)
A	RHS-1	10	/	/	8–80	31,168
	RHS-2	30	/	/	5.5–55	13,803
B	NC-N-1	10	0	1.91	8–80	104,362
	NC-N-2	30	0	1.91	5.5–55	64,599
C	NC-P-1	10	22	1.91	8–80	232,055
	NC-P-2	30	22	1.91	5.5–55	491,014
D	HC-N-1	10	0	4.60	8–80	112,173
	HC-N-2	30	0	4.60	5.5–55	194,579

Table 2
Material properties of steel, CFRP and adhesive.

Property	Steel	CFRP-1	CFRP-2	Adhesive
f_y (MPa)	298	–	–	–
f_u (MPa)	368	3089	1500	28.6
E_1 (GPa)	190	191	460	1.9
E_2 (GPa)	–	10.8	18.4	–
ν_{12}	0.30	0.27	0.30	0.36
G_{12} (GPa)	–	6.0	7.7	–
t (mm)	6.00	1.40	1.55	0.40

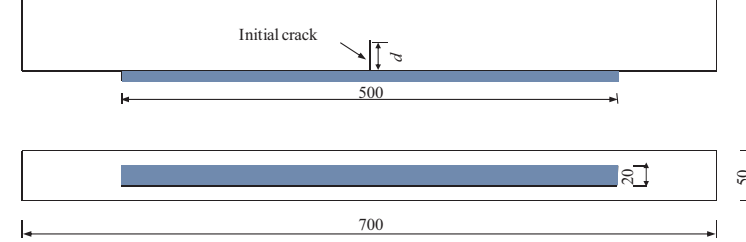
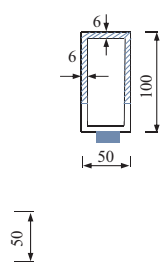
CFRP plate with high Young's modulus.

Tensile coupon tests were performed for steel tubes and results showed in Table 2. All the steel tubes were fabricated from one batch of material. The material properties of the steel, CFRP plates and adhesive are given in Table 2.

2.2. Specimen preparation

The specimen preparation consists of surface grinding, applying adhesives and patching CFRP plates. A major challenge of exploiting the high tensile strength of CFRP is prestressing the CFRP plate during specimen preparation. In this research, an instrumentation was employed to fulfill the prestressing process (Fig. 2). A bare specimen was positioned with the prestressing instrumentation. Thereafter, a CFRP plate was bolted at one end with the specimen using mechanical anchorage systems. The other end was clamped by steel plates that lined to the far end steel plate trough steel bars. Subsequently, a hydraulic jack was used to pull the steel bars. Strain gauges were mounted on CFRP plate surface to monitor the prestressing level until designed values. The anchorage systems was also used to fix both CFRP plate ends to delay or prevent debonding between CFRP plate and steel beam for non-prestressed CFRP repaired specimens. Thereafter, specimens were subjected to fatigue loading, and propagation phenomena were recorded.

Fig. 1. Geometry configurations (unit: mm).





Anchorage system
RHS specimen
CFRP plate
Adhesive

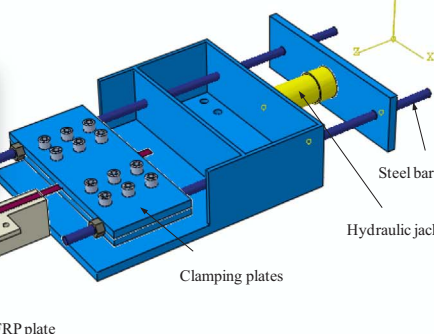


Fig. 2. Prestressing instrumentation.

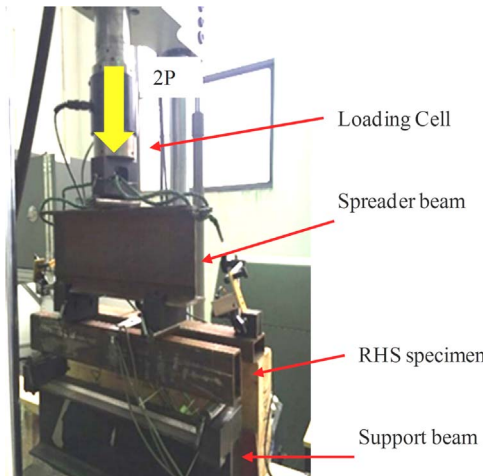


Fig. 3. Test setup.

2.3. Test setup

The fatigue tests were conducted on a MTS servo hydraulic testing machine with a capacity of 250 kN as shown in Fig. 3. Simply supported boundary conditions were applied at the ends of the specimens. A vertical load was applied to the center of spreader beam. All specimens were tested under an 8 Hz constant amplitude sinusoidal tension-tension fatigue loading with a loading ratio of 0.1. Different load ranges were applied to specimens with various initial crack depths (Table 1). The objective was to limit the fatigue crack propagation life less than one million cycles for all specimens.

2.4. Experimental results

The last column of Table 1 also summarizes the fatigue crack propagation life of all specimens. It can be observed that CFRP strengthened specimens can considerably increase fatigue life of cracked specimens. With regard to non-prestressed CFRP strengthened specimens, the fatigue lives were 3.35–14.10 times longer than that of controlled specimens. It was also found that high modulus CFRP achieved better fatigue performance. Meanwhile, the prestressed technique improved the fatigue life up to 7.45–35.57 times that of unrepairs steel beams. It also enhanced the utilization efficiency of CFRP material. Regardless of the initial crack depth, all repaired specimens had enhanced fatigue crack propagation lives.

The specimens that failed by fracture of the RHS steel beams were accompanied by rupture or pulling out of the CFRP patch from the steel beams. Fig. 4 shows typical failure patterns of strengthened specimens after the failure. Fig. 4(a) shows specimens failed with end slippage at

the anchorage region. Fig. 4(b) displays typical CFRP failure at anchorage region, while Fig. 4(c) illustrates representative CFRP breakage for specimens repaired by high modulus CFRP plates.

3. Fatigue crack growth prediction

In the context of linear elastic fracture mechanics (LEFM), the modeling of the fatigue crack propagation can be performed with stress intensity factors ranges from the crack front. Stress intensity factors can be obtained with numerical models specified with various crack depths. With integration of a propagation law, the number of cycles to propagated can be determined.

Several models have been developed to account for other factors based on the empirical form proposed by Paris and Erdogan [34]. In this study, the NASGRO Eq. (1) [35] was employed to estimate the crack propagation life. The equation is expressed as,

$$\frac{da}{dN} = \frac{C \cdot (1-f)^m \cdot \Delta K^m \cdot \left(1 - \frac{\Delta K_{th}}{\Delta K}\right)^p}{(1-R)^m \cdot \left(1 - \frac{\Delta K}{(1-R)K_c}\right)^q} \quad (1)$$

$$\Delta K = K_{\max} - K_{\min} = K_{\max}(1-R); R = (K_{\min}/K_{\max}) \quad (2)$$

where a = crack length; N = number of fatigue cycles; da/dN = instantaneous crack growth rate; ΔK = stress intensity factor range; R = stress ratio; C and m = material parameters; p and q = the exponents, ΔK_{th} = the threshold stress intensity factor range; f = the crack opening function; K_c = the critical stress intensity factor; K_{\max} = the maximum stress intensity factor and K_{\min} = the minimum stress intensity factor.

Fatigue crack closure effect is considered by introducing crack opening function, f , which is defined as [36]:

$$f = \frac{K_{op}}{K_{\max}} = \max\{R; A_0 + A_1 \cdot R + A_2 \cdot R^2 + A_3 \cdot R^3\} \quad 0 \leq R \leq 1 \quad (3)$$

where,

$$A_0 = (0.825 - 0.34\alpha + 0.05\alpha^2) \left[\cos\left(\frac{\pi}{2}\right) SR \right]^{1/\alpha} \quad (4)$$

$$A_1 = (0.415 - 0.017\alpha) SR \quad (5)$$

$$A_2 = 1 - A_0 - A_1 - A_3 \quad (6)$$

$$A_3 = 2A_0 + A_1 - 1 \quad (7)$$

$$SR = \frac{S_{\max}}{\sigma_0} \quad (8)$$

where α = the plain stress/strain constraint factor with a value of 2.5 for current steel as recommended by BEASY [37]; S_{\max} = the maximum applied stress; σ_0 = the flow stress, taken to be the average of the uniaxial yield stress and uniaxial ultimate tensile strength of the

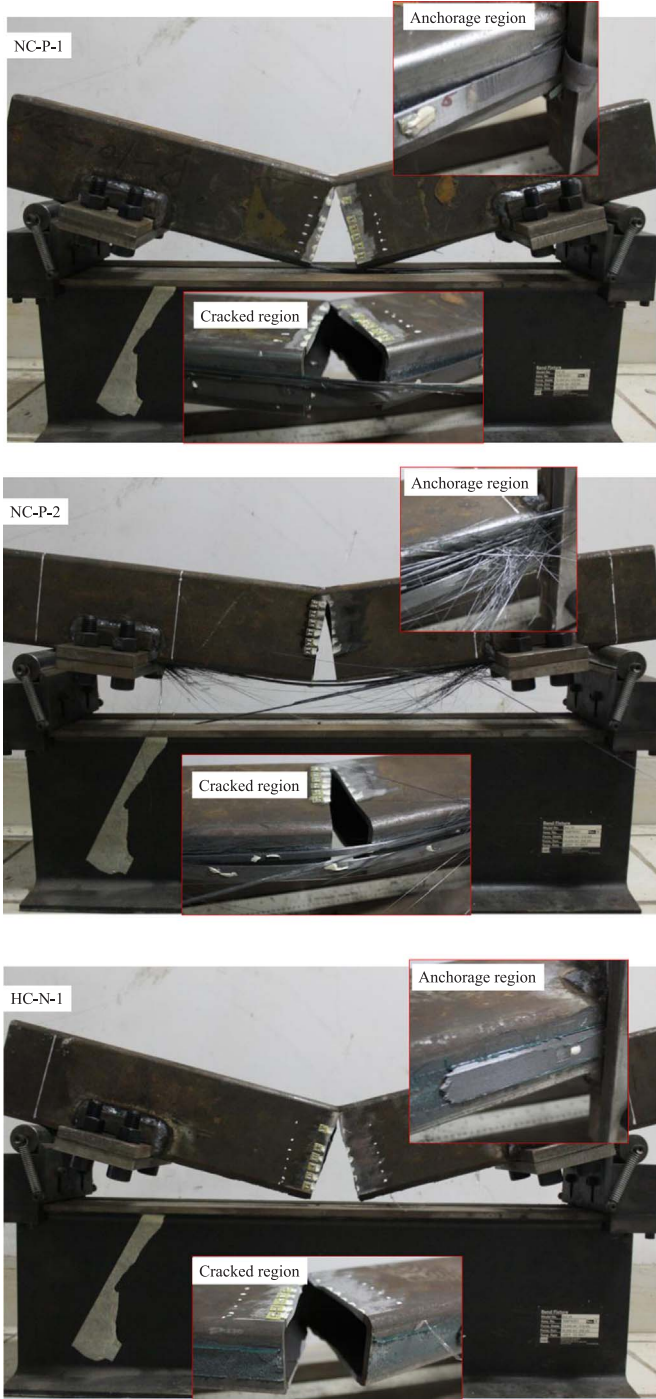


Fig. 4. Final failure of strengthened specimens.

material and K_{op} = the opening stress intensity factor below which the crack is closed.

3.1. Numerical model description

Finite element models were developed based on tested specimens by using the commercial finite element software package ABAQUS to predict the stress intensity factors. To reduce computational time consumption, a half finite element (FE) model was developed due to symmetry. The numerical model is mainly comprised of steel beam, CFRP plate and adhesive layer. A general view of the three-dimensional model is presented in Fig. 5. The supports were also modeled and specified with constraints as test settings. Two concentrated loads were

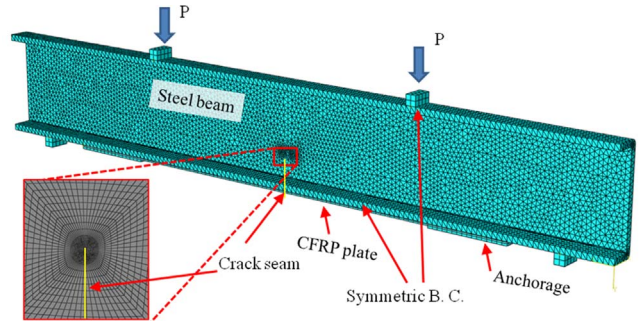


Fig. 5. Half FE model details.

applied to the top of the specimens. The prestressing stress of the CFRP plate can be simulated by applying an initial stress or by decreasing the temperature of CFRP plates [38]. The later approach was adopted in this study. We defined a decreasing temperature field to the CFRP plates before loading step. This can introduce prestress to the prescribed prestressing level after several iterations.

The adopted geometries and material properties were the same as those used for the tested specimens. The steel and CFRP materials were modeled as a linear, elastic material with Poisson's ratios of 0.3 and 0.2, respectively. The adhesive layer was modeled with cohesive elements (COH3D8) of mesh size $0.4 \text{ mm} \times 5 \text{ mm}$. The triangular cohesive zone model (CZM) formulation was chosen for its simplicity. And the traction separation law assumes an initial linear elastic behavior followed by a linear damage evolution. Damage initiation was specified by the maximum nominal stress criterion. The initial stiffness were determined from the adhesive material properties. The normal modulus (E) is 1900 MPa and shear modulus (G_1, G_2) are both 699 MPa. Debonding was not modeled considering the fatigue loading levels are not high during the test [39].

The steel was modeled using 3D, 10-node quadratic tetrahedron elements while the CFRP was modeled using 3D, 8-node elements with reduced integration. A mesh convergence study was conducted to achieve reliable results and guarantee simulation efficiency. Two concentrated loads were applied to the two rigid blocks. Supports were also defined as experimental settings. Crack tip singularity was modeled using classical wedge-shaped crack tip elements able to capture the crack tip feature. The SIFs at the crack front of cracked RHS steel beams were determined by the J-integral approach. Fig. 6 illustrates SIF values with crack lengths of specimens with a 30 mm initial crack depth. It can be observed that CFRP plate repairing brought down the SIFs compared to bare specimens.

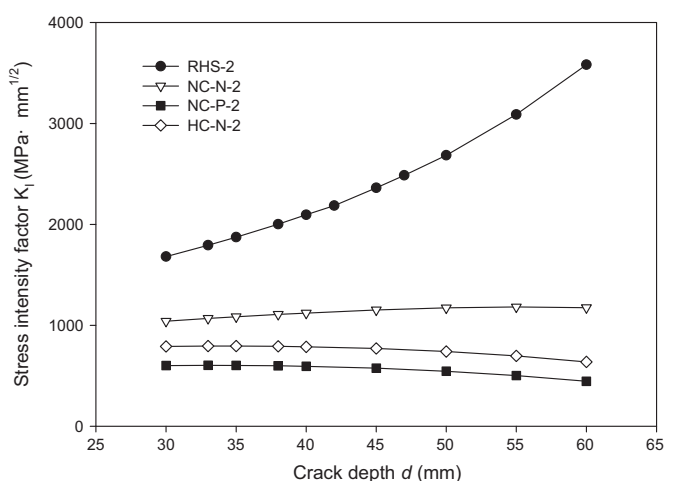


Fig. 6. Stress intensity factor values.

3.2. Validation using experimental results

To validate the numerical simulation technique of the cracked beams under fatigue loading, the results from the numerical simulations were compared with those from the experimental testing data. The fatigue life calculation method is well established in LEFM for cracked members. It includes following procedures: (i) SIF values extracted from numerical simulation with various crack depths; (ii) fitting equations for dotted numerical results; (iii) crack propagation life by integrating Eq. (1) as

$$N = \int_{a_i}^{a_f} \frac{(1-R)^m \cdot \left(1 - \frac{\Delta K}{(1-R)K_c}\right)^q}{C \cdot (1-f)^m \cdot \Delta K^m \cdot \left(1 - \frac{\Delta K_{th}}{\Delta K}\right)^p} \quad (9)$$

The initial crack depth, a_i , was defined for a tested beam. The final crack depth, a_f , was determined as 60% of beam height. With the employment of the NASGRO crack growth equation, the effects of stress ratio, which is 0.1 as used in the fatigue test, is considered. Material constants C and m , which are 3.98×10^{-13} (da/dN in mm/cycle and ΔK in MPa mm $^{1/2}$) and 2.88, were adopted as recommended by the British Standards Institution (BSI) for steel in air [40]. Constants p and q are both assumed as 0.5 by referring to the NASGRO database in Beasy [37]. The values of ΔK_{th} and K_c are recommended by BSI as 148.6 MPa mm $^{1/2}$ and 6950 MPa mm $^{1/2}$, respectively.

Experimental data and numerical predictions are presented in Fig. 7 for comparison. Moreover, Fig. 7 shows a reasonably good agreement between the simulated and experimental results in terms of fatigue life.

4. Parametric study

The fracture mechanics method with finite element model was then used to perform several parametric studies on RHS steel beams. Several RHS steel beams with a 10 mm initial crack were selected as specimens to be repaired with various parameters. The considered parameters are CFRP width W_c , Young's modulus of CFRP E_c and a prestressing stress level of CFRP plate. The width ranges from 10 mm to 30 mm. Young's modulus of CFRP plates were specified as 1.00×10^5 MPa, 1.91×10^5 MPa and 3.00×10^5 MPa. With prestressed CFRP, two levels were chosen at 12% and 22%, which correspond to 384 MPa and 680 MPa in CFRP plates as summarized in Table 3. Their effects on crack propagation life were discussed under the same fatigue loadings of the specimen RHS-1 that range from 8 kN to 80 kN.

4.1. Influence of CFRP plate width

To investigate the influence of the amount of the repairing CFRP on

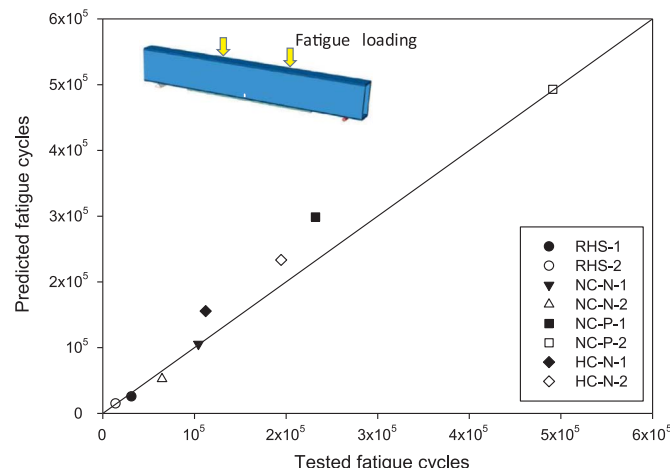


Fig. 7. Comparison of experimental fatigue life and numerical results.

Table 3
Parametric study matrix.

Group	CFRP width W_c (mm)	CFRP modulus E_c ($\times 10^5$ MPa)	CFRP prestressing level (%)
E	10	1.91	0, 12, 22
F	30	1.91	0, 12, 22
G	10	1.00	0, 12, 22
H	10	3.00	0, 12, 22
I	30	1.00	0, 12, 22
J	30	3.00	0, 12, 22
K	20	1.00	0
L	20	3.00	0

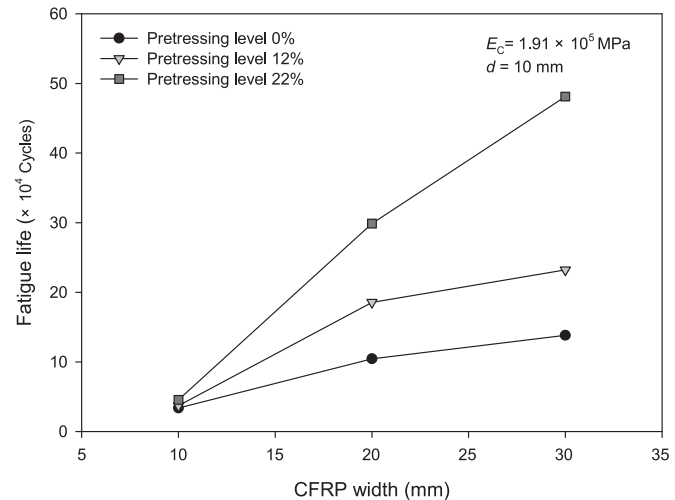


Fig. 8. Influence of CFRP plate widths on fatigue life.

fatigue life of the cracked RHS beams, three different widths of 10 mm, 20 mm and 30 mm were considered with other identical geometric parameters. Meanwhile, the prestressing levels in CFRP plates were also considered. Their fatigue crack propagation lives are plotted in Fig. 8. It is clear that by increasing CFRP widths, the fatigue propagation life increases. When the cracked specimens were patched with non-prestressed CFRP plates with various widths, the fatigue life was increased from 3.39×10^4 cycles to 13.81×10^4 cycles. With prestressing level of 22% CFRP repaired specimens, the fatigue life was increased from 4.54×10^4 cycles to 48.12×10^4 cycles when plate widths increased from 10 mm to 30 mm.

Fig. 9 illustrates the fatigue life (N) ratio, R_N , between repaired and

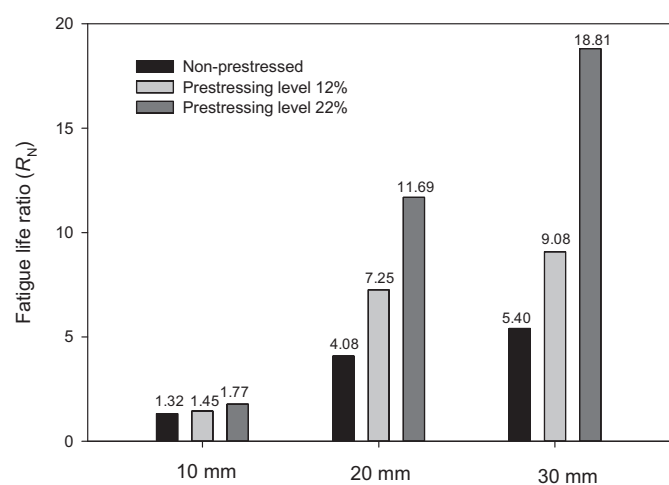


Fig. 9. Increment of crack propagation life with respect to the CFRP plate widths.

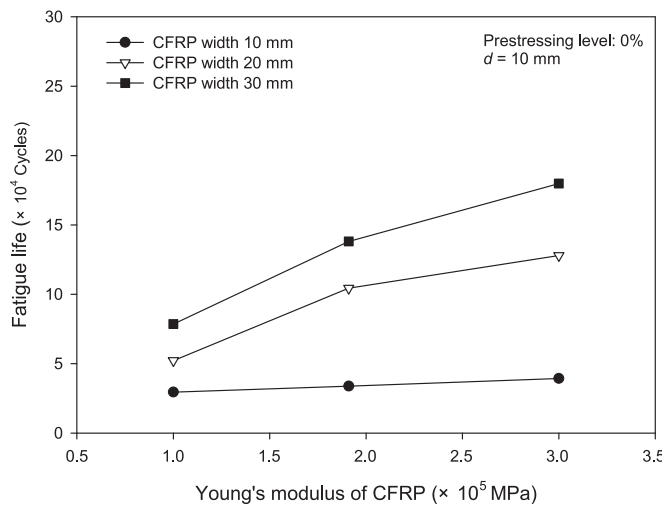


Fig. 10. Influence of CFRP moduli on fatigue life.

un-repaired specimens predicted by a numerical approach. When specimens were repaired with non-prestressed CFRP plates, R_N increased from about 1.32–5.40 (an increment of about 308%) when the CFRP widths increased from 10 mm to 30 mm. When the prestressing level in CFRP plates were 22% of the ultimate strength, R_N increased from about 1.77–18.81 (an increment of about 960%) with the augment of CFRP width. The increment effect was significant for higher prestressing levels.

4.2. Influence of CFRP plate modulus

In this section, cases using non-prestressed CFRP plates with various Young's moduli were analyzed on the fatigue crack propagation life. All parameters were same except for the CFRP modulus, which was taken as 1.00×10^5 MPa, 1.91×10^5 MPa and 3.00×10^5 MPa, respectively. A general trend in Fig. 10 is that a higher value of the CFRP modulus resulted in a longer fatigue crack propagation life.

The results were discussed with modulus and plate width. It can be observed from Fig. 11 that the fatigue life ratios, R_N , were about 1.15, 1.32 and 1.54 when CFRP width was 10 mm. The R_N were about 3.07, 5.40 and 7.03 when the CFRP width was 30 mm. It can be concluded that the CFRP modulus had a moderate effect on fatigue life increment compared to CFRP width.

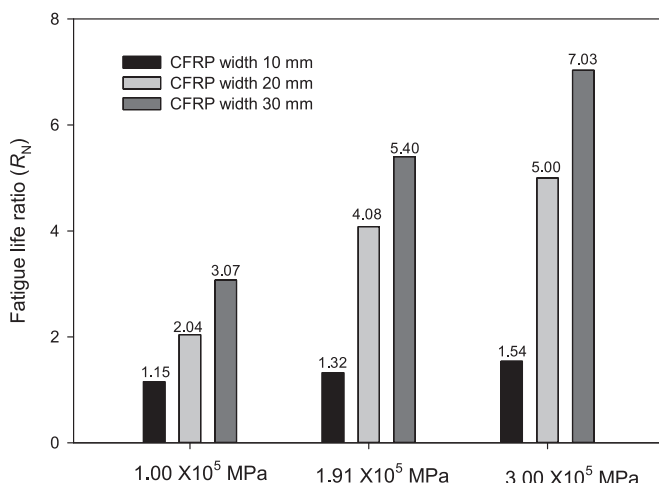


Fig. 11. Increment of crack propagation life with respect to the CFRP moduli.

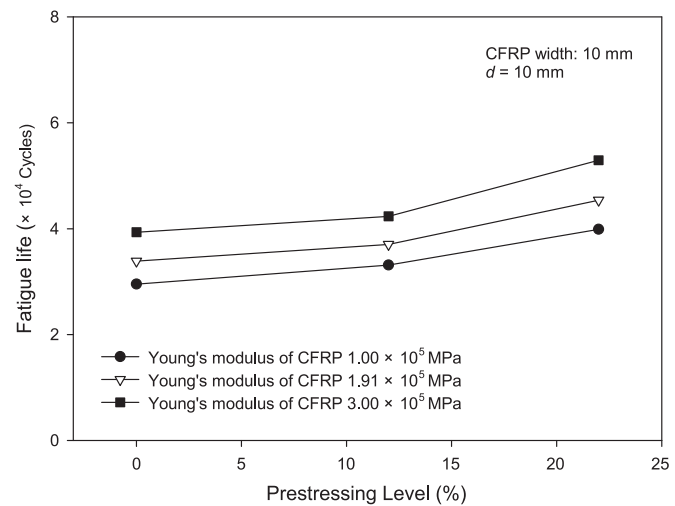


Fig. 12. Influence of CFRP prestressing levels on fatigue life.

4.3. Influence of CFRP plate prestressing level

To study the effect of CFRP plate prestressing levels on fatigue lives, specimens were patched with CFRP plates of certain widths. The prestressing levels were 12% and 22% considering the test scheme. They were compared with non-prestressed CFRP repaired specimens. Fig. 12 illustrates fatigue lives with prestressing levels when the CFRP width was 10 mm. It is evident that higher prestressing levels result in longer lives. The fatigue lives increased to about 1.32, 1.45 and 1.77 times that of the unrepairs specimens when the CFRP modulus was 1.91×10^5 MPa (Fig. 13). When the CFRP width increased to 30 mm, the fatigue life ratios, R_N , were significantly enhanced to 5.40, 9.08 and 18.81 (Fig. 9). It can be concluded that higher prestressing levels yield better fatigue life enhancement with wider CFRP plates.

5. Conclusions

This paper presents the effects of the CFRP strengthening method on the fatigue crack propagation life of RHS steel beams through application of a validated numerical approach. Fatigue tests were carried out to cracked RHS steel beams with various initial crack depths, material moduli and prestressing levels in CFRP. Thereafter, three-dimensional finite element models were developed based on the configurations of the test specimens. Fatigue life prediction with numerical approach was validated with experimental data with reasonable accuracy. A

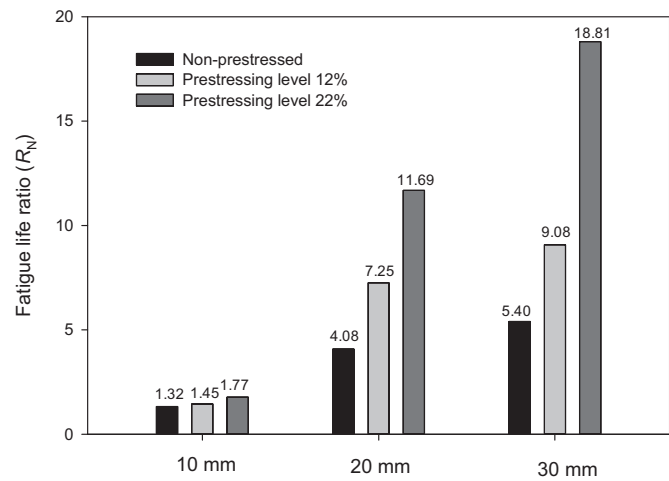


Fig. 13. Increment of fatigue crack propagation life with respect to the CFRP prestressing levels.

parametric study was then performed to evaluate the effect of CFRP configurations on the fatigue crack propagation life of repaired specimens. The results showed that prolonged fatigue crack propagation life could be achieved by increasing the width, the Young's modulus and the prestressing level of CFRP plates. The effect of CFRP prestressing level became more prominent with a wider CFRP plate. These enhancements can be estimated to design future rehabilitation of cracked RHS steel beams with prestressed CFRP plates.

Acknowledgments

This work was financially supported by NSFC (Grant no. 51678440), the Fundamental Research Funds for the Central Universities and the National Key Technology R & D Program (Grant no. 2014BAD08B01).

References

- [1] R.E. Koller, I. Stoecklin, S. Valet, G.P. Terrasi, CFRP-strengthening and long-term performance of fatigue critical welds of a steel box girder, *Polymer* 6 (2014) 443–463, <http://dx.doi.org/10.3390/polym6020443>.
- [2] J.M. Ricles, M.F. Hebor, Residual strength and epoxy-based grout repair of corroded offshore tubulars, 1994.
- [3] T.G. Ghazijahani, H. Jiao, D. Holloway, Fatigue tests of damaged tubes under flexural loading, *Steel Compos. Struct.* 19 (2015) 223–236.
- [4] J. Haedir, X.L. Zhao, Design of CFRP-strengthened steel CHS tubular beams, *J. Constr. Steel Res.* 72 (2012) 203–218, <http://dx.doi.org/10.1016/j.jcsr.2011.12.004>.
- [5] J. Wardenier, J. a. Packer, X.L. Zhao, G.J. Van der Vegt, *Hollow Sections in Structural Applications*, Bouwen met Staal, Zoetermeer, The Netherlands, 2010.
- [6] X.L. Zhao, L. Zhang, State-of-the-art review on FRP strengthened steel structures, *Eng. Struct.* 29 (2007) 1808–1823, <http://dx.doi.org/10.1016/j.engstruct.2006.10.006>.
- [7] J.G. Teng, T. Yu, D. Fernando, Strengthening of steel structures with fiber-reinforced polymer composites, *J. Constr. Steel Res.* 78 (2012) 131–143, <http://dx.doi.org/10.1016/j.jcsr.2012.06.011>.
- [8] J. Haedir, M.R. Bambach, X.L. Zhao, R.H. Grzebieta, Strength of circular hollow sections (CHS) tubular beams externally reinforced by carbon FRP sheets in pure bending, *Thin-Walled Struct.* 47 (2009) 1136–1147, <http://dx.doi.org/10.1016/j.tws.2008.10.017>.
- [9] A.W. Al Zand, W.H.W. Badaruzzaman, A.A. Mutalib, S.J. Hilo, Rehabilitation and strengthening of high-strength rectangular CFST beams using a partial wrapping scheme of CFRP sheets: experimental and numerical study, *Thin-Walled Struct.* 114 (2017) 80–91, <http://dx.doi.org/10.1016/j.tws.2017.01.028>.
- [10] Q.Q. Yu, T. Chen, X.L. Gu, X.L. Zhao, Z.G. Xiao, Fatigue behaviour of CFRP strengthened steel plates with different degrees of damage, *Thin-Walled Struct.* 69 (2013) 10–17, <http://dx.doi.org/10.1016/j.tws.2013.03.012>.
- [11] P. Feng, L. Hu, X.L. Zhao, L. Cheng, S. Xu, Study on thermal effects on fatigue behavior of cracked steel plates strengthened by CFRP sheets, *Thin-Walled Struct.* 82 (2014) 311–320, <http://dx.doi.org/10.1016/j.tws.2014.04.015>.
- [12] R. Emdad, R. Al-mahaidi, Effect of prestressed CFRP patches on crack growth of centre-notched steel plates, *Compos. Struct.* 123 (2015) 109–122, <http://dx.doi.org/10.1016/j.compositstruct.2014.12.007>.
- [13] Y. Huawen, C. König, T. Ummenhofer, Q. Shizhong, R. Plum, Fatigue performance of tension steel plates strengthened with prestressed CFRP laminates, *J. Compos. Constr.* 14 (2010) 609–615, [http://dx.doi.org/10.1061/\(ASCE\)CC.1943-5614.000111](http://dx.doi.org/10.1061/(ASCE)CC.1943-5614.000111).
- [14] P. Colombi, A. Bassetti, A. Nussbaumer, Crack growth induced delamination on steel members reinforced by prestressed composite patch, *Fatigue Fract. Eng. Mater. Struct.* 26 (2003) 429–437, <http://dx.doi.org/10.1046/j.1460-2695.2003.00642.x>.
- [15] B. Täljsten, C.S. Hansen, J.W. Schmidt, Strengthening of old metallic structures in fatigue with prestressed and non-prestressed CFRP laminates, *Constr. Build. Mater.* 23 (2009) 1665–1677, <http://dx.doi.org/10.1016/j.conbuildmat.2008.08.001>.
- [16] E. Ghafoori, M. Motavalli, J. Botsis, A. Herwig, M. Galli, Fatigue strengthening of damaged metallic beams using prestressed unbonded and bonded CFRP plates, *Int. J. Fatigue* 44 (2012) 303–315, <http://dx.doi.org/10.1016/j.ijfatigue.2012.03.006>.
- [17] P. Colombi, A. Bassetti, A. Nussbaumer, Analysis of cracked steel members reinforced by pre-stress composite patch, *Fatigue Fract. Eng. Mater. Struct.* 26 (2003) 59–66, <http://dx.doi.org/10.1046/j.1460-2695.2003.00598.x>.
- [18] H. Nakamura, Y. Yamamura, H. Ito, F. Lin, K. Maeda, Development of Pre-Tensioning Device for CFRP Strips and Applicability to Repair of Cracked Steel Members, *Adv. Struct. Eng.* 17 (2014) 1705–1718, <http://dx.doi.org/10.1260/1369-4332.17.12.1705>.
- [19] Y.J. Kim, K.A. Harries, Fatigue behavior of damaged steel beams repaired with CFRP strips, *Eng. Struct.* 33 (2011) 1491–1502, <http://dx.doi.org/10.1016/j.engstruct.2011.01.019>.
- [20] J. Deng, M.M.K. Lee, Fatigue performance of metallic beam strengthened with a bonded CFRP plate, *Compos. Struct.* 78 (2007) 222–231, <http://dx.doi.org/10.1016/j.compositstruct.2005.09.003>.
- [21] A. Hmidan, Y.J. Kim, S. Yazdani, CFRP repair of steel beams with various initial crack configurations, *J. Compos. Constr.* 15 (2011) 952–962, [http://dx.doi.org/10.1061/\(ASCE\)CC.1943-5614.0000223](http://dx.doi.org/10.1061/(ASCE)CC.1943-5614.0000223).
- [22] M. Elchalakani, Rehabilitation of corroded steel CHS under combined bending and bearing using CFRP, *J. Constr. Steel Res.* 125 (2016) 26–42, <http://dx.doi.org/10.1016/j.jcsr.2016.06.008>.
- [23] D. Linghoff, M. Al-Emrani, R. Kliger, Performance of steel beams strengthened with CFRP laminate - Part 1: laboratory tests, *Compos. Part B Eng.* 41 (2010) 509–515, <http://dx.doi.org/10.1016/j.compositesb.2009.05.008>.
- [24] D. Linghoff, M. Al-Emrani, Performance of steel beams strengthened with CFRP laminate - Part 2: Fe analyses, *Compos. Part B Eng.* 41 (2010) 516–522, <http://dx.doi.org/10.1016/j.compositesb.2009.07.002>.
- [25] P. Colombi, G. Fava, Experimental study on the fatigue behaviour of cracked steel beams repaired with CFRP plates, *Eng. Fract. Mech.* 145 (2015) 128–142, <http://dx.doi.org/10.1016/j.engfracmech.2015.04.009>.
- [26] H. Jiao, H.B. Phan, X.L. Zhao, Fatigue behaviour of steel elements strengthened with stand CFRP sheets, *Adv. Struct. Eng.* 17 (2014) 1719–1728, <http://dx.doi.org/10.1260/1369-4332.17.12.1719>.
- [27] Q.Q. Yu, Y.F. Wu, Fatigue strengthening of cracked steel beams with different configurations and materials, *J. Compos. Constr.* (2016), [http://dx.doi.org/10.1061/\(ASCE\)CC.1943-5614.0000750](http://dx.doi.org/10.1061/(ASCE)CC.1943-5614.0000750).
- [28] S. Walbridge, K. Soudki, F. Vatandoost, Fatigue retrofitting of welded steel cover plates using Pre-stressed carbon fibre reinforced polymer strips, *Struct. Eng. Int. J. Int. Assoc. Bridg. Struct. Eng.* 21 (2011) 279–284, http://dx.doi.org/10.2749/101686611_x13049248220122.
- [29] E. Ghafoori, M. Motavalli, Lateral-torsional buckling of steel I-beams retrofitted by bonded and un-bonded CFRP laminates with different pre-stress levels: experimental and numerical study, *Constr. Build. Mater.* 76 (2015) 194–206, <http://dx.doi.org/10.1016/j.conbuildmat.2014.11.070>.
- [30] M. Elchalakani, CFRP strengthening and rehabilitation of degraded steel welded RHS beams under combined bending and bearing, *Thin-Walled Struct.* 77 (2014) 86–108, <http://dx.doi.org/10.1016/j.tws.2013.12.002>.
- [31] M. Elchalakani, Plastic collapse analysis of CFRP strengthened and rehabilitated degraded steel welded RHS beams subjected to combined bending and bearing, *Thin-Walled Struct.* 82 (2014) 278–295, <http://dx.doi.org/10.1016/j.tws.2014.05.002>.
- [32] Z.G. Xiao, X.L. Zhao, Cfrp repaired welded thin-walled cross-beam connections subject to in-plane fatigue loading, *Int. J. Struct. Stab. Dyn.* 12 (2012) 195–211, <http://dx.doi.org/10.1142/S0219455412004653>.
- [33] R.E. Koller, I. Stoecklin, S. Valet, G.P. Terrasi, CFRP-strengthening and long-term performance of fatigue critical welds of a steel box girder, *Polymer* 6 (2014) 443–463, <http://dx.doi.org/10.3390/polym6020443>.
- [34] P. Paris, F. Erdogan, A critical analysis of crack propagation laws, *J. Basic Eng.* 85 (1963) 528–533, <http://dx.doi.org/10.1115/1.3656900>.
- [35] R.G. Forman, S.R. Mettu, Behavior of surface and corner cracks subjected to tensile and bending loads in a Ti-6Al-4V alloy (1990).
- [36] J.C. Newman, A crack opening stress equation for fatigue crack growth, *Int. J. Fract.* 24 (1984) R131–R135, <http://dx.doi.org/10.1007/BF00020751>.
- [37] BEASY Ltd, BEASY 10.14, Ashurst, Southampton SO40 7AA, United Kingdom: Ashurst Lodge. (2016).
- [38] W. Ren, L.H. Sneed, Y. Yang, R. He, Numerical simulation of prestressed precast concrete bridge deck panels using damage plasticity model, *Int. J. Concr. Struct. Mater.* 9 (2015) 45–54, <http://dx.doi.org/10.1007/s40069-014-0091-2>.
- [39] H.B. Liu, X.L. Zhao, R. Al-Mahaidi, Effect of fatigue loading on bond strength between CFRP sheets and steel plates, *Int. J. Struct. Stab. Dyn.* 10 (2010) 1–20, <http://dx.doi.org/10.1142/S0219455410003348>.
- [40] British Standards Institution, Guide to Methods for Assessing the Acceptability of Flaws in Metallic Structures, British Standards Institution, London, 2005.



Fatigue strength of repaired cracks in base material of high strength steels



A. Akyel ^{a,b,*}, M.H. Kolstein ^b, F.S.K. Bijlaard ^b

^a Materials Innovation Institute (M2i), Delft, Netherlands

^b Delft University of Technology, Delft, Netherlands

ARTICLE INFO

Article history:

Received 6 October 2016

Received in revised form 27 September 2017

Accepted 4 October 2017

Available online 10 October 2017

Keywords:

Very high strength steels

Repair weld

Base material

Artificial crack

Fatigue

ABSTRACT

Fatigue crack formation is an inevitable issue for welded steel structures subjected to cyclic loading. Accordingly, repair of the fatigue crack in welded steel structures is unavoidable to prolong fatigue life. However, there is limited knowledge available about the procedure to be adopted for the repair and the life extension to be expected after the repair. The current paper is focused on the effects of the repaired artificial crack in the base material of S690 and S890 high strength rolled steels on the fatigue strength of the material. An artificial crack was created in the middle of the plate test specimens by spark machining and subsequently, the crack was repaired by using the FCAW (flux-cored arc welding) process. The repaired specimens were tested in a four point bending test rig with a constant amplitude loading for creating a uniform bending moment at the weld region such that the weld cap to be exposed to tensile stresses. The test results show that most of the fatigue cracks initiated at the start-stop points of the weld cap and the fatigue crack initiation life of the specimens occupy approximately 45% of the total fatigue life. The statistical analysis of the test results revealed that the characteristic fatigue strength of the repaired specimens is very close to the detail category 160 of EN 1993-1-9 [5].

© 2017 Elsevier Ltd. All rights reserved.

1. Introduction

Modern steel manufacturing techniques make it possible to produce very high strength steels for various application purposes. The application of very high strength steels has enormously increased in the automotive industry in the course of the last decades. Although very high strength steels with good weldability, toughness and yield strength up to 1300 MPa are available for structural application purposes, the use of very high strength steels in the civil engineering structures is rather limited due to lack of knowledge about consequences of manufacturing process and limited available experimental evidence of the structural behaviour of the material.

The use of very high strength steels results in slender members with reduced wall thicknesses which lead to low self-weight and volume of structures. This results in cost savings in production, transportation and erection. In case of welded connections, the slender member with thin wall thicknesses will allow for the smaller weld volumes hence, decrease in weld consumables and lower energy consumption to make the welded connections. Nevertheless, low self-weight of very high strength steel structure causes a high stress variation under live load. Consequently, the fatigue strength of very high strength steel structures is one of the main design criteria for the effective application.

Gurney [1] determined that the fatigue strength of the material becomes more sensitive to the entity of notches and to the surface condition with the enhancement of the material yield strength. In accordance with this, the fatigue sensitivity can be reduced with the reduction of stress concentrations. With the disregarding surface condition of the material, the fatigue strength increases with the higher yield strength of the material. Maddox [2] concluded that the fatigue strength of welded connections is independent of the material yield strength. This was based on the assumption that the welding application leads to micro-cracks which are likely to give rise to fatigue cracks. Accordingly, the fatigue crack propagation life is determinant for the fatigue life of welded connections and depends on the stress ranges, being independent of yield strength. The determination of the fatigue strength of the base material and welded connections made of very high strength steels has become one of the main research topics in the last decade. Demofonti et al. [3] performed fatigue tests on the butt welded specimens with 10 mm thickness and made of S355 up to S960. The results showed that no significant fatigue strength difference exists under constant amplitude loading condition while the beneficial effects of S960 steel investigated under variable amplitude loading condition. In addition, the advantage of very high strength steels on the fatigue strength was determined with reduction of the notch factor which was achieved by machining of the welds. In the framework of a research program of ECSC, Puthli et al. [4] carried out fatigue tests on various butt welded specimens with a thickness of 6–8 mm made of S690, S960 and S1100. The characteristic fatigue strength for all steel

* Corresponding author at: Materials Innovation Institute (M2i), Delft, Netherlands.
E-mail address: a.akyel@tudelft.nl (A. Akyel).

Table 1

Chemical compositions of test materials [%wt].

Grade	C %	Si %	Mn %	P %	S %	Cr %	Mo %	Ni %
S690	0.16	0.19	0.87	0.012	0.002	0.33	0.22	0.06
S890	0.168	0.281	0.98	0.012	0.0008	0.494	0.511	0.98
Grade	V %	Nb %	Al %	Cu %	N %	B %		
S690		0.026	0.085		0.0038	0.002		
S890		0.041	0.011	0.074	0.024		0.0022	

Table 2

Mechanical properties of test materials.

Grade	R _{p,0.2} [MPa]	R _m [MPa]	A5 %	KVC	
				−40 °C [J]	−20 °C [J]
S690	800	830	17		251
S890	985	1051	14.3	36	

grades was found to be above of the recommended design values of EN 1993-1-9 [5]. The test results of the specimens made of S1100 showed the tendency for the decrease of the free slope to $m = -5$. Pijpers et al. [6] concluded from the fatigue tests on the base material and transverse butt welded specimens made of S690 and S1100 that the fatigue crack initiation life of very high strength steels is longer than mild strength steels. Kuhlmann et al. [7] showed that the post weld impact treatments are very effective for improving the fatigue strength of welded connections made of very high strength steels. The effectiveness of post weld impact treatments on fatigue strength of very high strength steels is already standardised in IIW recommendations [8]. Berg et al. [17] concluded that the fatigue strength of high frequency hammer peening treated welded connections made of S960, S1100 and S1300 is at least twice the fatigue strength of the as-welded condition.

As concluded by Gurney [1] and Pijpers [9], the fatigue strength of very high strength steels is susceptible to the surface conditions and the presence of notches. Therefore, the base material with high surface roughness might cause the fatigue crack initiation in the structural elements or even in the base material of welded connections made of very high strength steels. Once the cracks are detected the repair of the base material becomes essential for fatigue life extension.

Yamasaki, et al. [10] focused on the effects of the repair weld on the fatigue crack growth behaviour in the base material of JIS SM50A steel plates with the yield strength of 323 MPa. Fatigue cracks with certain length were created in the pre-notched specimens. The created fatigue cracks were repaired by X-shape welding under three conditions: with applying an axial tensile stress, without external stress and open cracks condition to induce compressive stress with releasing open state after the repair. The results showed that the fatigue crack growth rate in the repaired specimens is higher than the growth rate in the base material and the artificially induced compressive stresses

improved the crack growth behaviour of the repaired specimens. Kudryavtsev et al. [11] investigated the effectiveness of various repairs and retrofit methods for the fatigue cracks in the base material of low alloyed steel with the yield strength of 367 MPa. The hole drilled plate test specimens were subjected to fatigue load to create fatigue cracks at the edge of the hole. The crack propagation was permitted until certain size and the fatigue crack were repaired/retrofitted by the following techniques: drilling a hole at the crack tips with and without cold working, drilling a hole at the crack tips with installation of high strength bolts, overloading of the section, local explosive treatment, local heat treatment, repair by welding with and without ultrasonic peening of the weld toes. The repair by welding with ultrasonic peening provided the longest fatigue life after the repair. According to the test results, the repair by welding without ultrasonic peening was the second effective method for the fatigue cracks repair.

The state of art shows that the fatigue strength of the base material improves with the increase of the yield strength of the material. Nevertheless, the surface conditions can influence of the fatigue strength of the material and lead to fatigue crack initiation in the base material. For fatigue life extension, the repair of the base material cracks becomes essential. However, limited knowledge is available for the fatigue cracks repair procedure, consequences of the repair on the base material of very high strength steels and possible fatigue life extension after the repair of the cracks. This paper presents the repair process of artificially created cracks in the base material of S690 and S890 rolled steels and the fatigue test results of the repaired specimens.

2. Plate material properties

Table 1 gives the chemical compositions and Table 2 the mechanical properties of the test materials. The values of the mechanical properties and the chemical compositions are taken from the material certificates.

3. Test specimens

The test specimens were cut from S690 and S890 plates by water cutting and have a length of 990 mm and a width of 160 mm. In the middle, the width of the specimens was reduced to 150 mm (see Fig. 1).

For performing the repair procedure, a crack is artificially created in the middle of the specimens. The predefined crack shape and crack size ensure a controllable material removal process and a repair weld with similar length and depth in all specimens. Consequently, this allows the appropriate evaluation for the test results straightforward without the influences of variation due to manufacturing process. The artificial cracks were created by electrical discharge machining (EDM) process.

In practice, the fitness for purposes analysis is carried out to determine the time period for fatigue crack propagation from the detected crack size to the allowable critical crack size. Accordingly, the inspection and repair intervals are specified based on this time period. For simplification of the analysis, half the thickness of the section is assumed to be the allowable critical crack depth unless any other restrictions are defined. With the same approach, the depth of the artificial crack is

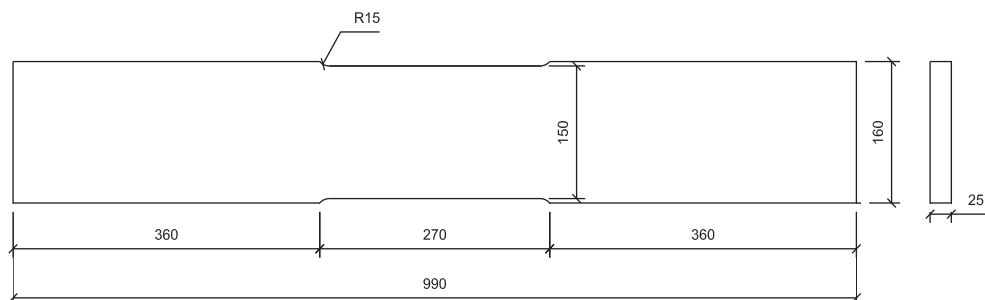


Fig. 1. Dimensions of the test specimens.

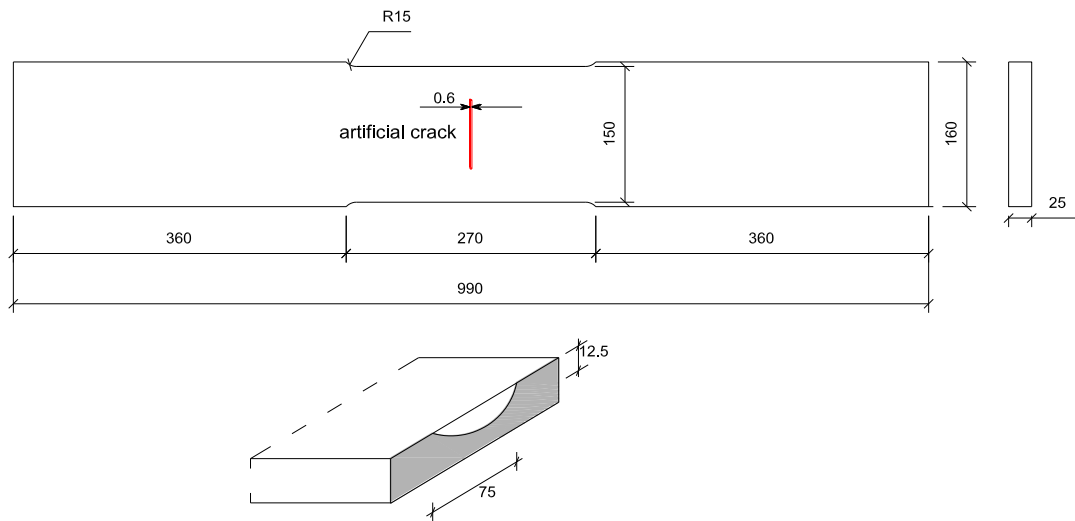


Fig. 2. Geometry of specimens and detail of artificial crack.

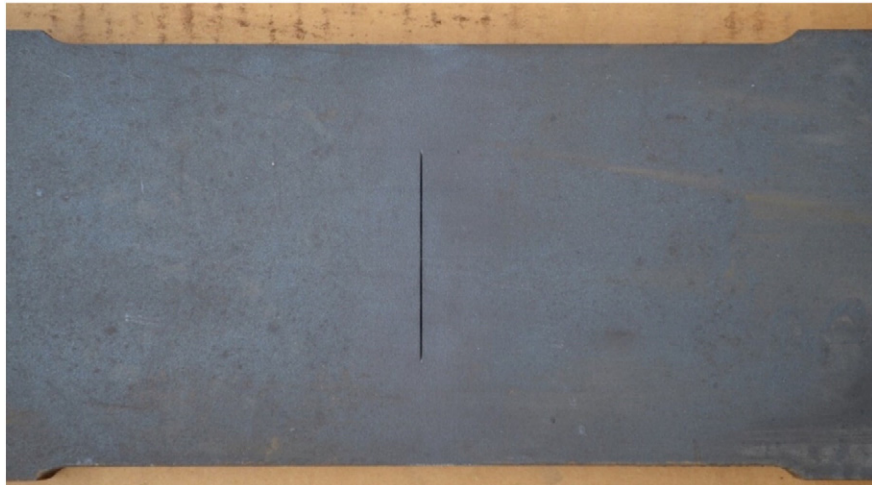


Fig. 3. Test specimen with artificial crack.

defined as half the thickness of the test plates; 12.5 mm. Since the fatigue induced cracks forms in a semi elliptical shape after the initiation, the artificial cracks were created with a semi elliptical shape to be more representative for real fatigue cracks. In this context, the crack length is defined as half the width of the plate which is 75 mm. Material removal process, the feasibility of welding and workability for the welder is taken into account for the determination of the crack length. Furthermore, the artificial crack width was kept as narrow as possible for more reflection a real fatigue crack and it is approximately equal to 0.6 mm. According to this description, the test specimen with an artificial crack is schematised in Fig. 2 and Fig. 3 shows the artificial crack in a test specimen.

For each steel grade, 9 test specimens were prepared and the specimens made of S690 steel grade are encoded as BR69x while BR89x encoding is used for the specimens made of S890 steel grade. Consequently, the experimental program consists of two test series.

4. Repairing artificial crack

The measurements took place on the length and the depth of the artificial crack in all specimens. The size of the crack was identical to the drawing in Fig. 2 while the shape of the crack showed some deviation

from the semi elliptical shape. Subsequently, border lines were drawn at the end of the crack length to specify the boundaries for the crack removal process herewith to avoid unnecessary material removal and



Fig. 4. Magnetic particle inspection after the crack removal process.

Table 3
Welding parameters for BR series.

Specimens	BR69x	BR89x
Rolled steel grade	S690	S890
Thickness [mm]	25	25
Length [mm]	990	990
Width [mm]	150	150
Preheat temperature °C (min)	100	125
Interpass temperature °C (max)	165	165
Weld metal	Megafill 742 M	Megafill 1100 M
Weld process	FCAW	FCAW
Heat input [kJ/mm]	1.2–1.8	1.2–1.8



Fig. 5. Reshaping start-stop points at the weld cap.

longer weld grooves. The crack removal process was executed with a disc grinder and burr grinder where the disc grinder was used at the initial stage to remove a small amount of the material and the further removal process was continued by the burr grinder.

One of the important requirements of fatigue cracks repair is to ensure complete crack removal as well as to prevent unnecessary material removal. In practice, the crack removal process is usually executed gradually with regular inspection of a non-destructive testing (NDT). However, for the test specimens, the depth of the cracks was known in advance and therefore, the execution of the crack removal proceeded until visually estimated that the prepared weld groove is reached to the

depth of the artificial crack. Subsequent to a magnetic particle inspection on the prepared weld groove to ensure the complete crack removal (see Fig. 4), the groove was filled by welding which was executed by the flux-core arc welding (FCAW) process. Megafill 742 M and Megafill 1100 M filler materials were used for the welding of the specimens made of S690 and S890 respectively. Table 3 summarises the geometry of the specimens and the welding procedure of the repair weld.

In the repair of fatigue cracks, care should be taken that the method used must not cause an additional possible fatigue crack initiation locations and reasons for the deterioration of fatigue strength. Especially in the case of welding application, imperfections might be formed such as cracks, inclusions, undercut etc. and these imperfections can have significant effects on the fatigue strength of welded connections. Therefore, the repair welds in the specimens were examined by magnetic particle and ultrasonic inspection. The repair weld satisfied the quality requirements of EN-ISO 5817 [12].

Furthermore, start and stop points of weld layers usually show different geometrical shapes where a bulge occurs at the start point and cavity at the stop point and as a result, these geometrical features induce a high stress concentration. In addition, these locations usually contain weld defects, therefore, the start-stop points of each weld pass are usually ground for the elimination of these defects. According to Zhang, et al. [13], the start-stop point of the weld also causes high residual stresses compared to other location of the weld layers. As it is known, all these issues negatively affect the fatigue strength of welded connections. For avoiding the occurrence of the start-stop points are therefore preferable; however, it is not possible in the most of the cases. For multi pass welding, start-stop points of the weld layers should be distributed along the weld length to avoid concentrated start-stop point at a location with undesirable effects of them. Since the artificial cracks were placed in the middle of the test specimens, it was difficult to execute the welding process without start-stop points and the length of the repair weld is too short for distributing the start-stop points along the weld length. On the other hand, the stress concentration effects at the start-stop of the weld toe can be reduced by reshaping the start-stop points. In accordance with this, the start-stop points at the weld cap of the specimens were reshaped by a grinding process (see Fig. 5).

5. Fatigue test rig

The fatigue tests were carried out in the Stevin II Laboratory of the Delft University of Technology. The fatigue tests were executed with a four point bending test rig. (see Fig. 6). The specimens were loaded cyclically to initiate fatigue cracks in the repair welds and the growth

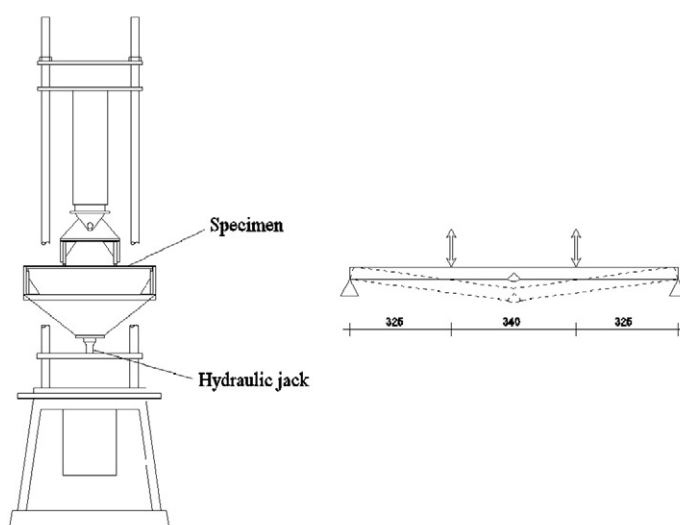


Fig. 6. Four point bending test rig.



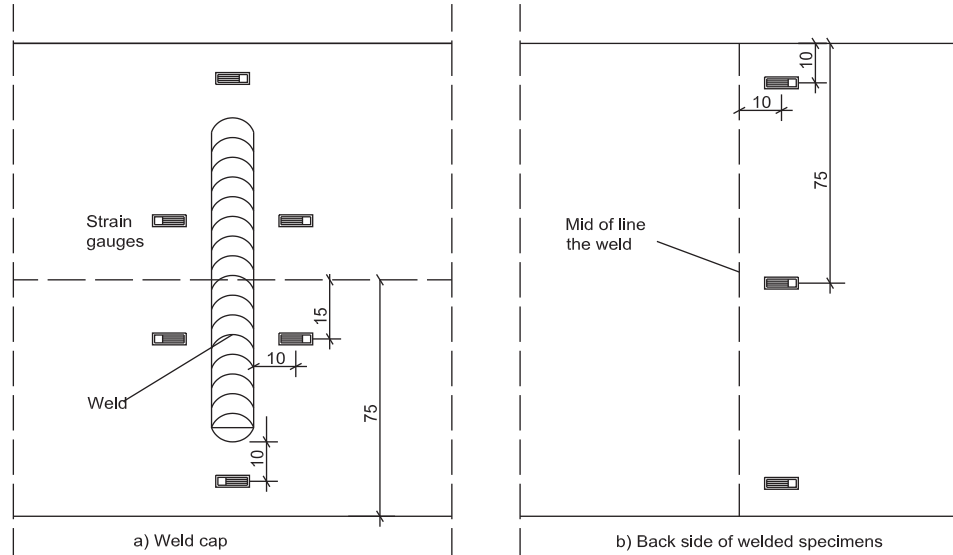


Fig. 7. Position of strain gauges on specimens.

of the cracks is monitored until failure which was defined such that the specimens broken into two pieces. The specimens were tested with force controlled loading, which means that the force range was constant during the test, even in the case of loss of stiffness when the cracks were growing.

By the use of the four point bending test setup, a uniform bending moment was created in the weld area, resulting in a compression and a tension zone over the thickness. The cap of the repair welds was in the tension zone and the tests were performed with stress ratio $R = 0.1$.

6. Crack monitoring

Strain gauges are attached to the specimens to measure the strain distribution at the surround of the repair weld and to monitor fatigue cracks development. The strain gauges were placed at 10 mm from the weld toe with a position relatively close to the expected locations of the fatigue crack initiation. At the both sides of the weld toe, two strain gauges were attached. In addition, one strain gauge was applied at 10 mm from both sides of the weld end, for detecting the crack

initiation at the end of start-stop points of the weld cap (see Fig. 7(a)). Moreover, three strain gauges were attached to the back side of the weld area to monitor crack propagation from the weld root which can be the case due to the remained crack tip in the test specimens during the crack removal process (see Fig. 7(b)). The average and range values of the measured forces, displacements and strains were digitally stored during the fatigue tests. The average values of the strain ranges were converted by the uniaxial Hook's law to determine the nominal stress range of each strain gauge and the nominal stress range from the strain gauge at the crack initiation location was used for the analysis.

In the initial stage of the fatigue tests, the range values of the strain gauges are approximately constant, straight line and the crack initiation is visible with the increase or decrease of the strain gauge range from the initial values. Increase or decrease of the values depends on the location of the strain gauges with the respect to the crack and the crack could lead to increase of tension, compression or release of the strain. Fig. 8 shows the strain ranges plots against the number of cycles of a fatigue specimen and the strain values start to deviate from its regular shapes at about 190,000 cycles which specify the fatigue crack initiation

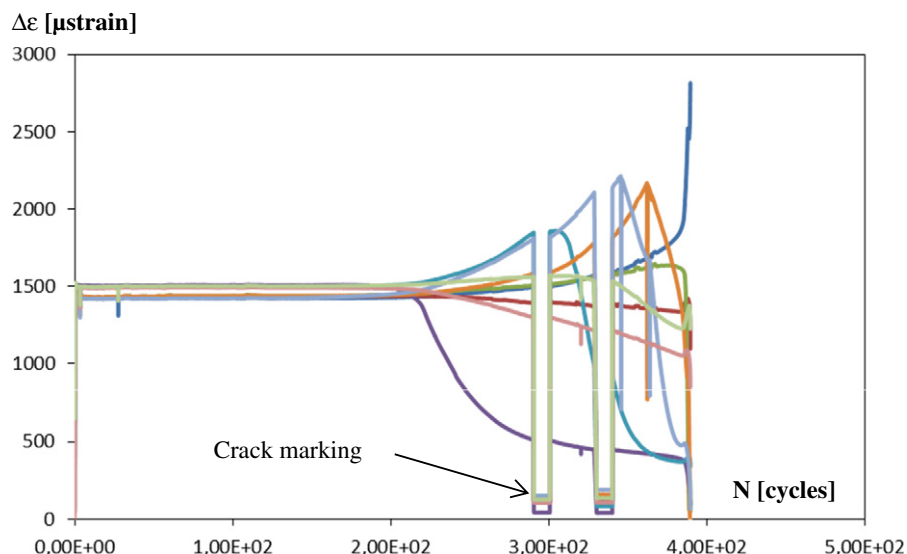


Fig. 8. Measured strain range versus the number of cycles.



Fig. 9. Beach marking on the fracture surface as result of crack marking procedure.

life of the specimen. An alarm system was used for the determination of the fatigue crack initiation life. The alarm system immediately shuts down the test rig in case of 0.0035 mm deviation in the displacement range which is the result of a decrease in the stiffness of the specimen due to the crack initiation. Thereafter, the fatigue cracks development was monitored by visual inspection.

The crack growth through the specimen thickness was monitored by the crack marking procedure. In this procedure, the lower stress level in the specimen rose to 90% of the upper stress level in the specimens while the upper level of the stress is kept identical and the test was executed for a limited number of cycles. Due to the alteration of the stress range, beach markings were created at the crack boundary and the beach marks became visible on the fracture surface after the failure of the specimens. Accordingly, the crack depth can be measured from the fracture surface and the crack size at the certain number of cycles can be specified. Fig. 9 presents the fracture surface of a specimen with the beach markings. Due to a low stress range during the crack marking procedure, the contribution of the crack marking cycles to the crack propagation is expected to be negligible and these cycles were excluded from the number of cycles at failure during the analysis.

7. Fatigue test results

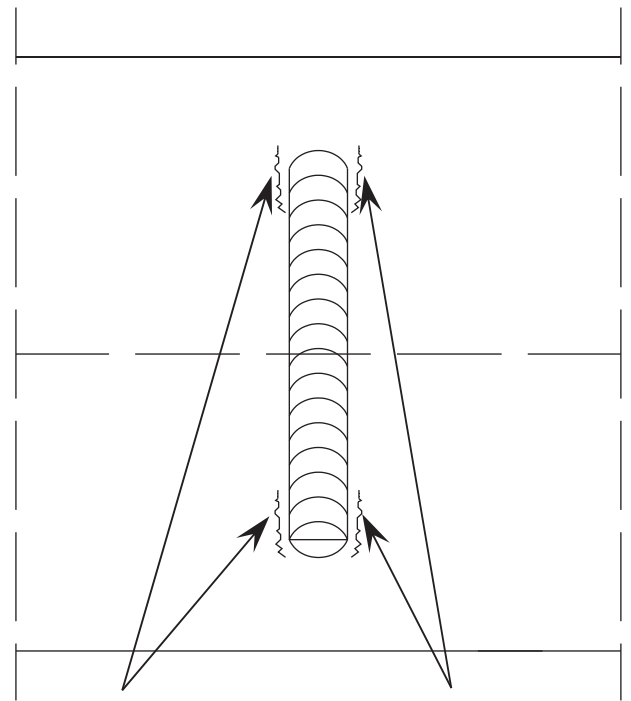
In all specimens, the crack initiation and propagation were observed at the weld toe, as expected. Although the surfaces of the start-stop points were ground to reduce stress concentration effect of these locations, the cracks were initiated at the start-stop points of the weld cap of the specimens made of S690 rolled steel plates. Fig. 10 indicates a schematic view of the fatigue crack initiation locations at the repair. After testing few specimens made of S890 steel plates, it was realised that the crack initiation also took place at the start-stop points of the repair weld. This can be explained by two features of start-stop points; high stress concentration because of the geometrical discontinuity and high residual tensile stresses. For further reduction of stress concentration effect, an additional grinding process was performed at the start-stop points of the welds to obtain a homogeneous weld shape and a smooth transition between the base material and the weld material (see Fig. 11). It was aimed to shift the crack initiation locations from the start-stop points of the weld to the middle of the weld toe. This additional grinding process resulted in a little shifting of the crack initiation points to the middle of the weld toe but not as desired. In one specimen of this series, no any crack initiation was observed after 3 million cycles and it is indicated as runout (Table 4).

Table 4 shows the applied nominal stress ranges to the specimens, $\Delta\sigma_n$, the number of cycles at the crack initiation, N_i , the fatigue crack propagation life, N_p and the number of cycles at failure, N_f of the specimens. In average, 45% of the fatigue life was occupied by the fatigue crack initiation life.

8. Evaluation of test results

The evaluation of the test results was made using the reference situation with the details presented in EN 1993-1-9 [5]. For the current specimens, it is difficult to make a comparison with a specific detail category of EN 1993-1-9 [5]. The specimens could not be assumed as base material since they contain the weld in the middle of them. In order to classify as a welded connection, the weld needs to be executed along the whole width and through the thickness of the specimens. Accordingly, the comparison was made with the detail categories of both situations; namely, the detail categories of the base material and V-shape welded connection. Fig. 12 shows the detail categories from EN 1993-1-9 [5] for the base material, V-shape welded connection and the applicable conditions of these detail categories.

The fatigue strength curves of EN 1993-1-9 [5] are categorised based on the characteristic stress range, $\Delta\sigma_c$, values at 2 million cycles. The characteristic stress range at 2 million cycles, $\Delta\sigma_c$, is calculated for a



Crack initiation locations

Fig. 10. Schema of the crack initiation locations in the test specimens.

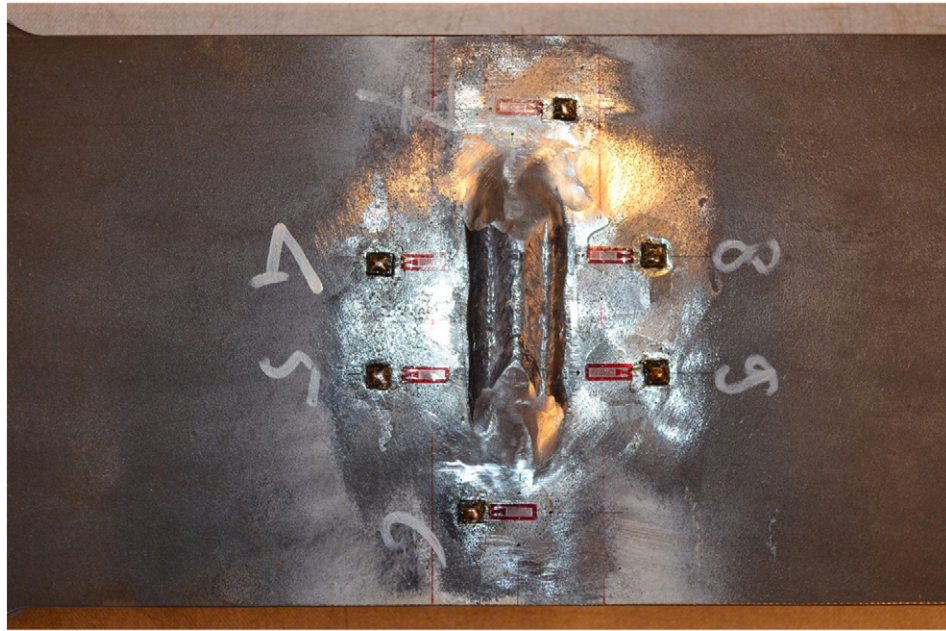


Fig. 11. A smooth transition between weld and base material of test specimen of BR89x series.

95% survival probability on a two-sided confidence level of 75% of the mean, parallel to the mean. Fatigue strength curve is represented by a log-log linear relationship between the nominal stress range, $\Delta\sigma_n$ and the number of cycles up to failure, N_f .

The statistical analysis was carried out on the test data according to Brozzetti et al. [14] and this analysis procedure is also utilised for the establishing fatigue strength curves of EN 1993-1-9 [5]. The fatigue strength curves of the test data were determined for a fixed slope -3 and a free slope which is calculated by the regression analysis. The fixed slope -3 is recommended by Brozzetti et al. [14] for the analysis and it is also convenient for the comparison with the detail categories of EN 1993-1-9 [5] which are calculated with the fixed slope -3 as well. The fatigue strength curves of the test data were determined for the mean, lower bound and upper bound of the data scatter. The lower bound curve of the data scatter was compared to the fatigue strength curves of EN 1993-1-9 [5]. The run-out test data were excluded from the calculation of the fatigue strength curves with the

fixed slope, -3 and included for the calculation of the fatigue strength curves with the free (calculated) slope.

Table 5 presents the statistical analysis results on the fatigue tests data of the repaired an artificial crack in the base material specimens made of S690 and S890.

Fig. 13 shows the lower bound of the data scatter of BR69x series, compared to the detail category 71, 125 and 160 of EN 1993-1-9 [5]. The calculated slope, $m = -3.05$ is very close to the fixed slope $m = -3$ which is used for the fatigue strength curves of EN 1993-1-9 [5]. For both slopes, the determined fatigue strength of the repaired base material is very close to the values of the detail category 160 of EN 1993-1-9 [5]. With $m = -3.05$, $\Delta\sigma_{mean} = 179$ MPa, $\Delta\sigma_c = 154$ MPa; with $m = -3$, $\Delta\sigma_{mean} = 178$ MPa, $\Delta\sigma_c = 154$ MPa.

Fig. 14 presents the lower bound of the data scatter of BR89x series, compared to the detail category 71, 125 and 160 of EN 1993-1-9 [5]. The calculated slope results in $m = -5.46$ which is much smaller than $m = -3$ the slope of the fatigue strength curves given in EN 1993-1-9 [5]. The fatigue strength curve of the test data with the fixed slope $m = -3$ is reasonably close to the detail category 160 of EN 1993-1-9 [5]. With $m = -5.46$, $\Delta\sigma_{mean} = 225$ MPa, $\Delta\sigma_c = 191$ MPa; with $m = -3$, $\Delta\sigma_{mean} = 173$ MPa, $\Delta\sigma_c = 151$ MPa.

The fatigue test results of the both series fall in the same scatter range. Since the fatigue strength curves of EN 1993-1-9 [5] are independent on the yield strength of steel, the test results of both series were combined and the statistical analysis was performed on the entire test data. In this way, the amount of test data was increased to perform a more reliable statistical analysis.

Fig. 15 shows the fatigue strength of the BR series with the lower band of the data scatter compared to the detail category 71, 125 and 160 of EN 1993-1-9 [5]. The slope according to the regression analysis

Table 4
Fatigue test results of both series.

Specimen	$\Delta\sigma_n$ [MPa]	N_i [cycles]	N_p [cycles]	N_r [cycles]	Percentage of N_i
BR691	253	169,423	276,599	446,022	37.99
BR692	287	248,143	252,253	500,396	49.59
BR693	257	400,383	354,425	754,808	53.04
BR694	224	578,058	381,769	959,827	60.23
BR695	307	189,479	180,001	369,480	51.28
BR696	273	208,737	217,981	426,718	48.92
BR697	298	278,974	243,503	522,477	53.29
BR698	192	861,753	1,094,883	1,956,636	44.04
BR699	290	265,024	301,861	566,885	46.75
BR891	312	131,804	166,390	298,194	44.20
BR892	257	260,297	283,195	543,492	47.89
BR893	292	193,805	218,760	412,565	46.98
BR894	309	242,539	208,949	451,488	53.72
BR895 ^a	308	188,651	334,304	522,955	36.07
BR896 ^a	307	165,550	154,271	319,821	51.76
BR897 ^a	236	0	3,234,243	3,234,243	run out
BR898 ^a	268	239,380	177,139	416,519	57.47
BR899 ^a	324	152,946	165,078	318,024	48.09

^a Additional grinding process executed at the start-stop points of the weld cap.

Table 5

Statistical analysis results on the repaired base material.

Steel type	S690	S890		
m	-3.05	-3	-5.46	-3
$\Delta\sigma_{mean,2-10}$	179	178	225	173
$\Delta\sigma_c$	154	154	191	151
Specimens	9	9	9	8

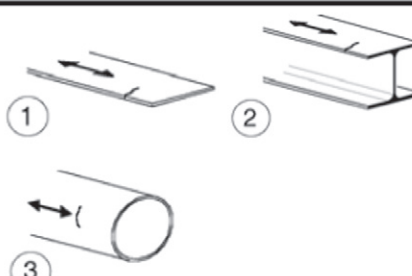
Detail category	Construction details	Description	Requirements
160		1) Plates and flats 2) Rolled sections 3) Seamless hollow sections either rectangular and circular	Sharp edges, surface and rolling flaws to be improved by grinding until removed and smooth transition achieved.
125		Material with machine gas cut edges having shallow and regular drag lines or manual gas cut material subsequently dressed to remove all edge discontinuities. Machine gas cut with cut quality according to EN 1090	Re-entrant corners to be improved by grinding (slope ≤ 1/4) or evaluated using the appropriate stress concentration factors. No repair by weld refill.
71	Size effect for t>25 mm: $k_s = (25/t)^{0.2}$	With backing strip; transverse splice 	Filled welds attaching the backing strip to terminate ≥ 10 mm from the edges of the stressed plates. Track weld inside of the shape of butt welds.

Fig. 12. Detail category of base material and V welded connection according to Table 8.1 and Table 8.3 of EN 1993-1-9 [5].

$m = -3.62$ is close to the slope, $m = -3$ of the fatigue strength curve of EN 1993-1-9 [5]. There was one run-out specimen and it was also included in the regression analysis to determine the fatigue strength curves for the free slope. Since the slope of the fatigue strength curves of EN 1993-1-9 [5] is $m = -3$, an appropriate comparison between the fatigue strength curve of test data and the detail categories of EN 1993-1-9 [5] can be made for the fixed slope $m = -3$. The lower band of the scatter of the BR series with $m = -3$ is laid just below the detail category 160 of EN 1993-1-9 [5] which is representing the fatigue strength of the base material without any weld. With $m = -3.62$, $\Delta\sigma_{\text{mean}} = 194 \text{ MPa}$, $\Delta\sigma_c = 161 \text{ MPa}$; with $m = -3$, $\Delta\sigma_{\text{mean}} = 176 \text{ MPa}$, $\Delta\sigma_c = 155 \text{ MPa}$.

Pijpers et al. [15] performed fatigue tests on the base materials of S690 and S1100 steel grades and the thickness of the test specimens was 12 mm and 10 mm respectively. The specimens were tested under axial load with a tensile test rig. The fatigue test data of both series were combined and a statistical analysis performed for this data set. To establish the influence of the repair weld, the test results of BR

series were compared to the results from fatigue tests on the base material. Pusch and Hübner [16] concluded that fatigue strength curves of very high strength steels show a tendency for lower slope, $m = -5$. Determining the fatigue strength with fixed slope $m = -3$ for this kind of data will cause the lower correlation between the curve and the data. Therefore, the comparison between the base material data and the repaired base material data was made according to the calculated slope from the regression analysis.

Fig. 16 presents the fatigue strength curve of the BR series with the lower band of the data scatter compared to the lower band of the data scatter of the base material tests. There is a large difference between the slopes of the curves. The slope of the fatigue strength curve of the repaired base material becomes closer to -3 which is expected for fatigue strength curves of welded connections. In high cycle region, the base material shows higher fatigue strength than the fatigue strength of the repaired base material. With $m = -3.62$, $\Delta\sigma_{\text{mean}} = 194 \text{ MPa}$, $\Delta\sigma_c = 161 \text{ MPa}$ for BR series; with $m = -6.11$, $\Delta\sigma_{\text{mean}} = 333 \text{ MPa}$, $\Delta\sigma_c = 243 \text{ MPa}$ for the test data of the base material.

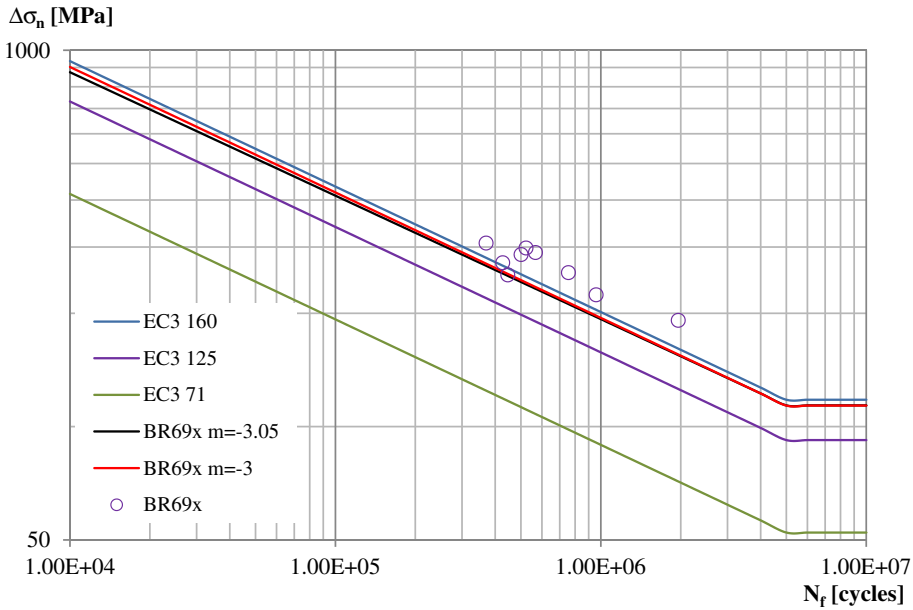


Fig. 13. Fatigue results of BR69x series, with the lower bound of the data scatter compared to the detail category 71,125 and 160 of EN 1993-1-9 [5].

9. Conclusions

In this study, artificially created crack in the base material of S690 and S890 steel plates were repaired and the repaired specimens were tested for the fatigue strength determination. The test results were compared to the detail categories of EN 1993-1-9 [5] and to the test results of the fatigue tests on the base material of S690 and S1100.

The fatigue strength of the repaired base material, $\Delta\sigma_c = 155$ MPa, is almost equal to fatigue strength of the detail category 160 of EN 1993-1-9 [5] which represents the fatigue strength of the base material. Consequently, it can be concluded that the repair weld has limited

negative influence on the fatigue strength of the material. This can be explained as follows;

- The welding application is not executed along the whole width of the specimens. It means that the residual tensile stresses due to the welding are locally available and the residual stresses will only influence the fatigue crack initiation and propagation at the location of the weld. The non-welded ligament of the specimens can contribute to the retardation of fatigue crack propagation in the specimens.
- In design curves of EN 1993-1-9 [5], fatigue cracks in base material are indicated at the edge of the specimens while the fatigue cracks were

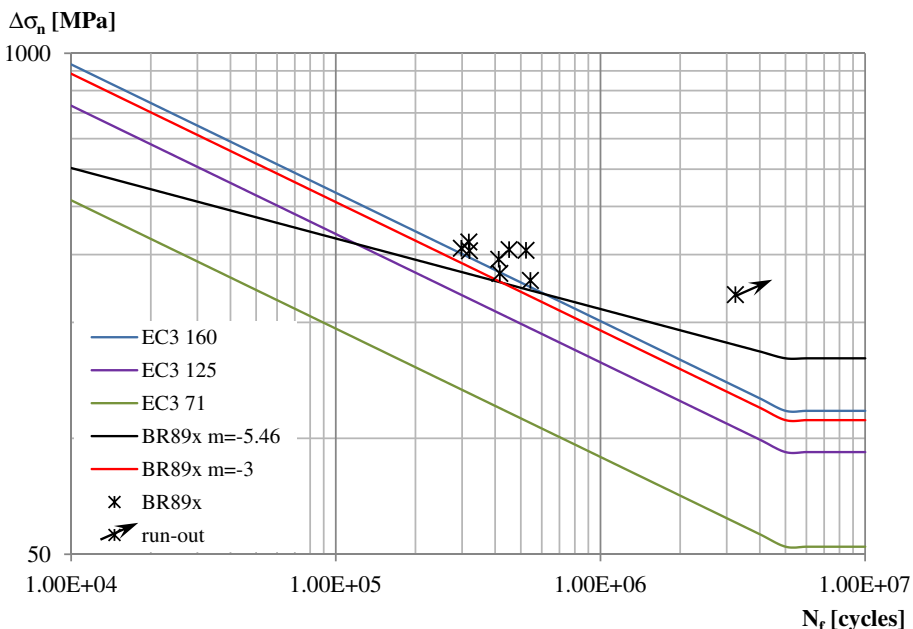


Fig. 14. Fatigue results of BR89x series, with the lower bound of the data scatter compared to the detail category 71,125 and 160 of EN 1993-1-9 [5].

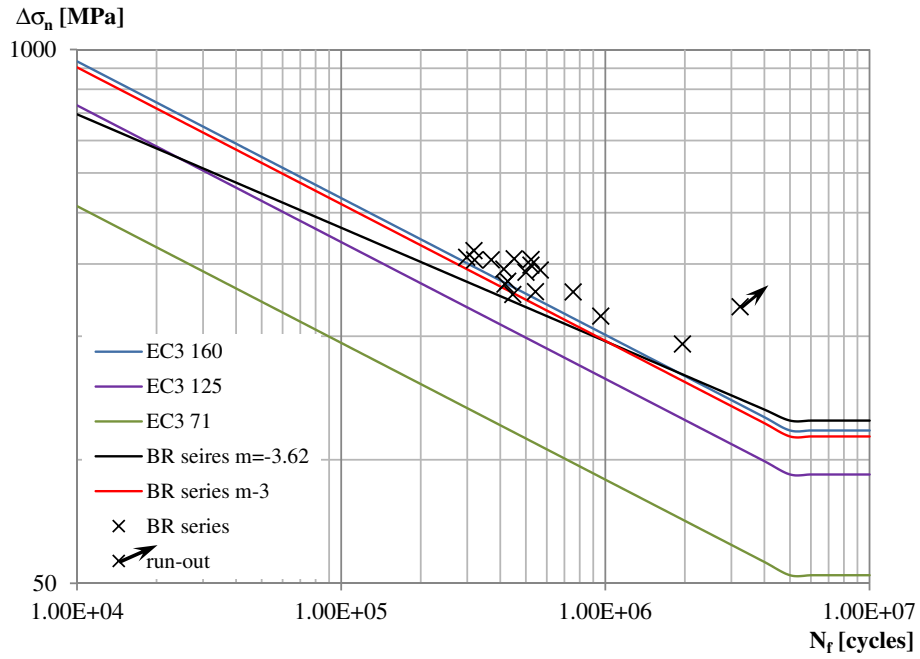


Fig. 15. Fatigue results of BR series with the lower band of the scatter compared to the detail category 71,125 and 160 of EN 1993-1-9 [5].

initiated and propagated in the middle of the current test specimens. The edge cracks have shorter fatigue crack propagation life than semi-elliptical cracks. This influence might have compensated the negative influence of the weld on fatigue strength of the base material.

- Pijpers [9] concluded that the fatigue crack initiation life in the welded connections made of very high strength steel is longer than the welded connections made of mild strength steels. This property of very high strength steels might have a contribution to such high fatigue strength of the current test specimens.

Comparison with the fatigue strength curve of the base material shows that the slope of the fatigue strength curve of the repaired specimens becomes higher than the slope of the fatigue strength curve of the base material. It confirms the commonly known phenomena that the slope of the fatigue strength curves of the base material of high strength steels decreases to -5 while it increases to -3 for the welded connections. The tendency of the increasing slope can be seen from the results of the repaired base material. For the high cycle regime, the characteristic fatigue strength of the base material was located at above the

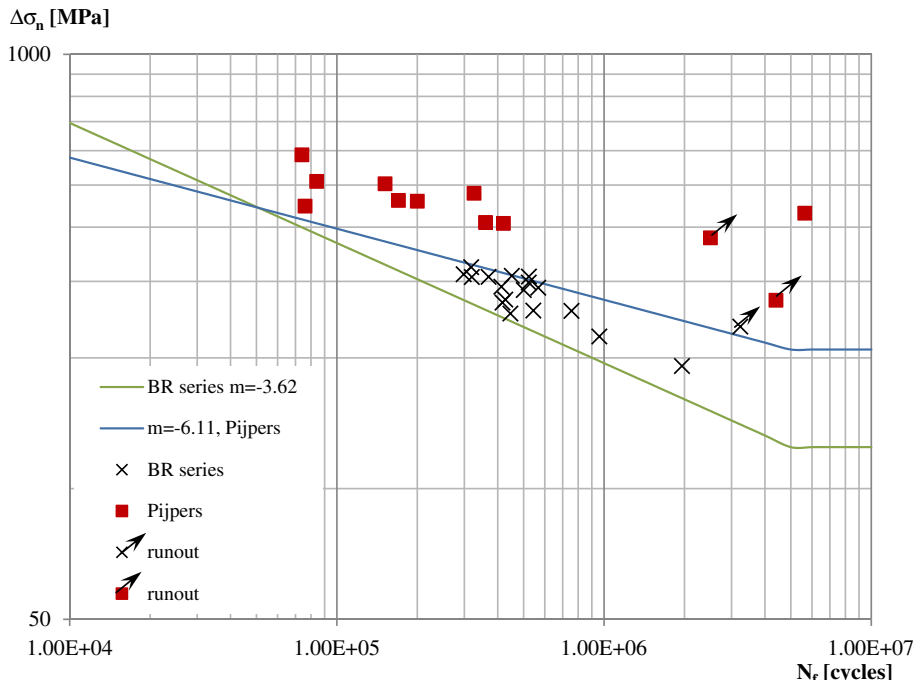


Fig. 16. Comparison between fatigue strength curve of BR series and fatigue strength curve of the base materials.

characteristic value of the repaired base material, mainly because of a large difference between the slopes of the curves.

Regarding the crack initiation and propagation phase, the crack initiation life and crack propagation life of the specimens are almost similar. Approximately, 45% of the fatigue life is occupied by the fatigue crack initiation life which is quite high compared to welded connections made of mild steels. Additional grinding on the start-stop points of some specimens BR89x series provides a little improvement for the crack initiation location. After the grinding process, the crack initiation points were shifted little in the direction of the middle of the weld.

Acknowledgement

This research was carried out under project number M82.8.12460 in the framework of the Research Program of the Materials Innovation Institute M2i (www.m2i.nl).

References

- [1] T.R. Gurney, Fatigue of Welded Structures, 1979 (Cambridge, UK).
- [2] S.J. Maddox, Fatigue design rules for welded structures, *Prog. Struct. Eng. Mater.* 2 (1) (2000) 102–109.
- [3] G. Demofonti, S. Riscuifuli, C.M. Sonsino, H. Kaufmann, G. Sedlacek, C. Müller, F. Hanus, H.G. Wegmann, High strength steels in welded state for lightweight constructions under high and variable stress peaks, Final Report EUR 19989, Luxembourg, 2001.
- [4] R. Puthli, S. Herion, J. Bergers, Untersuchungen zum Ermüdungsverhalten von hochfesten Stählen im Rahmen von LIFTHIGH, *Stahlbau* 11 (75) (2006) 916–924.
- [5] EN 1993-1-9, Design of Steel Structures - General- Part 1.9: Fatigue Strength of Steel Structure, European Committee for Standardization, Brussels, 2006.
- [6] R.J.M. Pijpers, M.H. Kolstein, A. Romeijn, F.S.K. Bijlaard, Fatigue experiments on very high strength steel base material and transverse butt welds, *Adv. Steel Constr.* 5 (1) (2009) 14–22.
- [7] U. Kuhlmann, A. Dürr, H.P. Günther, Verbesserung der ermüdungsfestigkeit höherfester baustähle durch anwendung der UIT nachbehandlung, *Stahlbau* 11 (75) (2006) 930–938.
- [8] G.B. Marquis, Z. Barsoom, IIW recommendations for the HFMI treatment for improving the fatigue strength of welded joints, IIW Collection, Springer, 2016.
- [9] R. Pijpers, Fatigue strength of welded connections made of very high strength cast and rolled teels, Doctoral Dissertation, Delft University of Technology, Delft, Netherlands, 2011.
- [10] T. Yamasaki, Y. Kawai, Y. Maeda, Fatigue life of welded and bolted repair parts, *J. Struct. Eng.* 110 (1984) 2499–2512.
- [11] Y. Kudryavtsev, J. Kleiman, V. Knysh, Fatigue strength of structural elements with crack repaired by welding, International Institute of Welding, IIW Document XIII-2236-08, 2008.
- [12] EN-ISO 5817, Welding – fusion welded joints in steel, nickel, titanium and their alloys beam welding excluded-Quality levels for imperfections, ISO Copyright Office, Geneva, 2007.
- [13] Y.H. Zhang, S. Smith, L. Wei, C. Johnston, Residual stress measurements and modeling, Health and Safety Executive, RP938, Cambridge, UK, 2012.
- [14] J. Brozzetti, M.A. Hirt, I. Ryan, G. Sedlacek, I.F.C. Smith, in: Eurocode Editorial Group (Ed.), Background Information on Fatigue Design Rules - Statistical Evaluation - Chapter 9 - Document 9.01, 1989.
- [15] R.J.M. Pijpers, M.H. Kolstein, A. Romeijn, F.S.K. Bijlaard, The fatigue strength of base material and butt welds made of S690 and S1100, 5th International Conference on Advances in Steel Structures, Singapore, 2007.
- [16] G. Pusch, P. Hübner, Bruchverhalten des Stahles StE 960 und seiner Schweißverbindung bei statischer und zyklischer Belastung, Final Report, EUR 17880 DE, Luxemburg, 1994.
- [17] J. Berg, N. Stranghoener, Fatigue strength of welded ultra high strength steels improved by high frequency hammer peening, *Procedia Material Science* 3 (2014) 71–76.



Local approaches and XFEM used to estimate life of CFRP repaired cracked welded joints under fatigue loading

Zhiyu Jie*, Wujun Wang, Chao Chen, Kainan Wang

Department of Civil Engineering, Ningbo University, Ningbo 315211, China



ARTICLE INFO

Keywords:

Welded joints
CFRP
Local approach
XFEM
Fatigue life assessment

ABSTRACT

Three different local approaches, the Theory of Critical Distances (TCD), the Notch Stress Intensity Factor (NSIF) and the Strain Energy Density (SED), and the Extended Finite Element Method (XFEM) were applied to estimate the fatigue life of unrepairs and CFRP patches repaired cracked welded joints. The effects of CFRP modulus and thickness on the fatigue life of welded joints with different initial crack depths were investigated. The fatigue damage evolution equation using the loading frequency as a new damage variable was used to describe the degradation process. Fatigue life assessment results and crack growth paths compared with experimental results using these methods. The results show that the fatigue life and fatigue strength decrease as the increase of the initial crack depth. Three different fatigue failure modes can be observed from experimental results. The TCD, NSIF, and SED can reliably predict the fatigue life of welded joints without CFRP patches, but it needs to further investigate the values of estimation parameters of welded joints with CFRP patches for the NSIF and the SED. Fatigue crack growth paths and lives predicted by the XFEM and actual results are in good agreement, and the accuracy and reliability are validated by test data.

1. Introduction

The welding as an important connection way is widely used in steel bridges, such as cruciform joints and T joints, etc. These welded joints under cyclic loading are very easy to produce fatigue cracks in view of the stress raiser and the welding residual stress. In order to improve the fatigue performance, some effective strengthening methods are devoted to reduce the stress at the crack tips. One of the most popular approaches is that carbon fiber reinforced polymer (CFRP) with the benefits of high strength, light weight, and anti-corrosion is employed to repair the damage regions. This new repairing method can greatly enhance the fatigue life of cracked components [1–3]. In this paper, we focus on that the quantitative variation of the fatigue life for cracked welded joints strengthened by CFRP patches and the use of different fatigue assessment methods. The nominal stress and hot spot stress approaches are commonly applied to the fatigue assessment of welded structures [4]. The nominal stress approach is suitable for the design of those simple weld geometries and loading conditions based on the reference S-N curves. The hot spot stress approach is more appropriate for complex welded structures when the nominal stress is not easy to determine. However, for cracked welded joints retrofitted with CFRP patches, these two methods are not able to charac-

terize the stress field and directly assess the fatigue life. Therefore, local approaches mainly including the Theory of Critical Distances (TCD) [5], the Notch Stress Intensity Factor (NSIF) [6], and the Strain Energy Density (SED) [7] are proposed for the fatigue assessment.

Recently, many researchers apply the TCD to the fatigue evaluation of notched components. This method considers the effect of stress concentrations and loading types via a simple finite element analysis. It avoids the S-N curve classification and requires less computational effort. Zhou et al. [8] predicted the fatigue crack initiation life of cope hole details in orthotropic steel deck via the TCD, and it agreed excellent with experimental values. Nie et al. [9] assessed the fatigue limits of notched components by using the TCD in very high cycle regime. Jie and Susmel [10] reanalyzed the literature data of corroded high strength steel wires and evaluated the fatigue life via the TCD. Besides, the use of the TCD has been extended to welded joints [11–13]. Karakas et al. [12] utilized the TCD to estimate the fatigue behavior of magnesium welded joints with different weld geometries and stress ratios. Baumgartner et al. [14] estimated the fatigue strength of TIG-dressed joints via the TCD, and fatigue details and critical distances were suggested. Al Zamzami et al. [15] assessed the fatigue strength of inclined steel joints in combination with the TCD and the Modified Wöhler Curve Method (MWCM). Gorouhi [16] investigated the fatigue

* Corresponding author.

E-mail address: jiezhiyu@nbu.edu.cn (Z. Jie).

Nomenclature

TCD	the Theory of Critical Distances	a_i	the extra degree of freedom to model the jump across crack faces
NSIF	The Notch Stress Intensity Factor	$H(x)$	the jump function
SED	the Strain Energy Density	$F_a(x)$	the enrich function
XFEM	the Extended Finite Element Method	b_i^a	the added degree of freedom associated with $F_a(x)$
$\Delta\sigma_{\text{eff}}$	effective stress range	x	an arbitrary point near the crack face
$\Delta\sigma_1$	the maximum principal stress range	x^*	the closest point to x located on the crack face
r, θ	the local polar coordinate	t, s	the local coordinate at the crack tip
L	the critical distance	C, m	fatigue crack growth material parameters
L_T	the threshold critical distance	a, a_i	the crack depth and the initial crack depth
ΔK_{th}	the threshold stress intensity factor range	ΔK	the stress intensity factor range
$\Delta\sigma_A$	the fatigue limit of a plain specimen	c_3, c_4	material parameters based on the energy release rate
N	fatigue life	ΔG	the energy release rate range
A, B	parameters related materials and stress ratios	$G_{\text{thresh}}, G_{\text{pl}}$	the threshold value and the upper limit value of energy release rate, respectively
L_s	the critical distance under static loading	c_1, c_2	material parameters of fatigue crack initiation
K_{Ic}	the fracture toughness	$\Delta K_{\text{I}}, \Delta K_{\text{II}}, \Delta K_{\text{III}}$	mode I, II, and III stress intensity factors
σ_b	the tensile strength	P_{\max}, P_{\min}	fatigue loading with the maximum and minimum values, respectively
σ_s	the strength under static loading	t	adhesive thickness
m	the negative inverse slope for the S-N curve	D	the damage variable
$\sigma_{\theta\theta}, \tau_{r\theta}$	stress components	f	the loading frequency
λ_1, λ_2	Williams' eigenvalues	f_0, f_f	are initial and final values of loading frequencies, respectively
2α	the notch opening angle	$\sigma_m, \Delta\sigma, n, N$	the mean stress, stress range, fatigue cycles, and fatigue life
K_1, K_2	Mode I and II NSIFs	α, β, b, M_0	fatigue damage material parameters determined by test data
$\Delta K_1, \Delta K_2$	Mode I and II NSIF ranges		
C_1, p	material parameters determined by the ΔK_1 - N curve		
ΔW	the elastic averaged SED range		
R_0	the control volume radius		
e_1, e_2	shape functions depending on 2α and Poisson's ratio ν		
V, E	Poisson's ratio and elastic modulus		
ΔK_{1A}	the reference value of the NSIF range of notched members		
N_i	the shape function		
u_i	the degree of freedom		

performance of riveted bridge details by using both the TCD and the S-N curve method. Fang et al. [17] employed the TCD to the fatigue assessment of a welded beam-to-column connection by the finite element analysis.

The NSIF approach is successfully proposed to the fatigue strength estimation of welded joints [18,19]. This method is based on William's solutions for V-notches with a zero radius. The use of NSIF generally required a very fine mesh, but Meneghetti et al. [20–22] tried to use coarse meshes to rapidly calculate it. Due to the fatigue assessment needing different curves for different opening angles, Lazzarin and Zambardi [23] applied the SED averaged over a control volume depending on different materials to the fatigue evaluation. The main benefits of the SED did not rely upon the opening angle and only needed a very coarse mesh for the finite element simulation [24]. Berto et al. [25,26] analyzed the fatigue estimation of different types of welded joints by the SED, and all the results were within the scatter band. Song et al. [27,28] extended the range of previous analytical solutions to estimate the averaged SED both at the weld toe and root in load-carrying cruciform welded joints and predicted different failure modes. Foti et al. [29] investigated the effects of geometrical parameters on the fatigue strength of different welded details using the SED and compared with Eurocode 3, but it resulted in a non-conservative estimation according to Eurocode 3. Luo et al. [30] studied the accuracy and feasibility of the SED used to the fatigue estimation of rib-to-deck welded joints in orthotropic steel deck, and the effect of the weld geometry on the fatigue strength was performed. Fischer et al. [31] reviewed the NSIF and SED approaches considering misalignment effects.

These local approaches cannot consider the crack propagation behavior, and fatigue assessment parameters are relatively single.

Comparing to traditional linear elastic fracture mechanics, the Extended Finite Element Method (XFEM) is another useful approach to study the crack growth and life prediction. There is no need to remesh for the crack growth simulation and define the crack tip with singular elements. Kraedegh [32] considered the effect of crack growth on the fatigue life of unstiffened and stiffened structures via the XFEM. Bergara et al. [33] validated the accuracy of the XFEM by simulating the fatigue crack propagation for a semielliptical crack in a beam under four-point bending. Nikfam et al. [34] reported that the XFEM was used to simulate the fatigue crack growth of welded T-joints, and prediction results agreed well with experiments. Wang et al. [35] investigated the fatigue crack propagation behavior in steel bridge web gaps, and multi-scale numerical analysis models were established using fracture mechanics and the XFEM. Other scholars focused on the use of the XFEM to crack propagation of components retrofitted by composite materials. Zarrinzadeh et al. [36] employed the XFEM to model fatigue crack growth of a cylindrical cracked aluminium pipe repaired with glass/epoxy composite patch. Valadi et al. [37] used the XFEM to investigate crack propagation of thin-walled steel pipes strengthened by fiber reinforced polymer composite. Lesiuk et al. [38] adopted the XFEM to analyze the fracture behavior of fiber-reinforced polymer reinforced beams.

According to the aforementioned analysis, there are few studies on the fatigue assessment of CFRP patches strengthening cracked welded joints by using the TCD, the NSIF, the SED, and the XFEM. In this paper, these methods are used to evaluate the fatigue life of unretrofitted and CFRP patches retrofitted cracked welded joints. Different CFRP modulus and thickness are constructed to investigate their effects on the fatigue life of welded joints with different crack depth based on fatigue tests and numerical simulations. The information

on fatigue life versus stress range is obtained, and different fatigue failure modes can be observed. The fatigue damage evolution equation using the loading frequency as a new damage variable is determined. Finite element analyses are performed using the software ABAQUS. Fatigue life predictions using the TCD, the NSIF, the SED, and the XFEM compare with experimental results. Fatigue crack propagation paths of welded joints retrofitted without and with CFRP patches are predicted by the XFEM. A comparison between simulation paths and actual paths is made. Finally, the accuracy and reliability of local approaches and the XFEM are validated.

2. Theoretical knowledge

2.1. Local approaches

2.1.1. Theory of critical Distances (TCD)

The TCD assumes that an effective stress range $\Delta\sigma_{\text{eff}}$ is adopted to conduct the fatigue assessment of notched specimens. First, a critical distance as a material property value can be obtained from standard experiments at the same conditions. Then, the TCD is characterized in three forms: the point method (PM), the line method (LM), and the area method (AM), as shown in Fig. 1 [39]. The PM assumes that $\Delta\sigma_{\text{eff}}$ is calculated at a certain distance from the maximum principal stress point (Fig. 1b). The LM postulates that $\Delta\sigma_{\text{eff}}$ is assessed by the maximum principal stress averaged over a line (Fig. 1c). The AM supposes that $\Delta\sigma_{\text{eff}}$ is determined by the maximum principal stress averaged over an area (Fig. 1d). Thus, the effective stress ranges based on the PM, the LM, and the AM can be expressed as, respectively:

$$\Delta\sigma_{\text{eff}} = \Delta\sigma_1 \left(\theta = 0, r = \frac{L}{2} \right) \quad (\text{Point Method}) \quad (1)$$

$$\Delta\sigma_{\text{eff}} = \frac{1}{2L} \int_0^{2L} \Delta\sigma_1(\theta = 0, r) \cdot dr \quad (\text{Line Method}) \quad (2)$$

$$\Delta\sigma_{\text{eff}} = \frac{4}{\pi L^2} \int_0^{\pi/2} \int_0^L \Delta\sigma_1(\theta, r) \cdot r \cdot dr \cdot d\theta \quad (\text{Area Method}) \quad (3)$$

where $\Delta\sigma_1$ is the maximum principal stress range, r and θ are the local polar coordinate, and L is the critical distance.

In Eqs. (1)–(3), the critical distance L_T can be obtained by the threshold stress intensity factor range ΔK_{th} and the fatigue limit of a plain specimen $\Delta\sigma_A$ as follows [40]:

$$L_T = \frac{1}{\pi} \left(\frac{\Delta K_{\text{th}}}{\Delta\sigma_A} \right)^2 \quad (4)$$

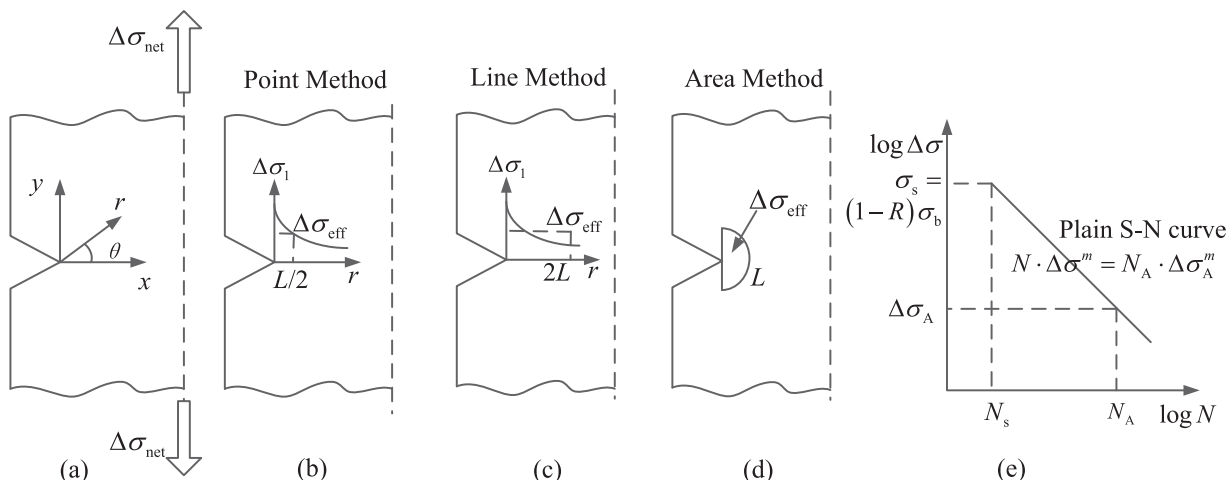


Fig. 1. Local coordinate system (a); the Point Method (b); the Line Method (c); the Area Method (d); plain S-N curve (e).

The values of ΔK_{th} and $\Delta\sigma_A$ should be determined via fatigue tests under the same loading conditions.

The linear-elastic TCD has been successfully used to predict the fatigue life of notched specimens in the medium and high-cycle fatigue region. The critical distance L as a function of the fatigue life N can be expressed as the following equation [41]:

$$L(N) = A \cdot N^B \quad \text{for } N \leq 5 \times 10^6 \text{ cycles} \quad (5)$$

where A and B related to materials and stress ratios are determined by fatigue tests. The critical distance under static loading L_s is expressed as follows:

$$L_s = \frac{1}{\pi} \left(\frac{K_{\text{lc}}}{\sigma_b} \right)^2 \quad (6)$$

where K_{lc} is the fracture toughness, and σ_b is the tensile strength. According to Fig. 1e and Eqs. (4) and (6), parameters A and B can be calculated by the following equations:

$$L_T(N_A) = A \cdot N_A^B = \frac{1}{\pi} \left(\frac{\Delta K_{\text{th}}}{\Delta\sigma_A} \right)^2 \quad (7)$$

$$L_s \left(N_s = \frac{N_A \cdot \Delta\sigma_A^m}{\sigma_s^m} \right) = A \cdot N_s^B = \frac{1}{\pi} \left(\frac{\Delta K_{\text{lc}}}{\sigma_b} \right)^2 \quad (8)$$

where σ_s is the strength under static loading at N_s cycles, m and $\Delta\sigma_A$ are the negative inverse slope and the reference stress range of plain specimens at N_A cycles, respectively. If an initial value of the fatigue life N_i is assumed, the corresponding critical distance can be obtained:

$$L(N_i) = A \cdot N_i^B \quad (9)$$

The effective stress range $\Delta\sigma_{\text{eff}}$ is determined by the numerical analysis. According to the S-N curve of the plain specimens, $\Delta\sigma_{\text{eff}}$ is used to recalculate the fatigue life N_j as follows:

$$N_j = N_A \left(\frac{\Delta\sigma_A}{\Delta\sigma_{\text{eff}}} \right)^m \quad (10)$$

If N_j is different from the initial value N_i , then the whole calculation had to be carried out again by imposing $N_i = N_j$ until convergence.

2.1.2. Notch stress intensity factor (NSIF)

A considerable research effort focuses on the use of the NSIF approach to fatigue assessment for notched components. According to Ref. [19], mode I and II NSIFs are defined as the following:

$$K_1 = \sqrt{2\pi} \lim_{r \rightarrow 0^+} r^{1-\lambda_1} \sigma_{\theta\theta}(r, \theta = 0) \quad (11)$$

$$K_2 = \sqrt{2\pi} \lim_{r \rightarrow 0^+} r^{1-\lambda_2} \tau_{r\theta}(r, \theta = 0) \quad (12)$$

where $\sigma_{\theta\theta}$ and $\tau_{r\theta}$ are stress components, λ_1 and λ_2 are Williams' eigenvalues related to the notch opening angle 2α , and K_1 and K_2 are Mode I and II NSIFs, respectively. For the same opening angle, the relationship between NSIF range and fatigue life can be written as:

$$\Delta K_1^p \cdot N = C_1 \quad \text{for } N \leq 5 \times 10^6 \text{ cycles} \quad (13)$$

where ΔK_1 is the Mode I NSIF rang, C_1 and p are material parameters determined by the $\Delta K_1 - N$ curve.

2.1.3. Strain energy density (SED)

The elastic averaged SED range over a defined volume embracing a sharp notch tip is expressed as [23]:

$$\bar{\Delta W} = \frac{1}{E} \left[e_1 \cdot \frac{\Delta K_1^2}{R_0^{2(1-\lambda_1)}} + e_2 \cdot \frac{\Delta K_2^2}{R_0^{2(1-\lambda_2)}} \right] \quad (14)$$

where ΔK_2 is the Mode II NSIF rang, R_0 is the control volume radius, and e_1 and e_2 are shape functions depending on 2α and Poisson's ratio ν . The rapid calculation equations for e_1 and e_2 are expressed as the following ($\nu = 0.3$):

$$e_1 = -5.373 \times 10^{-6} (2\alpha)^2 + 6.151 \times 10^{-4} (2\alpha) + 0.1330 \quad (15)$$

$$e_2 = 4.809 \times 10^{-6} (2\alpha)^2 - 2.346 \times 10^{-4} (2\alpha) + 0.3400 \quad (16)$$

According to Eq. (14), the control radius R_0 can be expressed as the following under mode I loading [23]:

$$R_0 = \left(\frac{\sqrt{2}e_1 \Delta K_{1A}}{\Delta \sigma_A} \right)^{\frac{1}{1-\lambda_1}} \quad (17)$$

where ΔK_{1A} is the reference value of the NSIF range of notched members. Ref. [42] suggests that the control radius R_0 is 0.28 mm for steel welded joints. The SED range as a function of the fatigue life takes on the following form:

$$\bar{\Delta W}^q \cdot N = C_2 \quad \text{for } N \leq 5 \times 10^6 \text{ cycles} \quad (18)$$

where C_2 and q are material parameters determined by the $\bar{\Delta W} - N$ curve.

2.2. Extended finite element method (XFEM)

Comparing to the traditional finite element analysis, the XFEM employs additional enrichment functions to describe the crack discontinuity. A near-tip asymptotic field function is used to deal with the crack tip singularity. A Heaviside discontinuous function is utilized to simulate the jump in the displacement field across crack faces. The displacement field considering the existence of a crack is given as follows [43]:

$$u = \sum_{i=1}^m N_i(x) \left[u_i + H(x)a_i + \sum_{\alpha=1}^4 F_\alpha(x)b_i^\alpha \right] \quad (19)$$

where N_i is the shape function, u_i is the degree of freedom, a_i is the extra degree of freedom to model the jump across crack faces, $H(x)$ is the jump function, $F_\alpha(x)$ is the enrich function, and b_i^α is the added degree of freedom associated with $F_\alpha(x)$. The jump function can be written as the following:

$$H(x) = \begin{cases} 1 & \text{if } (x - x^*)n \geq 0 \\ -1 & \text{otherwise} \end{cases} \quad (20)$$

where x is an arbitrary point near the crack face, x^* is the closest point to x located on the crack face, and t and s are the local coordinate

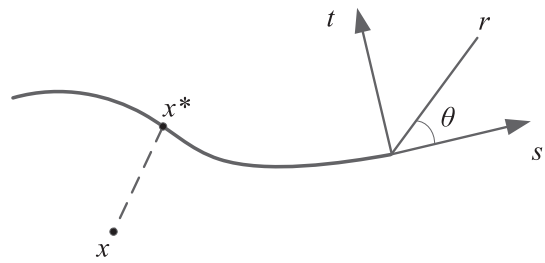


Fig. 2. Definition of x and x^* points. [44]

at the crack tip (Fig. 2). The crack tip enrichment function is taken as follows:

$$F_\alpha(x) = \left[\sqrt{r} \sin\left(\frac{\theta}{2}\right), \sqrt{r} \cos\left(\frac{\theta}{2}\right), \sqrt{r} \sin(\theta) \sin\left(\frac{\theta}{2}\right), \sqrt{r} \sin(\theta) \cos\left(\frac{\theta}{2}\right) \right] \quad (21)$$

The energy release rate at the crack tip is employed for the fatigue analysis in ABAQUS software. The fatigue crack growth life is calculated using the Paris equation, which is presented as follows:

$$\frac{da}{dN} = C \cdot \Delta K^m \quad (22)$$

where C and m are fatigue crack growth material parameters, a is the crack depth, and ΔK is the stress intensity factor range. When $G_{\text{thresh}} < \Delta G < G_{\text{pl}}$, Eq. (22) in the form of the energy release rate is rewritten as:

$$\frac{da}{dN} = c_3 \cdot \Delta G^{c_4} \quad (23)$$

where c_3 and c_4 are material parameters based on the energy release rate, ΔG is the energy release rate range, G_{thresh} and G_{pl} are the threshold value and the upper limit value of the energy release rate, respectively. The initiation criterion of fatigue crack growth is given as:

$$f = \frac{N}{c_1 \Delta G^{c_2}} \geq 1 \quad (24)$$

where c_1 and c_2 are material parameters of the fatigue crack initiation. Due to the ABAQUS software only taking ΔG to investigate the fatigue crack growth, the relationship between ΔG and ΔK can be written as follows for plane strain conditions:

$$\Delta G = \frac{1 - \nu^2}{E} (\Delta K_I^2 + \Delta K_{II}^2) + \frac{1 + \nu}{E} \Delta K_{III}^2 \quad (25)$$

where ΔK_I , ΔK_{II} , and ΔK_{III} are mode I, II, and III stress intensity factor ranges.

3. Experimental program

3.1. Configuration of specimens

Cruciform welded joints were fabricated by using Q345qC steel plate [45]. The formation of welds used carbon dioxide gas shielded welding technology. In order to simulate the actual fatigue cracking, an artificial initial crack through the plate width at the weld toe was manufactured. The configuration of cracked cruciform joints is illustrated in Fig. 3. The full penetration weld was an isosceles right triangle with 8 mm sides. The curvature radius at weld toe was assumed to be zero. The numerical analysis did not consider the influence of very small misalignments. Fig. 4 plots the repairing situations of CFRP patches. The adhesive layer between steel plate and CFRP patches adopted epoxy resin. Fatigue loading conditions of cruciform joints with three different initial crack depths unstrengthened and strengthened by three different CFRP patches are shown in Table 1. All speci-

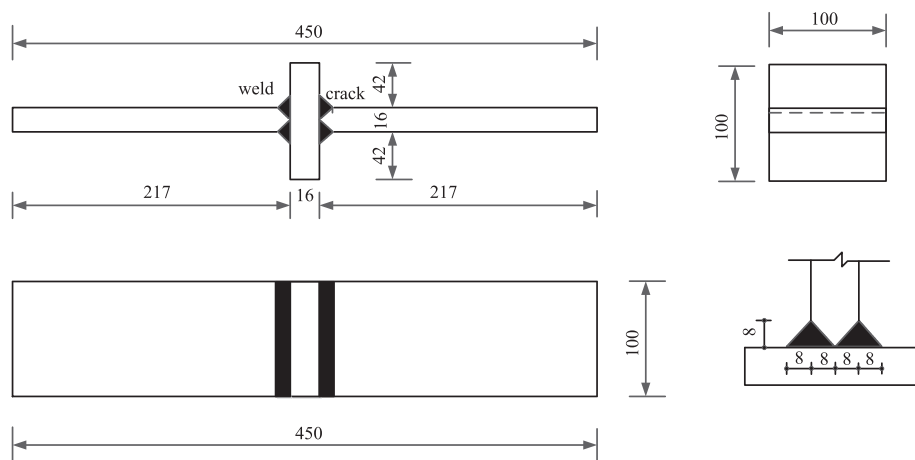


Fig. 3. Configuration of a cracked cruciform joint.

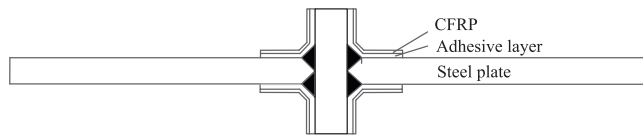


Fig. 4. CFRP patches repairing situation.

mens in as-welded are tested subjected to constant amplitude tensile fatigue loading with the maximum and minimum values of $P_{\max} = 248.9$ kN and $P_{\min} = 24.9$ kN, respectively, as shown in Fig. 5. These loads were applied at the gross section of the long plate end, and the loading frequency was about 120 Hz. The applied stress has been checked by strain gauges in order to ensure the accuracy of fatigue loading.

3.2. Test results

The fatigue life is generally defined when the initial crack depth reaches half the plate thickness [46]. The relationship of nominal stress range versus fatigue life for cracked cruciform joints is shown in Fig. 6. It can be seen that CFRP retrofitting can improve the fatigue life, and the maximum increase in the fatigue life for welded joints strengthened with CFRP patches reaches to 66%. For repairing specimens, fatigue strengths increase from FAT50 (a stress range of 50 MPa at 2 million cycles with a survival probability of $P_s = 97.7\%$), FAT40, and FAT36 to FAT63, FAT50, and FAT40 for $a_i = 1$ mm, 2 mm, and 3 mm, respectively. When $a_i = 3$ mm, the fatigue strength is only about one half of undamaged cruciform joints at 2

million cycles. The remaining fatigue life and fatigue strength decrease as the increase of initial crack depth. The strengthening effect for the same CFRP patches is more discrete. The possible reasons are that (1) if the interface between steel plate and CFRP is not smooth, it will affect the reinforcement effect; (2) there are about 5–10% errors in the initial crack manufacturing process.

It can observe three fatigue failure modes for all the specimens: (a) fatigue failure at initial pre-cracks or accompanying the destruction of the adhesive layer, (b) fatigue failure at welds, and (c) fatigue failure both at initial cracks and welds, as shown in Fig. 7. It may occasionally produce the destruction of the adhesive layer when fatigue crack enters the rapid growth stage. The main reason is that the cross-sectional area decreases as the increase of the crack depth, and the adhesive layer and CFRP are subjected to higher stresses. In the fatigue life estimation analysis, it is assumed that there is a good bonding performance between CFRP and steel plate, not considering the effect of adhesive layer debonding. Only a few specimens fail at welds or both at initial cracks and welds. The poor weld quality and the fabrication error may result in these phenomena.

3.3. Fatigue damage evolution

Fatigue damage is a continuous degradation process for materials under external loads. Damage variables are used to reflect the decrease in material stiffness. So far, a variety of methods for defining and measuring damage variables have been proposed. Different damage variables have different measurement methods, which are divided into the direct measurement and the indirect measurement. The cross-sectional area is usually used as the direct measurement damage vari-

Table 1
Types and fatigue loading conditions of specimens.

Initial Crack depth a_i	Specimen Number	CFRP type	Nominal Stress range (MPa)	Stress ratio	P_{\max} (kN)	P_{\min} (kN)
1 mm	D1C0	Without CFRP	140	0.1	248.9	24.9
	D1C1	$E = 2.4 \times 10^5$ MPa, $t = 0.167$ mm				
	D1C2	$E = 1.8 \times 10^5$ MPa, $t = 0.111$ mm				
	D1C3	$E = 2.4 \times 10^5$ MPa, $t = 0.111$ mm				
2 mm	D2C0	Without CFRP	140	0.1	248.9	24.9
	D2C1	$E = 2.4 \times 10^5$ MPa, $t = 0.167$ mm				
	D2C2	$E = 1.8 \times 10^5$ MPa, $t = 0.111$ mm				
	D2C3	$E = 2.4 \times 10^5$ MPa, $t = 0.111$ mm				
3 mm	D3C0	Without CFRP	140	0.1	248.9	24.9
	D3C1	$E = 2.4 \times 10^5$ MPa, $t = 0.167$ mm				
	D3C2	$E = 1.8 \times 10^5$ MPa, $t = 0.111$ mm				
	D3C3	$E = 2.4 \times 10^5$ MPa, $t = 0.111$ mm				

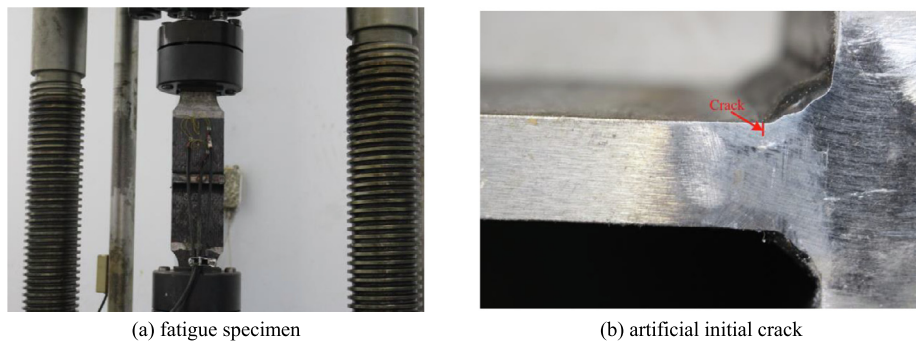


Fig. 5. Fatigue test.

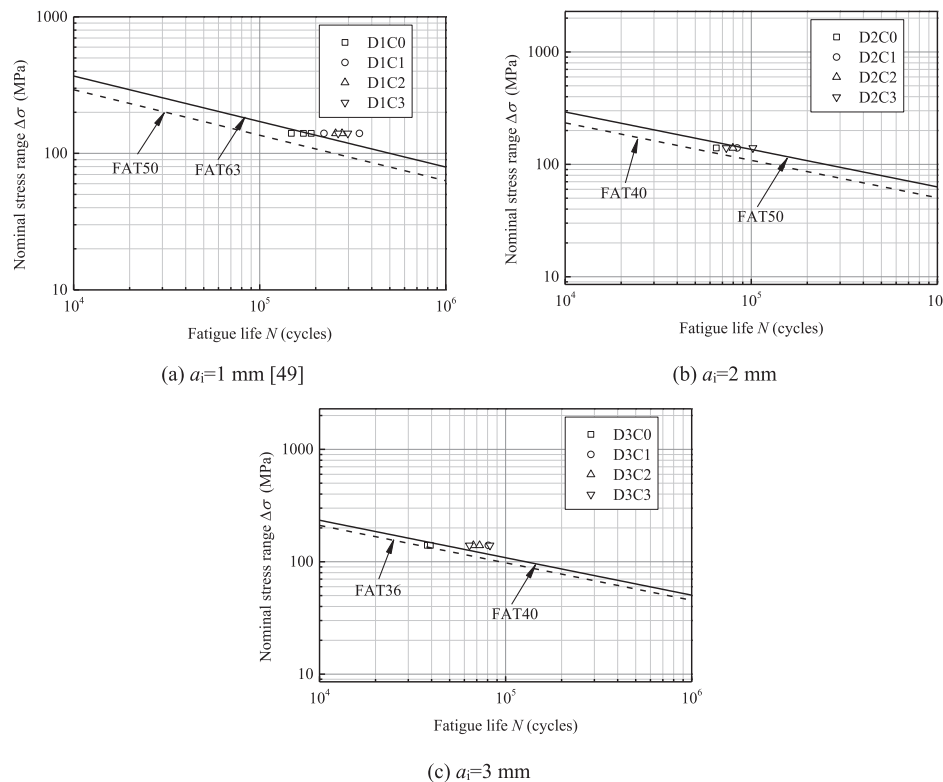


Fig. 6. The relationship of nominal stress range versus fatigue life.

able, but it is difficult to operate in actual conditions. Therefore, it is necessary to use the indirect measurement damage variable. There are many damage variables measured indirectly, such as the elastic modulus, the electric potential (the cross section and the electric resistance changing with the crack growth), and the stress range. It is found that the loading frequency varies with the fatigue crack propagation during the fatigue process. It means that the loading frequency correlates with fatigue damage. Thus, the loading frequency is used to reflect the degradation of the stiffness. The loading frequency decreases with an increase of crack depth due to the cross section not resisting external fatigue loads. The damage variable D is defined as:

$$D = 1 - \frac{f_f - f_{f_0}}{f_{f_0} - f_f} \quad (26)$$

where f is the loading frequency, f_0 and f_f are initial and final values of loading frequencies, respectively.

A nonlinear cumulative fatigue damage model has been proposed to characterize the degradation of materials, and the expression is given as [48]:

$$\frac{dD}{dn} = \left[1 - (1 - D)^{1+\beta} \right]^\alpha \left[\frac{\Delta\sigma}{M_0(1 - b\sigma_m)(1 - D)} \right]^\beta \quad (27)$$

where σ_m is the mean stress, n is the loading cycles, and α , β , b , and M_0 are the fatigue damage material parameters determined by test data. Integrating from $D = 0$ to 1, Eq. (27) gives the relationship between N and $\Delta\sigma$:

$$N = \frac{1}{1-\alpha} \frac{1}{1+\beta} \left[\frac{M_0(1-b\sigma_m)}{\Delta\sigma} \right]^\beta \quad (28)$$

The damage variable D is rewritten as the form of n/N :

$$D = 1 - \left[1 - \left(\frac{n}{N} \right)^{1/(1-\alpha)} \right]^{1/(1-\beta)} \quad (29)$$

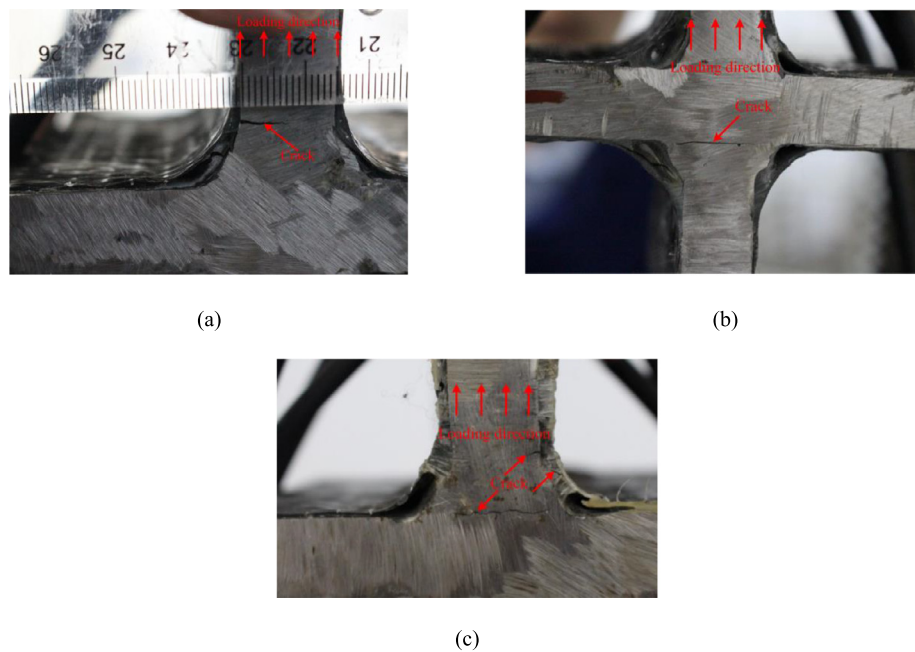


Fig. 7. Fatigue failure modes.

According to loading frequency results, damage variables for unpaired and CFRP repaired specimens can be determined by Eq. (26). The relationship between D and n/N is plotted in Fig. 8. Then, Eq. (29) is applied to fit these test data via the least squares method, and the regression equations for cruciform joints without and with CFRP patches are expressed as:

$$D_0 = 1 - \left[1 - \left(\frac{n}{N} \right)^{5.6497} \right]^{0.5201} \quad \text{C0} \quad (30)$$

$$D_1 = 1 - \left[1 - \left(\frac{n}{N} \right)^{14.2248} \right]^{0.4405} \quad \text{C1} \quad (31)$$

$$D_2 = 1 - \left[1 - \left(\frac{n}{N} \right)^{8.7566} \right]^{0.5968} \quad \text{C2} \quad (32)$$

$$D_3 = 1 - \left[1 - \left(\frac{n}{N} \right)^{8.9847} \right]^{0.5551} \quad \text{C3} \quad (33)$$

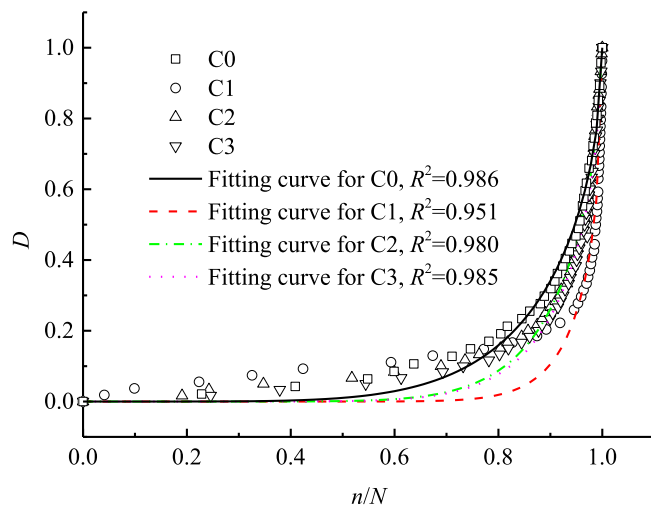


Fig. 8. D versus n/N based on the Chaboche model.

It is evident that the Chaboche model can be effective to simulate the fatigue damage degradation due to the good correlation. CFRP patches can effectively delay the fatigue damage degradation process. When n/N is equal to 0.8, welded joints are in the rapid growth stage. Thus, the loading frequency is an important parameter to indirectly reflect the fatigue crack propagation. It is beneficial for understanding the fatigue crack initiation and growth mechanism.

4. Fatigue life estimation

4.1. Local approaches

4.1.1. TCD

An 8-node plane strain element (CPE8) was used to model the steel plate, the adhesive layer, and CFRP patches by using ABAQUS. A finite element model of a cracked welded joint with CFRP patches is plotted in Fig. 9. The global mesh size was about 1 mm according to the size of specimens. The mesh convergence analysis was conducted for a large number of finite element models, and it suggested that the mesh size in the vicinity of the crack was around 0.1 mm to obtain sufficiently accurate effective stresses. Total number of nodes and elements were 315,698 and 104,672, respectively. A fixed constraint was imposed at one end of steel plate, and a uniform tensile stress 140 MPa was applied at the other end according to the fatigue test machine. Material properties of steel, adhesive, and CFRP patches (C1, C2, and C3) are listed in Table 2.

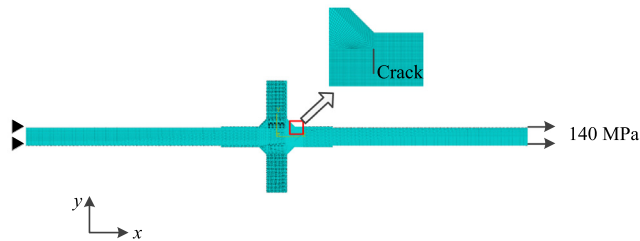


Fig. 9. Finite element model of a cracked welded joint with CFRP patches.

Table 2
Material properties of steel, adhesive, and CFRP patches.

Material type	Yield strength (MPa)	Ultimate strength (MPa)	Poisson's ratio	Elastic modulus (MPa)
Steel	345	490	0.3	2.1×10^5
Adhesive	–	–		1000
C1	–	3870		2.4×10^5
C2	–	3216		1.8×10^5
C3	–	3325		2.4×10^5

According to Ref. [49], a recommended constant critical distance value of 0.5 mm can be used for steel welded joints in view of simplicity. Thus, Eq. (10) is directly employed to evaluate the fatigue life of cracked specimens using the PM. The fatigue strength of plain specimens $\Delta\sigma_A$ is 160 MPa at $N_A = 2$ million cycles, and the negative inverse slope m is 3 [50]. Based on the finite element calculated results, the relationship between effective stress range and crack depth under different strengthening CFRP patches is shown in Fig. 10. The effective stress range increases with the increase of the crack depth. The effect of different types of CFRP patches on the effective stress range is nearly the same. Fig. 11 shows that fatigue life predictions

compare with test data via the TCD approach. Most estimated data are within an error band of 3. The TCD can be successfully utilized to estimate the fatigue life of cracked welded joints repaired without and with CFRP patches.

4.1.2. NSIF

When $2\alpha = 0$, the value of ΔK_{IA} was set to 180 MPa mm^{0.5} at 5 million cycles, and the inverse slope p was -3 [42]. According to Eq. (11), Fig. 12 plots the NSIF range varies with r for D1 specimens. The NSIF range is determined based on the averaged value. Similarly, Fig. 13 plots the all calculated results of NSIF ranges in the same way. The NSIF range increases with the increase of the crack depth. The effect of different types of CFRP patches on the NSIF range is nearly the same. Fig. 14 shows that fatigue life predictions compare with test data via the NSIF approach. Only half estimated data are within an error band of 3. All unstrengthened cruciform joints agree excellent with test results, but there is a relative large error for cruciform joints strengthened with CFRP patches. Existing assessment parameters for the NSIF method are needed to further in-depth study based on fatigue test results.

4.1.3. SED

For fatigue cracks initiate at the weld toe or root, the control radius $R_0 = 0.28$ mm was usually applied to evaluate the fatigue strength of steel welded joints considering the practical application [42]. The mean value of the SED range at 2 million cycles was 0.105 MJ/m³, and the negative inverse slope q of the ΔW - N curve on a log-log scale was 1.5 [42]. Thus, the fatigue life can be conveniently and easily obtained. Fig. 15 shows that fatigue life predictions compare with test results via the SED approach. Only half estimated data are within an error band of 3. Assessment data of all unstrengthened specimens agree excellent with experimental results, but there is a relative large error for cruciform joints strengthened with CFRP patches. Existing assessment parameters for the NSIF method are needed to further in-depth study based on fatigue test results.

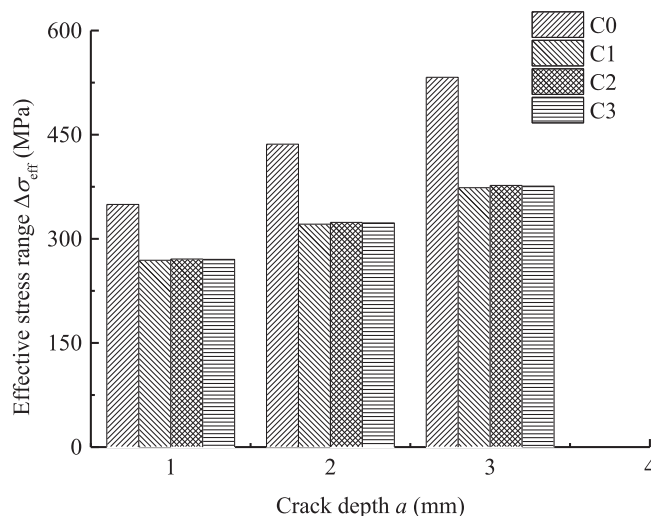


Fig. 10. Effective stress range versus crack depth.

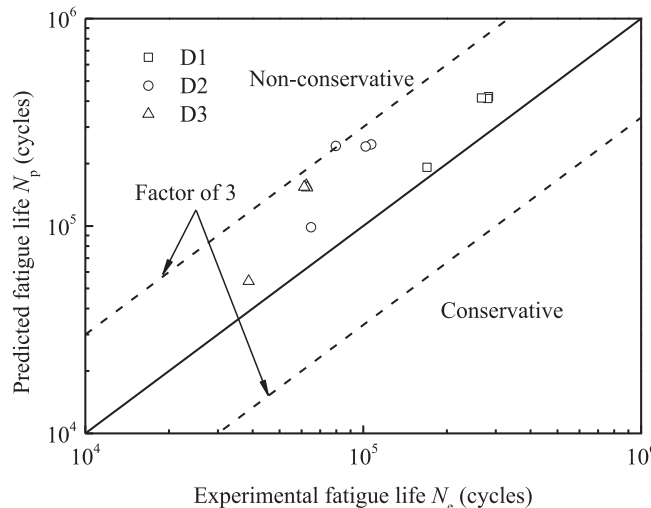


Fig. 11. Fatigue life predictions compare with test data via the TCD approach.

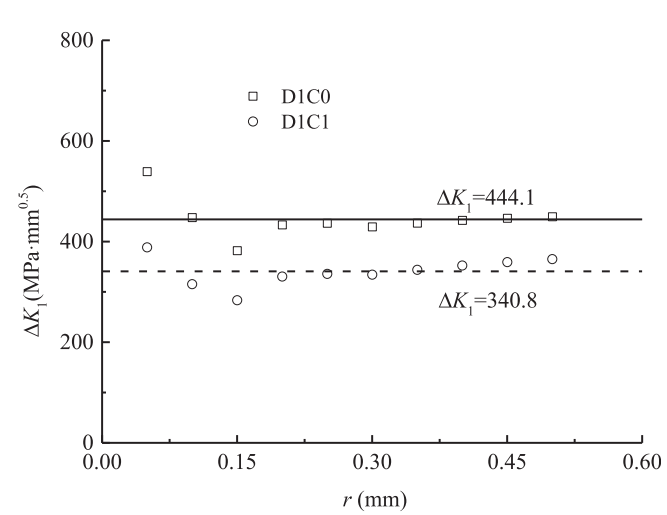


Fig. 12. The relationship between NSIF range and r .

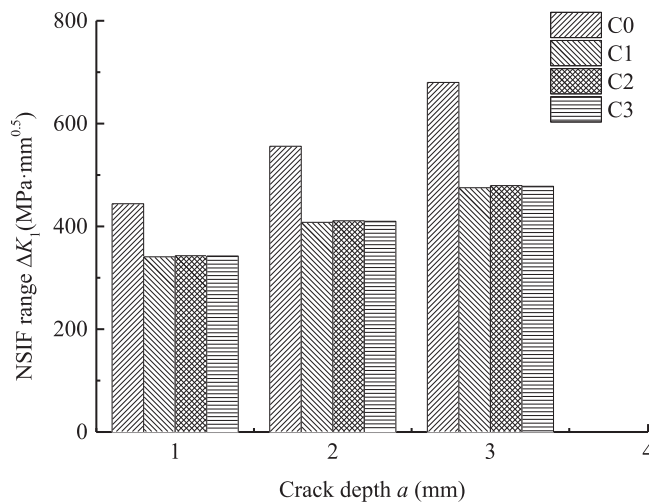


Fig. 13. The relationship between NSIF range and crack depth.

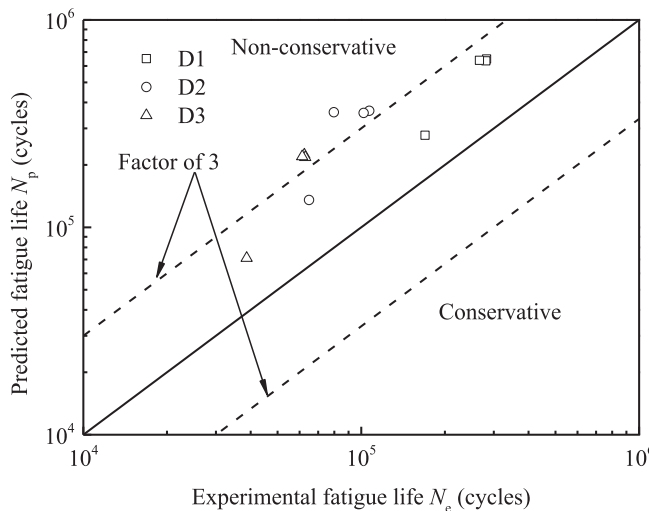


Fig. 14. Fatigue life predictions compare with test data via the NSIF approach.

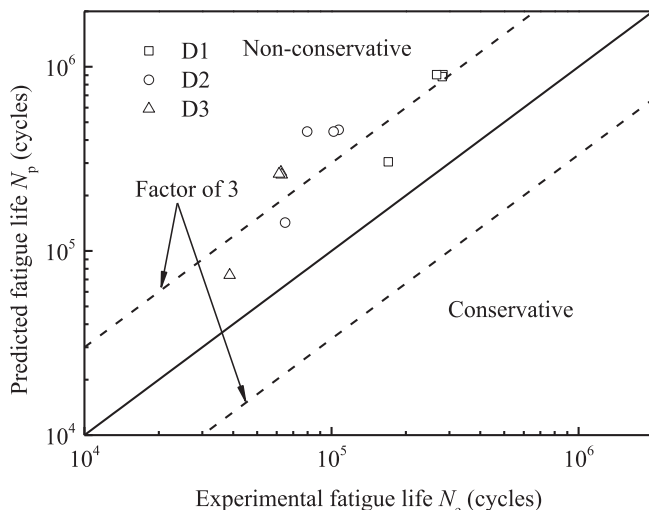


Fig. 15. Fatigue life predictions compare with test data via the SED approach.

to Section 4.1.1, it is found that fatigue life predicted results using the SED are generally larger than those using the TCD. More accurate results are obtained by the TCD. It needs to study suitable assessment parameters for the SED method.

4.2. XFEM

For unreinforced specimens, material constants C and m are recommended to be 3.98×10^{-13} and 2.88 [51], respectively. For CFRP strengthening specimens, the crack tip stress significantly reduces, and CFRP patches restrict the crack opening. Thus, material constants C and m are taken from the values of 6.03×10^{-15} and 3.639 [52], respectively. Eq. (25) is inserted into Eq. (22) only considering the effect of ΔK_I . Fatigue crack propagation equations of cracked cruciform welded joints repairing without and with CFRP patches in the form of ΔG can be expressed as:

$$\frac{da}{dN} = \begin{cases} 2.10 \times 10^5 (\Delta G)^{1.44} & \text{for without CFRP} \\ 3.46 \times 10^5 (\Delta G)^{1.82} & \text{for with CFRP} \end{cases} \quad (34)$$

Fatigue crack growth can be simulated by the direct cycle in ABAQUS. In order to assure the fatigue crack propagation, material parameters c_1 and c_2 are set to 0.001 and 0, respectively [53]. The relationship between a and N obtained from numerical simulations is plotted in Fig. 16. Figs. 17 and 18 show fatigue crack growth simulation paths of unrepaired and CFRP repaired welded joints at different time. Fatigue crack growth actual paths are illustrated in Fig. 19. It is obvious that 80% of the fatigue life is in a slow and stable crack growth stage, and there is an agreement with the variation of the loading frequency. A small deflection angle at the beginning stage of the fatigue crack growth is generated, and then it grows linearly. The main reason is that mode II energy release rates decrease as the increase of crack depth. It agrees reasonably with actual paths. Fig. 20 plots that fatigue life predictions compare with test data using the XFEM. All results are within an error band of 2. The XFEM used to predict the fatigue life is verified by experimental data.

5. Conclusions

Based on the above numerical simulation and fatigue test analyses, the conclusions can be drawn.

- (1) CFRP patches can effectively improve the fatigue life of cruciform welded joints with initial cracks. But there is little difference in strengthening effects between different CFRP patches. The remaining fatigue life and fatigue strength decrease as the increase of initial crack depth. Fatigue strength of welded joints with initial crack depth equal to 3 mm is only about one half of undamaged welded joints at 2 million cycles. There is a large scatter on the fatigue life increase for the same CFRP patches. Three fatigue failure modes can be obtained from the fatigue crack growth. Fatigue damage evolution equations of cruciform joints strengthened without and with CFRP patches are regressed using the fatigue test data.
- (2) The TCD, NSIF, and SED can be successfully used to predict the fatigue life of cruciform joints without CFRP patches. However, it needs to further investigate the values of corresponding estimation parameters for cruciform joints with CFRP patches for the NSIF approach and the SED approach. The XFEM is effective and convenient to estimate the fatigue life of cracked cruciform welded joints repaired without and with CFRP patches. Fatigue crack growth paths and lives simulated agree well with actual results. The accuracy and reliability are validated by fatigue test results.

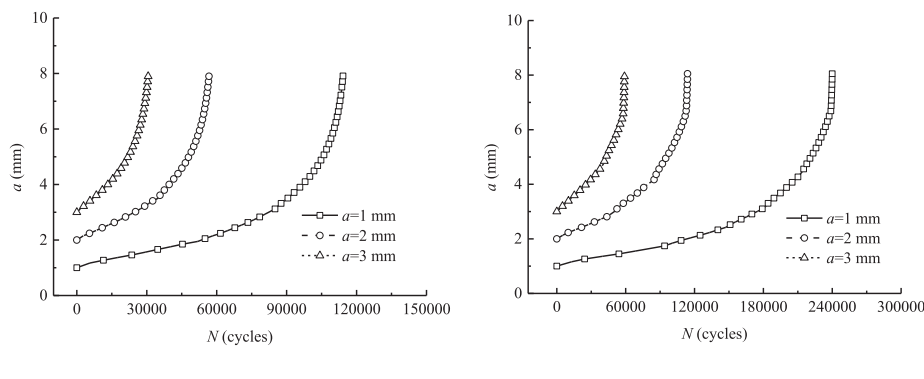
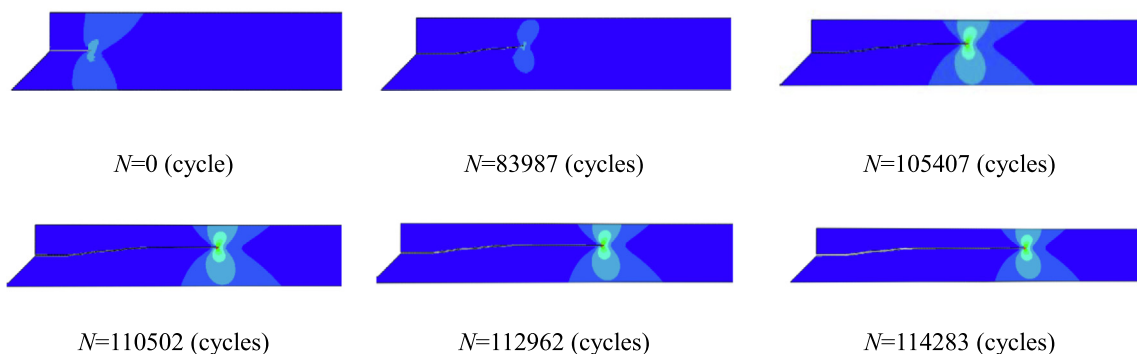
Fig. 16. Crack depth a versus the number of cycles to failure N .

Fig. 17. Fatigue crack growth simulation path for D1C0 specimen.

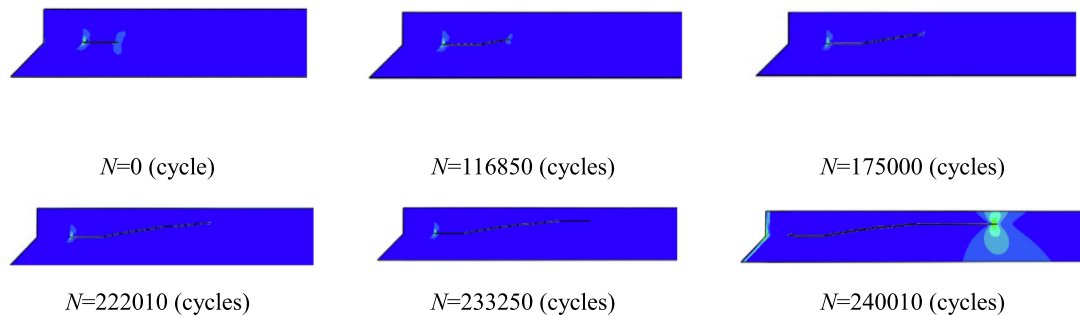


Fig. 18. Fatigue crack growth simulation path for D1C1 specimen.

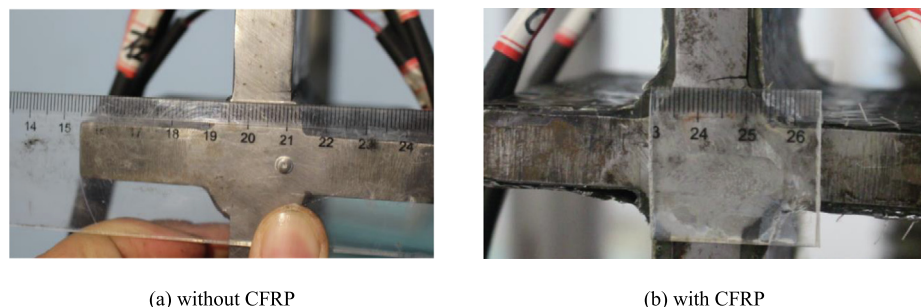


Fig. 19. Fatigue crack growth actual path.

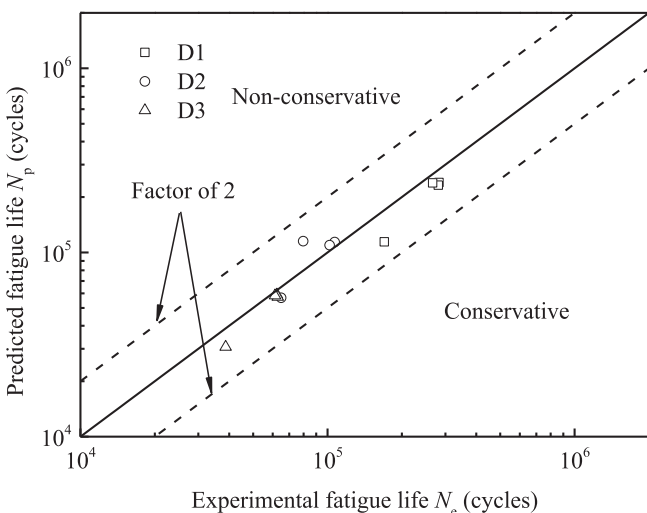


Fig. 20. Fatigue life predictions compare with test data via the XFEM.

CRediT authorship contribution statement

Zhiyu Jie: Conceptualization, Methodology, Investigation. **Wujun Wang:** Software, Validation. **Chao Chen:** Data curation, Formal analysis. **Kainan Wang:** Investigation.

Declaration of Competing Interest

The authors declare that they have no known competing financial interests or personal relationships that could have appeared to influence the work reported in this paper.

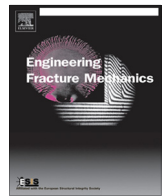
Acknowledgements

This work is sponsored by National Natural Science Foundation of China (51708305), Zhejiang Provincial Natural Science Foundation of China (LQ17E080005) and K. C. Wong Magna Fund in Ningbo University.

References

- [1] Hassan NK, Ahmed YF, Sayed TH. Fatigue life of cruciform welded joint strengthened with CFRP. *World Appl Sci J* 2015;33(5):823–30.
- [2] Wang Z, Wang Q, Li L, Zhang N. Fatigue behaviour of CFRP strengthened open-hole steel plates. *Thin Wall Struct* 2017;115:176–87.
- [3] Wang H, Wu G. Crack propagation prediction of double-edged cracked steel beams strengthened with FRP plates. *Thin Wall Struct* 2018;127:459–68.
- [4] Radaj D, Sonsino CM, Fricke W. Recent developments in local concepts of fatigue assessment of welded joints. *Int J Fatigue* 2009;31(1):2–11.
- [5] Taylor D. The theory of critical distances. *Eng Fract Mech* 2008;75(7):1696–705.
- [6] Pluvinage G. Fatigue and fracture emanating from notch; the use of the notch stress intensity factor. *Nucl Eng Des* 1998;185:173–84.
- [7] Lazzarin P, Livieri P, Berto F, Zappalorto M. Local strain energy density and fatigue strength of welded joints under uniaxial and multiaxial loading. *Eng Fract Mech* 2008;75(7):1875–89.
- [8] Zhou H, Wen J, Wang Z, Zhang Y, Du X. Fatigue crack initiation prediction of cope hole details in orthotropic steel deck using the theory of critical distances. *Fatigue Fract Eng M* 2016;39(9):1051–66.
- [9] Nie B, Chen D, Zhao Z, Zhang J, Meng Y, Gao G. Notch effect on the fatigue behavior of a TC21 titanium alloy in very high cycle regime. *Appl Sci* 2018;8(9):1614.
- [10] Jie Z, Susmel L. High-strength steel wires containing corrosion pits: stress analysis and critical distance based fatigue life estimation. *Fatigue Fract Eng M* 2020;43(8):1611–29.
- [11] Al Zamzami I, Susmel L. On the accuracy of nominal, structural, and local stress based approaches in designing aluminium welded joints against fatigue. *Int J Fatigue* 2017;101:137–58.
- [12] Karakaş Ö, Zhang G, Sonsino CM. Critical distance approach for the fatigue strength assessment of magnesium welded joints in contrast to Neuber's effective stress method. *Int J Fatigue* 2018;112:21–35.
- [13] Al Zamzami I, Davison B, Susmel L. Nominal and local stress quantities to design aluminium-to-steel thin welded joints against fatigue. *Int J Fatigue* 2019;123:279–95.
- [14] Baumgartner J, Yildirim HC, Barsoum Z. Fatigue strength assessment of TIG-dressed welded steel joints by local approaches. *Int J Fatigue* 2019;126:72–8.
- [15] Zamzami IA, Susmel L. On the use of hot-spot stresses, effective notch stresses and the Point Method to estimate lifetime of notched welds subjected to uniaxial fatigue loading. *Int J Fatigue* 2018;117:432–49.
- [16] Gorouhi H. Novel fatigue analysis of old metallic bridges through the theory of critical distances (TCD). Guildford, UK: University of Surrey; 2017.
- [17] Fang Z, Li A, Ding Y, Li W. Wind-induced fatigue assessment of welded connections in steel tall buildings using the theory of critical distances. *Eur J Environ Civ Eng* 2018;1:26.
- [18] Lazzarin P, Tovo R. A unified approach to the evaluation of linear elastic stress fields in the neighborhood of cracks and notches. *Int J Fracture* 1996;78(1):3–19.
- [19] Lazzarin P, Tovo R. A notch intensity factor approach to the stress analysis of welds. *Fatigue Fract Eng M* 1998;21(9):1089–103.
- [20] Meneghetti G, Campagnolo A. State-of-the-art review of peak stress method for fatigue strength assessment of welded joints. *Int J Fatigue* 2020;105705.
- [21] Campagnolo A, Vormwald M, Shams E, Meneghetti G. Multiaxial fatigue assessment of tube-tube steel joints with weld ends using the peak stress method. *Int J Fatigue* 2020;135:105495.
- [22] Campagnolo A, Zuin S, Meneghetti G. Averaged strain energy density estimated rapidly from nodal displacements by coarse FE analyses: Cracks under mixed mode loadings. *Fatigue Fract Eng M* 2020;43(8):1658–85.
- [23] Lazzarin P, Zambardi R. A finite-volume-energy based approach to predict the static and fatigue behavior of components with sharp V-shaped notches. *Int J Fracture* 2001;112(3):275–98.
- [24] Leonardi A. Advanced local approach for the fatigue assessment of aluminium weldments. Trondheim, Norway: Norwegian University of Science and Technology; 2018.
- [25] Berto F, Vinogradov A, Filippi S. Application of the strain energy density approach in comparing different design solutions for improving the fatigue strength of load carrying shear welded joints. *Int J Fatigue* 2017;101:371–84.
- [26] Berto F, Campagnolo A, Chebat F, Cincera M, Santini M. Fatigue strength of steel rollers with failure occurring at the weld root based on the local strain energy values: Modelling and fatigue assessment. *Int J Fatigue* 2016;82:643–57.
- [27] Song W, Liu X, Berto F, Wang P, Xu J, Fang H. Strain energy density based fatigue cracking assessment of load-carrying cruciform welded joints. *Theor Appl Fract Mec* 2017;90:142–53.
- [28] Song W, Liu X, Razavi SMJ. Fatigue assessment of steel load-carrying cruciform welded joints by means of local approaches. *Fatigue Fract Eng M* 2018;41(12):2598–613.
- [29] Foti P, Berto F, Filippi S. Fatigue assessment of welded joints by means of the Strain Energy Density method: Numerical predictions and comparison with Eurocode 3. *Frattura ed Integrità Strutturale* 2019;13(47):104–25.
- [30] Luo P, Zhang Q, Bao Y, Zhou A. Fatigue evaluation of rib-to-deck welded joint using averaged strain energy density method. *Eng Struct* 2018;177:682–94.
- [31] Fischer C, Fricke W, Rizzo CM. Review of the fatigue strength of welded joints based on the notch stress intensity factor and SED approaches. *Int J Fatigue* 2016;84:59–66.
- [32] Kraedeh AMA. Fatigue crack growth in T welded joint of aluminium alloy. Belgrade, Serbia: University of Belgrade; 2018.
- [33] Bergara A, Dorado JI, Martin-Meizoso A, Martínez-Esnaola JM. Fatigue crack propagation in complex stress fields: Experiments and numerical simulations using the Extended Finite Element Method (XFEM). *Int J Fatigue* 2017;103:112–21.
- [34] Nikfam MR, Zeinoddini M, Aghebati F, Arghaei AA. Experimental and XFEM modelling of high cycle fatigue crack growth in steel welded T-joints. *Int J Mech Sci* 2019;153:178–93.
- [35] Wang C, Wang Y, Cui B, Duan L, Ma N, Feng J. Numerical simulation of distortion-induced fatigue crack growth using extended finite element method. *Struct Infrastruct E* 2020;16(1):106–22.
- [36] Zarrinzadeh H, Kabir MZ, Deylami A. Experimental and numerical fatigue crack growth of an aluminium pipe repaired by composite patch. *Eng Struct* 2017;133:24–32.
- [37] Valadi Z, Bayesteh H, Mohammadi S. XFEM fracture analysis of cracked pipeline with and without FRP composite repairs. *Mech Adv Mater Struc* 2018;23:1–12.
- [38] Lesiuk G, Katkowski M, Correia J, de Jesus AM, Blazewski W. Fatigue crack growth rate in CFRP reinforced constructional old steel. *Int J Struct Integr* 2018;9(3):381–95.
- [39] Louks R, Susmel L. The linear-elastic Theory of Critical Distances to estimate high-cycle fatigue strength of notched metallic materials at elevated temperatures. *Fatigue Fract Eng M* 2015;38(6):629–40.
- [40] El Haddad MH, Smith KN, Topper TH. Fatigue crack propagation of short cracks. *J Eng Mater Technol* 1979;101(1):42–6.
- [41] Susmel L, Taylor D. A novel formulation of the theory of critical distances to estimate lifetime of notched components in the medium-cycle fatigue regime. *Fatigue Fract Eng M* 2007;30(7):567–81.
- [42] Livieri P, Lazzarin P. Fatigue strength of steel and aluminium welded joints based on generalised stress intensity factors and local strain energy values. *Int J Fracture* 2005;133(3):247–76.
- [43] Mohammadi S. Extended finite element method: for fracture analysis of structures. Oxford, UK: John Wiley & Sons; 2008.
- [44] Amiri Rad A, Forouzan MR, Sadeghi DA. Three-dimensional fatigue crack growth modelling in a helical gear using extended finite element method. *Fatigue Fract Eng M* 2014;37(6):581–91.

- [45] GB/T 714-2015. Structural steel for bridge. China, 2015. (in Chinese)
- [46] Fricke W. IIW guideline for the assessment of weld root fatigue. *Weld World* 2013;57(6):753–91.
- [47] Jie Z, Wang W, Fang R, Zhuge P, Ding Y. Stress intensity factor and fatigue analysis of cracked cruciform welded joints strengthened by CFRP sheets considering the welding residual stress. *Thin Wall Struct* 2020;154:106818.
- [48] Jie Z, Li Y, Wei X, Zhuge P. Fatigue life prediction of welded joints with artificial corrosion pits based on continuum damage mechanics. *J Constr Steel Res* 2018;148:542–50.
- [49] Susmel L. Modified Wöhler curve method, theory of critical distances and Eurocode 3: A novel engineering procedure to predict the lifetime of steel welded joints subjected to both uniaxial and multiaxial fatigue loading. *Int J Fatigue* 2008;30(5):888–907.
- [50] EN 1993-1-9. Eurocode 3: Design of Steel Structures Part 1-9: Fatigue. 2005.
- [51] BS 7910. Guide to methods for assessing the acceptability of flaws in metallic structures. British Standards Institution, 2013.
- [52] Wang H. Study on the fatigue behavior of CFRP plate strengthened steel structures and its design method. Nanjing, China: Southeast University; 2016 (in Chinese).
- [53] Gupta RS. Prediction of Fatigue Crack Propagation in Orthotropic Steel Decks using XFEM based on LEFM and VCCT. Delft, Netherlands: Delft University of Technology; 2019.



Verification of the repair effect for fatigue cracks in members of steel bridges based on thermoelastic stress measurement



Takahide Sakagami ^{a,*}, Yoshiaki Mizokami ^b, Daiki Shiozawa ^a, Taisei Fujimoto ^a, Yui Izumi ^c,
Taku Hanai ^b, Akira Moriyama ^b

^a Department of Mechanical Engineering, Kobe University, 1-1 Rokkodai-cho, Nada-ku, Kobe 657-8501, Japan

^b Honshu-Shikoku Bridge Expressway Company Limited, 4-1-22 Onoe-dori, Chuo-ku, Kobe 651-0088, Japan

^c Department of Mechanical Systems Engineering, University of Shiga Prefecture, 2500 Hassaka-cho, Hikone 522-0057, Japan

ARTICLE INFO

Article history:

Received 15 January 2017

Received in revised form 15 May 2017

Accepted 17 May 2017

Available online 27 May 2017

Keywords:

Nondestructive evaluation

Thermoelasticity

Infrared thermography

Fatigue cracks

Steel bridges

ABSTRACT

Ageing steel bridges suffer fatigue cracks thereby necessitating immediate inspection, structural integrity evaluation or repair in the life cycle of steel bridges. We propose non-destructive evaluation techniques employing infrared thermography enabling us to remotely inspect the fatigue cracks in steel bridges and evaluate the structural integrity on the basis of thermoelastic stress measurement. This study presents a structural integrity assessment of steel bridges using remote measurement of the stress field around the fatigue cracks. We focus upon experimental results confirming reduction in the severity of the stress distribution around the fatigue cracks after the repair or reinforcement of members in steel bridges.

© 2017 Elsevier Ltd. All rights reserved.

1. Introduction

Propagation of fatigue cracks from welded joints in steel bridges is one of the most serious problems associated with the deterioration of ageing infrastructure. Inspection of the deterioration such as fatigue damage or corrosion is necessary for ensuring safety and estimating the remaining strength of the steel bridges. In this respect, nondestructive testing (NDT) and nondestructive evaluation (NDE) techniques play important roles. Conventional NDT techniques for steel bridges include visual testing, eddy-current testing, magnetic-particle testing and ultrasonic testing. However, these are time- and labor-intensive techniques that require special equipment for inspection such as scaffoldings or vehicles for high-lift work. The Japan Ministry of Land, Infrastructure, Transport and Tourism has reported that there are over 0.7 million bridges requiring inspection [1]. This means that it is not realistically possible to employ conventional NDT techniques for ageing bridges; hence, a high-performance NDT method is essential for their effective maintenance. In addition, structural integrity evaluation is considered essential for the fitness for service evaluation of ageing steel bridges. For an accurate structural integrity evaluation, the actual applied-stress distribution around a fatigue crack and its history owing to the moving wheel load caused by vehicles on the bridge needs to be obtained. Conventional stress- and strain-measurement techniques are insufficient for these requirements.

Thermoelastic stress analysis (TSA) using infrared thermography has come into widespread use in the industry as an effective, experimental, full-field stress measurement technique [2–5]. Especially innovative research works on the TSA

* Corresponding author.

E-mail address: sakagami@mech.kobe-u.ac.jp (T. Sakagami).

technique are found in structural integrity evaluations for steel structures as well as composite structures related with fracture mechanics evaluations and/or fatigue damage analyses. As for steel structural members, evaluation schemes of the fracture mechanics parameters have been investigated taking advantages of the TSA technique [6]. The fracture mechanics parameters such as stress intensity factor or J -integral were determined from the directly measured stress distribution around crack tips in objective structures [7–10]. These techniques have been successfully applied on the fatigue life assessment. Tomlinson et al. [11] investigated fatigue crack propagation under the mixed mode loading. Diaz et al. [12] applied their improved TSA technique for evaluating stress intensity factors in the fatigue test of weld specimen demonstrating the potential of TSA for crack growth analysis influenced by crack closure or residual stress field. Ummenhofer et al. [13] also investigated the applicability of the TSA technique for fatigue damage evaluation in welded joints. The TSA technique has been also employed as a powerful tool for evaluating impact or fatigue damages in composite materials and structures [14–17]. Emery et al. [18] showed the feasibility of the TSA for evaluating fiber breakage, matrix cracking and delamination damage in composites. Fruehmann et al. [19] applied the TSA technique for the assessment of fatigue damage evolution in woven composite materials. Paynter and Dutton [20] applied the TSA technique to wind turbine blade composite structure, in which successful results were obtained in damage evaluation using second harmonic signal correlation. Jones and Molent [21] showed the applicability of the TSA technique for in situ measurement during redesign, reinforcement or repair in aircraft structures.

These literatures showed the strong advantages of the TSA technique for the remote, noncontact, nondestructive and full-field stress measurement, as well as its applicability for various types of structural damages. Therefore, a useful and powerful technique for evaluating structural integrity related with fatigue damage evolution can be developed based on the TSA technique for the maintenance of ageing steel bridges.

This study focuses on the TSA-based in situ evaluation technique for stress reduction and restoration of structural integrity after repair or reinforcement. Fatigue cracks were found in the structural members of the Seto-Ohashi Bridges connecting the Honshu and Shikoku islands in Japan during their 21st-year inspection. Several repair methods have been investigated by experimental studies at the site. The stress distributions around the fatigue cracks were measured by employing the TSA technique when live loading acted on the bridge and the effectiveness of the severity reduction using these repair methods was investigated.

2. Fatigue crack evaluation in the life of steel bridges

The present authors [22] developed remote NDT- and NDE-techniques using infrared thermography for the maintenance of ageing steel structures. Fig. 1 shows a schematic of the proposed life cycle NDT- and NDE-techniques for steel bridges using infrared thermography. The first sign of deterioration in ageing steel bridges is the initiation of fatigue cracks. It would be beneficial to predict the occurrence and location of fatigue crack initiation. The feasibility of dissipated energy measurement was investigated for predicting the fatigue-crack initiation [23]. After the initiation of fatigue cracks, detection of these cracks is required for the maintenance of the steel bridges. The present authors [24] developed a relatively simple but useful

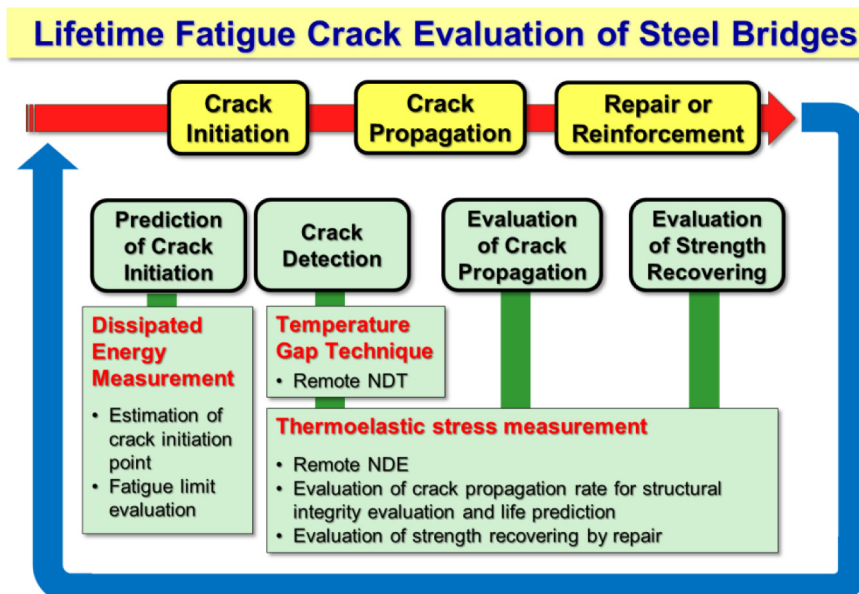


Fig. 1. Development of the NDT- and NDE-techniques using infrared thermography for fatigue cracks in steel bridges.

NDT technique for fatigue-crack detection on the basis of the temperature gap that appears on the surfaces of the structural members because of the thermal-insulation effect of the cracks. Fatigue cracks can be also detected on the basis of the stress distribution around the crack tips measured by the TSA technique using infrared thermography. Sakagami et al. [25] developed a self-reference lock-in thermography technique for the signal-noise ratio (S/N) improvement that requires no external reference signals and can be employed even under irregular-waveform loading. Once a fatigue crack is initiated, it is necessary to evaluate its size and propagation rate, and fracture-mechanics analysis needs to be conducted to evaluate the bridge's remaining strength. The TSA technique was effectively applied for a full-field stress-distribution measurement around the crack tips, followed by a fracture-mechanics evaluation using the stress intensity factor [22].

Finally after an ample crack propagation, steel bridges require repair or reinforcement to prolong their life. Various repair-and reinforce-methods have been investigated for fatigue damages in welded steel structures. Matsumoto et al. [26] compared the fatigue-life extension effects among three different types of repairs, namely, crack removal by grinder treatment, impact crack-closure retrofit (ICR) treatment and stop-hole technique. Yuan Zhou et al. [27] also investigated the effect of ICR treatment on welded joints using strain gauges and finite element method (FEM) analyses. Aoki et al. [28] examined the stiffener-bonding repair technique for through-thickness fatigue cracks at the vertical stiffener end in an orthotropic steel deck.

In almost all previous studies, the effect of stress-severity reduction by repair work was investigated only by strain measurement using strain gauges or FEM analyses. The authors consider it is essential to experimentally confirm the severity reduction of the stress distribution around the damaged portion after the repair or reinforcement of the structural members in steel bridges. Therefore, the TSA-based in situ evaluation technique for stress reduction and restoration of structural integrity after repair or reinforcement was developed.

3. Thermoelastic stress measurement

Dynamic stress change causes a very small temperature change under adiabatic conditions in a solid. This phenomenon is known as the thermoelastic effect and is described by Lord Kelvin's equation [29], which relates the temperature change (ΔT) to the sum of the changes in the principal stresses ($\Delta\sigma$) under cyclic variable loading as follows.

$$\Delta T = -\frac{\alpha}{\rho C_p} T \Delta\sigma \quad (1)$$

here, α is the coefficient of thermal expansion, ρ is the mass density, C_p is the specific heat at constant pressure and T is the absolute temperature. The sum of the changes in the principal stresses ($\Delta\sigma$) is obtained by measuring the temperature change (ΔT) using high-performance infrared thermography.

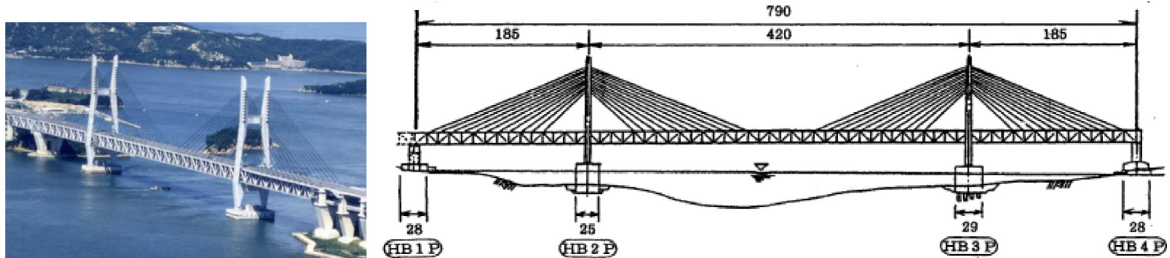
As thermoelastic temperature changes are very small and sometimes hidden by the thermal noise of the infrared camera, lock-in infrared thermography using reference signals synchronized with the stress changes is commonly employed to improve the accuracy of stress measurements. The conventional TSA technique requires a lock-in algorithm with a reference-loading signal extracted from the load cell or strain gauge to improve the signal-noise ratio. However, it is difficult to obtain a reference signal from steel bridges that are in service. Furthermore, the observed load signal contains an irregular waveform because of the wheel loading by vehicles on the bridge. These problems cause difficulties for the conventional lock-in infrared thermography to be employed for on-site thermoelastic stress measurements.

The present authors [25] solved these problems by developing a self-reference lock-in thermography technique that does not require any external reference signals and can be employed even under irregular-waveform loading. In this technique, a reference signal is constructed from a reference region that is arbitrarily set to the same sequential infrared images as those showing thermoelastic temperature changes. The distribution of the relative intensity of the thermoelastic temperature change against that in the reference region can then be obtained using the least-squares approach developed by Lesniak et al. [30], even under irregular-waveform loading, provided that the temperature change in the reference region has a similar and an in-phase waveform as that in the objective area under measurement. As a result of the self-reference lock-in data processing, stress-distribution images with improved S/N can be obtained.

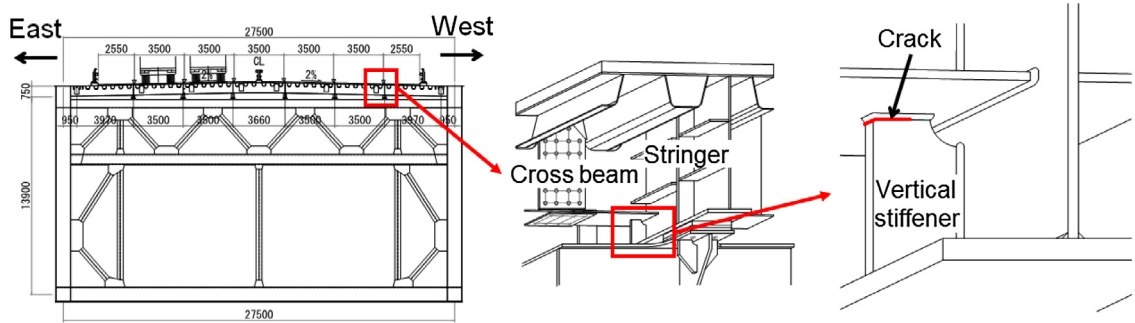
4. Objective steel members for evaluating the severity reduction of stress distribution by repair

Objective members for evaluating the reduction in the severity of the stress distribution after repair are the vertical stiffeners at the supports of steel decks where stringers intersect with cross beams in cable-stayed bridges in the part of the Seto-Ohashi Bridges as shown in Fig. 2. Fatigue cracks were detected at the upper weld part of the vertical stiffeners.

Fig. 3 shows the three different repair methods, i.e., (b) circular-arc cutout method, (c) stiffening-plate method (type I) and (d) improved stiffening-plate method (type II), examined in this study. All the repair methods were intended to mitigate the high stress concentration in the weld part located at the top of the stiffeners by transferring the high stress to the arc cutout or the stiffening plate. In areas where the above repair methods were applied, fatigue cracks were found to propagate in the eastern vertical stiffeners along the boxing-welding sections, as shown in Fig. 2. The results of magnetic-particle testing showed that the detected fatigue cracks varied in surface length from 20 mm to 40 mm.



(a) Hitsuishijima bridge in the part of the Seto-Ohashi Bridges



(b) Cross-section of bridge and details of objective member

Fig. 2. Objective member for evaluating the reduction in the severity of the stress distribution after repair in Hitsuishijima bridge in the part of the Seto-Ohashi Bridges.

The repair works and the thermoelastic-stress measurements were performed through the following stages: First, thermoelastic stress measurements around the fatigue cracks were conducted before repair. Second, each repair method was applied to the vertical stiffeners, while the cracks themselves were left as they were. Then, thermoelastic stress measurement was conducted to investigate the stress-reduction effect of the applied repair methods. Finally, the fatigue cracks were removed using the grinder treatment and the thermoelastic stress measurement was conducted again. For several vertical stiffeners additional re-welding treatment was applied followed by thermoelastic stress measurement.

5. In situ thermoelastic stress measurement under wheel loading

The stress distributions on the vertical stiffeners were measured before the repair and after each repair stage, as described at the end of Section 3. For each measurement, the objective structure was loaded with a vehicle driving on the traffic lane of the bridge at a constant speed of 80 km an hour. A sprinkler truck with three axles as shown in Fig. 4 was employed as a loading vehicle. The total vehicle load and each axle load were measured by the axle-load meter after filling up the water tank. The results were shown in Fig. 4. The thermoelastic temperature measurements were conducted more than 8 times at each experimental study under the same condition, and it was confirmed that reproducibility of the measurement is sufficient.

The thermoelastic stress measurement was conducted using a high-performance infrared camera with a QVGA InSb array detector (temperature resolution 20 mK), as shown in Fig. 5. The integration time and framing rate of the infrared camera were set to 1292 μ s and 157 Hz, respectively. The dominant frequency of the thermoelastic temperature change was estimated to be more than 5 Hz. This value was estimated from measured waveform of the thermoelastic temperature change, vehicle speed and the distance between front and center of rear tandem axles. Therefore the adiabatic condition required for the TSA was satisfied in this experimental study. From the temperature change observed by the infrared camera, the change in the sum of the principal stresses was calculated using Eq. (1), material properties of the structural steel (JIS SS400: $\alpha = 11.8 \times 10^{-6}/\text{K}$, $\rho = 7.86 \times 10^3 \text{ kg/m}^3$, $C_p = 473 \text{ J/kg}\cdot\text{K}$) and the ambient temperature. In this study the obtained sequential infrared data were processed using the self-reference lock-in technique to obtain S/N improved stress distribution images.

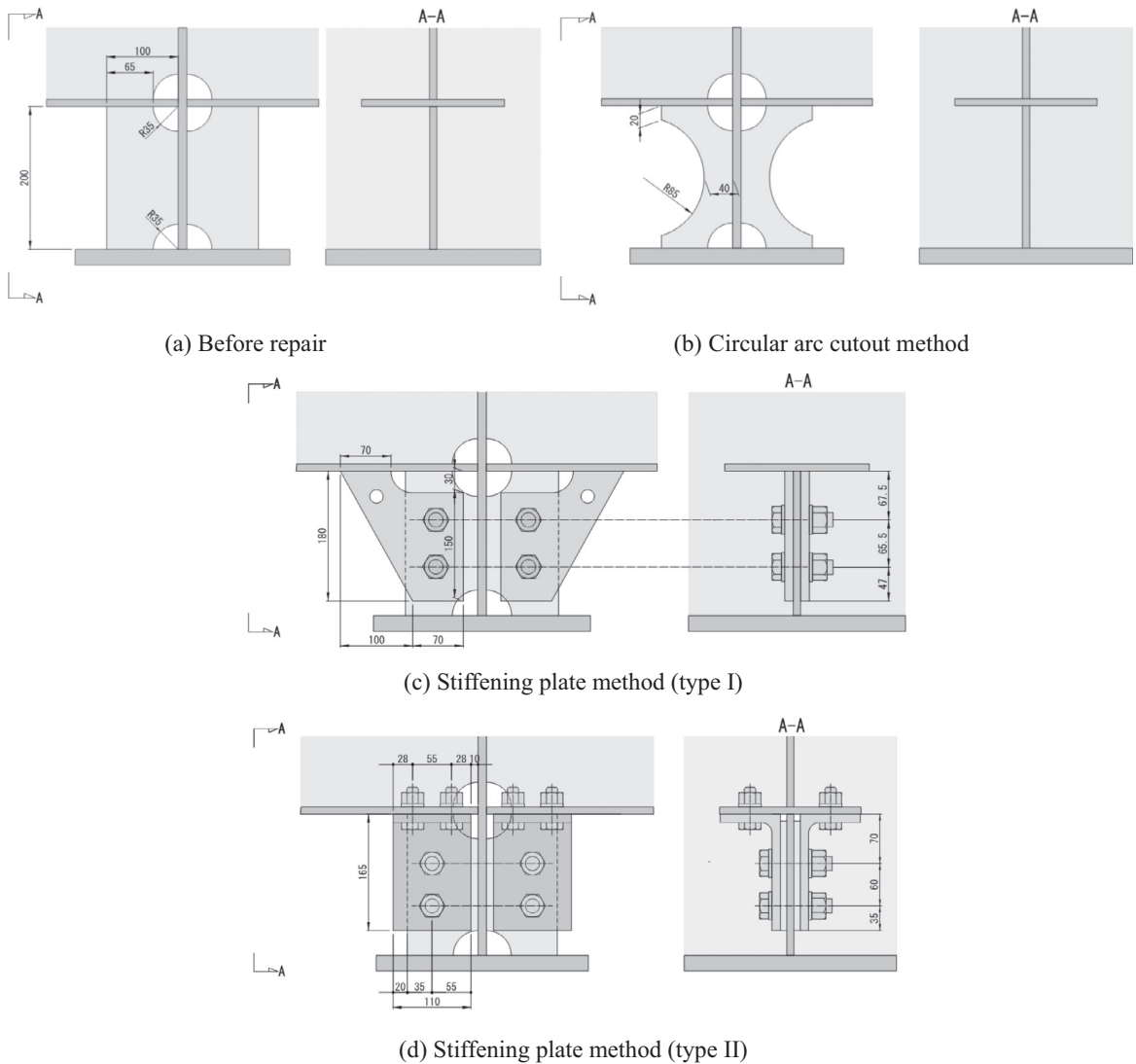


Fig. 3. Illustrations of vertical stiffener and employed repair methods.

6. Experimental results obtained for the circular-arc cutout repair method

Retrofitting measures applied to the weld of the vertical stiffeners by semicircular cutout treatment have been employed for effective repair of orthotropic steel decks [31]. The aim of this retrofitting measure is to reduce the stress concentration at the weld part and transfer the stress concentration point from that weld to the edge of the semicircular arc, which has a higher fatigue resistance.

The size of the circular cutout was determined by FEM analyses conducted prior to the on-site repair work. FEM analysis results are shown in Fig. 6. It is found that the high-stress concentration points are located in the upper weld regions of the original vertical stiffeners. In contrast, after the circular-arc cutout repair, the stress concentration areas are transferred from the weld part to the edges of the circular arc. The determined radius of the circular cutout was 85 mm.

Experimental thermoelastic stress measurement results obtained for the circular-arc cutout repair method are shown in Fig. 7. It is found from Fig. 7(a) that a high stress concentration can be observed at the crack tip before the repair. In contrast Fig. 7(b) shows that the stress concentration is observed at the edge of circular arc after the circular-arc cutout repair. The change in the sum of the principal stresses at the maximum stress concentration point was reduced by 50% after the circular-arc cutout repair. This experimental result is consistent with that of the FEM analysis, as shown in Fig. 6. From Fig. 7(c), it can be seen that the stress distribution obtained after re-welding did not change much. This experimental study clarified that this method can successfully transfer the high stress concentration from the weld part at the top of the stiffener to the edge of the circular arc where the fatigue resistance is higher. In this experimental study, stress values were simultaneously

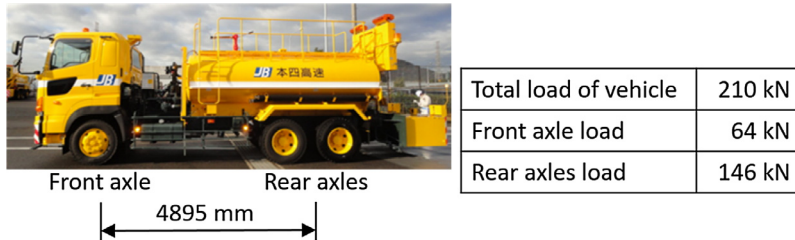


Fig. 4. Employed loading vehicle and axle load.

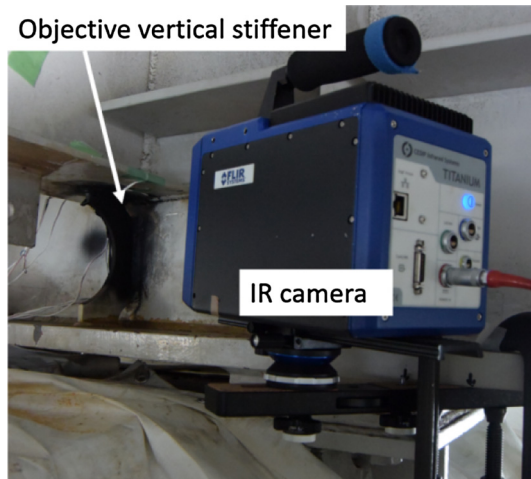


Fig. 5. Thermoelastic temperature measurement using infrared cameras.

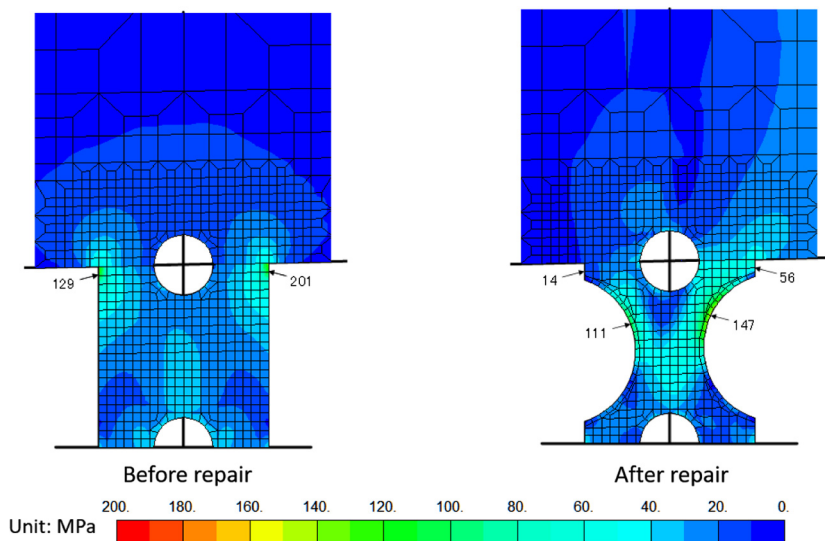


Fig. 6. Results of FEM analyses indicating the principal stress distributions before and after repair.

measured by strain gauges at several points on the vertical stiffener. Locations of the strain gauges and measured stress values are shown in Fig. 8. The results of stress reduction by the repair work show the same trend as that shown by the TSA results.

It is worth noting that the circular-arc cutout repair method was applied again to another vertical stiffener for which the radius of the circular cutout was reduced to 75 mm. The procedures of this repair work is compared with that for a circular

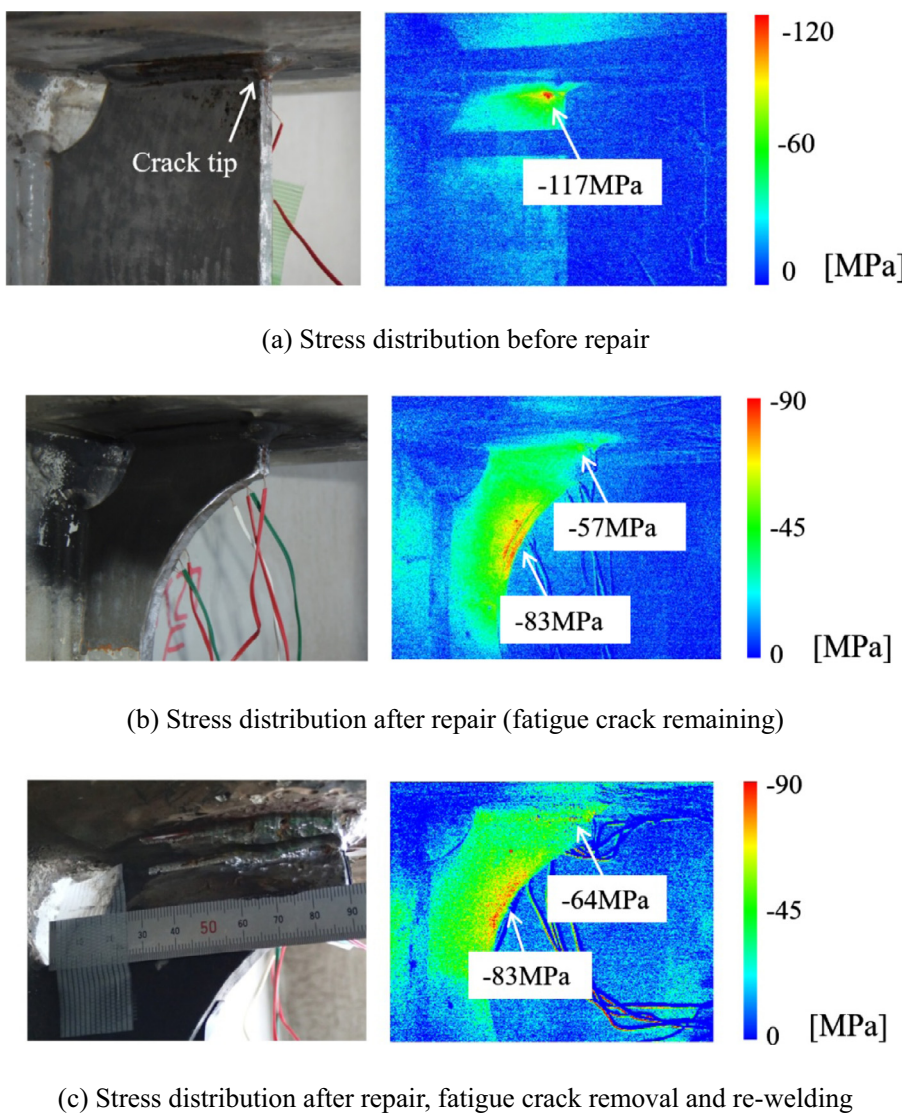


Fig. 7. Results of the thermoelastic stress distribution measurement for the circular-arc cutout repair method.

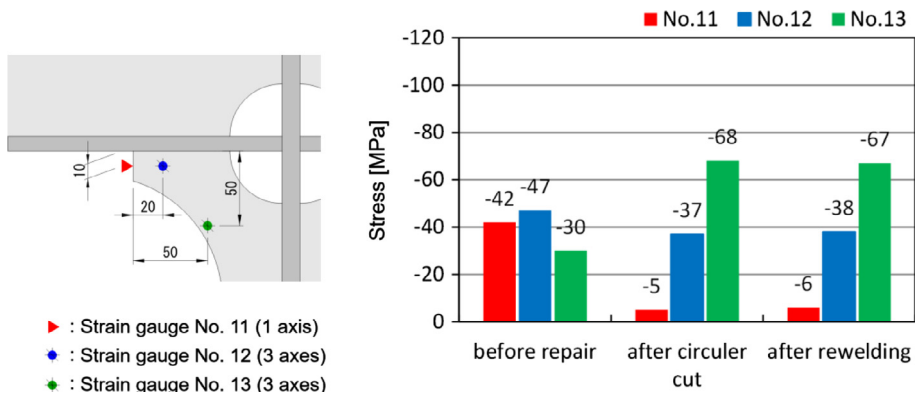


Fig. 8. Results of stress measurement by strain gauges obtained for the circular-arc cutout repair method.

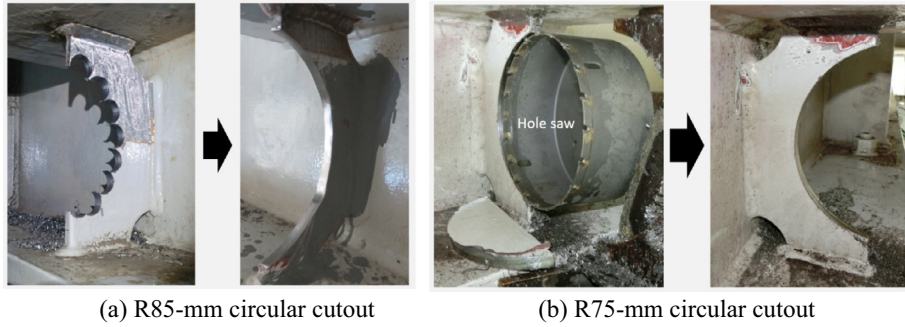


Fig. 9. Comparison of the machining processes used in semi-circular arc cutout repair.

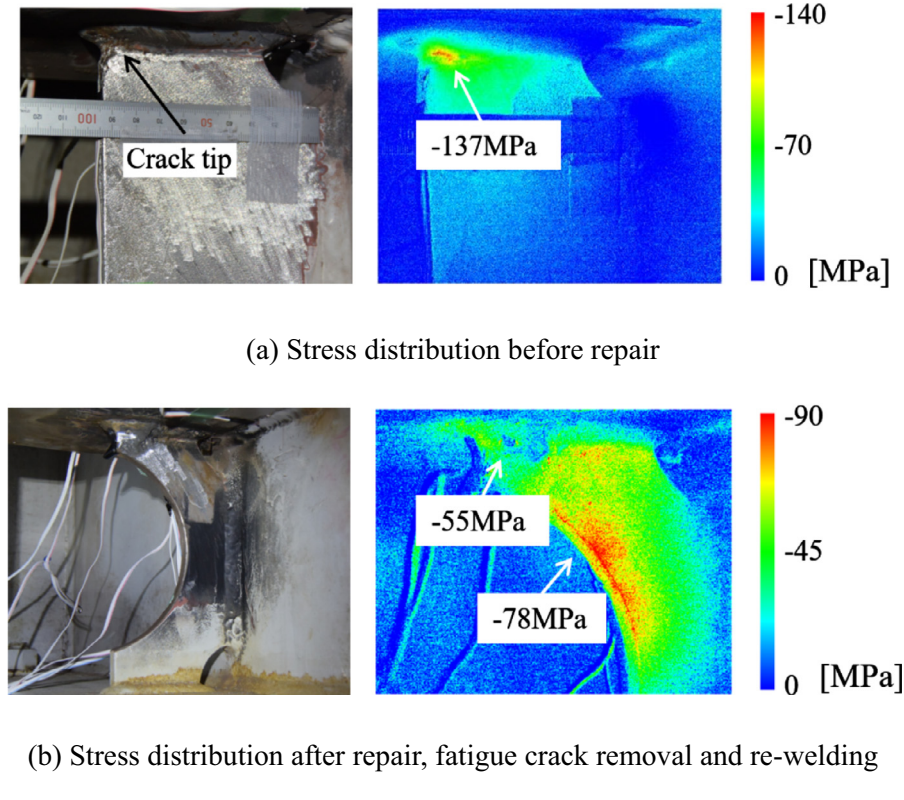


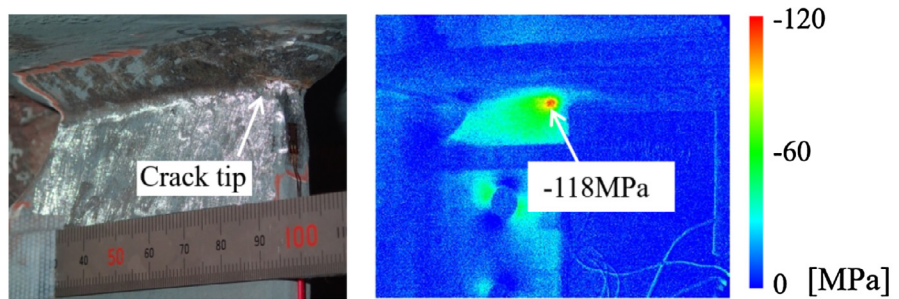
Fig. 10. Results of the thermoelastic stress distribution measurement for R75-mm circular arc cutout repair.

cutout with a radius of 85 mm, as shown in Fig. 9. It is found that the machining process of the R75-mm cutout is much simpler and less time consuming than that of the R85-mm cutout. The experimental results of the stress reduction effect are shown in Fig. 10. It was found that a comparable stress reduction effect was achieved in the case of a smaller cutout radius. R75-mm cutout repair is more beneficial for on-site repair work in terms of the effectiveness of stress reduction as well as the machining efficiency.

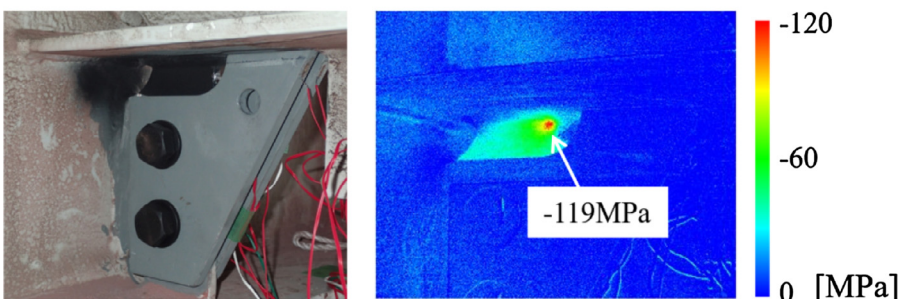
7. Experimental results obtained from the stiffening-plate repair method

Stiffening-plate repair is a well-known retrofitting measure for the structural members of orthotropic steel decks [32]. The aim of this repair technique is to reduce the high stress concentration in the weld part by sharing the loading paths among the vertical stiffener and stiffening plates. In this study, the stress mitigation effects of two different types of stiffening-plate repair techniques (as shown in Fig. 3(c) and (d)) were examined.

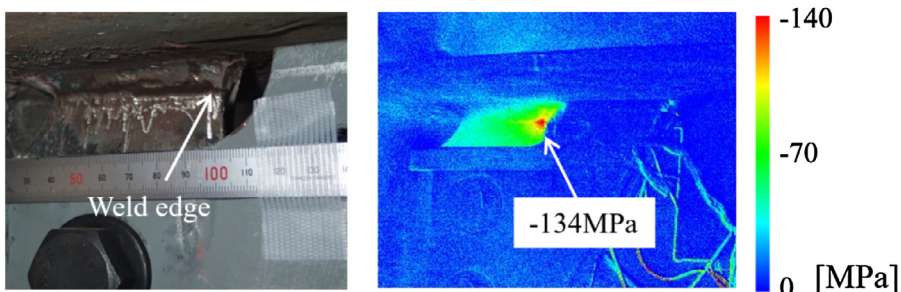
The experimental results of the thermoelastic stress measurement obtained for the type I stiffening-plate repair method are shown in Fig. 11. It is found from the figures that the high stress concentration at the crack tip was not mitigated even after the repair work was conducted. It seemed that the stiffening plates did not share the loading paths, thus the high stress



(a) Stress distribution before repair



(b) Stress distribution after repair (fatigue crack remaining)



(c) Stress distribution after repair, fatigue crack removal and re-welding

Fig. 11. Results of thermoelastic stress distribution measurements for type I stiffening-plate repair.**Fig. 12.** Results of stress measurement by strain gauges obtained for type I stiffening-plate repair.

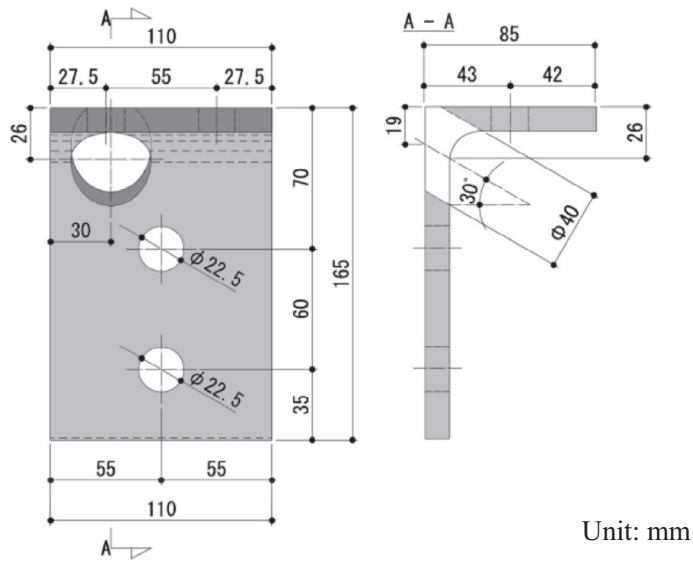


Fig. 13. Observation window in angle stiffener plate for infrared measurement.

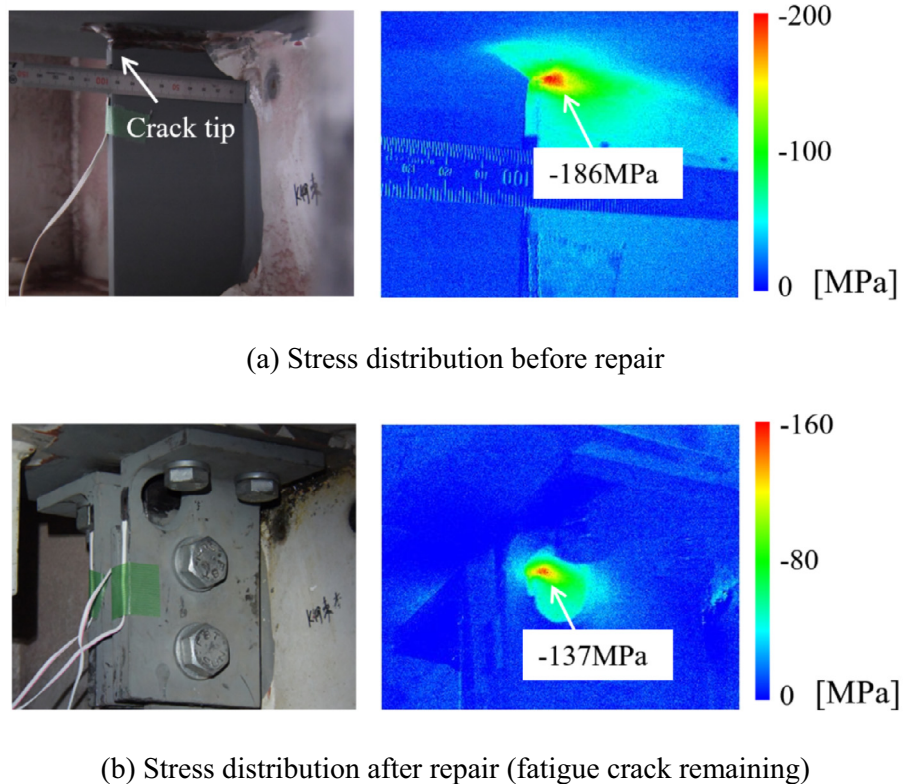


Fig. 14. Results of the thermoelectric stress distribution measurement for the type II stiffening-plate repair.

concentration in the weld part at top of the stiffener did not transfer to the stiffening plate. One possible cause is the incomplete contact of the upper edges of the stiffening plates with the lower surface of the cross-beam flange because of the incomplete finishing of the contact surfaces. This study clearly shows the benefit and importance of the in situ evaluation of the actual stress distribution achieved by the TSA technique. Stress values measured using the strain gauges are shown

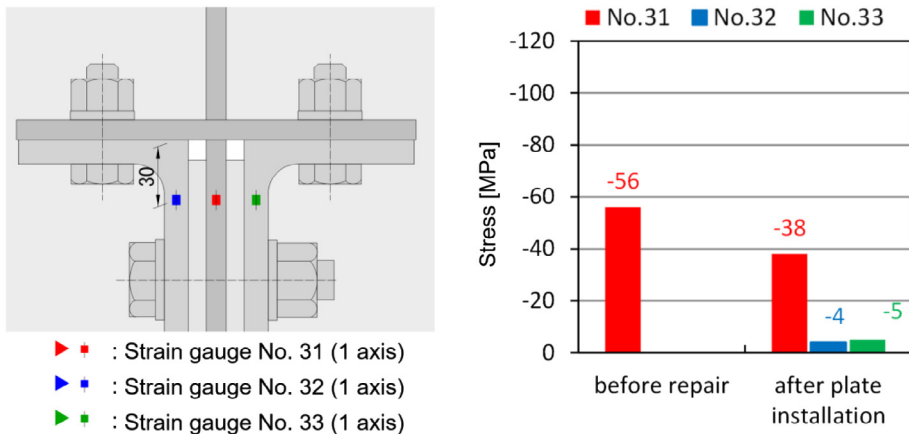


Fig. 15. Results of stress measurement by strain gauges obtained for type II stiffening-plate repair.

in Fig. 12. It is found that the high stress concentration near the crack tip was not mitigated after the repair work, and the stiffening plates did not share the loading.

In response to the unsuccessful stress reduction result of the type I stiffening-plate repair, the improved type II stiffening-plate repair method was examined. In this technique, four angle-stiffener plates were fastened to the vertical stiffeners and the lower cross beam flange using fastening bolts to better integrate the stiffeners and structural members. To avoid the problem of the infrared-measurement area being hidden by the angle-stiffener plate, an observation window was made in one of the plates, as shown in Fig. 13.

The experimental results of the thermoelastic stress measurement obtained for the improved type II stiffening-plate repair method are shown in Fig. 14. It is found from Fig. 14(b) that the stress concentration at the weld edge is observed even after stiffening-plate repair work. However in comparison to the stress value shown in Fig. 14(a), the maximum stress value in the vicinity of the crack tip is drastically decreased after the repair work. This result demonstrates that the improved type II stiffening-plate repair was successfully applied for stress mitigation at the crack tip by sharing the loading paths. Stress values measured using the strain gauges are shown in Fig. 15. It is found that the stress value on the edge surface was mitigated after the repair work since the stiffening plates shared the loading. Details of the fatigue life prolonging effect by stress mitigation will be investigated in future fracture mechanics studies by the present authors.

8. Conclusions

This study focused on repair techniques for the members of steel bridges with fatigue cracks as well as confirmation of the reduction in the severity of the stress distribution around the repaired portions using the TSA technique. Three different repair methods were investigated by in situ experiments and the following results were obtained.

- (1) It was found from experimental results of the circular-arc cutout repair method that the stress concentration around the fatigue crack tip at the top of stiffener was mitigated, and the high stress concentration area was successfully transferred from the weld part at the top of the stiffener to the edge of the circular arc, where the fatigue resistance is higher.
- (2) Experimental studies using two different types of stiffening-plate repair techniques showed that type I stiffening-plate repair did not effectively mitigate the stress because of the incomplete sharing of the loading paths caused by the incomplete contact between the upper edges of the stiffening plates and the lower surface of the cross-beam flange. In contrast, the improved type II stiffening-plate repair was successfully applied for stress mitigation at the crack tip.

This study clearly showed the benefit and importance of in situ evaluation of the actual stress distribution using TSA techniques. Thermoelastic stress measurement is effective for confirming the effectiveness of the repair works in bridge maintenance.

Acknowledgements

The authors would like to acknowledge that the research works shown in this paper were partly supported by a Grant-in-Aid for Scientific Research from the Japan Society for the Promotion of Science (B: 26289009) and Casio Science Foundation. The authors also would like to thank T. Higashi, Y. Terauchi and R. Ichihashi for their technical assistance with the experiments and data processing.

References

- [1] The Road Committee of the Panel on Infrastructure Development, The Japan Ministry of Land, Infrastructure, Transport and Tourism. Recommendations for Full-scale Maintenance of Aging Roads, http://www.mlit.go.jp/road/road_e/pdf/recommendation.pdf; 2014 [accessed 17.01.14].
- [2] Greene RJ, Patterson EA, Rowlands RE. Thermoelastic stress analysis. In: Springer handbook of experimental solid mechanics. LLC New York: Springer Science + Business Media; 2008. p. 743–67.
- [3] Dulieu-Barton JM, Stanley P. Development and applications of thermoelastic stress analysis. *J. Strain Anal Eng Des* 1998;33:93–104.
- [4] Dulieu-Barton JM. Introduction to thermoelastic stress analysis. *Strain* 1999;35:35–9.
- [5] Pitarresi G, Patterson EA. A review of the general theory of thermoelastic stress analysis. *J. Strain Anal Eng Des* 2003;38:405–17.
- [6] Tomlinson RA, Olden EA. Thermoelasticity for the analysis of crack tip stress fields – a review. *Strain* 1999;35:49–55.
- [7] Ju SH, Lesniak JR, Sandor BI. Numerical simulation of stress intensity factors via the thermoelastic technique. *Exp Mech* 1997;37:278–84.
- [8] Tomlinson RA, Nurse AD, Patterson EA. On determining stress intensity factors for mixed mode cracks from thermoelastic data. *Fatigue Fract Eng Mater Struct* 1997;20:217–26.
- [9] Diaz FA, Patterson EA, Tomlinson RA, Yates JR. Measuring stress intensity factors during fatigue crack growth using thermoelasticity. *Fatigue Fract Eng Mater Struct* 2004;27:571–83.
- [10] He KY, Rowlands RE. Determining stress intensity factors in orthotropic composites from far-field measured temperatures. *Exp Mech* 2004;44:555–61.
- [11] Tomlinson RA, Marsavina L. Thermoelastic investigations for fatigue life assessment. *Exp Mech* 2004;44:487–94.
- [12] Diaz FA, Yates JR, Patterson EA. Some improvements in the analysis of fatigue cracks using thermoelasticity. *Int J Fatigue* 2004;26:365–76.
- [13] Ummenhofer T, Medgenberg J. On the use of infrared thermography for the analysis of fatigue damage processes in welded joints. *Int J Fatigue* 2009;31:130–7.
- [14] Zhang D, Sandor BI. Thermographic analysis of stress concentrations in a composite. *Exp Mech* 1989;29:121–5.
- [15] Jones R, Heller M, Sparrow JG, Ryall TG. A new approach to structural optimization. *Compos Struct* 1990;16:1–32.
- [16] Zhang D, Enke NF, Sandor BI. Thermographic stress analysis of composite materials. *Exp Mech* 1990;30:68–73.
- [17] Emery TR, Dulieu-Barton JM, Earl JS, Cunningham PR. A generalized approach to the calibration of orthotropic materials for thermoelastic stress analysis. *Compos Sci Technol* 2008;68:743–52.
- [18] Emery TR, Dulieu-Barton JM. Thermoelastic stress analysis of damage mechanisms in composite materials. *Composites: Part A* 2010;41:1729–42.
- [19] Fruehmann RK, Dulieu-Barton JM, Quinn S. Assessment of fatigue damage evolution in woven composite materials using infra-red techniques. *Compos Sci Technol* 2010;70:937–46.
- [20] Paynter RJH, Dutton AG. The use of a second harmonic correlation to detect damage in composite structures using thermoelastic stress measurements. *Strain* 2003;39:73–8.
- [21] Jones R, Molent L. Application of constitutive modeling and advanced repair technology to F111C aircraft. *Compos Struct* 2004;66:145–57.
- [22] Sakagami T. Remote nondestructive evaluation technique using infrared thermography for fatigue cracks in steel bridges. *Fatigue Fract Eng Mater Struct* 2015;38:755–79.
- [23] Shiozawa D, Inaba K, Akai A, Sakagami T. Experimental study of relationship between energy dissipation and fatigue damage from observation of slip band by atomic force microscope. *Adv Mater Res* 2014;891:606–11.
- [24] Sakagami T, Izumi Y, Kobayashi Y, Mizokami Y, Kawabata S. Applications of infrared thermography for nondestructive testing of fatigue cracks in steel bridges. *Proc. SPIE* 2014; 9105: 0S-1–8.
- [25] Sakagami T, Nishimura T, Kubo S. Development of a self-reference lock-in thermography and its application to crack monitoring. *Proc SPIE* 2005;5782:379–87.
- [26] Matsumoto R, Ishikawa T, Tsukamoto S, Awazu Y, Kawano H. Comparison of repair methods for fatigue crack initiated at welded toe between steel deck plate and vertical stiffener. *J Japan Soc Civil Eng, Ser. A1 (Struct Eng Earthq Eng (SE/EE))* 2016; 72(1): 192–205.
- [27] YuanZhou Z, Ji B, Fu Z, Ge H. Local stress variation in welded joints by ICR treatment. *J. Constr Steel Res* 2016;120:45–51.
- [28] Aoki Y, Ishikawa T, Matsumoto R, Kawano H, Adachi Y. Patch bonding repair of through-thickness crack in orthotropic steel deck at vertical stiffener end. *J Struct Eng A* 2015;61A:408–15.
- [29] Thomson W. (Lord Kelvin) On the dynamical theory of heat. *Trans R Soc* 1853;20:261–83.
- [30] Lesniak J, Boyce B, Hovenwater G. Thermoelastic measurement under random loading. In: Proc. SEM Spring Conf. Soc. Exp. Mech. 1998. p. 504–507.
- [31] Takada Y, Kawakami Y, Sakai Y, Sakano M. Study on retrofit measures in weld of vertical stiffener cutting treating of the semicircle in orthotropic steel deck. *JSSC Steel Constr Eng* 2009;16(62):35–46.
- [32] Cheng X, Duan L, Najjar WS. Rehabilitation and strengthening of highway bridge superstructures. In: Chen W, Duan L, editors. Bridge engineering handbook. CRC Press: Boca Raton; 2013. p. 465–70.



Application of short repairs for fatigue life extension

J.E. Rodriguez-Sanchez ^{a,*}, W.D. Dover ^b, F.P. Brennan ^b

^a Instituto Mexicano del Petroleo, Eje Central Lazaro Cardenas 152, Edificio SIPE, No. 28, Piso 1, Cubiculo 105, 07730 Mexico D.F., Mexico

^b University College London, Department of Mechanical Engineering, Torrington Place, London WC1 7JE, UK

Received 15 March 2002; received in revised form 22 April 2003; accepted 18 July 2003

Abstract

The application of a new fatigue crack repair concept defined as ‘short repair’ is presented. This concept is based on crack removal by cutting. The objective of using a short repair is to extend the fatigue life of cracked welded connections. A short repair is an option to repair fatigue cracks, particularly for offshore structures where diving intervention is of high risk and the application of remote operated vehicles is an alternative.

Short repairs were machined on welded T-butt plates by disc cutting. Experimental data have been analysed to determine crack growth rates, crack initiation and fatigue life extension after crack repair. Conclusions and recommendations are given.

© 2003 Elsevier Ltd. All rights reserved.

Keywords: Fatigue; Repair; Crack

1. Introduction

Fatigue cracks in offshore structures are originated by the effect of wave forces acting on the structure. Fatigue cracks occur at the welded connections where structural members join. A structural member can disconnect from a joint as cracks propagate through the member thickness. This situation reduces the load capacity of the structure leading to a loss of safety and even a collapse.

Fatigue crack repairs are of high relevance to maintain the integrity of offshore structures. Fatigue crack repair options depend on the crack growth extension; in early stages of growth, grinding is applicable to remove cracks. For the cases when cracks have propagated through the thickness disconnecting one or more members of a joint, a mechanical or grouted clamp is applicable to reinstall the load transmission between members. Inspection of offshore structures for fatigue crack detection in early stages of growth can reduce the cost and effectiveness of a repair since a grind repair can be used instead of a clamp.

Fatigue crack grind repair has been investigated for about 20 years, demonstrating that grinding is a feasible

option for the repair of fatigue cracks. In this research, the grind repair profiles used have shown that if cracks reinitiate, this occurs in the bottom of the repair groove. Thus, fatigue life after repair relies on the remaining member thickness through which the crack propagates. On the other hand, short repairs have a depth/length ratio that if cracks reinitiate after being removed, this occurs out of the groove at the repair ends. Thus, cracks that reinitiate have the intact plate thickness for propagation. Additionally, short repairs facilitate subsequent inspection activities since inspection on a surface has a higher probability of detection compared with the inspection of a narrow groove in underwater conditions.

The short repair concept is based on two robust studies. First, the stress concentration gradient was studied using finite elements theory on three-dimensional models. It was found that for short repairs the maximum stress concentration is a function of the radius and depth of the repair, and is always located at the repair longitudinal ends, out of the repair groove. Thus, if cracks reinitiate, these always occur at these points [4], see Fig. 1. A fracture mechanics analysis of crack shape development under pure bending fatigue loading using stress intensity factors calibrations was undertaken by Scott and Thorpe [5]. Their calculated results are in accordance with the experimental crack shape development for short repairs described in this paper.

* Corresponding author. Tel.: +52-55-3003-7266; fax: +52-55-3003-7255.

E-mail address: ersanche@imp.mx (J.E. Rodriguez-Sanchez).

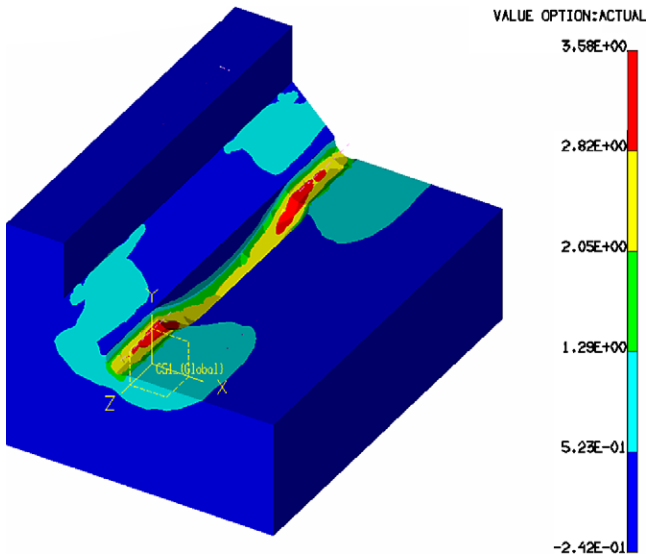


Fig. 1. Stress concentrations at the repair ends determined by 3-D finite element analysis.

Second, research on crack shape evolution was made; this work showed that crack shape ratio is definitive to determine if a crack propagates in depth or in length. This concept was taken to design a repair profile with a shape factor such that if cracks reinitiate, the repair shape first induces a repair extension in length rather than in depth. This is a different approach to explain why cracks reinitiate at the repair ends in short repairs. A comprehensive study of crack shape development under the bending loading of surface defects for the design of short crack repairs is presented in [6].

2. T-butt-welded specimens

Experimentation on T-butt-welded plate specimens has been used extensively to explain fatigue behaviour of more complex welded structures. The specimens used for the experimental work here are T-butt-welded plate connections in the as-welded condition and T-butts with short repairs machined. Although, particular stress distributions found in tubular connections (geometric stresses) are not reproduced when testing T-butt specimens, extrapolation of the results to tubular welded connections is possible.

2.1. Specimens design

T-butts under a uniform cyclic distribution of nominal stress develop edge cracks along the weld toe in most of the cases. Edge cracks are not the interest of this study since cracks on offshore tubular joints are normally surface cracks. Increasing the weld toe radius at both sides of a central as-welded weld toe region is a reliable procedure to obtain surface cracks on T-butts, whilst main-

taining a uniform distribution of nominal stress along the plate width. A uniform distribution of nominal stress along the plate width makes fracture mechanics calculations and extrapolation of the results easier. Tubular joint repair could well include crack removal and removal of adjacent weld toe regions to increase the weld toe radius. Additionally, the increase of the weld toe radius reduces the stress concentration factor at the repair ends. Thus, fatigue life is also increased where cracks reinitiate.

2.2. Dimensions

A 20-mm plate thickness was used for the T-butt-welded specimens, main and attachment plates were of the same thickness, specimen width was 300 mm. Fig. 2 shows the specimen dimensions.

2.3. Manufacture and material properties

Specimens were manufactured using steel which had to comply with the requirements defined in BS EN 10025 Grade S355J2G4 [1].

T-butt specimens were cut out in pairs from a T-butt-welded joint 400 mm wide \times 700 mm long which had 50 mm from both longitudinal ends cut-off. The purpose was to eliminate the plate ends where defects accumulate due to poor fusion during welding. The attachment plate was bevelled to 45° for a full penetration weld.

3. Applied loading

It was considered convenient for the purposes of the research to test only under bending loading since it was identified that, for tubular joints, the stress field near the weld is predominantly bending, even under axial loading [2].

A four point bending set-up was used for testing. This set-up produces a constant moment distribution between

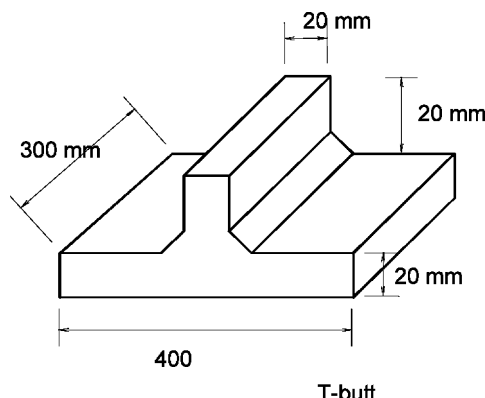


Fig. 2. T-butt specimen dimensions.

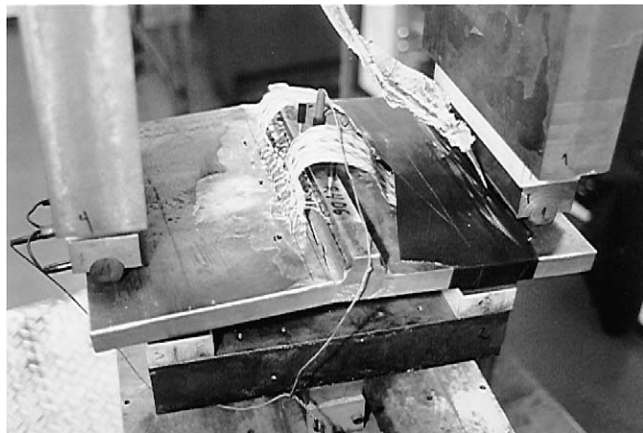


Fig. 3. Loading set-up and instrumentation of a T-butt specimen after failure.

the two internal loading points, see Fig. 3. All the tests were performed under load control, so even when the stiffness of the specimen changed the magnitude of the load cycle applied did not change.

3.1. Fatigue crack depth monitoring

Crack depth evolution was monitored from early stages of growth using the alternating current potential difference (ACPD) technique applied by a U-10 crack microgauge. The technique requires the injection of an alternating current on the surface of the specimen. The current follows the contour of surface-breaking defects, such as cracks, and since the potential gradient on the metal surface and on the crack faces is assumed to be linear, measurements of the potential difference across the crack and adjacent to the crack can be used for the calculation of the crack depth.

4. Fatigue test programme

Table 1 shows the fatigue tested specimens and relevant experimental parameters that will be introduced through the remainder of this section.

With the experience gained from previous experimentation, a comparison study was planned considering four T-butt specimens. The purpose was to quantify the fatigue life extension of repaired specimens against specimens in the as-welded condition. Thus, specimens 1 and 2 represented the case of as-welded condition. Prior to testing, these specimens had weld toes machined R4D0.5, except in a central 30 mm long region on one side of the specimen. This forced crack initiation at the centre of the specimen avoiding multiple initiation and then edge cracking. The average measured weld toe radius of the as-welded region was 0.8 mm. The repaired condition was represented by specimens 3 and 4; they had machined repairs prior to testing of dimensions R4D6L60 and R4D9L60, respectively. Repairs were made with a disc cutter. The weld toes were left in as-welded condition and the average measured weld toe radius was 0.8 mm. Dimensions and other experimental parameters are presented in Table 1. Results will be presented in Section 6.

It is clear that it would be preferable to determine the fatigue life extension on the same T-butt. In this work the as-welded and the repaired cases were represented by different T-butt specimens. Fatigue life extension was determined by addition of the number of cycles of the as-welded T-butt, when the crack reached the depth dimension of the repaired T-butt plus the fatigue life of the repaired specimen. Contribution from prior fatigue loading is not considered in the repaired specimens since repairs were carried out on as-welded condition. However, previous experimentation demonstrated that fatigue life extension determined from a single T-butt fatigue loaded in the as-welded condition and then repaired with increased weld toe radius regions adjacent to the repair reported approximately the same fatigue life extension as the approach presented here using two T-butts. Removal of weld defects at the weld toes adjacent to both sides of the repair, increasing the weld toe radius by cutting 0.5 mm deep with the same tool used for crack removal, extends the fatigue life since crack initiation is inhibited. This procedure was also used to inhibit fatigue cracking along the weld toe on the T-butt side where

Table 1
Fatigue tested specimens and relevant experimental parameters

Specimen	Connection/Manufacture	T (mm)	W (mm)	Repair/Procedure	Nominal stress (MPa)	Life (million cycles)	Comments
1	T-butt/Automatic welding	20	300		300	0.195	AW, F, SC
2	T-butt/Automatic welding	20	300		250	0.21	AW, BF, SC
3	T-butt/Automatic welding	20	300	R4D6L60/DC	200	0.384	F, SC
4	T-butt/Automatic welding	20	300	R4D9L60/DC	200	0.2525	F, SC

R, repair radius; DC, disc cutter; AW, As-welded tested; D, repair depth; SC, surface crack; F, specimen tested until failure; L, repair length; BF, test stopped before failure.

neither as-welded nor repaired fatigue life was determined. As mentioned before, tubular joint repair could well include crack removal and removal of adjacent weld toe regions to increase the weld toe radius.

An advantage of this approach is that during experimentation the time spent on inspection after crack removal is not required. During the progress of the experimental work it was demonstrated that if a minimum length of the crack front is left after the crack removal, the effect of the repair is practically nil. This and future research will help to define an adequate depth allowance to ensure that the crack front is totally removed depending on the inspection technique used.

4.1. Test stress levels

Experience obtained from previous experimentation suggested stress range levels for testing between 180 and 300 MPa, see Table 1. Since the determination of an S-N curve was not a concern, the stress levels for fatigue testing were kept as high as possible to shorten the testing time.

5. Fatigue crack repair

The objective pursued during the design of the ‘short repair’ profile was to ensure that the maximum stress concentration factor is located at the repair ends out of the repair groove; if cracks reinitiate after being removed, this occurs out of the groove at the repair ends thus, cracks that reinitiate again have the intact plate thickness for propagation.

During the experiments, three repair radii of 4, 8 and 12 mm were used and from the amount of weld cut when using radius 12 mm it is considered that in practice a review of the static load capacity of the member should be conducted prior to use of a cutting tool with radius equal or greater than 12 mm [3].

The longitudinal repair profile of the grooves machined on the specimens was always semicircular and the transverse repair profile varied from semicircular to U-shaped depending on the depth/radius ratio. A robust study based on finite element theory allowed determination of the optimum repair profile to be used and the stress concentration factor associated to a particular repair profile [3].

5.1. Disc cutter machining

The repair profiles were cut using disc blade cutters driven by a numerically controlled machine. Fig. 4 shows disc cutters radii 4, 8 and 12 mm used during the study. It is obvious that this technique could not possibly be applied to a real underwater repair of a fatigue crack, but repair profiles obtained using this technique could



Fig. 4. Disc cutters used for machining repair profiles.

provide a good base line to evaluate novel applications of underwater machining, such as electrochemical machining technique (ECM) [4]. Dimensions of the repair profiles machined are shown in Table 1 and a disc cut repair D4R8L60 is shown in Fig. 5.

The use of disc blade cutters driven by a numerically controlled machine provided the opportunity of obtaining optimum quality repair profiles since it was possible to have: precise positioning of the repair in the specimen, good quality surface repair and total control of the longitudinal and transverse repair profile dimensions. The numerically controlled machine used is at University College London Mechanical Engineering Workshop.

6. Fatigue test results

6.1. Crack growth curves

Crack growth curves relate the number of cycles to crack depth. For surface cracks the crack growth at the deepest section is usually presented. In some cases, for comparison purposes, the crack growth at the repair ends and in the bottom of the repair are presented together to illustrate how cracks develop in short repairs.

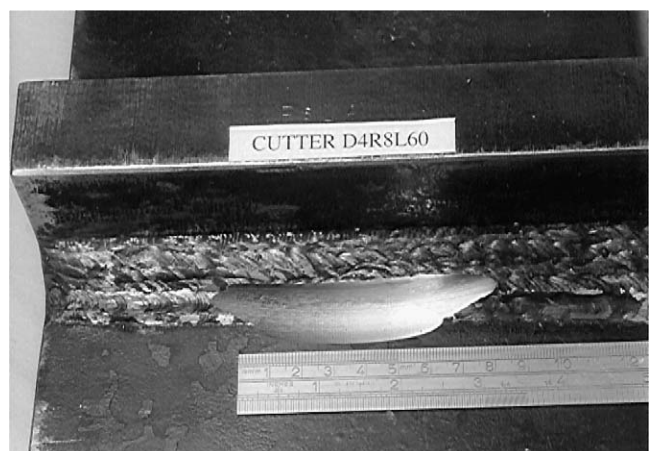


Fig. 5. Disc cut repair profile D4R8L60 on T-butt specimen.

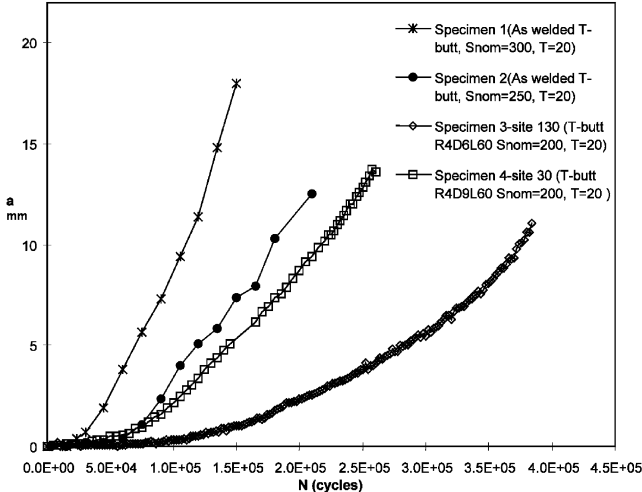


Fig. 6. Fatigue crack growth for T-butt specimens 1 to 4.

Fig. 6 shows the crack growth curves for specimens 1 to 4. The legend provides the test stress level and the specimen thickness. It can be observed that the fatigue life increases as the nominal stress level is reduced. Repaired specimens 3 and 4 were tested under the same stress level, but with different repair depths. Therefore, the stress concentration produced by the repair was reflected in the fatigue life. Results from a robust finite element study [4] showed that for repair profiles, increments of the stress concentration factor are associated to a combined effect of repair radius reduction and repair depth increment and vice versa. Specimen 3 with shallower repair R4D6L60 showed a longer fatigue life than specimen 4 with deeper repair R4D9L60. The crack growth curves presented in Fig. 6 for the repaired specimens correspond to crack initiation sites 30 for 4 and 130 for 3, which are located on the as-welded weld toes out of the repair groove, 20 mm from the repair ends, see Figs. 7 and 8.

Figs. 9 and 10 show crack growth at the repair ends outside the repair groove (sites 30, 130) and in the bottom of the groove (site 80) for specimens 3 and 4,

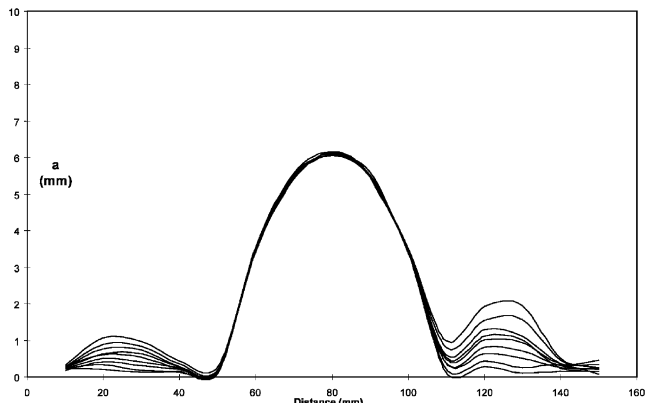
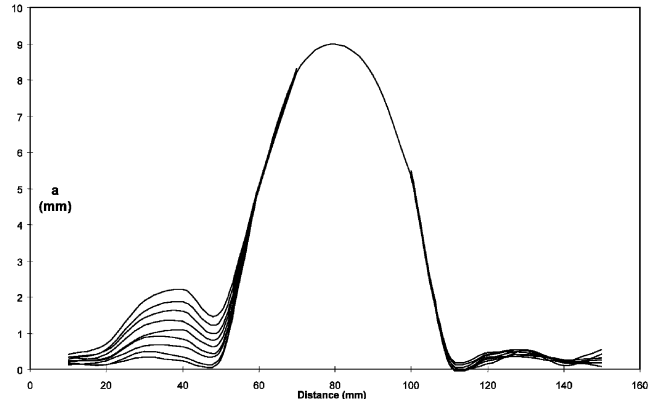
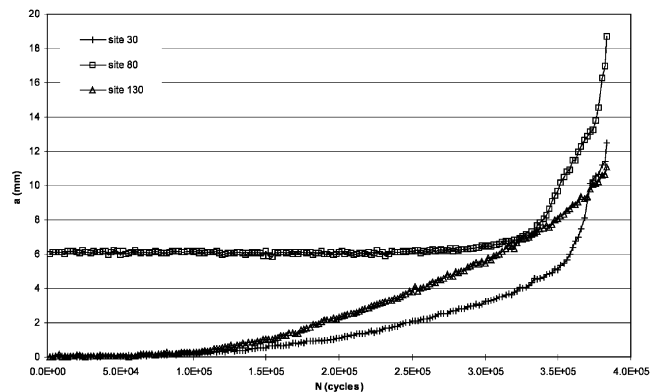
Fig. 7. Fatigue crack initiation for specimen 3 up to 0.9×10^5 cycles.Fig. 8. Fatigue crack initiation for specimen 4 up to 1.8×10^5 cycles.

Fig. 9. Fatigue crack growth at various sites for specimen 3.

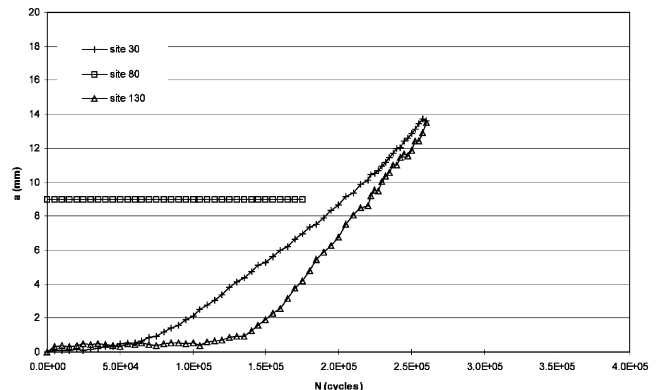


Fig. 10. Fatigue crack growth at various sites for specimen 4.

respectively. As noted here, cracks initiated at sites 30 and 130, but cracking had not initiated in the repair grooves at the number of cycles indicated. As Fig. 9 shows, cracks only initiated at site 80 after the crack at site 130 was approximately 5 mm deep, that is 1 mm before reaching the repair depth.

For specimen 3, crack initiation at site 80 started after the cracks that initiated at sites 30 and 130 had merged and continued growing as one crack; see crack growth

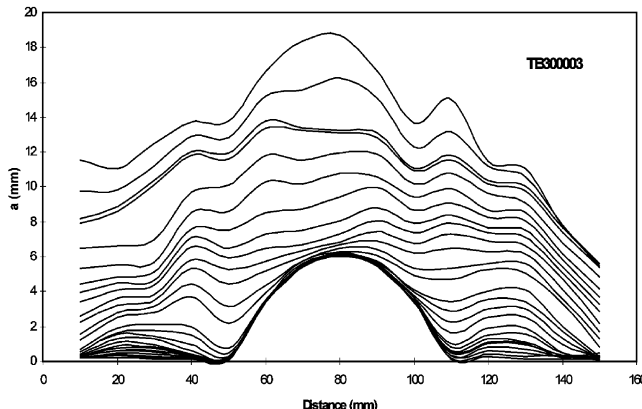


Fig. 11. Fatigue crack growth evolution for repaired specimen 3.

evolution in Fig. 11. Unfortunately, for specimen 4 it was not possible to determine crack growth in the repair groove region due to a high gain setting for the U10 crack microgauge, causing voltage overflow.

6.2. Fatigue crack growth rates

Figs. 9 and 10 show that for a considerable period, crack growth rates are nil in the bottom of the repairs (sites 80) of specimens 3 and 4. This is due to the effect of short repairs that force the cracking pattern in the repaired region to grow from the repair ends on the surface, extending the repair first longitudinally and then in depth.

6.3. Fatigue crack initiation

From the experimental results presented in Figs. 9 and 10 it can be observed that for the purposes of life extension it is more effective if crack initiation after repair is located outside the repair groove. This is because the new crack again has the total plate thickness for crack initiation and propagation. However, locating crack initiation outside the repair groove becomes increasingly less likely as the length of the repair increases. This is addressed when explaining crack shape development [4].

Considering 0.4 mm as the crack depth for determining initiation life the initiation to total fatigue life ratios for the specimens are presented in Table 2. Fig. 12

Table 2
Fatigue initiation life to total fatigue life ratios

Specimen	Nominal stress MPa	Fatigue initiation life (Ni)	Total fatigue life (Nt)	Ni/Nt
1 (As-welded)	300	22 800	150 000	0.15
2 (As-welded) ^a	250	60 000	300 000	0.20
3 (R4D6L60)	200	112 000	383 700	0.29
4 (R4D9L60)	200	50 000	260 000	0.19

^a Extrapolated total fatigue life.

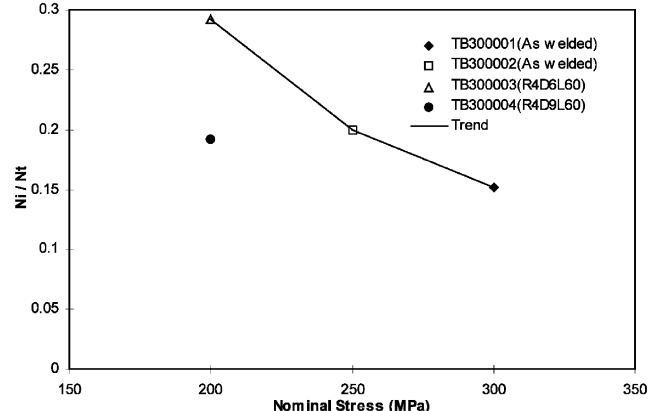


Fig. 12. Fatigue initiation to total fatigue life ratios for T-butt specimens 1 to 4.

shows the trend of initiation to total fatigue life ratio for the specimens. It can be observed that although specimens 3 and 4 were tested under the same stress level, the latter has a shorter initiation to total fatigue life ratio (Ni/Nt) as a result of the high stress concentration produced by a deeper repair (R4D9L60) with respect to specimen 3 (R4D6L60). Therefore, specimen 4 is outside the trend defined considering as-welded specimens and it can be inferred that its initiation life is less than an as-welded specimen under the same stress. However, it is worth noting that the weld toes of specimen 4 were in as-welded condition. Thus, it is expected that Ni/Nt would increase substantially if the weld toes are machined.

6.4. Fatigue life extension

Calculations of the fatigue life extension obtained after crack repairing are presented here. Calculation will be based on the approximate cubic relation between stress ranges and fatigue life, since different stress levels were used in as-welded and repaired conditions. The stress difference was due to specimens 1 and 2 which belonged to an extensive testing programme where higher stress levels were used.

To demonstrate the approximation of the cubic relation, a prediction of fatigue life for specimen 2 based on the fatigue life of specimen 1 is presented and then compared with the real data.

For $a = 6$ mm, see Fig. 6.

Specimen	Stress range	$N \times 10^5$
1	300	0.8
2	250	1.4

From the cubic relation: $(300/250)^3 = 1.73$. Thus, the estimated fatigue life for specimen 2 at $a = 6$ mm would

be: $1.73 \times 0.8 \times 10^5 = 1.4 \times 10^5$ which is equal to the real data obtained from Fig. 6. This validation can be performed for various crack depths and close approximation to the real data would always be obtained.

Using the cubic relation verified above, prediction of fatigue life extension after repair is presented for specimens 3 and 4.

For a repair depth $D = 6$ mm as in specimen 3, see Fig. 6.

Specimen	Stress range	$N \times 10^5$
1	300	0.8
3	200	3.1

From the cubic relation: $(300/200)^3 = 3.38$. Thus, the estimated fatigue life for specimen 3 at $a = 6$ mm in as-welded condition would be: $3.38 \times 0.8 \times 10^5 = 2.7 \times 10^5$.

Thus, after repair the fatigue life extension obtained would be $(2.7 + 3.1)/2.7 = 2.1$ times the as-welded fatigue life. The relation between repair depth and plate thickness is $100 \times (6/20) = 30\%$.

For a repair depth $D = 9$ mm as in specimen 4, see Fig. 6.

Specimen	Stress range	$N \times 10^5$
2	250	1.7
4	200	2

From the cubic relation: $(250/200)^3 = 1.95$. Thus, the estimated fatigue life for specimen 4 at $a = 9$ mm in as-welded condition would be: $1.95 \times 1.7 \times 10^5 = 3.3 \times 10^5$.

Thus, after repair the fatigue life extension obtained would be $(3.3 + 2)/3.3 = 1.6$ times the as-welded fatigue life. For this case the relation between repair depth and plate thickness is $(9/20) \times 100 = 45\%$.

It can be deduced from the limited results presented that a 100% fatigue life extension can be obtained when repair depths are up to 30% of the plate thickness. However, results from other specimens showed that increasing the weld toe radius at the repair ends can still provide a fatigue life extension at least equal to the fatigue life in as-welded condition for repair depths up to 48% the plate thickness [4].

The results presented above are summarized in Table 3. These results are based on limited experimental data, thus an extensive validation is recommended for its application in the industry.

With regard to the effect of defect scatter associated with welding, which could lead to the assumption that

cracking can take place out of the region of the repair ends, this paper reports the findings of only two worked specimens welded automatically. However, other manually welded specimens were fatigue tested and showed crack initiation at the ends of shorts repairs. It is important to consider that the weld geometry influence on the stress distribution through the thickness under bending is up to 5% the plate thickness. Thus, after the repair is done the weld toe has been removed and the influence of the stress concentration induced by the repair geometry is much larger than the effect of the weld. This effect is increased when weld toes are machined at both sides of the repair using the same repair tool. Therefore, this practice is strongly recommended. The effect of weld defects is reduced substantially since increasing the weld toe radius by machining at both sides of the repair removes a large number of them. None of the fatigue-tested specimens (worked or not) showed crack initiation due to weld defects.

Due to the limited number of worked specimens, the fatigue testing scatter on the fatigue life extension after repair is not presented. However, for the manually welded specimens that were fatigue tested and showed crack initiation at the ends of the shorts repairs, its fatigue life extension was determined and showed that it was in the range of the worked specimens. Additionally, it can be considered that regardless of the scatter, if crack initiation after crack removal takes place on the plate surface at the repair ends as with the use of short repairs, the original plate thickness of the component is reinstalled and its fatigue life is greater than in the case when cracks initiate and are not prevented from continuing propagating through the plate thickness.

7. Conclusions

The application of short repairs has experimentally demonstrated that the fatigue life of cracked welded connections can be extended by a factor of two in many cases. The successfulness of fatigue life extension using short repairs depends mainly on two considerations:

- (a) The crack is totally removed before it extends further than 30% of the plate thickness;
- (b) The repair depth and length comply with a short repair profile to force crack initiation to take place at the repair ends.

The experimental results obtained also showed that the application of short repairs in some cases can provide extensions of fatigue life greater than a factor of two. This is more likely to occur when the cracks are repaired in early stages of growth and the weld toes at the repair ends are increased to remove weld defects.

Machining the repair ends can be undertaken easily

Table 3
Fatigue life extension of crack repaired specimens

Specimen	Repair profile	Weld toes	Nominal stress (MPa)	Repair depth thickness ratio	Crack depth after repair (mm)	Fatigue life increment
3	R4D6L60	As-welded	200	30%	6	2.1
4	R4D9L60	As-welded	200	45%	9	1.6

by lengthening the cutting path of the same tool used to machine the short repair. For underwater conditions, this task appears especially suitable for the ECM technique.

In addition to the fatigue life extension, short repairs induce crack initiation outside the repair notch, so the total thickness for crack propagation is reinstated and easier access for inspection is provided.

References

- [1] BS EN 10025:1993, Hot rolled products in weldable fine grain structural steels, British Standards Institution, 1993. (This specification supersedes the BS 4360:1990.)
- [2] United Kingdom Offshore Steels Research Project-Phase I, Final Report, OTH 88 282, Prepared by the Safety and Reliability Directorate for the Department of Energy, 1988.
- [3] Rodríguez JE, Brennan FP, Dover WD. Minimisation of stress concentration factors in fatigue crack repairs. *International Journal of Fatigue* 1998;20(10):719–25.
- [4] Rodríguez JE. Fatigue crack repair for offshore structures. PhD thesis, University College London, UK, 1999.
- [5] Scott PM, Thorpe TW. A critical review of crack tip stress intensity factors for semi-elliptic cracks. *Fatigue of Engineering Materials and Structures* 1981;4(4):291–309.
- [6] Rodríguez JE, Dover WD, Brennan FP. Design of crack removal profiles based on shape development of surface defects. In: Proceedings of OMAE 2003, 22nd International Conference on Offshore Mechanics and Arctic Engineering, OMAE 2003-37198. 2003.



Considerations on corrosion and weld repair effects on the fatigue strength of a steel structure critical to the flight-safety

Marcelino P. Nascimento *, Herman J.C. Voorwald

Department of Materials and Technology – State University of São Paulo, UNESP/FEG/DMT 333, Ariberto Pereira da Cunha Ave., 12516-410, Guaratinguetá City, São Paulo State, Brazil

ARTICLE INFO

Article history:

Received 30 July 2009

Received in revised form 24 December 2009

Accepted 31 December 2009

Available online 7 January 2010

Keywords:

AISI 4130 steel

Fatigue behavior

Corrosion

Weld repairs

Flight-safety

ABSTRACT

The aim of this study is to analyze the effects of corrosion and successive tungsten inert gas (TIG) welding repairs on the reverse bending fatigue strength of AISI 4130 steel used in components critical to the flight-safety. The tests were performed on hot-rolled steel plate specimens, 1.10 mm and 1.60 mm thick, by means of a SCHENK PWS equipment, with load ratio $R = -1$, constant amplitude, 30 Hz frequency and room temperature. It was observed that the reverse bending fatigue strength of AISI 4130 steel decreases due to the corrosion and the TIG welding and re-welding processes.

© 2010 Elsevier Ltd. All rights reserved.

1. Introduction

According to flight-safety foundation [1], “Aircraft accidents means an occurrence associated with the operation of an aircraft, which takes place between the time any person boards the aircraft with the intention of flight until such time as all such persons have disembarked, and in which any person suffers death or serious injury as a result of being in or upon the aircraft or by direct contact with the aircraft or anything attached thereto, or in which the aircraft received substantial damage (damage or structural failure that adversely affects the structural strength, performance, or flight characteristics of the aircraft, and which would normally require major repair or replacement of the affected component)”. Based in such definition, the accident rates (i.e., accidents per million departures) have been at 1.2, or 12,000 accidents, in the occidental world [2]. In the search for a zero accident rates, the flight-safety has been the main concern of the aeronautical authorities all over the world.

Basically, the aeronautical projects should take into account the difficulties of transporting a load against the gravity force during take-off and flight, and discharge it in an efficient way, with minimum cost and maximum safety, because failures in any of these stages will implicate catastrophic accidents, involving human lives [3]. In general, structural failures during flight are attributed to

aerodynamic overloads or fatigue of materials, as a consequence of inadequate project or any notch produced during manufacturing or maintenance of aircrafts [4–7]. Since the catastrophic accidents involving the English model “Comet” in the 1950’s, the fatigue process has been the most important project and operational consideration for both civil and military aircrafts [4,5,8]. On the other hand, many fractures of materials are also caused by corrosion as a consequence of aggressive environment.

Since the aircrafts become more complex, the environmental effects assumed great importance. As a result of older aircrafts flying nowadays, problems such as stress-corrosion cracking, corrosion-fatigue (simultaneously or separately) and wear are also expected to occur [4,5,9,10]. Due to several aggressive environments in which the aircrafts are subjected, particularly marine, corrosion is the most important factor of maintenance and inspection for the aeronautic sector [4,5,9,10]. Hence, corrosion is undoubtedly a real and critic issue acting on aircrafts, flowing with the time even on those not operational. Usually, the corrosion control is accomplished by adoption of prevention methods with high-quality periodic inspections associated to damage tolerance philosophy, for taking into account its effect on the fatigue life of a structural component [4,5,10–12]. Such issues will request extensive investment, planning, researches and development on repair methods and maintenance procedures towards assure the safe and continued airworthiness.

For several aircraft models (e.g. agricultural, military training and acrobatic) the most solicited and repaired component is one that supports the motor, called “Motor-Cradle” (Fig. 1) [13]. This

* Corresponding author. Tel.: +55 12 3123 2865; fax: +55 12 3123 2852.

E-mail addresses: pereira@feg.unesp.br, marcelino.nascimento@gmail.com (M.P. Nascimento), voorwald@feg.unesp.br (H.J.C. Voorwald).

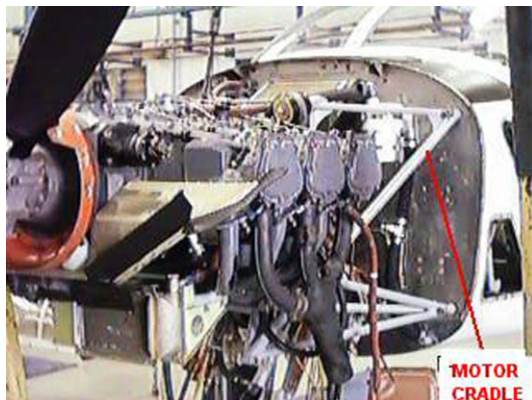


Fig. 1. Motor-cradle assembly in a T-25 Universal Brazilian aircraft.

component presents a geometrically complex structure made from AISI 4130 tubular steel of different dimensions and TIG welded in several angles [13,14]. For the Brazilian aircrafts T-25 Universal and T-27 Tucano, for example, besides supporting the motor in balance, the motor-cradle also maintains the nose landing gear fixed at the other extremity. Since the motor-cradle is a component critical to the flight-safety, the aeronautic standards are extremely rigorous in its manufacturing, by imposing a “zero-defect index” on the final weld seam quality (Safe-Life philosophy), which is 100% inspected by non-destructive testing/NDT [13–15]. For this reason, welded aeronautic structures are frequently subjected to successive repairs in accomplishment to current standards. As a consequence, components approved by NDT may contain a historic record of welding repairs whose effects on their structural integrity are not computed. In addition, these structures are also submitted to weld repairs along their operational life, turning this question more complex.

As a part of this research-work, an investigation on 157 motor-cradles fracture reports indicates that all of them occurred at welded joints as a result of fatigue cracks, reducing the “Time-Before-Fail” from 4.000 h to 50 h of flight [13]. Motivated by high fracture incidence of this particular component, an extensive research program to evaluate the manufacturing and maintenance weld repair effects on the structural integrity, mechanical properties and microstructural changes has been conducted [13].

Although the maintenance repairs of parts and components are a multibillion-dollar industry [16] and that, particularly for the transport sector, the welding repairs are an essential and frequently used process [17], few papers approaching this issue have been published, being all of them on either aged and degenerated materials [18,19] in petrochemical, offshore and power industries [20], by means of finite element method – FEM - [21–23].

In this paper, special emphasis was attributed to a standardized weld repair procedure, widely employed during manufacture of welded aeronautic structures and characterized by removing the previously defective weld bead and by applying a new weld seam by means of the gas tungsten arc welding/GTAW (or tungsten inert gas/TIG) process with filler metal.

The aim of this study is to analyze the effect of the corrosive process and the successive TIG welding repairs on the reverse bending fatigue strength of AISI 4130 steel specimens made from hot-rolled steel plates, 1.60 mm and 1.10 mm thick, respectively. Analyses of microstructure, microhardness and residual stresses from the base-material (BM), heat-affected zone (HAZ) and weld metal (WM), as well as the effects of the surface roughness and weld bead geometry complemented this study.

In the sequence, a brief comment on the current weld repair procedures is presented.

1.1. Current Welding Repair Procedure and Applications

When defects (such as porosity, impurity, undercut) are found in the welding joints, the main international standards (e.g. API, AWS, BSI and ASME) request that the defective welded joints are corrected. However, in a general form, none of the above standards make mention to number of permissible repairs.

In general, repair welding usually involves the complete shut-down of the equipment, the removal of all dead loads and the carrying out welding to original manufacturing standards [24]. Two typical procedures of weld repairs, complete repair and partial repair, include mechanics removal of the damaged material and the restoration of the geometry and integrity of the component, followed for a post-welding heat treatment (PWHT), which will depend mainly on type and thickness of material [21]. PWHT has as a function to reduce or eliminate residual stresses and to temper the metallurgical structure of heat-affected zone (HAZ). However, PWHT is very expensive, time consuming and, depending on local, difficult or impracticable.

An important application of weld repair techniques is to avoid PWHT, generating HAZ with structures of fine grains [24]. Such an objective can be reached by minimizing the size of original grain in HAZ, by minimizing the thermal contribution during the welding process or by refining the size of the initial coarse-grain region of HAZ [24]. For this purpose, two welding repair techniques are employed, viz:

- i. Half-bead welding (HBW): the beads are removed before welding the next layer.
- ii. Temper-bead welding (TBW): the subsequent weld bead partially does heat-treat the previous passes, after that the deposited weld layer is removed.

Both techniques involve removal of the upper passes and they are employed to avoid PWHT, to reduce or eliminate residual stresses, to avoid hydrogen cracking, to improve fracture toughness and to reduce welding cost and time [24].

For the aeronautic sector, in accordance with IIS/IW – 956-87 Doc [25], when repairing a weld seam in critical aeronautic components is requested that the defect is also located and removed. The removal process should be always carried out from the side that propitiates the smallest weld material loss. Soon after, to maintain the uniformity of the deposited metal along the weld seam, the repair is applied [25].

However, the weld bead removal can be uneconomical, impracticable or even impossible in certain engineering applications due to urgency or emergency, difficult access to the component or appropriate equipments. As a consequence, along the useful life of the aircraft many non-standardized weld repairs are carried out by putting upon several weld bead, without removal of the previous pass. The subject to be answered up is whether or not the weld repairs are a viable and effective procedure, capable of extending the in-service life of components and structures. At present, due to the increase of residual stresses, the distortion in the geometry and deterioration of the microstructure caused by the thermal cycles, the effectiveness of the weld repairs on cracked structures is not well understood and investigated. Differently to the considerable data volume on the effects of original weld on fatigue life for steels and aluminum from the literature, data on welds repairs are scarce. In this context, the availability of experimental data on weld repair effects on the fatigue behavior may be very useful in determining inspection intervals in high-responsibility welded structures.

2. Material and methods

2.1. Material

For the present research-work flat welded specimens from hot-rolled AISI 4130 aeronautic steel, 1.10 mm and 1.60 mm thick, were used. The chemical compositions (wt%), from the base-material and from the weld (filler) metal, are presented in Table 1 (Fe in balance). The mechanical properties obtained from smooth flat samples and original welded specimens (OR) – with central weld seam crossed to the hot-rolled plate direction –, are indicated in Table 2. The hot-rolled plates presented 65 HR_A in the “as-received” condition.

The monotonic tensile tests were performed in accordance with ASTM E 8 M by means of a servo-hydraulic INSTRON test machine, applying 0.5 mm/min displacement rate and a preload equal to 0.1 kN.

2.2. Welding and re-welding procedures

The most commonly employed welding process for manufacturing of aeronautical structures is tungsten inert gas (TIG), or gas tungsten arc welding (GTAW), which is appropriate to weld thin thickness materials and to allow the necessary variable control, resulting in high-quality and defect-free weld beads. The TIG welding process was carried out in accordance with the Brazilian Aeronautic Industry – EMBRAER NE 40–056 TYPE 1 – Standard (for components critical to the flight-safety), with a protective 99.95% purity argon-gas and filler metal AMS 6457 B – Turballoy 4130. A Square Wave TIG 355 – Lincoln equipment was manually employed by an expert aeronautic welder. All the welding parameters were controlled, and the main ones are indicated in Table 3. Also, all the welded joints were subjected to X-ray non-destructive analysis by the Brazilian Aerospace Technical Centre (CTA/IFI), which proved the acceptable quality of the welds, according to MIL-STD-453, EMBRAER – NE-57-002 and ASTM E-390 standards.

The welding direction was always perpendicular to hot-rolling process (direction) of the plate. Before welding, samples were cleaned with chlorinated solvent to oxide removal and fixed on a backing bar, to avoid contamination and porosity in the weld root. After the welding/re-welding process neither subsequent heat treatment to residual stresses relief nor subsequent removal of the weld bead was carried out, in order to simulate the real condition of the original aeronautic structure. Due to the plate thickness,

only one weld single-pass was required. For re-welding process, a manual grinding machine capable to reach 22,000 rpm was used to remove the previous weld metal. The heat-input applied was kept constant for all the welded and re-welded specimens.

2.3. Corrosion process

To analyze the effects of the corrosive process on the fatigue behavior of AISI 4130 steel, specimens were submitted to atmospheric corrosion (urban environment), accelerated by means of constant wetting during thirty days. Periodically, the specimens were moved so that all the surfaces were uniformly corroded.

2.4. Reverse bending fatigue tests

For experimental bending fatigue tests, welded and non-welded flat specimens were manufactured according to SCHENCK model PWS requirements (Fig. 2), following the LT direction of the hot-rolled plate. The specimens were fatigue tested upon a sinusoidal load, constant amplitude, load ratio $R = -1$, at 30 Hz frequency and room temperature. The superficial average roughness, obtained by means of a Mitutoyo 301 equipment, with cut-off equal to 0.8 mm × 5 mm, was $R_a = 0.24 \mu\text{m} \pm 0.16 \mu\text{m}$.

2.5. Microstructural and microhardness analyses

For microstructural analysis, a Nital 2% chemical etching was applied during 5 s. Vickers microhardness measurements were obtained at 0.0254 mm intervals throughout the regions under analysis (base-material, HAZ regions and weld metal), applying a 1 N load.

Table 3
TIG welding parameters.

Direct current	DCEN
Welding position	Flat
Welding voltage	12 V
Welding current	30 A
Welding average speed	19.0 cm min ⁻¹
Pre heating	NONE
Flow rate	4–12 L min ⁻¹
Theoretical heat input	1.2 kJ cm ⁻¹
Filler metal diameter	1.6 mm

Table 1
Chemical compositions (wt%).

Composition (wt%)	C	Mn	P _{max}	S _{max}	Si	Mo	Cr	Cu
Specified BM ^a	0.28–0.33	0.40–0.60	0.035	0.040	0.15–0.30	0.15–0.25	0.80–1.10	0.10
Specified WMB ^b	0.28–0.33	0.40–0.60	0.008	0.008	0.15–0.35	0.15–0.25	0.80–1.10	0.10
Weld (filler) metal	0.30	0.50	0.004	0.003	0.25	0.18	0.91	0.042
Plate #1.10 thick	0.33	0.53	0.010	0.003	0.28	0.17	1.04	0.02
Plate #1.60 thick	0.28	0.49	0.009	0.004	0.24	0.18	0.93	0.02

^a AMS 6457 B – turballoy 4130 steel.

^b AMS T 6736 A (2003) – for chromium–molybdenum (4130) seamless and welded steel tubing of aircraft quality.

Table 2
Mechanical properties obtained from the welded and non-welded specimens.

Specimens	Yielding (0.2% offset)	Ultimate strength	Rupture stress	Elongation (25 mm length)	Yielding/ultimate strength ratio
Base-metal	746 ± 21	843 ± 9	655 ± 26	9.80 ± 1.87	0.88 ± 0.02
Welded	671 ± 20	778 ± 17	643 ± 26	3.81 ± 0.26	0.86 ± 0.01

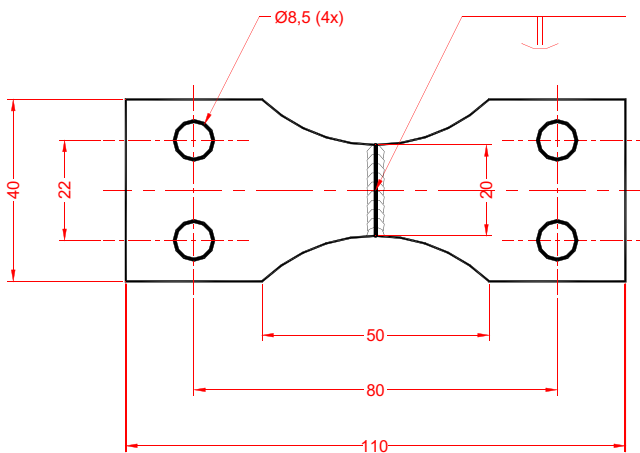


Fig. 2. Flat bending fatigue specimen (mm).

2.6. Residual stresses determination

The residual stresses field induced by welding and re-welding processes was determined by X-ray diffraction method, using the Raystress equipment (whose features are described in [26]) with couple exhibition, φ goniometer geometer, two anodes of chrome Cr- κ radiation and registration of {2 2 1} diffraction lines, tension source of 25 kV, current of 1.5 mA, X-ray convergence angle of 50°. The accuracy of the stress measurements was $\Delta\sigma = \pm 20$ MPa. In order to obtain the stress distribution by depth, the layers of specimens were removed by electrolytic polishing with a non-acid solution.

3. Results and discussion

3.1. Monotonic tests

First of all, it is important to pay attention to the high mechanical strength values and reasonable ductility from the hot-rolled AISI 4130 steel plate (as presented in index 2.1). It is also interesting to observe the decrease of all that mechanical properties after the first TIG welding application on AISI 4130 steel specimens, particularly the elongation (3.8% average), typical of fragile material. However, for both welded and non-welded conditions the yield tensile stress/maximum tensile stress ratio (σ_y/σ_m) was around 0.8, which is an appropriate value for structures as the aeronautical ones [27]. Historically, values from 0.80 to 0.86 have been considered appropriate for specification, project and analysis of structural

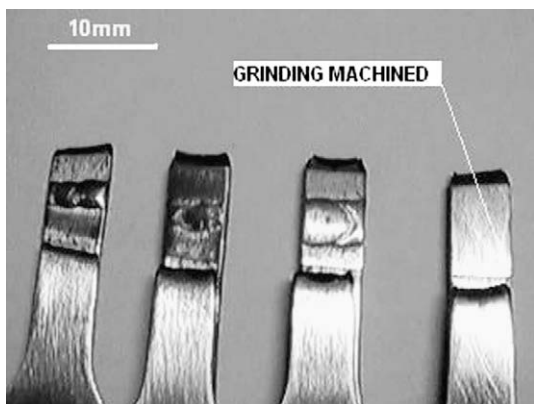


Fig. 3. Specimens fractured by monotonic tension tests.

integrity, by providing high capacity of plastic deformation and consequent margin of safety against fracture [27]. Yet, all the monotonic specimens tested, including those grinding machined, fractured at the sub-critical HAZ (SCHAZ)/base-material interface (strength-overmatch), despite any stress concentration originated at the weld toe, as illustrated in Fig. 3. This means that the influence of the microstructural variations along HAZ is more deleterious for tensile strength than the geometric features induced by the welding process. That is, for the monotonic test the material was not sensitive to stress concentration at the weld toe.

3.2. Reverse bending fatigue tests

3.2.1. Effect of the corrosion process

Fig. 4 presents the SN (stress vs. number of cycles) curves for corroded and non-corroded AISI 4130 steel specimens. For seek of comparison with the welded specimen, it was added the fatigue curve obtained with base-material specimens (BM) 1.10 mm thick. Considering that for all the specimens just the thickness was altered (1.60–1.10 mm), it is possible to verify that the higher the thickness the lower the fatigue strength. It is in accordance with Murakami [28,29], who mentions that the larger specimens the higher amount of existent defects. Makkonen [30] also mentions that there is a great amount of microcracks previously nucleated in specimens submitted to cyclic loads, whose population increases when their dimensions increase.

From Fig. 4 it is also possible to verify that the fatigue curves diverge in the short fatigue life range/SFL ($<10^5$ cycles). This is due to the maximum stress at the surface, as a function of the type of fatigue test. That is, for reverse bending fatigue tests also in SFL the specimens are sensitive to fatigue-notch effect, K_f , which is defined as the ratio of the fatigue strength of a smooth specimen to the fatigue strength of a notched specimen at the same number of cycles.

It is also possible to observe in Fig. 4 the detrimental effect of the corrosive process on the reverse bending fatigue strength of the AISI 4130 steel. Thus, for 359 MPa and 303 MPa stress levels, the respective numbers of cycles were about 1.10×10^5 and 1.90×10^5 , corresponding to 300% and 500% reduction in comparison to those non-corroded. It is well known that the fatigue behavior of any mechanical component is sensitive to its surface finishing. Thus, since there was not simultaneity between the fatigue and corrosion processes (when the anodic condition at the

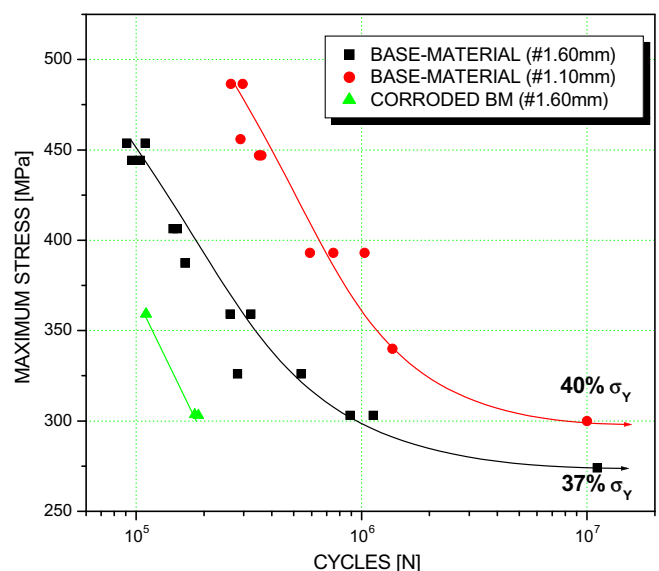


Fig. 4. SN curves for corroded and non-corroded specimens of base-material.

crack tip accelerates the corrosive process and vice versa), the main factor controlling the fatigue behavior presented is related to surface roughness of the specimens tested. In fact, the average surface roughness measured provided $R_a = 0.24 \mu\text{m} \pm 0.16 \mu\text{m}$ for non-corroded specimens and $R_a = 1.95 \mu\text{m} \pm 0.18 \mu\text{m}$ for those corroded. The corrosive process generated a Grant No. of pits, which gave rise to local stress concentration and reduced the number of cycles for crack nucleation. Additionally, the local stress concentration can also reduce the stress intensity factor threshold (ΔK_{th}) and allows that the small cracks grow [10–12]. Therefore, it is necessary to protect the surface of aeronautic structures against the aggressive environment acting on an aircraft.

3.2.2. Effect of the TIG welding/re-welding process

Fig. 5 presents the SN curves of welded and re-welded specimens. The horizontal line indicates the nominal stress value ($\sigma_n \approx 247 \text{ MPa}$), which corresponds to yielding stress divided by the safety-factor equal to 3 (for welded components critical to the flight-safety), in accordance with the EMBRAER NE 40–056 TYPE 1 Standard.

From Fig. 5, one can observe the significant decreasing in bending fatigue strength of the AISI 4130 steel, whose endurance limit was about 37% of its yielding stress (σ_y). However, the endurance limit is still above the nominal stress, σ_n (horizontal line). Nevertheless, a subsequent reduction in bending fatigue strength for welded specimens is observed in comparison with the base-material specimens (BM), mainly in the short fatigue life (SFL) range. In the long fatigue life (LFL) range, it is possible to verify that the endurance limit is located close to the horizontal line, corresponding to specified nominal stress (σ_n). On the other hand, with the first weld repair (1R), no-subsequent reduction in bending fatigue strength is observed. For both original (OR) and first time re-welded (1R) specimens, one can observe practically the same fatigue behavior. However, the second weld repair (2R) resulted in a decreasing of the fatigue strength, with the endurance limit below the nominal stress value, σ_n (horizontal line). Since the aircrafts are submitted to high fatigue cycles during flight, as a result of abrupt maneuvers, wind bursts, motor vibration and helixes efforts, it is not recommended or favorable to the flight-safety the second weld repair (2R) application. This behavior is also due to the increase in volume of the weld bead with consequent increase of the stress concentration factor at the weld toe. In addition, the re-welding process can increase the HAZ dimensions and its coarse-grain re-

Table 4
Vickers microhardness values (HV).

Microstructure	Original weld	one-repair	two-repairs
Base-material	267.7 ± 16.4	285.5 ± 15.8	286.5 ± 19.7
CGHAZ	362.9 ± 55.7	373.4 ± 22.8	477.80 ± 59.15
Weld metal	573.2 ± 69.8	507.5 ± 47.4	399.9 ± 22.8

gion (CGHAZ), which is located exactly at the weld toe and characterized by low fracture toughness and considerable hardness (as can be verified in Table 4).

From Fig. 5, it is also possible to verify the larger scattering of the fatigue results obtained with both welded and re-welded specimens. This is due to volume variations of the deposited weld metal, the higher heating/cooling rate and the uneven stress concentration values at the weld toe notch. Fig. 5 also shows that the fatigue strength reduction due to welding process tends to be more pronounced when the number of cycles is also reduced (divergence between BM and OR fatigue curves in SFL). This observation is very important taking into account the efforts due to landing operations (typical for SFL regime) along the operational life of the aircraft. On the other hand, it is observed that the divergence between both endurance limits (10^7 cycles) was low, i.e.: from 37% σ_y for base-material to 32% σ_y after welding (close to σ_n). In the same way, this is a very important result, taking into account the abrupt maneuvers or wind bursts during flight (typical for LFL regime). This implicates that special cares should be adopted during design and, particularly, maintenance of welded aeronautical structures against any accidental tool marks capable to introduce local stress concentration on the structure. Since for bending loads the maximum stress occurs at the surface, the fatigue resistance is sensitive to any geometric change of material (notch-sensitivity).

From Fig. 5, comparing the first (1R) and second weld repairs (2R) fatigue curves in the SFL ($<10^5$ cycles) regime, one can observe that the reduction was minimum, with both curves converging to a same point in high stress levels (SFL). On the other hand, one can also observe high divergence between the aforementioned curves in LFL regime, reaching a maximum at the endurance limit level (10^7 cycles). Since the material is notch-sensitive in LFL, such a behavior was due to the abrupt geometric change generated by the weld bead in addition to the microstructural alterations induced by the new cooling rate. On the other hand, comparatively to the fatigue behavior of base-material (BM), as in SFL as LFL (endurance limit) regimes the tendency of the second weld repair (2R) fatigue curve shows practically the same fatigue-notch sensitivity [$q = (K_f - 1)/(K_t - 1)$], or fatigue-notch factor, K_f (Eq. (1) [32]). This observation becomes evident considering the parallelism presented by both base-material (BM) and two weld repairs (2R) fatigue curves. In fact, the fatigue-notch factor values (K_f) in 10^7 , 10^6 and 2.8×10^5 cycles were: 2.00, 2.15 and 2.07, respectively, which confirms the mentioned parallelism. Since the welding repair procedure applied was by removing the previous weld bead, the geometric alteration was hoped to be low (as can be seen in Table 5 ahead). Thus, the increase of the notch sensitivity (fatigue-notch factor) with the second weld repair (2R) was also due to the microstructural variations resulting of successive heating/cooling cycles imposed to the material. Therefore, based on the results obtained and considering that the welding repair is necessary, it can be admitted only one weld repair (1R) during fabrication of the critical to the flight-safety structures, without compromising their reverse bending fatigue strength. On the other hand, being necessary to make some subsequent repair along the operational life, this study indicates that cares should be adopted in the sense of avoiding abrupt maneuvers and/or overloads on the aircraft. In

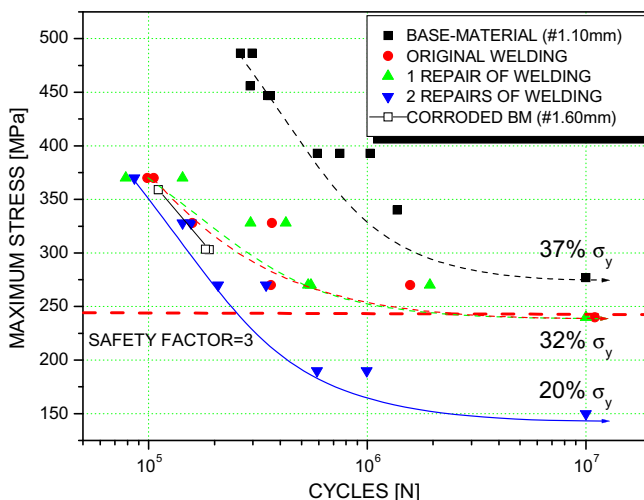


Fig. 5. Reverse bending fatigue SN curves for base-material and (re-)welded specimens (1.10 mm thick).

Table 5

Geometry factor values from the weld bead (in accordance with Fig. 6).

Group	W (mm)	T (mm)	Root (mm)	Angle (α)	Radius (mm)	HAZ (mm)	K_f (Eq. (1))
OR	3.75 ± 0.35	0.89 ± 0.20	0.77 ± 0.19	$141.9^\circ \pm 14.4^\circ$	1.03 ± 0.36	2.89 ± 0.25	1.290
1R	4.49 ± 0.33	1.17 ± 0.32	0.82 ± 0.27	$146.1^\circ \pm 8.6^\circ$	0.75 ± 0.21	3.11 ± 0.12	1.305
2R	4.80 ± 0.23	0.96 ± 0.20	0.79 ± 0.30	$138.6^\circ \pm 7.5^\circ$	0.93 ± 0.40	3.22 ± 0.23	2.178

$$K_f = 1 + \frac{K_t - 1}{1+a/r}$$

where: $a = 0.1659$ (Peterson's material parameter for steel); r = notch-root; K_f = fatigue-notch factor.

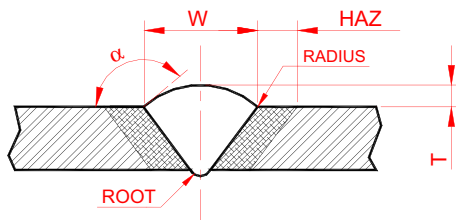


Fig. 6. Geometry factors of the welded joints (values presented in Table 5).

addition, it becomes necessary lower inspection intervals for flaws as-crack determination at the weld joints of structural components.

Finally, although it is not appropriate to directly compare both fatigue behaviors of welded specimens with those corroded due to their different thickness, it is interesting to observe the similar deleterious effect caused by the corrosive process on the fatigue strength of AISI 4130 steel.

Table 4 presents the microhardness values measured in the three interest areas. Firstly, one can observe the high microhardness values for weld metal and CGHAZ as a consequence of TIG welding and re-welding process. This is due to high cooling speed associate to the low heat-input applied, which resulted in martensitic structures. Since the heat input was kept constant for all the (re-)welding process, it is important to mention that just the weld reinforcement was removed. Consequently, the different microhardness values verified were due to remaining weld material volumes (e.g. weld root), which unevenly affected the cooling speed of the weld metal. Thus, from Table 4, one can observe that for both the original weld (OR) and the first welding repair (1R) the microhardness values were close and coherent with each other. This can explains the bending fatigue behavior presented in Fig. 5. However, it is also important to pay attention to the great dispersion of microhardness results in both CGHAZ and weld metal (standard-deviation). It is also possible to observe the highest microhardness value from the original weld metal than for all the other conditions. This implicate that probably the second welding repair promoted the tempering of the previous microstructure, but with no improvement on their bending fatigue strength, as verified in Fig. 5. After the second welding repair it is also possible to observe higher microhardness value for the CGHAZ, implicating a grain size reduction in that region, but again with no improvement on the bending fatigue strength, as illustrate in Fig. 5. It is well known that the lower the grain size the higher the material toughness. In the same way, the higher the grain size, the lower the hardness/mechanical strength.

Considering that the weld profile affects the fatigue resistance of a welded structure, Table 5 and Fig. 6 present the main geometric factors that compose a weld joint and their corresponding values, obtained by image analysis tools. Thus, from Table 5 and Fig. 6, it is possible to confirm all the results presented in Fig. 5 on the effect of welding repairs on the bending fatigue behavior of AISI 4130 steel. Therefore, it can be observed that the welding repairs reduced both angle (α) and radius at the weld toe notch that, com-

bined, are considered the main geometric factors controlling the fatigue behavior of welded components and structures [13,31]. In addition, the great scattering on the geometric factors measured is in consonance with the great scattering of the fatigue results presented by the welded specimen groups. Yet, from Table 5, we can observe: the increase of the stress concentration factor (K_f) at the weld toe notch with the successive welding repairs; the largest extension of HAZ due to the successive heat-input applied and, consequently, the increase of the CGHAZ as well; the effect of both weld reinforcement (T) and weld root dimensions, again, on the angle (α) and radius reduction and, consequently, on the bending fatigue strength of welded specimens. On this subject, it is important

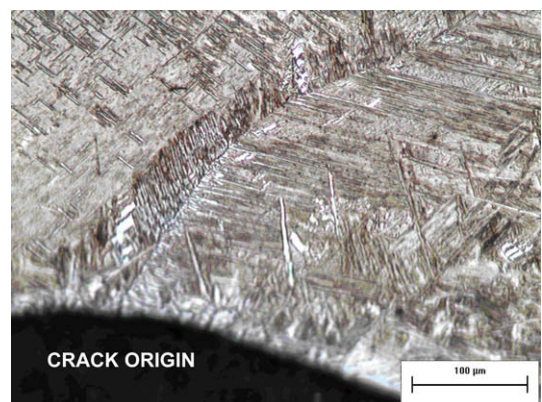


Fig. 7. Crack initiation at the weld toe of a non-fractured fatigue specimen (500×). Nital 2%.

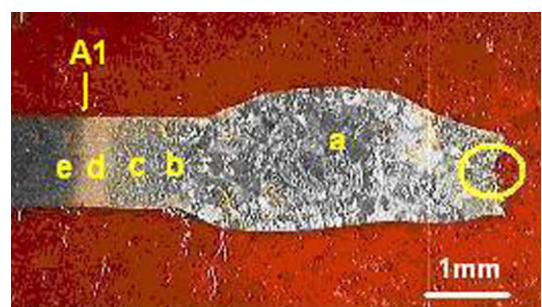


Fig. 8. Macrography of a fatigue specimen fractured by reverse bending loads. Nital 2%.



Fig. 9. Secondary crack propagation from the fracture surface of a reverse bending fatigue specimen (500×). Nital 2%.

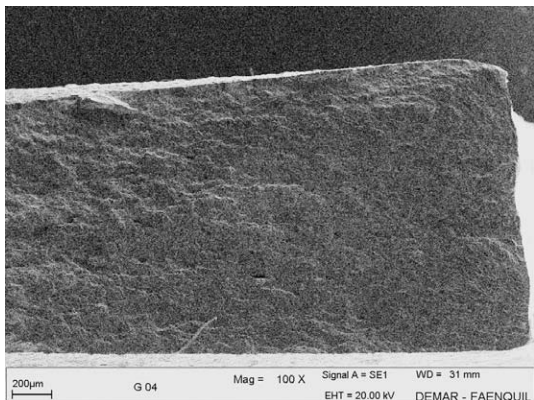


Fig. 10. Edge fatigue crack origin and propagation for a fractured specimen of base-material, 1.60 mm thick.

to mention that all the welded specimens fractured at the weld toe notch, as illustrated in Figs. 7 and 8. In fact, Fig. 7 illustrates a crack in a non-fractured specimen, which initiated at the weld toe notch and propagated through grain boundary into weld metal (intergranular crack).

Fig. 8 presents the macrography of a fractured specimen that was submitted to two welding repairs (2R), in which we can observe: (a) the weld metal region with well delineated equiaxial coarse-grains; the HAZ extension with the sub-regions, (b) coarse-grain/CGHAZ, (c) fine-grain/FGHAZ, (d) inter-critical/ICHAZ and (e) sub-critical/SCHAZ near to A_1 line (lower critical tempera-

ture); as well as the welded joint irregularity as a consequence of the deformation generated by the reverse bending loads applied.

Fig. 9 presents the transgranular secondary crack, originate from the fracture surface of the specimen in Fig. 8. This secondary crack implicates that the reverse bending fatigue specimens may have been subjected to either Modes I and II or Modes I and III of loading combination (or all of them), turning the laboratorial test more severe due to friction process by both free crack surfaces, accelerating its propagation. In fact, bending loads also introduce shear stresses in the specimens (Mode II of fracture) and/or tearing stress (Mode III of fracture) whether crack initiation occurs at the edge of the specimen, as illustrated in Fig. 10. On this subject, Veidt [33] mentions that the radius in the notch root has little effect on the stress intensity factor in Mode II of fracture.

Figs. 11 and 12 present the base-material, HAZ and weld metal microstructures for all the proposed conditions. Fig. 11a shows the normal products of transformation from austenite, i.e. ferrite and perlite. From Fig. 11b-d the beginning of the transformation from perlite to austenite is observed (to martensite, upon subsequent cooling) along the SCHAZ/ICHAZ regions (A_1 line).

Fig. 12 presents the microconstituent of the weld metal (original, one and two weld repairs) and respectives CGHAZ, basically constituted by martensite, which is a very hard and fragile microstructure. As aforementioned, the higher the hardness the higher the resistance to fatigue crack initiation.

Fig. 13 presents the residual stresses field in the weld metal, HAZ and base-material of all the conditions analyzed. It is well known that residual stresses are present in welded components [22,34–36] and have great effect on fatigue crack nucleation and propagation [34]. Thus, from Fig. 13, one can observe that the

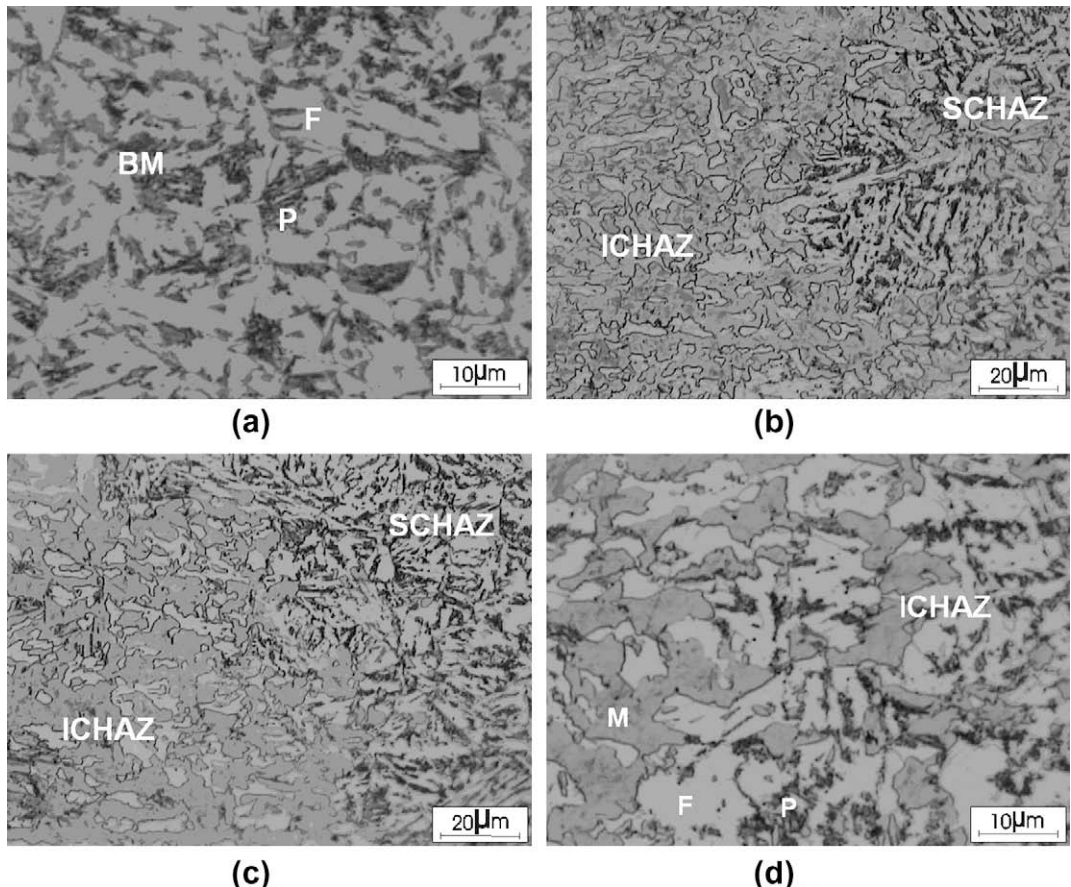


Fig. 11. Base-material and base-material/HAZ transition microstructures: (a) Base-material (typical); (b) SCHAZ-ICHAZ of the original weld; (c) SCHAZ-ICHAZ of the first welding repair; and (d) ICHAZ of the second welding repair. Nital 2%. (F = Ferrite; P = Perlite; M = Martensite).

TIG (re-)welding process induced high compressive residual stresses for all conditions upon analysis, as weld metal as in HAZ and base-material (up to 20 mm from the fusion line). Such residual stresses were relieved internally in some point along the length of the specimens, because no deformation was verified on the samples. Yet, it is observed that all the residual stress profiles presented similar tendency, i.e., maximum values in weld metal (-600 MPa for original weld; -450 MPa for one weld repair and -330 MPa for two weld repairs), followed by HAZ (-400 MPa for original weld; -75 MPa for one weld repair and -50 MPa for two weld repairs) and last base-material up to 20 mm far-away from the fusion line (-300 MPa for original welding; -160 MPa for one weld repair and -100 MPa for two weld repairs).

Many factors might have contributed to compressive residual stresses induced by the TIG (re-) welding process, viz: (i) austenite-martensite transformation (which generate up to 4% increase in volume of material) and which initiate at the surface due to higher cooling speed; (ii) the thin thickness and good mechanical properties in high temperature of the base-material, particularly low deformation in high temperature; (iii) subsequent contraction in the core of the weld metal (after the martensitic transformation at the surface) due to relatively lower cooling speed in that region; (iv) constraint to natural expansion of the weld metal and HAZ by the base-material volume around; and (v) the clamps applied at the extremities of the specimens during the (re-)welding process, etc. However, some aspects get the attention from the Fig. 13 as:

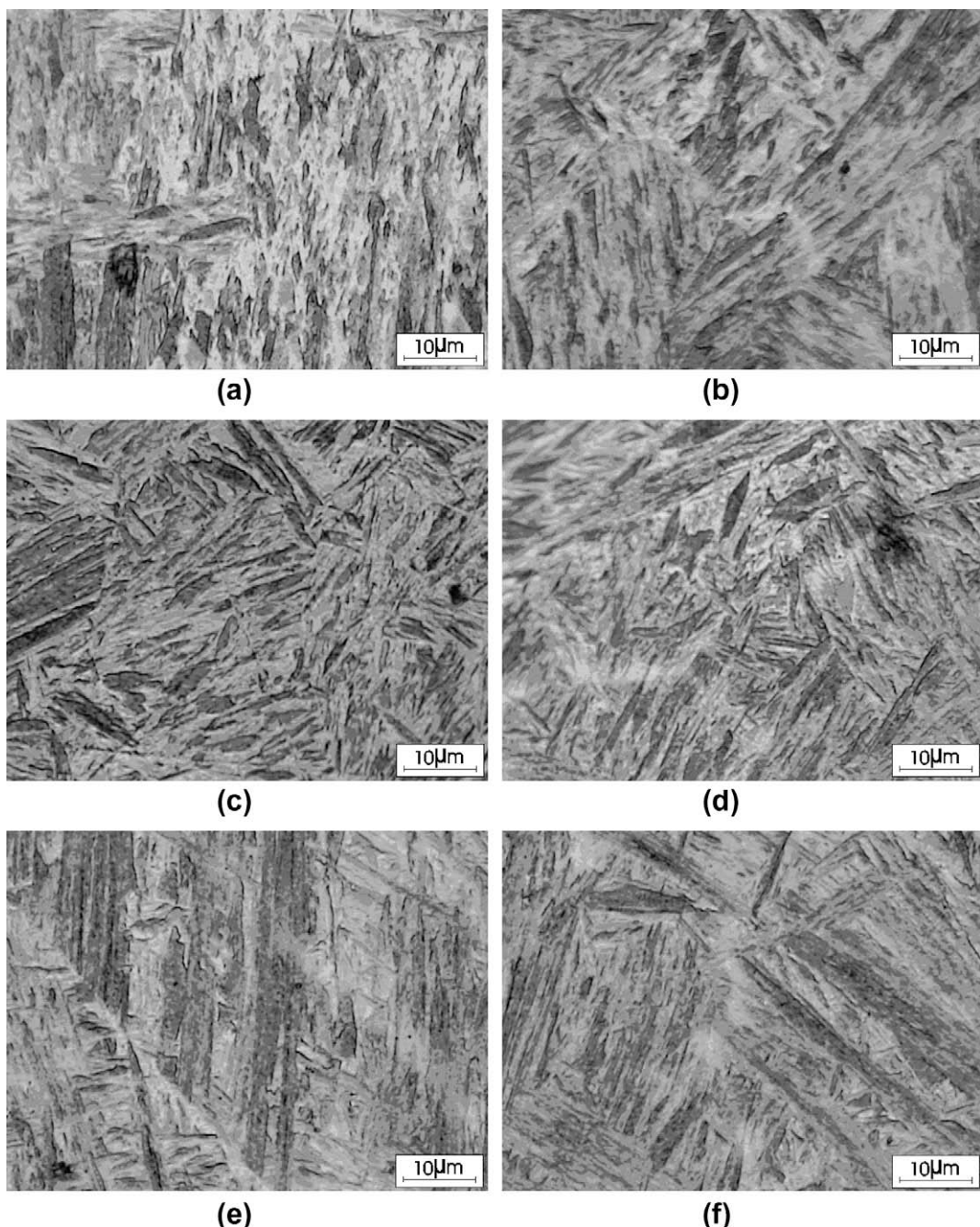


Fig. 12. Microscopic analysis of the weld metal and CGHAZ: (a) original CGHAZ; (b) original weld metal; (c) CGHAZ of the first welding repair; (d) weld metal of the first welding repair; (e) CGHAZ of the second welding repair; and (f) weld metal of the second welding repair. Nital 2%.

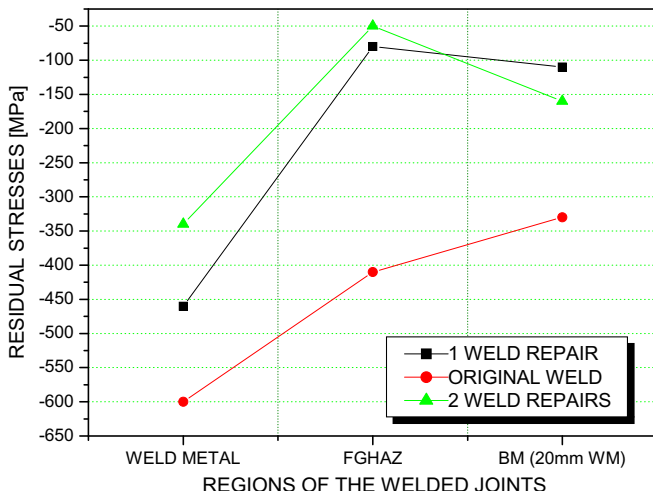


Fig. 13. Residual stress profiles of all the conditions tested.

the high values of compressive residual stresses, which were higher in the weld metal than HAZ; all the compressive stress fields were still compressive up to 20 mm distance from weld fusion line.

It is well known that the residual stresses largely affect the fatigue behavior of components, and that compressive residual stresses are benefit towards inhibit the crack nucleation. Thus, the results presented in Fig. 13 are in accordance with the fatigue behavior of specimens with original weld (OR), as well as those with one (1R) and two (2R) weld repairs presented in Fig. 5. In addition: the higher the hardness, the higher the fatigue strength as well. Consequently, from Table 4 and Fig. 5, it could be observed better fatigue behavior for the originally welded (OR) specimens in comparison with the one (1R) weld repair condition. However, considering the fatigue crack propagation stage, it is well known that the increase of the hardness increases the propagation rate (da/dN). In this context, the existence of compressive residual stresses highlight the stress concentration effect induced by the weld geometry on the fatigue strength reduction verified. That is, although a mechanical component possess high compressive residual stresses, their effects or benefits will be minimized (or annulled in case the stress relief) when this component presents a stress concentrator (geometric factor) that reduces the number of cycles necessary to fatigue crack initiation. Thus, it is possible that the geometric stress concentration factor, which is located at the weld toe/fusion line/CGHAZ region, overcomes the compressive residual stress field induced by the (re-)welding process, relief it. Certainly, the compressive residual stresses field as far as possible delayed the fatigue crack nucleation and propagation by reducing the stress intensity factor (ΔK), as mentioned by Wei & Chen [34].

4. Conclusions

Motivated by high fracture incidence at welded joints of a specific and critical to the flight-safety component, called "motor-craddle", experimental reverse bending fatigue tests on welded and re-welded specimens were carried out. Based on the results obtained, the following conclusions may be drawn:

1. The AISI 4130 steel possess good mechanical properties, but low elongation in the "as-received" condition (not heat-treated).
2. All the monotonic specimens tested, including those grinding machined, fractured at the sub-critical HAZ (SCHAZ)/base-material interface (strength-overmatch), despite any stress concentration originated at the weld toe.

3. The reverse bending loads significantly decrease the fatigue strength of the AISI 4130 steel, whose endurance limit were about 37% and 40% of the yielding stress (σ_y) for specimens 1.60 mm and 1.10 mm thick, respectively.
4. The corrosive process strongly reduced the reverse bending fatigue strength of AISI 4130 steel.
5. In comparison with specimens from the base-material a reduction in bending fatigue strength for TIG welded specimens (OR) was observed. After the first weld repair (1R), no-subsequent reduction in bending fatigue strength was observed in comparison with the original weld. The second weld repair (2R) again resulted in decreasing of the fatigue strength in comparison with that subjected to the first weld repair. Consequently, it is not recommended or favorable to the flight-safety the second weld repair (2R) on critical to the flight-safety components.
6. The TIG (re-)welding procedure induced high compressive residual stress values in the AISI 4130 steel.
7. It was verified increase of the stress concentration factor, K_t , at the weld toe with the successive welding repairs, which overcomes the compressive residual stress field induced by the (re-)welding process. As a result, all the welded fatigue specimens fractured at that region.

Acknowledgement

The authors are grateful to FAPESP/Process No. 99/11948-6, CNPq and FUNDUNESP.

References

- [1] Flight Safety Foundation – Available from <<http://www.flightsafety.org>>; 2009 [accessed 10.2009].
- [2] National Civil Aviation Agency – Brazil. Available from <<http://www.anac.gov.br>>; 2004 [accessed 10.2003].
- [3] Godefroid LB. Fatigue crack growth under constant and variable amplitude loading in aluminium alloys of aeronautical applications. Ph.D. Thesis, COPPE/UFRJ, Brazil: Federal University of Rio de Janeiro; 1993.
- [4] Goranson UG. Fatigue issues in aircraft maintenance and repairs. Int J Fatigue 1993;19:S3–S21.
- [5] Payne AO. The fatigue of aircraft structures. Eng Fract Mech 1976;8:157–203.
- [6] Wenner CA, Drury CG. Analysing human error in aircraft ground damage incidents. Int J Ind Ergonom 2000;26:177–99.
- [7] Latorella KA, Prabhu PV. A review of human error in aviation maintenance and inspection. Int J Ind Ergonom 2000;26:133–61.
- [8] Bhaumik SK, Sujata M, Venkataswamy MA. Fatigue failure of aircraft components. Eng Fail Anal 2008;15:675–94.
- [9] Carpenter M. Managing the fleet: materials degradation and its effect on aging aircraft. Amptiac, News Lett 2001;4(5):7–19.
- [10] DOT/FAA/AR-00/22. US Department of Transportation, Federal Aviation Administration, Corrosion and Corrosion Fatigue of Airframe Materials, final report, July 2002. 2002, 79p.
- [11] Wang QY, Kawagoishi N, Chen Q. Effect of pitting corrosion on very high cycle fatigue behavior. Scripta Mater 2003;49:711–6.
- [12] Murtaza G, Akid R. Corrosion fatigue short crack growth behaviour in a high strength steel. Int J Fatigue 1996;18:557–66.
- [13] Nascimento MP. Effects of TIG welding repair on the structural integrity of AISI 4130 aeronautical steel. In: Ph.D. Thesis in mechanical engineering. State University of São Paulo/UNESP-FEG, Brazil (in Portuguese); Code CDU 620.92, 2004. 240p.
- [14] Nascimento MP, Voorwald HJC. An evaluation on the fatigue crack growth in re-welded AISI 4130 aeronautical steel. In: Eighth international fatigue congress/FATIGUE 2002, vol. 5, Stockholm-Sweden; 2002. p. 3463–72.
- [15] Nascimento MP, Ribeiro RB, Voorwald HJC. Fatigue crack growth in re-welded AISI 4130 high strength steel. In: Fourteenth European congress on fatigue/ECF 14, vol. 2, Cracow, Poland; 2002. p. 1–3116.
- [16] Vern Sutter, Robert J. Dybas, repair welding. In: ASM International, American Society for Metals, Editors, Metals Handbook, Welding, Brazing and Soldering, vol. 6, Metals Park, Ohio; 2002. p. 1103–7.
- [17] Kroes MJ, Watkins WA, Delp F. Aircraft maintenance and repair. 6th ed. New York: Glencoe – Macmillan/McGraw-Hill; 1993. 648p.
- [18] Vega EO, Hallen JM, Villagomez A, Contreras A. Effect of multiple repairs in girth welds of pipelines on the mechanical properties. Mater Charact 2008;59:1498–507.
- [19] Liming L, Xin Du, Meili Z, Guoqing C. Research on the microstructure and properties of weld repairs in TA15 titanium alloy. Mater Sci Eng A 2007;445–446:691–6.

- [20] Shankar K, Weidong Wu. Effect of welding and weld repair on crack propagation behaviour in aluminium alloy 5083 plates. Mater Des 2002;23:201–8.
- [21] Sun W, Hyde TH, Becker AA, Williams JA. Some key effects on the failure assessment of weld repairs in CrMoV pipelines using continuum damage modeling. Eng Fail Anal 2005;12:839–50.
- [22] Dong P, Hong JK, Bouchard PJ. Analysis of residual stresses at weld repairs. Int J Pres Ves Pip 2005;82:258–69.
- [23] Hyde TH, Sun W, Becker AA, Williams JA. Life prediction of repaired welds in a pressurised CrMoV pipe with incorporation of initial damage. Int J Pres Ves Pip 2004;81:1–12.
- [24] Aloraijer AS, Ibrahim RN, Ghojet J. Eliminating post-weld heat treatment in repair welding by temper bead technique: role bead sequence in metallurgical changes. J Mater Process Technol 2004;153–154:392–400.
- [25] Doc IIS/IIW-956-87. (ex. doc. XV-648-87) prepared by commission XV “fundamentals of design and fabrication for welding” of the IIW, recommendations for repairs and/or strengthening of steel structures. Welding in the world 1988; 26(11/12): 292–306.
- [26] Ivanov SA, Monim VI, Teodósio JR. New method of X-ray tensometry. In: International conference on experimental mechanics. Lisboa; 1994. p. 757–61.
- [27] Bannister AC, Ocejo JR, Gutierrez-Solana F. Implications of the yield stress/tensile stress ratio to the SINTAP failure assessment diagrams for homogeneous materials. Eng Fract Mech 2000;67:547–62.
- [28] Murakami Y. Inclusion rating by statistics of extreme values and its application to fatigue strength prediction and quality control of materials. J Res Nat Inst Stand Technol 1994;4:99–107.
- [29] Murakami Y, Usuki H. Quantitative evaluation of effects of non-metallic inclusions on fatigue strength of high strength steels. II: fatigue limit evaluation based on statistics for extreme values of inclusion size. Int J Fatigue 1989;5(11):299–307.
- [30] Makkonen M. Statistical size effect in the fatigue limit of steel. Int J Fatigue 2001;23:395–402.
- [31] Lancaster JF. Metallurgy of welding. 5th ed. London: Chapman and Hall Incorporation; 1993. 389p.
- [32] Peterson RE. Stress Concentration design factors. 5th ed. New York: John Wiley and Sons Incorporation; 1966 [155p].
- [33] Veidt M. On the Effect of notch radius and local friction on the Mode I and Mode II fracture toughness of a high-strength steel. Eng Fract Mech 1997;58:223–31.
- [34] Wei MY, Chen C. Fatigue crack growth characteristics of laser-hardened 4130 steel. Scripta Metall Mater 1994;10(31):1393–8.
- [35] Brown TB, Dauda TA, Truman CE, Smith DJ, Memhard D, Pfeiffer W. Predictions and measurements of residual stress in repair welds in plates. Int J Pres Ves Pip 2006;83:809–18.
- [36] Chiarelli M, Lanciotti A, Sacchi M. Fatigue resistance of MAG welded steel elements. Int J Fatigue 1999;1:1099–110.



Considerations on corrosion and weld repair effects on the fatigue strength of a steel structure critical to the flight-safety

Marcelino P. Nascimento *, Herman J.C. Voorwald

Department of Materials and Technology – State University of São Paulo, UNESP/FEG/DMT 333, Ariberto Pereira da Cunha Ave., 12516-410, Guaratinguetá City, São Paulo State, Brazil

ARTICLE INFO

Article history:

Received 30 July 2009

Received in revised form 24 December 2009

Accepted 31 December 2009

Available online 7 January 2010

Keywords:

AISI 4130 steel

Fatigue behavior

Corrosion

Weld repairs

Flight-safety

ABSTRACT

The aim of this study is to analyze the effects of corrosion and successive tungsten inert gas (TIG) welding repairs on the reverse bending fatigue strength of AISI 4130 steel used in components critical to the flight-safety. The tests were performed on hot-rolled steel plate specimens, 1.10 mm and 1.60 mm thick, by means of a SCHENK PWS equipment, with load ratio $R = -1$, constant amplitude, 30 Hz frequency and room temperature. It was observed that the reverse bending fatigue strength of AISI 4130 steel decreases due to the corrosion and the TIG welding and re-welding processes.

© 2010 Elsevier Ltd. All rights reserved.

1. Introduction

According to flight-safety foundation [1], “Aircraft accidents means an occurrence associated with the operation of an aircraft, which takes place between the time any person boards the aircraft with the intention of flight until such time as all such persons have disembarked, and in which any person suffers death or serious injury as a result of being in or upon the aircraft or by direct contact with the aircraft or anything attached thereto, or in which the aircraft received substantial damage (damage or structural failure that adversely affects the structural strength, performance, or flight characteristics of the aircraft, and which would normally require major repair or replacement of the affected component)”. Based in such definition, the accident rates (i.e., accidents per million departures) have been at 1.2, or 12,000 accidents, in the occidental world [2]. In the search for a zero accident rates, the flight-safety has been the main concern of the aeronautical authorities all over the world.

Basically, the aeronautical projects should take into account the difficulties of transporting a load against the gravity force during take-off and flight, and discharge it in an efficient way, with minimum cost and maximum safety, because failures in any of these stages will implicate catastrophic accidents, involving human lives [3]. In general, structural failures during flight are attributed to

aerodynamic overloads or fatigue of materials, as a consequence of inadequate project or any notch produced during manufacturing or maintenance of aircrafts [4–7]. Since the catastrophic accidents involving the English model “Comet” in the 1950’s, the fatigue process has been the most important project and operational consideration for both civil and military aircrafts [4,5,8]. On the other hand, many fractures of materials are also caused by corrosion as a consequence of aggressive environment.

Since the aircrafts become more complex, the environmental effects assumed great importance. As a result of older aircrafts flying nowadays, problems such as stress-corrosion cracking, corrosion-fatigue (simultaneously or separately) and wear are also expected to occur [4,5,9,10]. Due to several aggressive environments in which the aircrafts are subjected, particularly marine, corrosion is the most important factor of maintenance and inspection for the aeronautic sector [4,5,9,10]. Hence, corrosion is undoubtedly a real and critic issue acting on aircrafts, flowing with the time even on those not operational. Usually, the corrosion control is accomplished by adoption of prevention methods with high-quality periodic inspections associated to damage tolerance philosophy, for taking into account its effect on the fatigue life of a structural component [4,5,10–12]. Such issues will request extensive investment, planning, researches and development on repair methods and maintenance procedures towards assure the safe and continued airworthiness.

For several aircraft models (e.g. agricultural, military training and acrobatic) the most solicited and repaired component is one that supports the motor, called “Motor-Cradle” (Fig. 1) [13]. This

* Corresponding author. Tel.: +55 12 3123 2865; fax: +55 12 3123 2852.

E-mail addresses: pereira@feg.unesp.br, marcelino.nascimento@gmail.com (M.P. Nascimento), voorwald@feg.unesp.br (H.J.C. Voorwald).

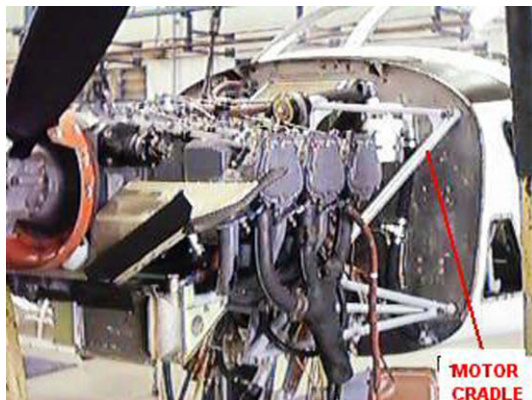


Fig. 1. Motor-cradle assembly in a T-25 Universal Brazilian aircraft.

component presents a geometrically complex structure made from AISI 4130 tubular steel of different dimensions and TIG welded in several angles [13,14]. For the Brazilian aircrafts T-25 Universal and T-27 Tucano, for example, besides supporting the motor in balance, the motor-cradle also maintains the nose landing gear fixed at the other extremity. Since the motor-cradle is a component critical to the flight-safety, the aeronautic standards are extremely rigorous in its manufacturing, by imposing a “zero-defect index” on the final weld seam quality (Safe-Life philosophy), which is 100% inspected by non-destructive testing/NDT [13–15]. For this reason, welded aeronautic structures are frequently subjected to successive repairs in accomplishment to current standards. As a consequence, components approved by NDT may contain a historic record of welding repairs whose effects on their structural integrity are not computed. In addition, these structures are also submitted to weld repairs along their operational life, turning this question more complex.

As a part of this research-work, an investigation on 157 motor-cradles fracture reports indicates that all of them occurred at welded joints as a result of fatigue cracks, reducing the “Time-Before-Fail” from 4.000 h to 50 h of flight [13]. Motivated by high fracture incidence of this particular component, an extensive research program to evaluate the manufacturing and maintenance weld repair effects on the structural integrity, mechanical properties and microstructural changes has been conducted [13].

Although the maintenance repairs of parts and components are a multibillion-dollar industry [16] and that, particularly for the transport sector, the welding repairs are an essential and frequently used process [17], few papers approaching this issue have been published, being all of them on either aged and degenerated materials [18,19] in petrochemical, offshore and power industries [20], by means of finite element method – FEM - [21–23].

In this paper, special emphasis was attributed to a standardized weld repair procedure, widely employed during manufacture of welded aeronautic structures and characterized by removing the previously defective weld bead and by applying a new weld seam by means of the gas tungsten arc welding/GTAW (or tungsten inert gas/TIG) process with filler metal.

The aim of this study is to analyze the effect of the corrosive process and the successive TIG welding repairs on the reverse bending fatigue strength of AISI 4130 steel specimens made from hot-rolled steel plates, 1.60 mm and 1.10 mm thick, respectively. Analyses of microstructure, microhardness and residual stresses from the base-material (BM), heat-affected zone (HAZ) and weld metal (WM), as well as the effects of the surface roughness and weld bead geometry complemented this study.

In the sequence, a brief comment on the current weld repair procedures is presented.

1.1. Current Welding Repair Procedure and Applications

When defects (such as porosity, impurity, undercut) are found in the welding joints, the main international standards (e.g. API, AWS, BSI and ASME) request that the defective welded joints are corrected. However, in a general form, none of the above standards make mention to number of permissible repairs.

In general, repair welding usually involves the complete shut-down of the equipment, the removal of all dead loads and the carrying out welding to original manufacturing standards [24]. Two typical procedures of weld repairs, complete repair and partial repair, include mechanics removal of the damaged material and the restoration of the geometry and integrity of the component, followed for a post-welding heat treatment (PWHT), which will depend mainly on type and thickness of material [21]. PWHT has as a function to reduce or eliminate residual stresses and to temper the metallurgical structure of heat-affected zone (HAZ). However, PWHT is very expensive, time consuming and, depending on local, difficult or impracticable.

An important application of weld repair techniques is to avoid PWHT, generating HAZ with structures of fine grains [24]. Such an objective can be reached by minimizing the size of original grain in HAZ, by minimizing the thermal contribution during the welding process or by refining the size of the initial coarse-grain region of HAZ [24]. For this purpose, two welding repair techniques are employed, viz:

- i. Half-bead welding (HBW): the beads are removed before welding the next layer.
- ii. Temper-bead welding (TBW): the subsequent weld bead partially does heat-treat the previous passes, after that the deposited weld layer is removed.

Both techniques involve removal of the upper passes and they are employed to avoid PWHT, to reduce or eliminate residual stresses, to avoid hydrogen cracking, to improve fracture toughness and to reduce welding cost and time [24].

For the aeronautic sector, in accordance with IIS/IW – 956-87 Doc [25], when repairing a weld seam in critical aeronautic components is requested that the defect is also located and removed. The removal process should be always carried out from the side that propitiates the smallest weld material loss. Soon after, to maintain the uniformity of the deposited metal along the weld seam, the repair is applied [25].

However, the weld bead removal can be uneconomical, impracticable or even impossible in certain engineering applications due to urgency or emergency, difficult access to the component or appropriate equipments. As a consequence, along the useful life of the aircraft many non-standardized weld repairs are carried out by putting upon several weld bead, without removal of the previous pass. The subject to be answered up is whether or not the weld repairs are a viable and effective procedure, capable of extending the in-service life of components and structures. At present, due to the increase of residual stresses, the distortion in the geometry and deterioration of the microstructure caused by the thermal cycles, the effectiveness of the weld repairs on cracked structures is not well understood and investigated. Differently to the considerable data volume on the effects of original weld on fatigue life for steels and aluminum from the literature, data on welds repairs are scarce. In this context, the availability of experimental data on weld repair effects on the fatigue behavior may be very useful in determining inspection intervals in high-responsibility welded structures.

2. Material and methods

2.1. Material

For the present research-work flat welded specimens from hot-rolled AISI 4130 aeronautic steel, 1.10 mm and 1.60 mm thick, were used. The chemical compositions (wt%), from the base-material and from the weld (filler) metal, are presented in Table 1 (Fe in balance). The mechanical properties obtained from smooth flat samples and original welded specimens (OR) – with central weld seam crossed to the hot-rolled plate direction –, are indicated in Table 2. The hot-rolled plates presented 65 HR_A in the “as-received” condition.

The monotonic tensile tests were performed in accordance with ASTM E 8 M by means of a servo-hydraulic INSTRON test machine, applying 0.5 mm/min displacement rate and a preload equal to 0.1 kN.

2.2. Welding and re-welding procedures

The most commonly employed welding process for manufacturing of aeronautical structures is tungsten inert gas (TIG), or gas tungsten arc welding (GTAW), which is appropriate to weld thin thickness materials and to allow the necessary variable control, resulting in high-quality and defect-free weld beads. The TIG welding process was carried out in accordance with the Brazilian Aeronautic Industry – EMBRAER NE 40-056 TYPE 1 – Standard (for components critical to the flight-safety), with a protective 99.95% purity argon-gas and filler metal AMS 6457 B – Turballoy 4130. A Square Wave TIG 355 – Lincoln equipment was manually employed by an expert aeronautic welder. All the welding parameters were controlled, and the main ones are indicated in Table 3. Also, all the welded joints were subjected to X-ray non-destructive analysis by the Brazilian Aerospace Technical Centre (CTA/IFI), which proved the acceptable quality of the welds, according to MIL-STD-453, EMBRAER – NE-57-002 and ASTM E-390 standards.

The welding direction was always perpendicular to hot-rolling process (direction) of the plate. Before welding, samples were cleaned with chlorinated solvent to oxide removal and fixed on a backing bar, to avoid contamination and porosity in the weld root. After the welding/re-welding process neither subsequent heat treatment to residual stresses relief nor subsequent removal of the weld bead was carried out, in order to simulate the real condition of the original aeronautic structure. Due to the plate thickness,

only one weld single-pass was required. For re-welding process, a manual grinding machine capable to reach 22,000 rpm was used to remove the previous weld metal. The heat-input applied was kept constant for all the welded and re-welded specimens.

2.3. Corrosion process

To analyze the effects of the corrosive process on the fatigue behavior of AISI 4130 steel, specimens were submitted to atmospheric corrosion (urban environment), accelerated by means of constant wetting during thirty days. Periodically, the specimens were moved so that all the surfaces were uniformly corroded.

2.4. Reverse bending fatigue tests

For experimental bending fatigue tests, welded and non-welded flat specimens were manufactured according to SCHENCK model PWS requirements (Fig. 2), following the LT direction of the hot-rolled plate. The specimens were fatigue tested upon a sinusoidal load, constant amplitude, load ratio $R = -1$, at 30 Hz frequency and room temperature. The superficial average roughness, obtained by means of a Mitutoyo 301 equipment, with cut-off equal to 0.8 mm × 5 mm, was $R_a = 0.24 \mu\text{m} \pm 0.16 \mu\text{m}$.

2.5. Microstructural and microhardness analyses

For microstructural analysis, a Nital 2% chemical etching was applied during 5 s. Vickers microhardness measurements were obtained at 0.0254 mm intervals throughout the regions under analysis (base-material, HAZ regions and weld metal), applying a 1 N load.

Table 3
TIG welding parameters.

Direct current	DCEN
Welding position	Flat
Welding voltage	12 V
Welding current	30 A
Welding average speed	19.0 cm min ⁻¹
Pre heating	NONE
Flow rate	4–12 L min ⁻¹
Theoretical heat input	1.2 kJ cm ⁻¹
Filler metal diameter	1.6 mm

Table 1
Chemical compositions (wt%).

Composition (wt%)	C	Mn	P _{max}	S _{max}	Si	Mo	Cr	Cu
Specified BM ^a	0.28–0.33	0.40–0.60	0.035	0.040	0.15–0.30	0.15–0.25	0.80–1.10	0.10
Specified WMB ^b	0.28–0.33	0.40–0.60	0.008	0.008	0.15–0.35	0.15–0.25	0.80–1.10	0.10
Weld (filler) metal	0.30	0.50	0.004	0.003	0.25	0.18	0.91	0.042
Plate #1.10 thick	0.33	0.53	0.010	0.003	0.28	0.17	1.04	0.02
Plate #1.60 thick	0.28	0.49	0.009	0.004	0.24	0.18	0.93	0.02

^a AMS 6457 B – turballoy 4130 steel.

^b AMS T 6736 A (2003) – for chromium–molybdenum (4130) seamless and welded steel tubing of aircraft quality.

Table 2
Mechanical properties obtained from the welded and non-welded specimens.

Specimens	Yielding (0.2% offset)	Ultimate strength	Rupture stress	Elongation (25 mm length)	Yielding/ultimate strength ratio
Base-metal	746 ± 21	843 ± 9	655 ± 26	9.80 ± 1.87	0.88 ± 0.02
Welded	671 ± 20	778 ± 17	643 ± 26	3.81 ± 0.26	0.86 ± 0.01

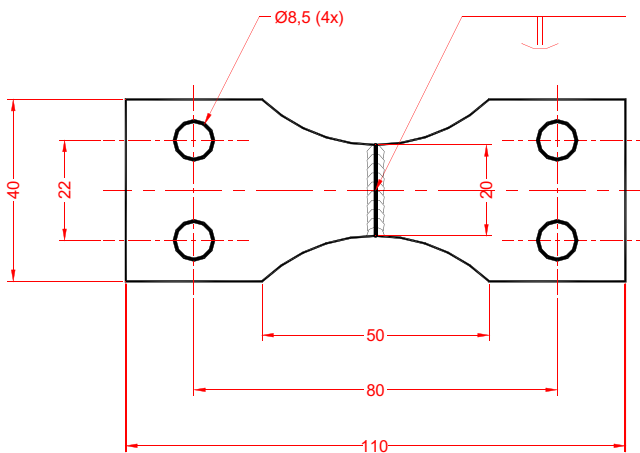


Fig. 2. Flat bending fatigue specimen (mm).

2.6. Residual stresses determination

The residual stresses field induced by welding and re-welding processes was determined by X-ray diffraction method, using the Raystress equipment (whose features are described in [26]) with couple exhibition, φ goniometer geometer, two anodes of chrome Cr- κ radiation and registration of {2 2 1} diffraction lines, tension source of 25 kV, current of 1.5 mA, X-ray convergence angle of 50°. The accuracy of the stress measurements was $\Delta\sigma = \pm 20$ MPa. In order to obtain the stress distribution by depth, the layers of specimens were removed by electrolytic polishing with a non-acid solution.

3. Results and discussion

3.1. Monotonic tests

First of all, it is important to pay attention to the high mechanical strength values and reasonable ductility from the hot-rolled AISI 4130 steel plate (as presented in index 2.1). It is also interesting to observe the decrease of all that mechanical properties after the first TIG welding application on AISI 4130 steel specimens, particularly the elongation (3.8% average), typical of fragile material. However, for both welded and non-welded conditions the yield tensile stress/maximum tensile stress ratio (σ_y/σ_m) was around 0.8, which is an appropriate value for structures as the aeronautical ones [27]. Historically, values from 0.80 to 0.86 have been considered appropriate for specification, project and analysis of structural

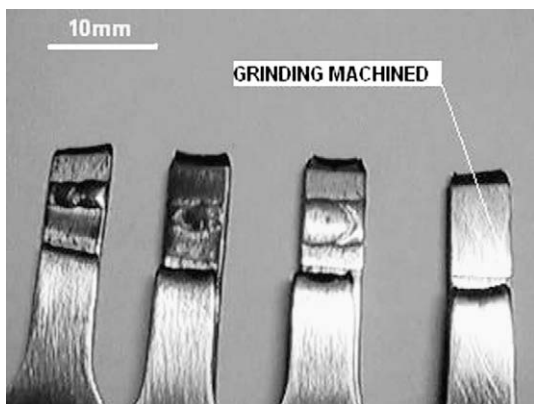


Fig. 3. Specimens fractured by monotonic tension tests.

integrity, by providing high capacity of plastic deformation and consequent margin of safety against fracture [27]. Yet, all the monotonic specimens tested, including those grinding machined, fractured at the sub-critical HAZ (SCHAZ)/base-material interface (strength-overmatch), despite any stress concentration originated at the weld toe, as illustrated in Fig. 3. This means that the influence of the microstructural variations along HAZ is more deleterious for tensile strength than the geometric features induced by the welding process. That is, for the monotonic test the material was not sensitive to stress concentration at the weld toe.

3.2. Reverse bending fatigue tests

3.2.1. Effect of the corrosion process

Fig. 4 presents the SN (stress vs. number of cycles) curves for corroded and non-corroded AISI 4130 steel specimens. For seek of comparison with the welded specimen, it was added the fatigue curve obtained with base-material specimens (BM) 1.10 mm thick. Considering that for all the specimens just the thickness was altered (1.60–1.10 mm), it is possible to verify that the higher the thickness the lower the fatigue strength. It is in accordance with Murakami [28,29], who mentions that the larger specimens the higher amount of existent defects. Makkonen [30] also mentions that there is a great amount of microcracks previously nucleated in specimens submitted to cyclic loads, whose population increases when their dimensions increase.

From Fig. 4 it is also possible to verify that the fatigue curves diverge in the short fatigue life range/SFL ($<10^5$ cycles). This is due to the maximum stress at the surface, as a function of the type of fatigue test. That is, for reverse bending fatigue tests also in SFL the specimens are sensitive to fatigue-notch effect, K_f , which is defined as the ratio of the fatigue strength of a smooth specimen to the fatigue strength of a notched specimen at the same number of cycles.

It is also possible to observe in Fig. 4 the detrimental effect of the corrosive process on the reverse bending fatigue strength of the AISI 4130 steel. Thus, for 359 MPa and 303 MPa stress levels, the respective numbers of cycles were about 1.10×10^5 and 1.90×10^5 , corresponding to 300% and 500% reduction in comparison to those non-corroded. It is well known that the fatigue behavior of any mechanical component is sensitive to its surface finishing. Thus, since there was not simultaneity between the fatigue and corrosion processes (when the anodic condition at the

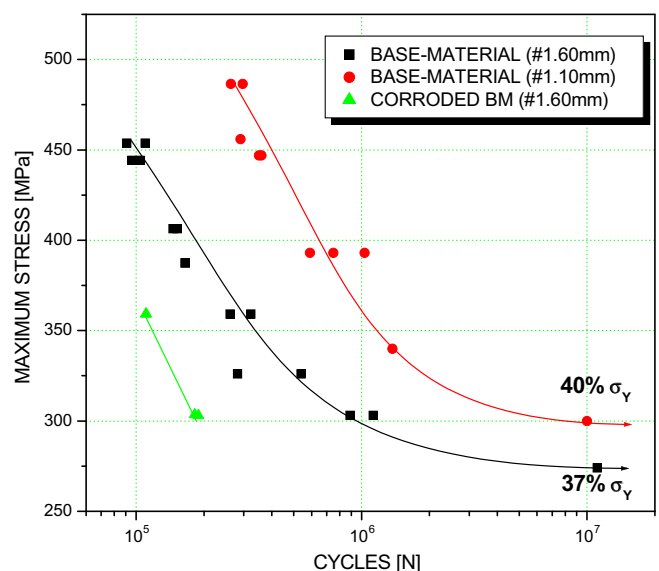


Fig. 4. SN curves for corroded and non-corroded specimens of base-material.

crack tip accelerates the corrosive process and vice versa), the main factor controlling the fatigue behavior presented is related to surface roughness of the specimens tested. In fact, the average surface roughness measured provided $R_a = 0.24 \mu\text{m} \pm 0.16 \mu\text{m}$ for non-corroded specimens and $R_a = 1.95 \mu\text{m} \pm 0.18 \mu\text{m}$ for those corroded. The corrosive process generated a Grant No. of pits, which gave rise to local stress concentration and reduced the number of cycles for crack nucleation. Additionally, the local stress concentration can also reduce the stress intensity factor threshold (ΔK_{th}) and allows that the small cracks grow [10–12]. Therefore, it is necessary to protect the surface of aeronautic structures against the aggressive environment acting on an aircraft.

3.2.2. Effect of the TIG welding/re-welding process

Fig. 5 presents the SN curves of welded and re-welded specimens. The horizontal line indicates the nominal stress value ($\sigma_n \approx 247 \text{ MPa}$), which corresponds to yielding stress divided by the safety-factor equal to 3 (for welded components critical to the flight-safety), in accordance with the EMBRAER NE 40–056 TYPE 1 Standard.

From Fig. 5, one can observe the significant decreasing in bending fatigue strength of the AISI 4130 steel, whose endurance limit was about 37% of its yielding stress (σ_y). However, the endurance limit is still above the nominal stress, σ_n (horizontal line). Nevertheless, a subsequent reduction in bending fatigue strength for welded specimens is observed in comparison with the base-material specimens (BM), mainly in the short fatigue life (SFL) range. In the long fatigue life (LFL) range, it is possible to verify that the endurance limit is located close to the horizontal line, corresponding to specified nominal stress (σ_n). On the other hand, with the first weld repair (1R), no-subsequent reduction in bending fatigue strength is observed. For both original (OR) and first time re-welded (1R) specimens, one can observe practically the same fatigue behavior. However, the second weld repair (2R) resulted in a decreasing of the fatigue strength, with the endurance limit below the nominal stress value, σ_n (horizontal line). Since the aircrafts are submitted to high fatigue cycles during flight, as a result of abrupt maneuvers, wind bursts, motor vibration and helixes efforts, it is not recommended or favorable to the flight-safety the second weld repair (2R) application. This behavior is also due to the increase in volume of the weld bead with consequent increase of the stress concentration factor at the weld toe. In addition, the re-welding process can increase the HAZ dimensions and its coarse-grain re-

Table 4
Vickers microhardness values (HV).

Microstructure	Original weld	one-repair	two-repairs
Base-material	267.7 ± 16.4	285.5 ± 15.8	286.5 ± 19.7
CGHAZ	362.9 ± 55.7	373.4 ± 22.8	477.80 ± 59.15
Weld metal	573.2 ± 69.8	507.5 ± 47.4	399.9 ± 22.8

gion (CGHAZ), which is located exactly at the weld toe and characterized by low fracture toughness and considerable hardness (as can be verified in Table 4).

From Fig. 5, it is also possible to verify the larger scattering of the fatigue results obtained with both welded and re-welded specimens. This is due to volume variations of the deposited weld metal, the higher heating/cooling rate and the uneven stress concentration values at the weld toe notch. Fig. 5 also shows that the fatigue strength reduction due to welding process tends to be more pronounced when the number of cycles is also reduced (divergence between BM and OR fatigue curves in SFL). This observation is very important taking into account the efforts due to landing operations (typical for SFL regime) along the operational life of the aircraft. On the other hand, it is observed that the divergence between both endurance limits (10^7 cycles) was low, i.e.: from 37% σ_y for base-material to 32% σ_y after welding (close to σ_n). In the same way, this is a very important result, taking into account the abrupt maneuvers or wind bursts during flight (typical for LFL regime). This implicates that special cares should be adopted during design and, particularly, maintenance of welded aeronautical structures against any accidental tool marks capable to introduce local stress concentration on the structure. Since for bending loads the maximum stress occurs at the surface, the fatigue resistance is sensitive to any geometric change of material (notch-sensitivity).

From Fig. 5, comparing the first (1R) and second weld repairs (2R) fatigue curves in the SFL ($<10^5$ cycles) regime, one can observe that the reduction was minimum, with both curves converging to a same point in high stress levels (SFL). On the other hand, one can also observe high divergence between the aforementioned curves in LFL regime, reaching a maximum at the endurance limit level (10^7 cycles). Since the material is notch-sensitive in LFL, such a behavior was due to the abrupt geometric change generated by the weld bead in addition to the microstructural alterations induced by the new cooling rate. On the other hand, comparatively to the fatigue behavior of base-material (BM), as in SFL as LFL (endurance limit) regimes the tendency of the second weld repair (2R) fatigue curve shows practically the same fatigue-notch sensitivity [$q = (K_f - 1)/(K_t - 1)$], or fatigue-notch factor, K_f (Eq. (1) [32]). This observation becomes evident considering the parallelism presented by both base-material (BM) and two weld repairs (2R) fatigue curves. In fact, the fatigue-notch factor values (K_f) in 10^7 , 10^6 and 2.8×10^5 cycles were: 2.00, 2.15 and 2.07, respectively, which confirms the mentioned parallelism. Since the welding repair procedure applied was by removing the previous weld bead, the geometric alteration was hoped to be low (as can be seen in Table 5 ahead). Thus, the increase of the notch sensitivity (fatigue-notch factor) with the second weld repair (2R) was also due to the microstructural variations resulting of successive heating/cooling cycles imposed to the material. Therefore, based on the results obtained and considering that the welding repair is necessary, it can be admitted only one weld repair (1R) during fabrication of the critical to the flight-safety structures, without compromising their reverse bending fatigue strength. On the other hand, being necessary to make some subsequent repair along the operational life, this study indicates that cares should be adopted in the sense of avoiding abrupt maneuvers and/or overloads on the aircraft. In

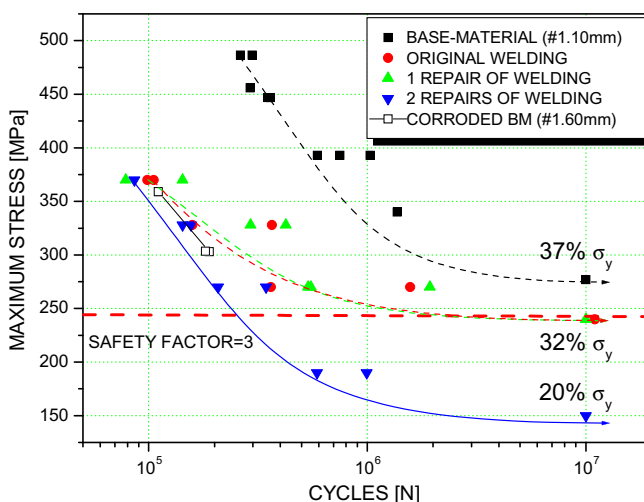


Fig. 5. Reverse bending fatigue SN curves for base-material and (re-)welded specimens (1.10 mm thick).

Table 5

Geometry factor values from the weld bead (in accordance with Fig. 6).

Group	W (mm)	T (mm)	Root (mm)	Angle (α)	Radius (mm)	HAZ (mm)	K_f (Eq. (1))
OR	3.75 ± 0.35	0.89 ± 0.20	0.77 ± 0.19	$141.9^\circ \pm 14.4^\circ$	1.03 ± 0.36	2.89 ± 0.25	1.290
1R	4.49 ± 0.33	1.17 ± 0.32	0.82 ± 0.27	$146.1^\circ \pm 8.6^\circ$	0.75 ± 0.21	3.11 ± 0.12	1.305
2R	4.80 ± 0.23	0.96 ± 0.20	0.79 ± 0.30	$138.6^\circ \pm 7.5^\circ$	0.93 ± 0.40	3.22 ± 0.23	2.178

$$K_f = 1 + \frac{K_t - 1}{1+a/r}$$

where: $a = 0.1659$ (Peterson's material parameter for steel); r = notch-root; K_f = fatigue-notch factor.

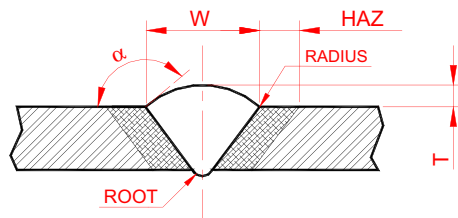


Fig. 6. Geometry factors of the welded joints (values presented in Table 5).

addition, it becomes necessary lower inspection intervals for flaws as-crack determination at the weld joints of structural components.

Finally, although it is not appropriate to directly compare both fatigue behaviors of welded specimens with those corroded due to their different thickness, it is interesting to observe the similar deleterious effect caused by the corrosive process on the fatigue strength of AISI 4130 steel.

Table 4 presents the microhardness values measured in the three interest areas. Firstly, one can observe the high microhardness values for weld metal and CGHAZ as a consequence of TIG welding and re-welding process. This is due to high cooling speed associate to the low heat-input applied, which resulted in martensitic structures. Since the heat input was kept constant for all the (re-)welding process, it is important to mention that just the weld reinforcement was removed. Consequently, the different microhardness values verified were due to remaining weld material volumes (e.g. weld root), which unevenly affected the cooling speed of the weld metal. Thus, from Table 4, one can observe that for both the original weld (OR) and the first welding repair (1R) the microhardness values were close and coherent with each other. This can explains the bending fatigue behavior presented in Fig. 5. However, it is also important to pay attention to the great dispersion of microhardness results in both CGHAZ and weld metal (standard-deviation). It is also possible to observe the highest microhardness value from the original weld metal than for all the other conditions. This implicate that probably the second welding repair promoted the tempering of the previous microstructure, but with no improvement on their bending fatigue strength, as verified in Fig. 5. After the second welding repair it is also possible to observe higher microhardness value for the CGHAZ, implicating a grain size reduction in that region, but again with no improvement on the bending fatigue strength, as illustrate in Fig. 5. It is well known that the lower the grain size the higher the material toughness. In the same way, the higher the grain size, the lower the hardness/mechanical strength.

Considering that the weld profile affects the fatigue resistance of a welded structure, Table 5 and Fig. 6 present the main geometric factors that compose a weld joint and their corresponding values, obtained by image analysis tools. Thus, from Table 5 and Fig. 6, it is possible to confirm all the results presented in Fig. 5 on the effect of welding repairs on the bending fatigue behavior of AISI 4130 steel. Therefore, it can be observed that the welding repairs reduced both angle (α) and radius at the weld toe notch that, com-

bined, are considered the main geometric factors controlling the fatigue behavior of welded components and structures [13,31]. In addition, the great scattering on the geometric factors measured is in consonance with the great scattering of the fatigue results presented by the welded specimen groups. Yet, from Table 5, we can observe: the increase of the stress concentration factor (K_f) at the weld toe notch with the successive welding repairs; the largest extension of HAZ due to the successive heat-input applied and, consequently, the increase of the CGHAZ as well; the effect of both weld reinforcement (T) and weld root dimensions, again, on the angle (α) and radius reduction and, consequently, on the bending fatigue strength of welded specimens. On this subject, it is important

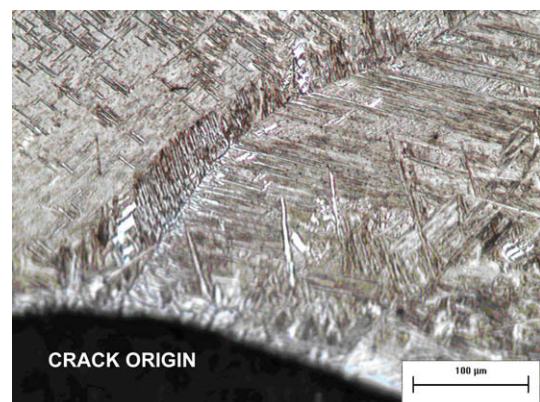


Fig. 7. Crack initiation at the weld toe of a non-fractured fatigue specimen (500×). Nital 2%.

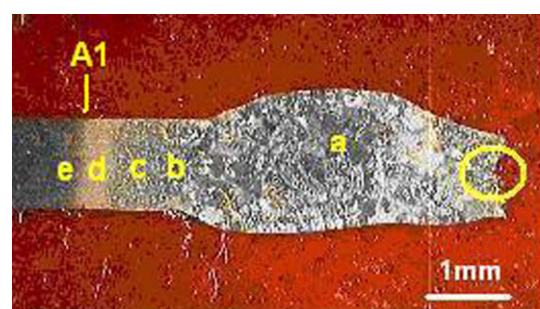


Fig. 8. Macrography of a fatigue specimen fractured by reverse bending loads. Nital 2%.



Fig. 9. Secondary crack propagation from the fracture surface of a reverse bending fatigue specimen (500×). Nital 2%.

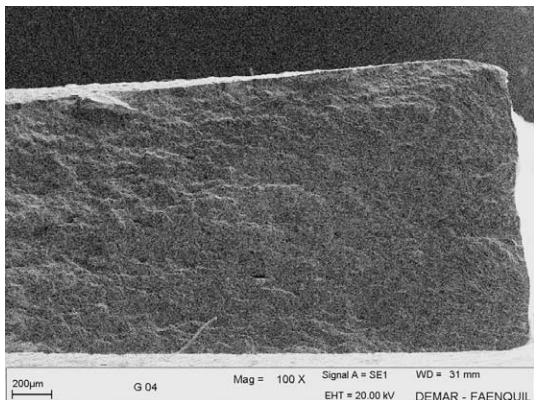


Fig. 10. Edge fatigue crack origin and propagation for a fractured specimen of base-material, 1.60 mm thick.

to mention that all the welded specimens fractured at the weld toe notch, as illustrated in Figs. 7 and 8. In fact, Fig. 7 illustrates a crack in a non-fractured specimen, which initiated at the weld toe notch and propagated through grain boundary into weld metal (intergranular crack).

Fig. 8 presents the macrography of a fractured specimen that was submitted to two welding repairs (2R), in which we can observe: (a) the weld metal region with well delineated equiaxial coarse-grains; the HAZ extension with the sub-regions, (b) coarse-grain/CGHAZ, (c) fine-grain/FGHAZ, (d) inter-critical/ICHAZ and (e) sub-critical/SCHAZ near to A_1 line (lower critical tempera-

ture); as well as the welded joint irregularity as a consequence of the deformation generated by the reverse bending loads applied.

Fig. 9 presents the transgranular secondary crack, originate from the fracture surface of the specimen in Fig. 8. This secondary crack implicates that the reverse bending fatigue specimens may have been subjected to either Modes I and II or Modes I and III of loading combination (or all of them), turning the laboratorial test more severe due to friction process by both free crack surfaces, accelerating its propagation. In fact, bending loads also introduce shear stresses in the specimens (Mode II of fracture) and/or tearing stress (Mode III of fracture) whether crack initiation occurs at the edge of the specimen, as illustrated in Fig. 10. On this subject, Veidt [33] mentions that the radius in the notch root has little effect on the stress intensity factor in Mode II of fracture.

Figs. 11 and 12 present the base-material, HAZ and weld metal microstructures for all the proposed conditions. Fig. 11a shows the normal products of transformation from austenite, i.e. ferrite and perlite. From Fig. 11b-d the beginning of the transformation from perlite to austenite is observed (to martensite, upon subsequent cooling) along the SCHAZ/ICHAZ regions (A_1 line).

Fig. 12 presents the microconstituent of the weld metal (original, one and two weld repairs) and respectives CGHAZ, basically constituted by martensite, which is a very hard and fragile microstructure. As aforementioned, the higher the hardness the higher the resistance to fatigue crack initiation.

Fig. 13 presents the residual stresses field in the weld metal, HAZ and base-material of all the conditions analyzed. It is well known that residual stresses are present in welded components [22,34–36] and have great effect on fatigue crack nucleation and propagation [34]. Thus, from Fig. 13, one can observe that the

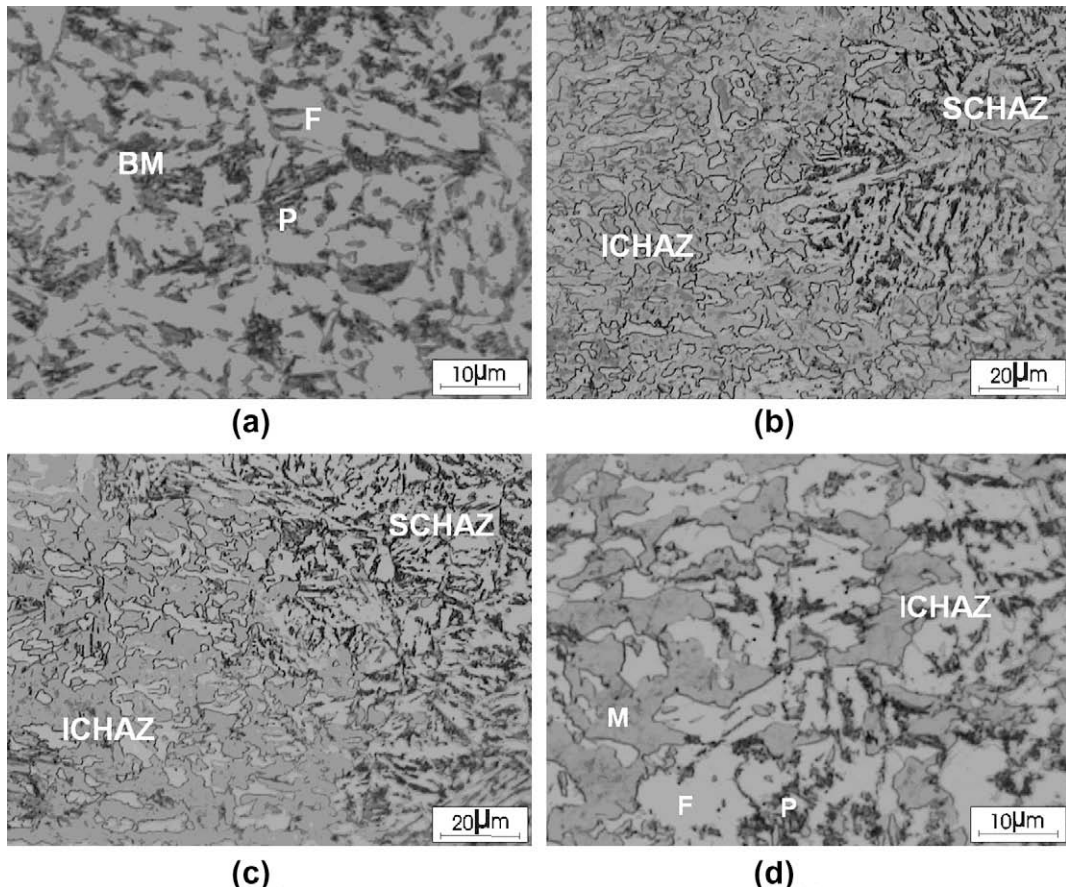


Fig. 11. Base-material and base-material/HAZ transition microstructures: (a) Base-material (typical); (b) SCHAZ-ICHAZ of the original weld; (c) SCHAZ-ICHAZ of the first welding repair; and (d) ICHAZ of the second welding repair. Nital 2%. (F = Ferrite; P = Perlite; M = Martensite).

TIG (re-)welding process induced high compressive residual stresses for all conditions upon analysis, as weld metal as in HAZ and base-material (up to 20 mm from the fusion line). Such residual stresses were relieved internally in some point along the length of the specimens, because no deformation was verified on the samples. Yet, it is observed that all the residual stress profiles presented similar tendency, i.e., maximum values in weld metal (-600 MPa for original weld; -450 MPa for one weld repair and -330 MPa for two weld repairs), followed by HAZ (-400 MPa for original weld; -75 MPa for one weld repair and -50 MPa for two weld repairs) and last base-material up to 20 mm far-away from the fusion line (-300 MPa for original welding; -160 MPa for one weld repair and -100 MPa for two weld repairs).

Many factors might have contributed to compressive residual stresses induced by the TIG (re-) welding process, viz: (i) austenite-martensite transformation (which generate up to 4% increase in volume of material) and which initiate at the surface due to higher cooling speed; (ii) the thin thickness and good mechanical properties in high temperature of the base-material, particularly low deformation in high temperature; (iii) subsequent contraction in the core of the weld metal (after the martensitic transformation at the surface) due to relatively lower cooling speed in that region; (iv) constraint to natural expansion of the weld metal and HAZ by the base-material volume around; and (v) the clamps applied at the extremities of the specimens during the (re-)welding process, etc. However, some aspects get the attention from the Fig. 13 as:

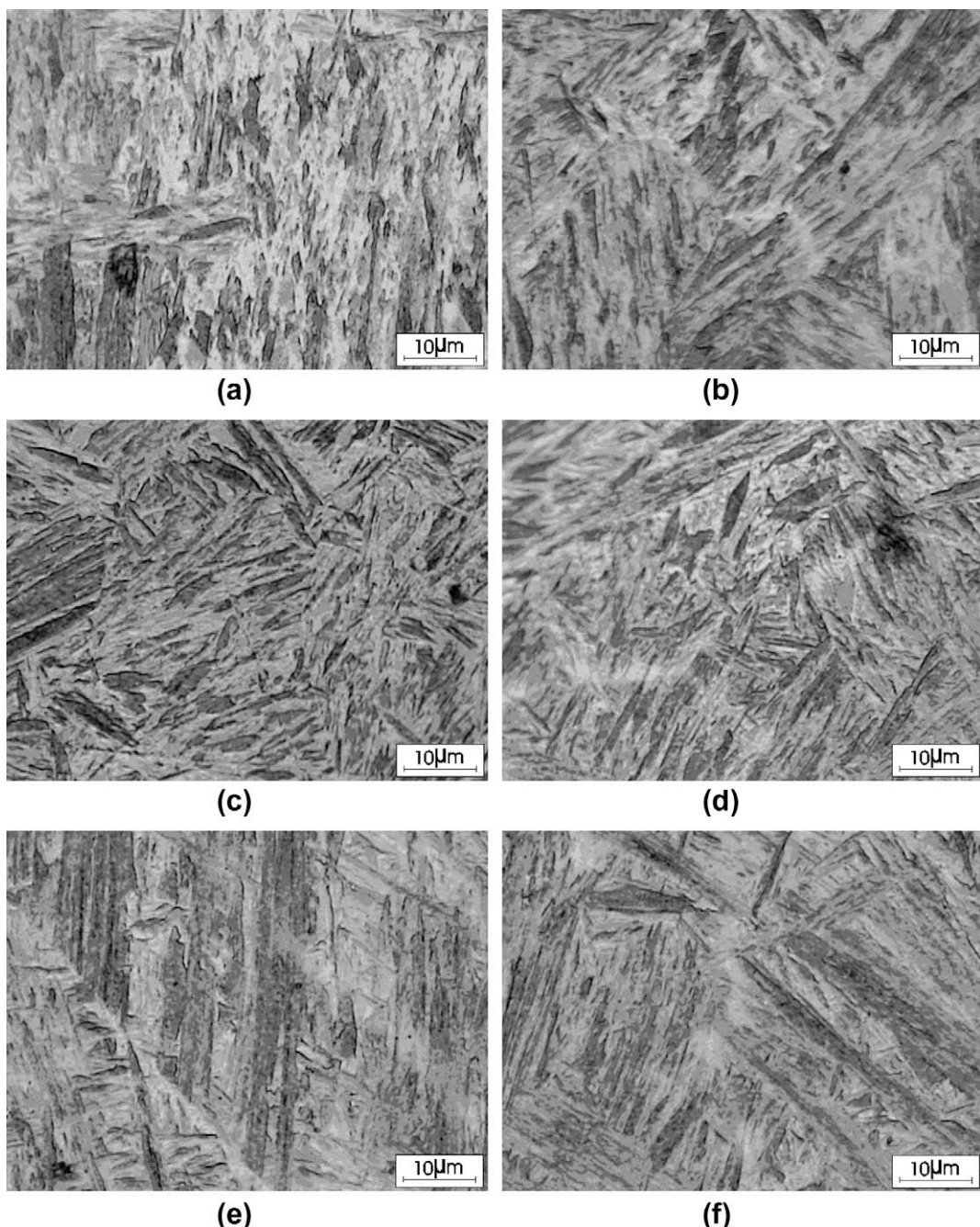


Fig. 12. Microscopic analysis of the weld metal and CGHAZ: (a) original CGHAZ; (b) original weld metal; (c) CGHAZ of the first welding repair; (d) weld metal of the first welding repair; (e) CGHAZ of the second welding repair; and (f) weld metal of the second welding repair. Nital 2%.

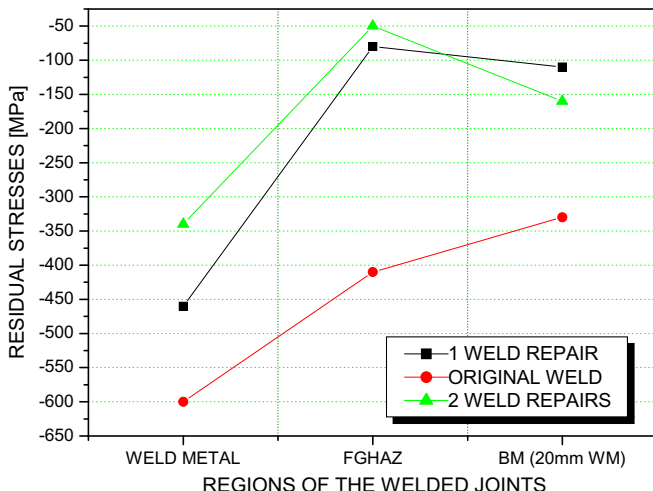


Fig. 13. Residual stress profiles of all the conditions tested.

the high values of compressive residual stresses, which were higher in the weld metal than HAZ; all the compressive stress fields were still compressive up to 20 mm distance from weld fusion line.

It is well known that the residual stresses largely affect the fatigue behavior of components, and that compressive residual stresses are benefit towards inhibit the crack nucleation. Thus, the results presented in Fig. 13 are in accordance with the fatigue behavior of specimens with original weld (OR), as well as those with one (1R) and two (2R) weld repairs presented in Fig. 5. In addition: the higher the hardness, the higher the fatigue strength as well. Consequently, from Table 4 and Fig. 5, it could be observed better fatigue behavior for the originally welded (OR) specimens in comparison with the one (1R) weld repair condition. However, considering the fatigue crack propagation stage, it is well known that the increase of the hardness increases the propagation rate (da/dN). In this context, the existence of compressive residual stresses highlight the stress concentration effect induced by the weld geometry on the fatigue strength reduction verified. That is, although a mechanical component possess high compressive residual stresses, their effects or benefits will be minimized (or annulled in case the stress relief) when this component presents a stress concentrator (geometric factor) that reduces the number of cycles necessary to fatigue crack initiation. Thus, it is possible that the geometric stress concentration factor, which is located at the weld toe/fusion line/CGHAZ region, overcomes the compressive residual stress field induced by the (re-)welding process, relief it. Certainly, the compressive residual stresses field as far as possible delayed the fatigue crack nucleation and propagation by reducing the stress intensity factor (ΔK), as mentioned by Wei & Chen [34].

4. Conclusions

Motivated by high fracture incidence at welded joints of a specific and critical to the flight-safety component, called "motor-craddle", experimental reverse bending fatigue tests on welded and re-welded specimens were carried out. Based on the results obtained, the following conclusions may be drawn:

1. The AISI 4130 steel possess good mechanical properties, but low elongation in the "as-received" condition (not heat-treated).
2. All the monotonic specimens tested, including those grinding machined, fractured at the sub-critical HAZ (SCHAZ)/base-material interface (strength-overmatch), despite any stress concentration originated at the weld toe.

3. The reverse bending loads significantly decrease the fatigue strength of the AISI 4130 steel, whose endurance limit were about 37% and 40% of the yielding stress (σ_y) for specimens 1.60 mm and 1.10 mm thick, respectively.
4. The corrosive process strongly reduced the reverse bending fatigue strength of AISI 4130 steel.
5. In comparison with specimens from the base-material a reduction in bending fatigue strength for TIG welded specimens (OR) was observed. After the first weld repair (1R), no-subsequent reduction in bending fatigue strength was observed in comparison with the original weld. The second weld repair (2R) again resulted in decreasing of the fatigue strength in comparison with that subjected to the first weld repair. Consequently, it is not recommended or favorable to the flight-safety the second weld repair (2R) on critical to the flight-safety components.
6. The TIG (re-)welding procedure induced high compressive residual stress values in the AISI 4130 steel.
7. It was verified increase of the stress concentration factor, K_t , at the weld toe with the successive welding repairs, which overcomes the compressive residual stress field induced by the (re-)welding process. As a result, all the welded fatigue specimens fractured at that region.

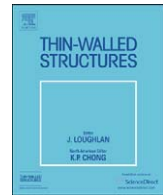
Acknowledgement

The authors are grateful to FAPESP/Process No. 99/11948-6, CNPq and FUNDUNESP.

References

- [1] Flight Safety Foundation – Available from <<http://www.flightsafety.org>>; 2009 [accessed 10.2009].
- [2] National Civil Aviation Agency – Brazil. Available from <<http://www.anac.gov.br>>; 2004 [accessed 10.2003].
- [3] Godefroid LB. Fatigue crack growth under constant and variable amplitude loading in aluminium alloys of aeronautical applications. Ph.D. Thesis, COPPE/UFRJ, Brazil: Federal University of Rio de Janeiro; 1993.
- [4] Goranson UG. Fatigue issues in aircraft maintenance and repairs. Int J Fatigue 1993;19:S3–S21.
- [5] Payne AO. The fatigue of aircraft structures. Eng Fract Mech 1976;8:157–203.
- [6] Wenner CA, Drury CG. Analysing human error in aircraft ground damage incidents. Int J Ind Ergonom 2000;26:177–99.
- [7] Latorella KA, Prabhu PV. A review of human error in aviation maintenance and inspection. Int J Ind Ergonom 2000;26:133–61.
- [8] Bhaumik SK, Sujata M, Venkataswamy MA. Fatigue failure of aircraft components. Eng Fail Anal 2008;15:675–94.
- [9] Carpenter M. Managing the fleet: materials degradation and its effect on aging aircraft. Amptiac, News Lett 2001;4(5):7–19.
- [10] DOT/FAA/AR-00/22. US Department of Transportation, Federal Aviation Administration, Corrosion and Corrosion Fatigue of Airframe Materials, final report, July 2002. 2002, 79p.
- [11] Wang QY, Kawagoishi N, Chen Q. Effect of pitting corrosion on very high cycle fatigue behavior. Scripta Mater 2003;49:711–6.
- [12] Murtaza G, Akid R. Corrosion fatigue short crack growth behaviour in a high strength steel. Int J Fatigue 1996;18:557–66.
- [13] Nascimento MP. Effects of TIG welding repair on the structural integrity of AISI 4130 aeronautical steel. In: Ph.D. Thesis in mechanical engineering. State University of São Paulo/UNESP-FEG, Brazil (in Portuguese); Code CDU 620.92, 2004. 240p.
- [14] Nascimento MP, Voorwald HJC. An evaluation on the fatigue crack growth in re-welded AISI 4130 aeronautical steel. In: Eighth international fatigue congress/FATIGUE 2002, vol. 5, Stockholm-Sweden; 2002. p. 3463–72.
- [15] Nascimento MP, Ribeiro RB, Voorwald HJC. Fatigue crack growth in re-welded AISI 4130 high strength steel. In: Fourteenth European congress on fatigue/ECF 14, vol. 2, Cracow, Poland; 2002. p. 1–3116.
- [16] Vern Sutter, Robert J. Dybas, repair welding. In: ASM International, American Society for Metals, Editors, Metals Handbook, Welding, Brazing and Soldering, vol. 6, Metals Park, Ohio; 2002. p. 1103–7.
- [17] Kroes MJ, Watkins WA, Delp F. Aircraft maintenance and repair. 6th ed. New York: Glencoe – Macmillan/McGraw-Hill; 1993. 648p.
- [18] Vega EO, Hallen JM, Villagomez A, Contreras A. Effect of multiple repairs in girth welds of pipelines on the mechanical properties. Mater Charact 2008;59:1498–507.
- [19] Liming L, Xin Du, Meili Z, Guoqing C. Research on the microstructure and properties of weld repairs in TA15 titanium alloy. Mater Sci Eng A 2007;445–446:691–6.

- [20] Shankar K, Weidong Wu. Effect of welding and weld repair on crack propagation behaviour in aluminium alloy 5083 plates. Mater Des 2002;23:201–8.
- [21] Sun W, Hyde TH, Becker AA, Williams JA. Some key effects on the failure assessment of weld repairs in CrMoV pipelines using continuum damage modeling. Eng Fail Anal 2005;12:839–50.
- [22] Dong P, Hong JK, Bouchard PJ. Analysis of residual stresses at weld repairs. Int J Pres Ves Pip 2005;82:258–69.
- [23] Hyde TH, Sun W, Becker AA, Williams JA. Life prediction of repaired welds in a pressurised CrMoV pipe with incorporation of initial damage. Int J Pres Ves Pip 2004;81:1–12.
- [24] Aloraijer AS, Ibrahim RN, Ghojet J. Eliminating post-weld heat treatment in repair welding by temper bead technique: role bead sequence in metallurgical changes. J Mater Process Technol 2004;153–154:392–400.
- [25] Doc IIS/IIW-956-87. (ex. doc. XV-648-87) prepared by commission XV “fundamentals of design and fabrication for welding” of the IIW, recommendations for repairs and/or strengthening of steel structures. Welding in the world 1988; 26(11/12): 292–306.
- [26] Ivanov SA, Monim VI, Teodósio JR. New method of X-ray tensometry. In: International conference on experimental mechanics. Lisboa; 1994. p. 757–61.
- [27] Bannister AC, Ocejo JR, Gutierrez-Solana F. Implications of the yield stress/tensile stress ratio to the SINTAP failure assessment diagrams for homogeneous materials. Eng Fract Mech 2000;67:547–62.
- [28] Murakami Y. Inclusion rating by statistics of extreme values and its application to fatigue strength prediction and quality control of materials. J Res Nat Inst Stand Technol 1994;4:99–107.
- [29] Murakami Y, Usuki H. Quantitative evaluation of effects of non-metallic inclusions on fatigue strength of high strength steels. II: fatigue limit evaluation based on statistics for extreme values of inclusion size. Int J Fatigue 1989;5(11):299–307.
- [30] Makkonen M. Statistical size effect in the fatigue limit of steel. Int J Fatigue 2001;23:395–402.
- [31] Lancaster JF. Metallurgy of welding. 5th ed. London: Chapman and Hall Incorporation; 1993. 389p.
- [32] Peterson RE. Stress Concentration design factors. 5th ed. New York: John Wiley and Sons Incorporation; 1966 [155p].
- [33] Veidt M. On the Effect of notch radius and local friction on the Mode I and Mode II fracture toughness of a high-strength steel. Eng Fract Mech 1997;58:223–31.
- [34] Wei MY, Chen C. Fatigue crack growth characteristics of laser-hardened 4130 steel. Scripta Metall Mater 1994;10(31):1393–8.
- [35] Brown TB, Dauda TA, Truman CE, Smith DJ, Memhard D, Pfeiffer W. Predictions and measurements of residual stress in repair welds in plates. Int J Pres Ves Pip 2006;83:809–18.
- [36] Chiarelli M, Lanciotti A, Sacchi M. Fatigue resistance of MAG welded steel elements. Int J Fatigue 1999;1:1099–110.



Experimental study on repair of fatigue cracks at welded web gusset joint using CFRP strips

Hitoshi Nakamura^{a,*}, Wei Jiang^a, Hiroyuki Suzuki^b, Ken-ichi Maeda^a, Takao Irube^c

^a Department of Civil and Environmental Engineering, Tokyo Metropolitan University, Japan

^b Department of Architecture, Meisei University, Japan

^c TTK Corporation, Japan

ARTICLE INFO

Available online 9 January 2009

Keywords:

Carbon fiber reinforced polymer strip
Lamination
Repair
Fatigue crack
Welded joint
Drill-hole

ABSTRACT

This paper presents repair methods of fatigue cracks using CFRP strips. In particular, the subject of repair is fatigue cracks initiated at **welded web gusset joints**, which are the typical details in steel bridges. Several repair methods were investigated experimentally focusing on weld details. In addition, more effective repair methods were also investigated using combination of CFRP strips and drill-holes. As a result, it was found that **fatigue life after repair was significantly improved**. Therefore, the authors confirmed the feasibility of the proposed technique as a useful repair method to improve fatigue life of steel structures.

© 2008 Elsevier Ltd. All rights reserved.

1. Introduction

In recent years, reports of fatigue damage to steel bridges have increased in Japan with the increase of vehicle load and volume of traffic [1]. Since fatigue cracks are often initiating in narrow locations, where some members are crossing each other and have complicated details peculiar to welded joints, it is difficult to repair and reinforce them. CFRP is expected to be a useful material for repairing and reinforcement of existing steel structures [2–4], because of its lightweight, high strength and excellent corrosion resistance. In addition, the joint method for CFRP strips is very simple and is also easy to apply on site. Recently, in order to utilize CFRP effectively, many researches have been done on welded connections and fatigue strengthening [5–9].

The fundamental studies have been performed experimentally and analytically using steel flat plates [10,11], and the validity of crack repair has been verified. Aiming at application to real structures, the examination was started in consideration of the welded detail [12,13]. The subject of repair is fatigue cracks initiated at welded web gusset joints, which are the typical details in steel bridges. Therefore, the authors have proposed the practical construction method using CFRP strips to repair fatigue cracks at welded web gusset joints.

This study examined a more suitable repair method, using specimens with out-of-plane welded gusset joints, and fatigue

tests were carried out with various bonding methods of CFRP strips and varying the number of laminations. The effects of repair and the progress of fatigue cracks after repair were also considered. Moreover, in order to increase the effectiveness of the repair, CFRP strips were used in combination with drill-holes. A drill-hole is a construction method, also called a stop-hole and is generally applied as a temporary repair method on site. Drill-holes are applied to reduce the stress concentration at the tips of cracks. Several combinations of CFRP strips and drill-holes were investigated by static loading tests and fatigue tests.

2. Experimental procedure

2.1. Specimens and material properties

The specimen is shown in Fig. 1. It was fabricated with gusset plates ($W100 \times T9 \times L140 \text{ mm}^3$) welded to both sides at the center of the steel plate ($W250 \times T9 \times L1040 \text{ mm}$). The mechanical properties of steel, the CFRP strip, and epoxy resin adhesive are shown in Table 1. The CFRP strip is 1.2 mm in thickness. The carbon fiber is arranged unidirectionally.

In addition, in order to investigate the effects of the bonding methods and the laminations on the bond strength, the tensile shear tests were conducted using double-lap adhesive joints. The specimen is shown in Fig. 2. Its width and thickness are 100 and 9 mm, respectively. It was cut off at the dashed line as shown in Fig. 1(a). The fatigue crack was initiated at the weld toe of the web gusset plate.

* Corresponding author.

E-mail address: hnaka@tmu.ac.jp (H. Nakamura).

Nomenclature

K	initial rigidity in linear relation of load–displacement curve
ΔP	incremental applied load
ΔD	incremental displacement
$\Delta\sigma_n$	nominal stress range of steel plate

σ	longitudinal stress
a	crack length
D	crack opening displacement
N_f	number of cycles from start of fatigue test to failure
N_i	number of cycles from start of fatigue test until the crack length reached 15 or 50 mm
N_p	number of cycles from restart after repair to failure

2.2. Repair method

Two series of repair methods using CFRP strips are shown in Fig. 3. The cracked specimens were repaired when the crack progressed to a length of approximately 15 mm (it is equivalent to 12% of the overall width) from the center of the specimen to both side edges by cyclic loading test. The repair methods are described as follows.

2.2.1. Series S

In series S as shown in Fig. 3(a), four single-layered CFRP strips ($W25 \times T1.2 \times L100$ mm) were simply bonded to both sides of the weld bead in order to reduce the stress concentration at crack tips.

2.2.2. Series M

First of all, in order to improve the bonding surface, the weld bead was finished using a pencil grinder. The multi-layered CFRP strips ($W50 \times T1.2 \times L200$ mm) with a rectangular slit in the center were bonded close to the weld bead. The single-layered CFRP strip ($W25 \times T1.2 \times L100$ mm) was bonded on both sides. In series M as shown in Fig. 3(b), the number of laminations was considered. The effective repair is expected by the reduction in the crack opening displacement, since the crack opening is perfectly covered with multi-layered CFRP strips. Fig. 4 shows an example of repair method in series M5 with five layers.

The used adhesive hardens at ordinary temperature, and reaches the required bond strength in a day. The specimens were cured at 40 °C for a week after repair, because of elimination of dispersion caused by the curing condition of the adhesive.

3. Adhesion performance of double-lap joints considering gusset details

3.1. Experimental series and testing procedure

The experimental series is shown in Table 2. As mentioned above, the repair was performed by the two repair methods as

shown in Fig. 5. In series DL-M, the number of laminations was 1, 3, 5 or 7 layers. In series DL-S, the CFRP strip was single-layered, and its length was changed as 100 and 200 mm. The bonding surface was sandblasted. The shear tensile tests were conducted using the universal testing machine with a capacity of 1000 kN. The loading speed is 5 mm/min by displacement control. As shown in Fig. 5 and Photograph 1, strains on CFRP strips and opening displacements at joints were measured using strain gages and crip-type displacement transducers.

3.2. Static loading test results

The relationships between the tensile load P and the opening displacement D at the joint is shown in Fig. 6. All the series show nonlinear behavior from the low level of tensile load. In DL-M5 and DL-M7, the tensile load decreased locally at approximately 200 kN because of the yielding in the narrow section of the grip.

In order to compare the rigidity of the adhesion joint, the initial rigidity K is calculated in the linear relation of the P - D curve shown in Fig. 6. The initial rigidity K is defined by the following equation:

$$K = \frac{\Delta P}{\Delta D} \quad (1)$$

where ΔP and ΔD are the incremental tensile load and the incremental displacement in the range from 20 to 40 kN. Fig. 7 shows the maximum tensile load P_{max} and the initial rigidity K of all the series. In series DL-S, maximum tensile load increases a little, so that the length of CFRP strips is long. In series DL-M, the

Table 1
Mechanical properties of steel, CFRP strip and epoxy resin adhesive.

	Steel plate (JIS SM400A)	CFRP strip	Epoxy resin adhesive
Yield point (MPa)	293	–	–
Tensile strength (MPa)	453	2664	30
Elongation (%)	23	1.9	–
Elastic modulus (GPa)	204.5	188	1.5

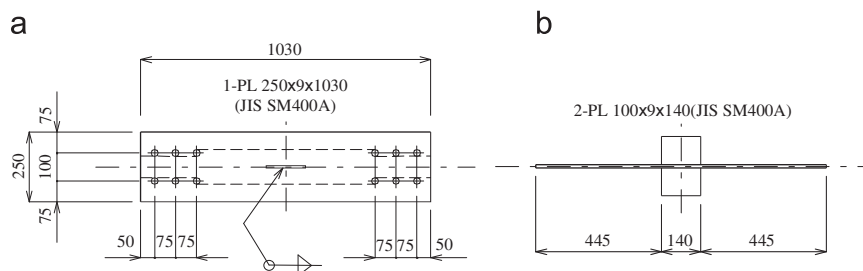


Fig. 1. Specimen configuration for fatigue test: (a) plan and (b) elevation.

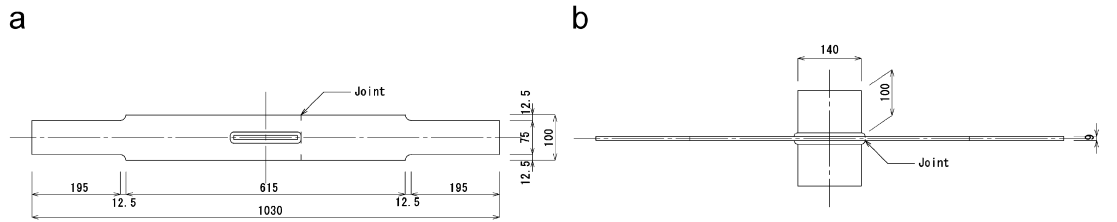


Fig. 2. Specimen configuration for double-lap adhesive joints: (a) plan and (b) elevation.

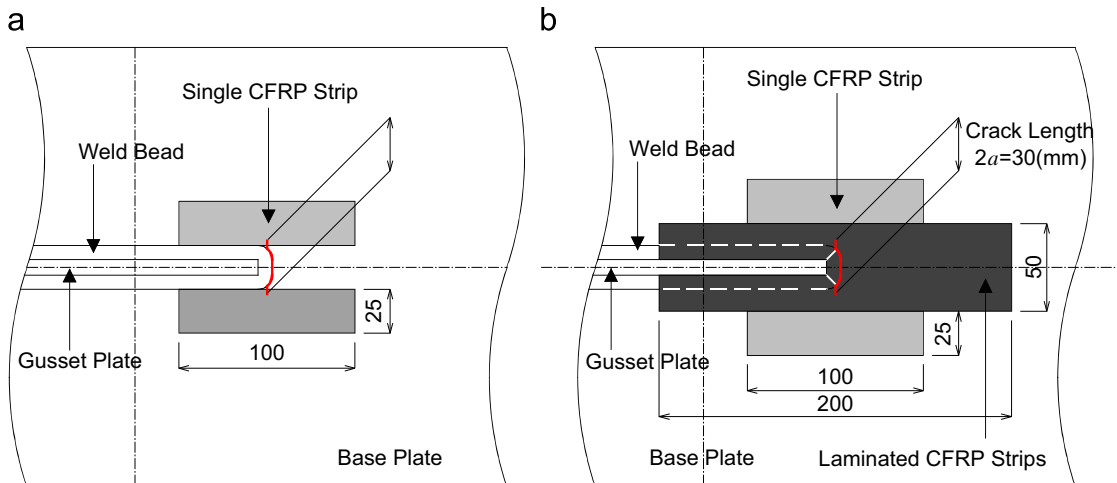


Fig. 3. Repair method: (a) series S and (b) series M.

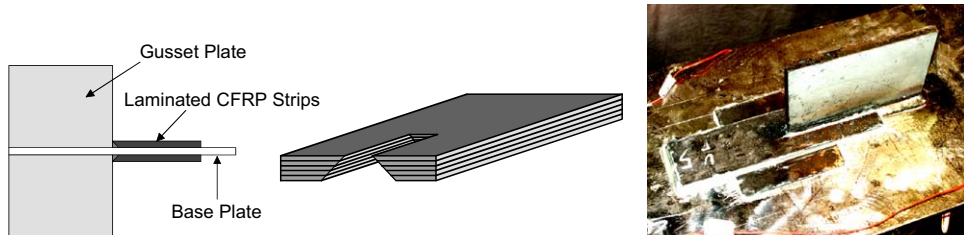
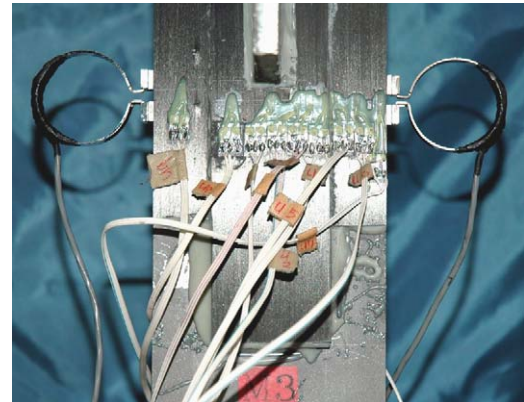


Fig. 4. Example of repair method in series M5.

Table 2
Experimental series of double-lap adhesive joints.

Series	Repair method	CFRP strip	
		Single-layered part (mm)	Multi-layered part
DL-S1	Fig. 5(a)	100	–
DL-S2	Fig. 5(a)	200	–
DL-M1	Fig. 5(b)	100	1-layer at 200 mm
DL-M3	Fig. 5(b)	100	3-layer at 200 mm
DL-M5	Fig. 5(b)	100	5-layer at 200 mm
DL-M7	Fig. 5(b)	100	7-layer at 200 mm

maximum tensile load is higher compared with series DL-S, and increasing the number of laminations. Although the initial rigidity K is equivalent in spite of the length of CFRP strips in series DL-S, it



Photograph 1. Test setup of series DL-M3.

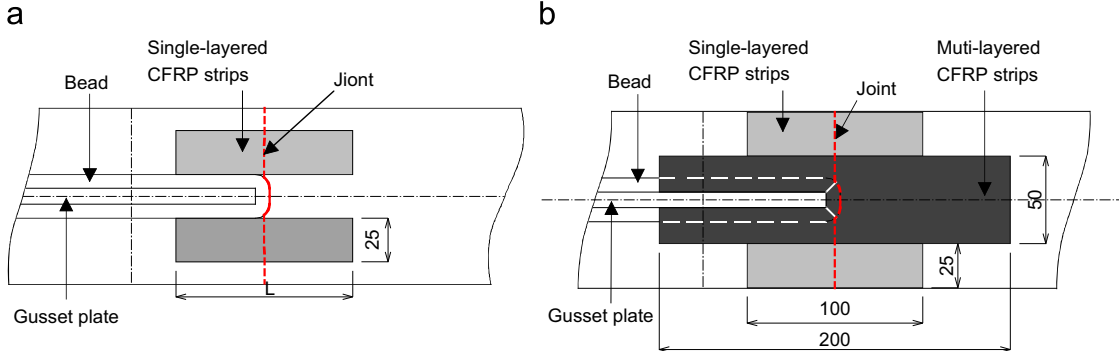


Fig. 5. Repair method for double-lap adhesive joints: (a) series DL-S and (b) series DL-M.

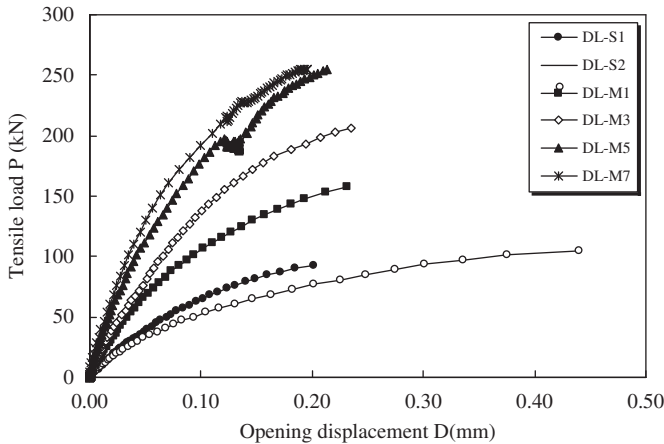


Fig. 6. Relationships between tensile load and opening displacements at joint.

is increased with increasing the number of laminations in series DL-M. Since the opening displacement becomes small increasing the initial rigidity, the effective repair can be expected in the case like a crack repair. Consequently, it can be considered that the required number of laminations is five layers regarding upper limits for the maximum tensile load and the initial rigidity.

Fig. 8 shows the relationships between the nominal stress σ_n and the tensile stresses on CFRP strips for multi-layered and single-layered parts, respectively. The nominal stress σ_n is the value of P/A , where P and A are the tensile load and the sectional area of the specimen, respectively. Tensile stresses were averaged for each of the multi-layered and single-layered parts using strain gages on CFRP strips. At the single-layered part of all the series, CFRP strips are subjected to the high tensile stresses of 750–1100 MPa in the ultimate. The stress of the single-layered part becomes small on increasing the number of laminations. It means that CFRP strips of multi-layered part are subjected to large tensile forces. On the other hand, the stress of the multi-layered part becomes lower as the number of laminations increases. From a viewpoint of the sharing force per layer, lamination of CFRP strips is not necessarily rational. However, as mentioned previously, since the lamination gives high rigidity, the effective reinforcement can also be expected in the case aiming at a crack repair.

Finally, an example of the fracture in DL-M7 is shown in Photograph 2. The brittle fracture including the delamination between CFRP strips was observed.

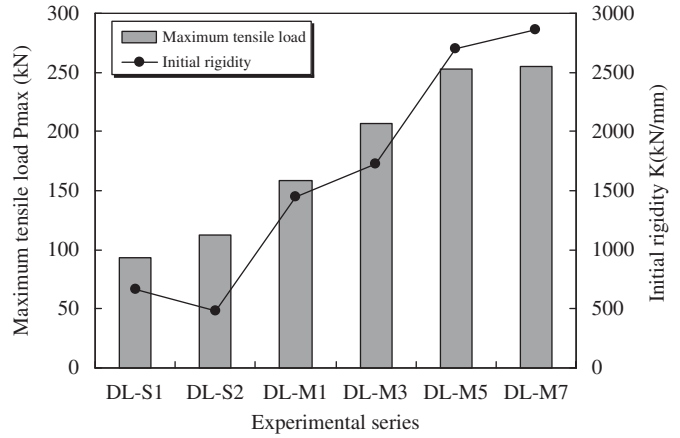


Fig. 7. Maximum tensile load and initial rigidity.



Photograph 2. An example of the fracture in series DL-M7.

4. Repair effects and fatigue durability

4.1. Testing procedure

The loading tests were conducted in order to verify repair effects. Fig. 9 and Photograph 3 show the loading system of the

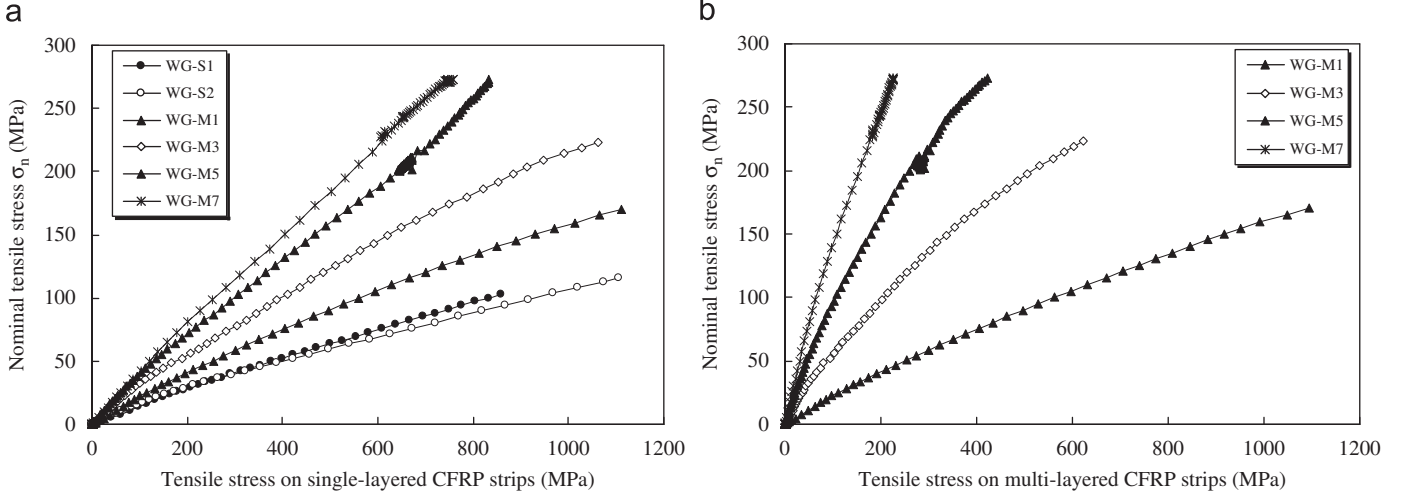


Fig. 8. Relationships between nominal stress and tensile stresses on CFRP strips: (a) on single-layered CFRP strips and (b) on multi-layered CFRP strips.



Photograph 3. Test setup of loading system.

I-shaped girder and test setup, respectively. The specimen was connected to the loading system with high-strength bolts. The load was applied by four-point bending. The uniform tensile stress was introduced into the specimen according to the uniform bending moment of the bottom flange. An electro-hydraulic servo actuator with a capacity 750 kN was used. In fatigue test, the waveform of the cyclic load was a sine wave with a frequency of 2 Hz. The minimum stress was approximately 20 MPa, and the maximum stress varied according to the nominal stress range $\Delta\sigma_n$ from 64 to 114 MPa. The experimental series is shown in Table 3. In series M, the number of laminations was 1, 3 or 5 layers.

4.2. Static loading test results

To begin with, the repair effects under the static loading are described. The cracks were initiated by fatigue test ($\Delta\sigma_n = 100$ MPa), and the simplest repair of series S was performed, when the crack length a reached 55.7 mm (it is equivalent to approximately 45% of the overall). The static loading test was carried out before and after repair. The distribution of longitudinal stress and crack opening displacement in the steel plate were investigated. They

were measured using strain gages and clip-type displacement transducers.

In addition, in order to evaluate the validity of experimental results, elasto-plastic finite displacement analysis was carried out with 3D FEA code, Msc. Marc. Fig. 10 shows the analytical model attached to the single-layered CFRP strip. Regarding symmetric boundary condition, only $\frac{1}{4}$ of the specimen was modeled. Same as in the experiment, the tensile stress of 120 MPa was uniformly applied.

As a result of experiment and analysis, the distribution of longitudinal stress and crack opening displacement are shown in Figs. 11 and 12. There is plastic zone by high stress concentration around the crack tip after repair. The longitudinal stresses reduced. The plastic zone decreased after repairing as shown in the analytical model. The crack opening displacements also reduced in general. For example, the crack opening displacement is lowered by about 40% in the center of the specimen. It can be seen that good agreement was achieved between the experimental and analytical results.

4.3. Fatigue test results

In order to evaluate fatigue life after repair, the S-N diagram was described using the number of cycles from the restart after repair to failure, N_p . In addition, N_f and N_i were defined as follows: N_f is the number of cycles from the start of fatigue test to failure, whereas N_i is the number of cycles from the start of fatigue test until the crack length reached 15 mm. The relationship between N_f , N_i and N_p can be shown as

$$N_f = N_i + N_p \quad (2)$$

N_i is considered to be significantly depending on the dispersion of initial conditions such as residual stress and weld bead shape. In this study, N_i was equivalent to 0.4–4.2 million cycles. Consequently, the difference in N_p can be purely evaluated as the effect of repair.

Fig. 13 shows the fatigue test results arranged by the fatigue life N_p after repair to failure. In all the series, the fatigue life N_p was remarkably improved compared with the non-repaired series N . In series M, the fatigue life increased as the number of laminations increased. In particular, in series M5, the fatigue life

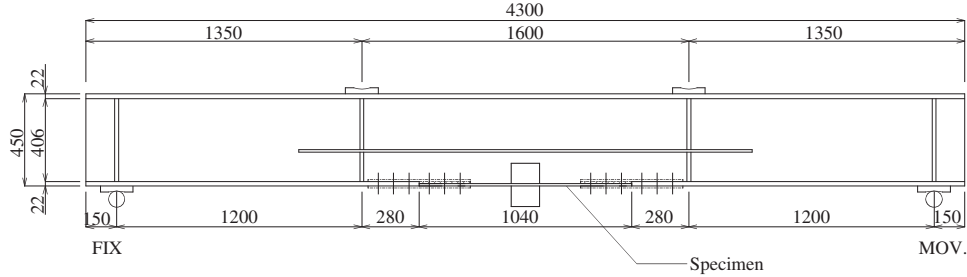


Fig. 9. Loading system.

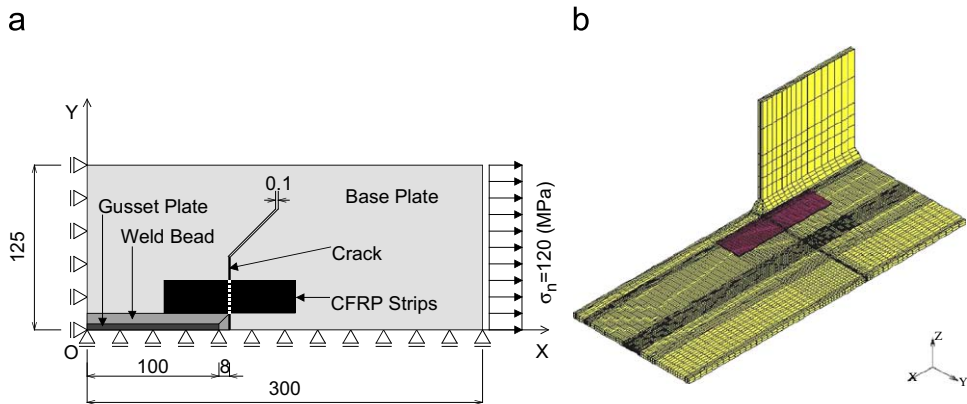


Fig. 10. Analytical model attached single-layered CFRP strip: (a) boundary conditions and (b) element division.

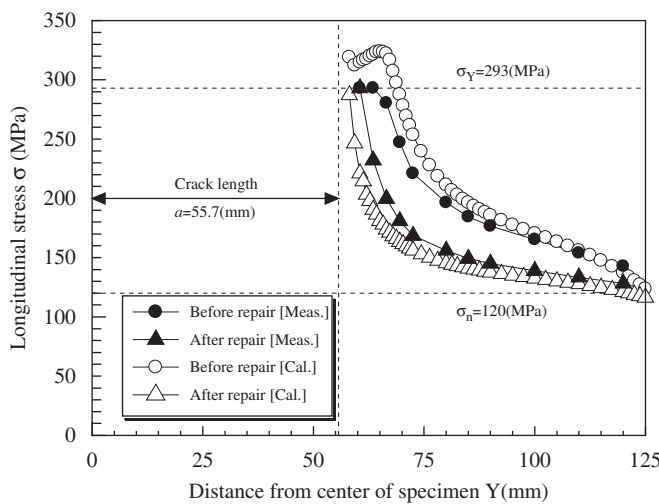


Fig. 11. Distribution of longitudinal stress.

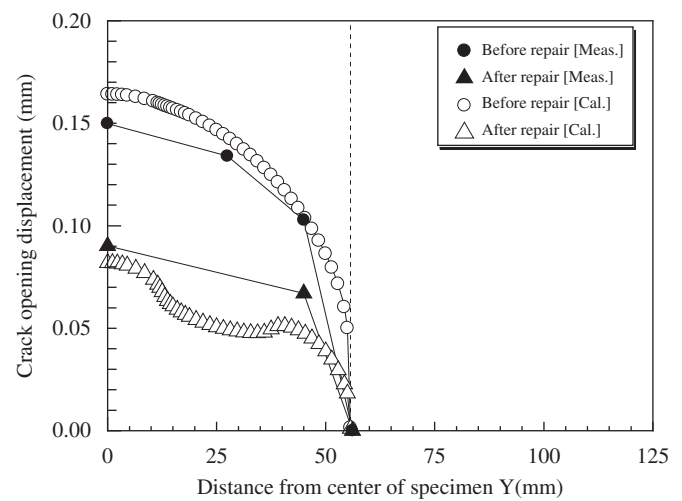


Fig. 12. Distribution of crack opening displacement.

improved remarkably in comparison with series N, indicating that a significant effect of repair was obtained. This is attributed to the fact that the crack opening was repaired by the high rigidity of multi-layered CFRP strips, and the opening displacement was sufficiently reduced. However, in this study, the fatigue limit was not obtained by series M5 within the stress range (64–114 MPa), although the fatigue life greatly exceeds 10 million cycles in the lowest stress range of 64 MPa.

Fig. 14 shows the relationship between the crack length and the number of cycles after repair in $\Delta\sigma_n = 64$ MPa. The crack lengths were measured within about 50–70 mm, using crack gages installed at the side of CFRP strips. Since crack lengths could not be measured in the bonding area of the CFRP strips, the dotted straight lines are shown in the figure. In series S and M, the fatigue life after repair is improved. The cracks progressed slowly in the bonding area of CFRP strips as shown by the dotted line in

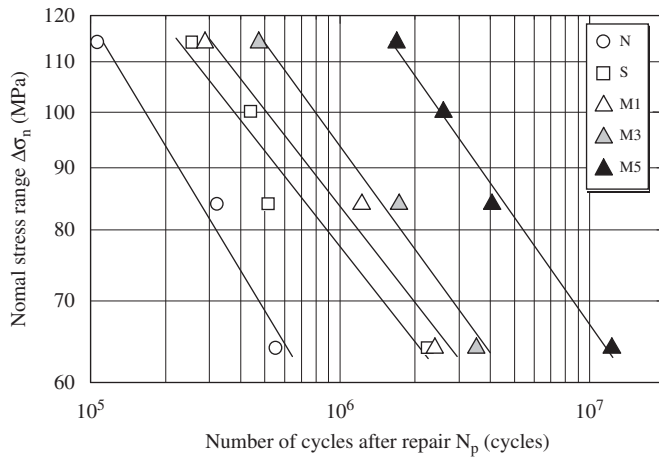
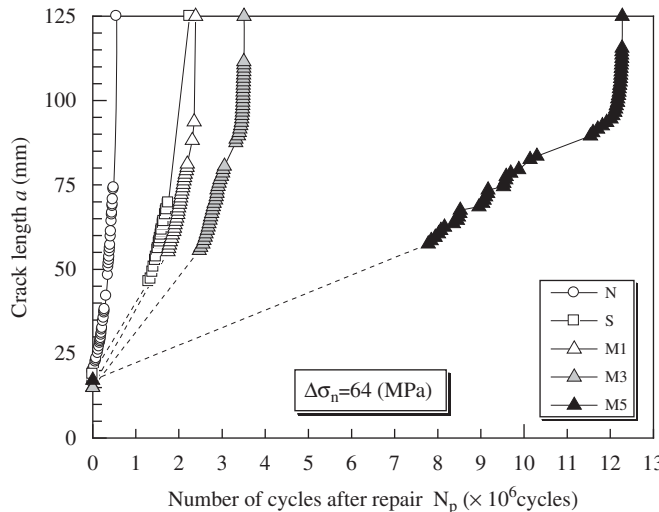
Fig. 13. S-N_p diagram.

Fig. 14. Relationship between number of cycles after repair and crack length.

comparison with series N. In particular, in series M5, it was found that the crack progress was controlled effectively even after cracks crossed the bonding area. The crack propagated rapidly when crack length reached more than 95 mm (equivalent to about 75% of the overall width).

In series S, M1 and M3, CFRP strips did not debond within the bonding area. However, the cracks progressed gradually, and CFRP strips debonded when the crack length reached from 75 to 80 mm (a crack length ranging from 60% to 65% of the overall width). On the other hand, in series M5, CFRP strips debonded immediately before the specimen collapsed. In all specimens, debonding occurred in the interface of adhesive and steel plate.

In order to observe the bonding condition of CFRP strips, the fatigue test was stopped when the crack length reached approximately 100 mm (a crack length of about 80% of the overall width) in $\Delta\sigma_n = 100$ MPa. The specimen was removed from the loading system, and then cut off. Fig. 15 shows two macrosections in series M5. The multi-layered CFRP strips were very close and bonded well to the weld bead, though some partial defects remained.

Table 3
Experimental series of fatigue test.

Series	Repair method	CFRP strip	
		Single-layered part (mm)	Multi-layered part
N	Not repaired	–	–
S	Fig. 3(a)	100	–
M1	Fig. 3(b)	100	1-layer at 200 mm
M3	Fig. 3(b)	100	3-layer at 200 mm
M5	Fig. 3(b)	100	5-layer at 200 mm

5. Combination of CFRP strips and drill-holes

5.1. Variation of repair methods and testing procedure

More effective repair methods were also investigated using combination of CFRP strips and drill-holes. A drill-hole is also called a stop-hole, and is often applied as a temporary repair method on site. Drill-holes are applied to reduce the stress concentration at the tips of cracks. Several combinations of CFRP strips and drill-holes were investigated by static loading tests and fatigue tests. The basic experimental procedure is the same as that mentioned above. In the specimen configuration, the width of the specimen was 300 mm in order to install two drill-holes of 25 mm diameter. Table 4 shows the material properties of steel, CFRP strips and epoxy resin adhesive.

Regarding variation in repair methods, four series of repair methods were examined as shown in Fig. 16 and Table 5. The cracked specimens were repaired when the crack progressed to 33 mm in length from the center towards the edge. The repair methods are described as follows:

- (a) Series DH: repaired only by drill-holes.
- (b) Series DHM: repaired with multi-layered CFRP strips (5 layers) and two drill-holes.
- (c) Series DHS: repaired with single-layered CFRP strips bonded above two drill-holes.
- (d) Series DHMS: repaired combining series DHM and DHS.

The diameter of drill-holes was 25 mm, which was similar to the diameter of a high-strength bolt. By installing drill-holes, the crack length was equivalent to 50 mm per side. The repair procedures and curing conditions are as mentioned above. In addition to these repair methods, the non-repaired series N was examined to give reference value.

Procedures of static and fatigue tests are the same as mentioned above. The nominal stress range $\Delta\sigma_n$ was 100 MPa in the fatigue test. Photograph 4 shows series DHMS as an example of repair methods. In addition, strain gages were installed on the surface of steel plate and CFRP strips, where the cracks would progress. The clip-type displacement transducers were installed in drill-holes and crack opening.

5.2. Static loading test results

Fig. 17 shows the longitudinal stress distribution of the steel plate in $\Delta\sigma_n = 100$ MPa (applied load: $\Delta P = 250$ kN) immediately after repair. The maximum stress was about five times the nominal tensile stress range $\Delta\sigma_n$ in series DH repaired only by drill-holes. In series DHS, DMS and DHMS, it was found that the maximum stress could be reduced by the combination of drill-holes and CFRP strips. In series DHMS, which was the most

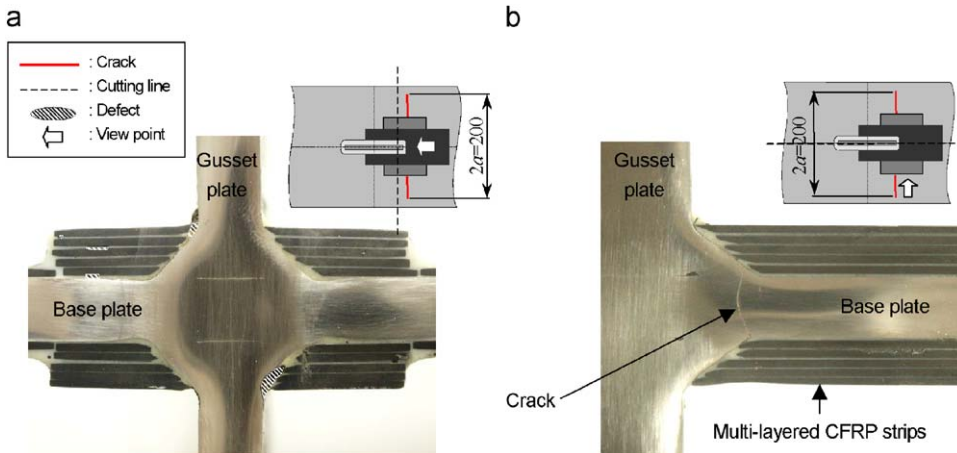


Fig. 15. Macrosections in series M5: (a) cross-sectional direction and (b) longitudinal direction.

Table 4

Mechanical properties of steel, CFRP strip and epoxy resin adhesive.

	Steel plate (JIS SM400A)	CFRP strip	Epoxy resin adhesive
Yield point (MPa)	285	—	—
Tensile strength (MPa)	443	2990	30
Elongation (%)	29	1.9	—
Elastic modulus (GPa)	206	172	1.5

effective repair, the maximum stress was reduced by about 50% compared with series DH.

Fig. 18 shows the longitudinal stress distribution on the CFRP strips. It can be said that the stress distribution in the multi-layered part of series DHMS was similar to that of series DHM. In the single-layered part of series DHMS, the stress distribution was lower than that of series DHS, it also showed that the stress on the steel plate was reduced as indicated above. Therefore, fatigue strength is expected to be the highest for series DHMS.

Fig. 19 shows the crack opening displacement (hereafter called the COD) in all series. In series DH, the COD after installing drill-holes (considered as 50 mm of the opening) obviously became larger compared with that before installing drill-holes (considered as 33 mm of the crack length). In series DHM, the COD could be remarkably reduced. On the other hand, in series DHS, the reduction of the COD at the center was small. In addition, the relationship between the applied load and the COD was almost linear.

5.3. Fatigue test results

Fig. 20 shows the $S-N_p$ diagram. N_p was the fatigue life after repair (considered as 50 mm of the crack length) to failure, as defined by Eq. (2). The fatigue life N_p of series DH and DHM were 1.6 and 5.0 times of the non-repaired series N, respectively. In series DHMS, where the fatigue test was continuing, N_p was prolonged for 80 or more times compared to series N, and for 50 or more times compared to series DH. The sufficient effects of repair were confirmed. In addition, in series M5 with 250 mm wide specimen, the equivalent N_p from 50 mm to failure was 1.15 million cycles. The fatigue life of series DHMS was greatly improved compared with that of series M5 without drill-holes.

More detail on fatigue tests is as follows. In series DHM, the multi-layered CFRP strips debonded on one side when N_p was about 0.20 million cycles. The fatigue test was stopped because the crack generated again at the edge of drill-holes at about 0.33 million cycles. On the other hand, in series DHMS, the multi-layered CFRP strips debonded, when N_p was about 0.47 million cycles on one side and about 4.30 million cycles on the other side, respectively. However, the debonding of single-layered CFRP strips and the recurrence of the crack at the edge of drill-holes were not observed even when N_p reached to about 5.65 million cycles.

Although the stress concentration was reduced by installing drill-holes, the COD became larger. Consequently, the increase of the COD associated with installing drill-holes may have the influence on the debonding of CFRP strips.

6. Conclusion

For fatigue cracks initiated at the weld toe of web gusset joints, the repairs were performed using CFRP strips and epoxy resin adhesive, and the effects of repair on the bond strength and the fatigue durability were examined experimentally and analytically. The following conclusions were obtained:

- (1) It was found that the proposed repair method greatly contributed to the increase of bond strength and the reduction of the opening displacement at the joint.
- (2) The sufficient performance of adhesion joints was confirmed when the number of laminations of CFRP strips increased to five layers.
- (3) The laminating of CFRP strips was found to be effective in preventing debonding and sharing axial force.
- (4) It was confirmed that as the number of laminations of CFRP strips increases, the post-repair fatigue life improved considerably and that a sufficient effect of repair was acquired in the case of five layers.
- (5) No fatigue limit was obtained from the discussed stress range. The proposed method was positioned as a first-aid repair to prolong the fatigue life, since no crack recurrence was prevented.

Moreover, regarding the more effective repair, some repair methods combining CFRP strips and drill-holes were also investigated experimentally. The repair method by combining

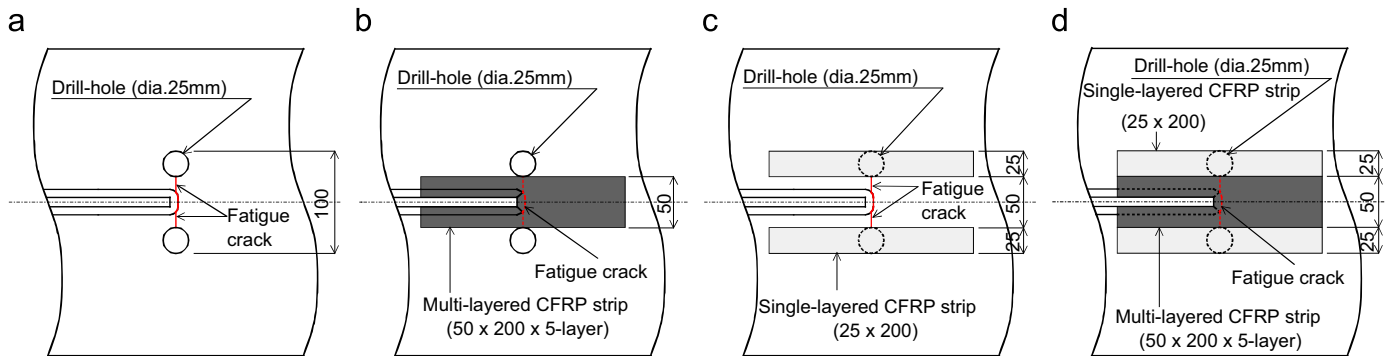


Fig. 16. Variation of repair methods: (a) series DH, (b) series DHM, (c) series DHS and (d) series DHMS.

Table 5
Experimental series in combination of CFRP strips and drill-holes.

Series	Repair method	Drill-holes	CFRP strip	
			Single-layered part (mm)	Multi-layered part
N	Not repaired	Without	-	-
DH	Fig. 16(a)	2-Dia.25 mm	-	-
DHS	Fig. 16(b)	2-Dia.25 mm	200	-
DHM	Fig. 16(c)	2-Dia.25 mm	-	5-layer at 200 mm
DHMS	Fig. 16(d)	2-Dia.25 mm	200	5-layer at 200 mm



Photograph 4. Repair method in series DHMS.

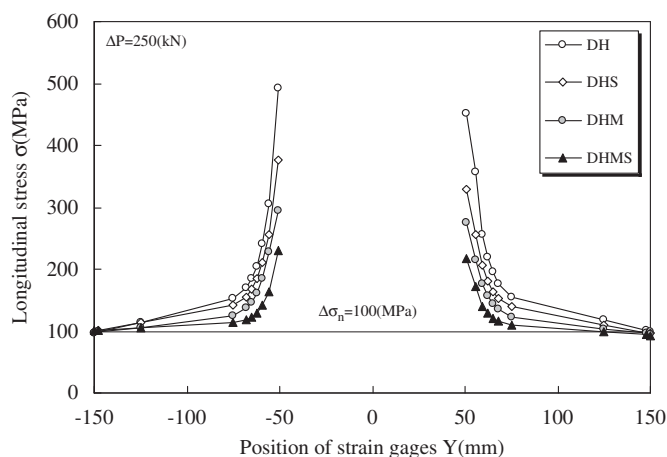


Fig. 17. Stress distribution of steel plate.

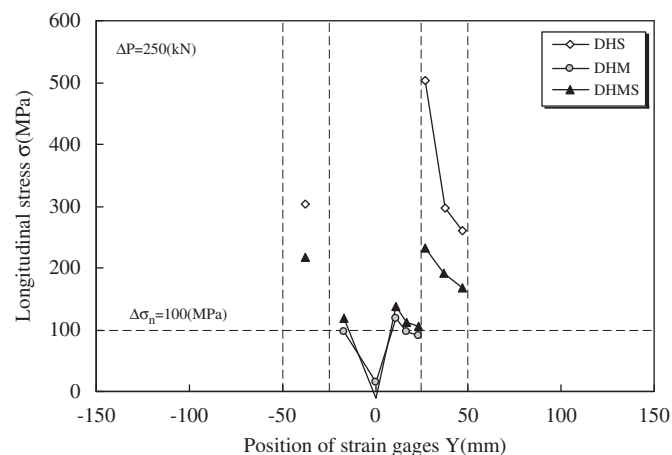


Fig. 18. Stress distribution of CFRP strips.

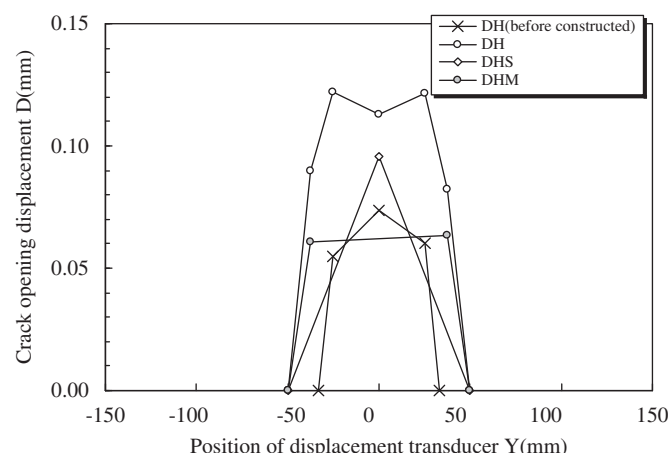


Fig. 19. Distribution of crack opening displacements.

CFRP strips and drill-holes was more effective compared with that without drill-holes.

It should be pointed out that the above conclusions were derived from the limited test data presented in this paper.

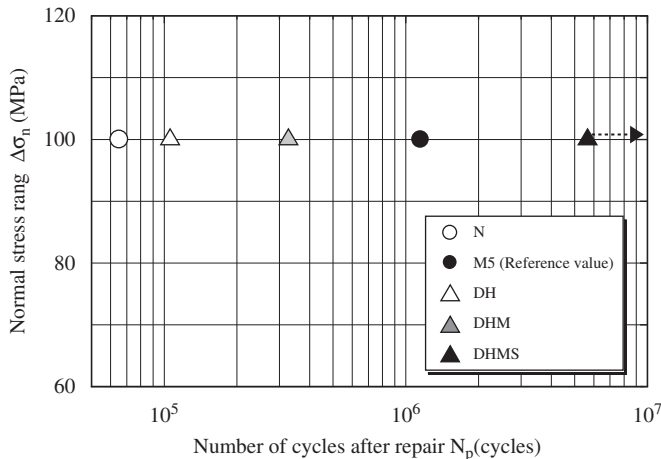


Fig. 20. S- N_p diagram.

References

- [1] Japan Road Association. Guidelines for fatigue design of steel highway bridges. Tokyo: Maruzen Co., Ltd.; 2002 [in Japanese].
- [2] Zhao X-L, Zhang L. State-of-the-art review on FRP strengthened steel structures. *Engineering Structures* 2007;29(8):1808–23.
- [3] Hollaway LC, Cadei J. Progress in the technique of upgrading metallic structures with advanced polymer composites. *Progress in Structural Engineering and Materials* 2002;4(2):131–48.
- [4] Smith ST. In: Proceedings of the first Asia-Pacific conference on FRP in structures—APFIS 2007, Hong Kong, 2007.
- [5] Jiao H, Zhao XL. CFRP strengthened butt-welded very high strength (VHS) circular steel tubes. *Thin-Walled Structures* 2004;42(7):963–78.
- [6] Miller TC, Chajes MJ, Mertz DR, Hastings JN. Strengthening of a steel bridge girder using CFRP plates. *Journal of Bridge Engineering, ASCE* 2001;6(6):514–22.
- [7] Bassetti A, Liechti P, Nussbaumer A. Fatigue resistance and repairs of riveted bridge members, fatigue design. Finland: Espoo; 1998. p. 535–46.
- [8] Jones SC, Civjan SA. Application of fiber reinforced polymer overlays to extend steel fatigue life. *Journal of Composites for Construction, ASCE* 2003;7(4):331–8.
- [9] Tavakkolizadeh M, Saadatmanesh H. Fatigue strength of steel girders strengthened with carbon fiber reinforced polymer patch. *Journal of Structural Engineering, ASCE* 2003;129(2):186–96.
- [10] Nakamura H, Yamasawa T, Maeda K, Doi T, Irube T, Takagi H, Suzuki H. Study on repair of steel members using CFRP strips. In: Proceedings of the 56th annual conference of JSCE, CD-ROM, 2001, 2 pages [in Japanese].
- [11] Yamauchi T, Nakamura H, Maeda K, Suzuki H. Fatigue test on repair of steel members using CFRP strips. In: Proceedings of the 57th annual conference of JSCE. 2002. p. 1339–40 [in Japanese].
- [12] Nakamura H, Moroi T, Suzuki H, Maeda K, Irube T. Repair of out-of-plane welded gusset joint using CFRP strips. *Journal of Construction Steel, JSSC* 2004;12:425–30 [in Japanese].
- [13] Jiang W, Nakamura H, Suzuki H, Maeda K, Irube T. Experimental study on adhesion characteristics of steel plate and CFRP strips. *Journal of Construction Steel, JSSC* 2006;14:595–602 [in Japanese].



Full length article

Fatigue behavior and remaining life evaluation of rib-to-deck joints using interior repair welds

Ming-zhe Li, Chuang Cui*, Hao Wang, Qing-hua Zhang, Le-tian Da, Yi-zhi Bu

Department of Bridge Engineering, Southwest Jiaotong University, Chengdu, Sichuan 610031, China

MOE Key Laboratory of High-speed Railway Engineering, Southwest Jiaotong University, Chengdu, Sichuan 610031, China



ARTICLE INFO

Keywords:

Orthotropic steel decks

Fatigue crack

Reinforcement

Interior repair welding

Remaining life evaluation

Fracture mechanics

ABSTRACT

The rib-to-deck joints are one of the most critical vulnerable details of orthotropic steel deck subjected to vehicle loads. Specially, fatigue cracks initiating from the weld root and propagating along the thickness of the deck at the rib-to-deck joints is most difficult to repair. In this study, the interior repair weld is adopted to enhance the fatigue resistance of rib-to-deck joint. Three specimens of rib-to-deck joint were designed and tested to investigate the effectiveness and applicability of the interior repair weld. The fracture mechanics method associated with numerical simulation is adopted to analyze the failure mechanism and remaining life of rib-to-deck joints after reinforcement. The results indicate that the region of fatigue crack initiation will be transferred from the interior weld root before repairing to the exterior weld toe after repairing. The interior repair weld can effectively prevent fatigue crack propagation and significantly improve the remaining fatigue life of the rib-to-deck joints. The simulated fatigue life agrees well with the measurement in fatigue tests, revealing the accuracy of fracture mechanics method to estimate the remaining life.

1. Introduction

Orthotropic steel deck (OSD) is widely used in long-span bridge due to the benefits such as light weight, high strength and quick construction. The fatigue cracks untimely occur in OSD at the early period of service [1–3]. Specially, the rib-to-deck welded joint is one of most critical vulnerable details [4–6], and fatigue crack of rib-to-deck welded joint will accelerate the damage of pavement and compromise the durability of steel bridge, as shown in Fig. 1. Although a lot of efforts have been done to enhance the performance of cracked OSD, it is still a challenge to repair those fatigue crack in OSD [7].

The reinforcements for cracked OSD mainly include welding repair reinforcement [8,9], cold reinforcement [10–13], and integral reinforcement [14,15]. Welding repair reinforcement is the use of welding techniques to directly repair cracks by grinding and rewelding the region around the crack. Cold reinforcement mainly includes crack-arrest hole [10], grinding and impact treatment [12,13], and assembly bonding methods [16,17]. Crack-arrest hole is effective to the crack in plane plate, but not for the rib-to-deck welded joint. Impact treatment can effectively prolong fatigue life by forming residual compressive stress at the weld toe and improving the geometry of the weld toe. But this method is used to eliminate surface micro-cracks, and requires a certain operating space and hardly repairs hidden cracks. The assembly bonding methods [11,16,17] reduce the strain near the crack tip and enhance the local stiffness. Moreover, Shao et al. [18] investigated the

integral reinforcement effect of ultra-high strength concrete structural layer on the vulnerable details of OSD. Although the integral reinforcement can increase the overall stiffness of OSD, it increases the weight of the bridge, which limits its application, except for the thin UHPC layer.

The rib-to-deck welded joint is one of the most critical components of OSD [19–22] (see Fig. 1). The current reinforcement methods mainly focus on the repair of toe-deck and root-throat cracks by assembly bonding methods, such as gluing or bolting steel plate [17], FRP plate [16] or U-shaped plate [11], which are ineffective to the root-deck crack. However, the FRP plate applied at the rib-to-deck joint form a concave and cannot effectively anchored; In addition, due to thermal effect, the high temperature on the deck plate will significantly reduce the elastic modulus of epoxy glue, affecting the reinforcement effect. The remelting method was used to repair the root-deck crack taking a large proportion of fatigue cracking modes [23–25], but the remelted rib-to-deck welded joint will crack with a low lifetime due to the ineluctable weld defects during remelting. At the same time, the root-deck crack is so secluded in the interior of closed rib that it is difficult to detect at the early stage of fatigue crack propagation. Therefore, the root-deck crack is extremely difficult to repair, and the effective reinforcement of root-deck crack should be further investigated.

This paper aims to propose a new repair method for the cracked rib-to-deck welded joint, and estimate the remaining life. An interior repair

* Corresponding author at: Department of Bridge Engineering, Southwest Jiaotong University, Chengdu, Sichuan 610031, China.

E-mail address: ccui@swjtu.edu.cn (C. Cui).

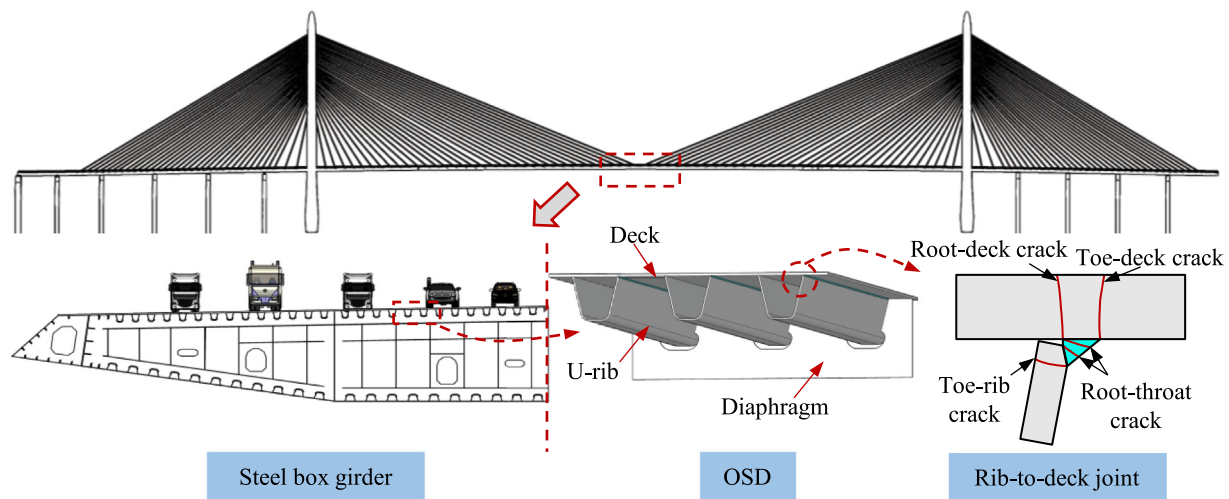


Fig. 1. The failure mode of rib-to-deck joint in OSD.

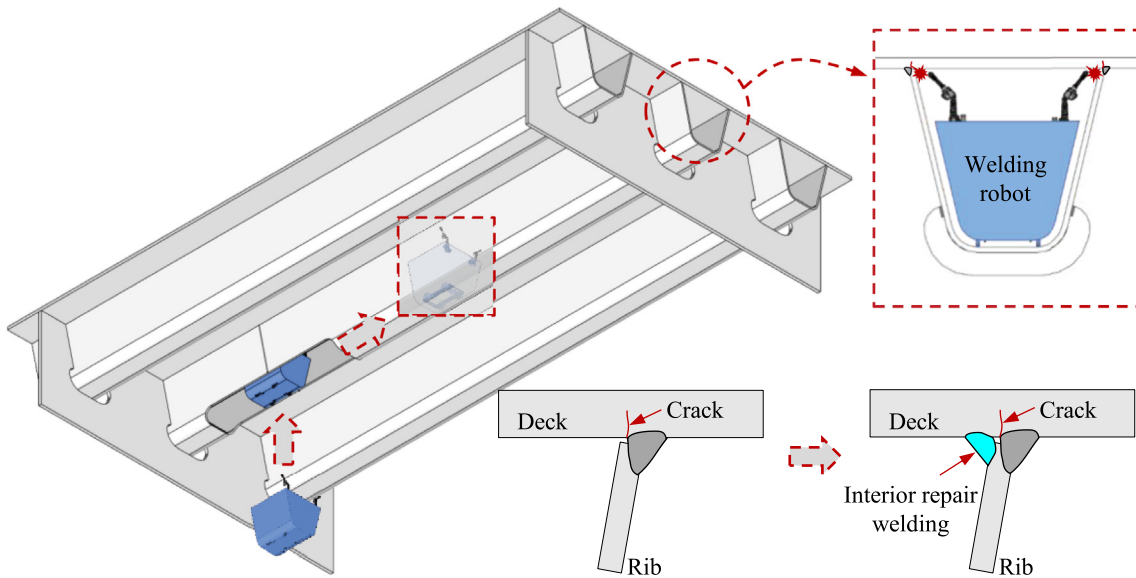


Fig. 2. The implementation process of interior repair welding.

weld was firstly proposed based on the automation welding technique. The fatigue test of rib-to-deck welded joint was conducted until the root-deck cracks appeared. Then, the reinforcement experiments of cracked rib-to-deck welded joint were carried out, and failure mechanism of enhanced rib-to-deck welded joint was analyzed. Finally, the remaining life of reinforced rib-to-deck joint was estimated by using fracture mechanics method.

2. Reinforcement tests of rib-to-deck joint using interior repair weld

2.1. Interior repair weld

The root-deck crack of rib-to-deck joint initiates from the weld root and propagates to the deck, which is located in the interior of closed U-rib. This fatigue cracking mode which is common in steel bridges is hardly reinforced by the traditional repair methods. The interior repair welding can be achieved, propelled by rapid advances in automation welding techniques which have been widely used to fabricate the double-side welded rib-to-deck joint [26–28]. Fig. 2 shows the abridged general view of interior repair welding using an automated welding

robot which can effectively close the surface of root-deck crack. To achieve interior welding repair in the real bridge, the hole at the butt weld or bolting of U-rib is cut to put the automated welding robot into the U-rib, and the welding robot passes through the hole. After interior repair welding, the hole shall be restored.

2.2. Specimen design

The specimens of rib-to-deck welded joint are composed of deck plate and U-rib. To investigate the enhancement effect of interior repair weld in OSDs, a special test device is designed as shown in Fig. 3(a). A specific stiffness constraint at the bottom of rib is set to adjust the stiffness of rib and ensure that fatigue crack initiates from the weld root of the joint and propagates along the thickness of deck plate. Besides, the stiffness constraint is an angle steel with a width of 300 mm, a height of 140 mm and a thickness of 8 mm. The bottom plate of longitudinal rib is connected with the angle steel by the high-strength bolts. The hinged supports are used to simulate the hinge constraint between the two sides of the deck and the pillar stiffener. The site layout of the specimen is shown in Fig. 3(b).

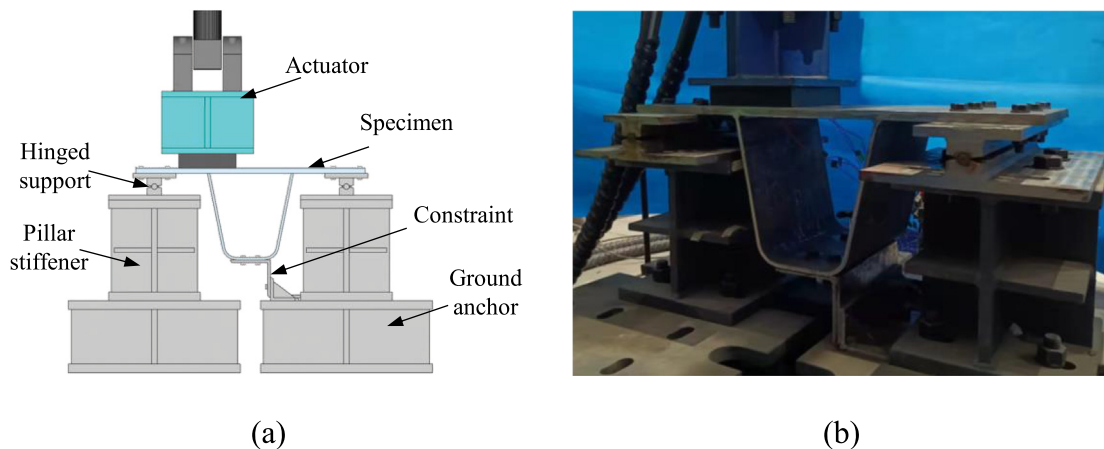


Fig. 3. Fatigue test specimen diagram: (a) fatigue test device; and (b) site layout.

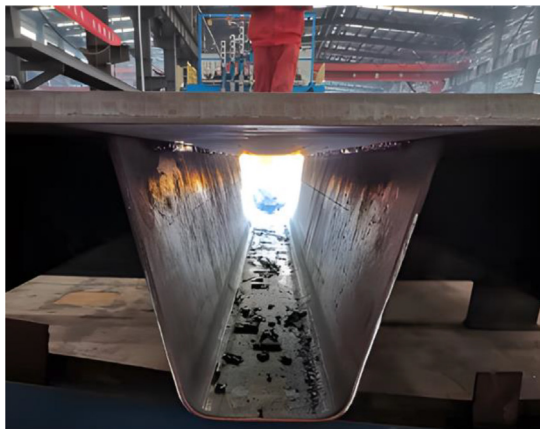


Fig. 4. Interior repair welding by the overhead fillet welds using the automated robot.

The fatigue tests were firstly conducted until the root-deck cracks appear. Then, the specimens were reinforced by the interior repair welding associated with the automation robot, as shown in Fig. 4. The specimen is not upside down and placed same as the real bridge. At last, the enhanced specimens would be reloaded using the fatigue test device in Fig. 3 until the specimens failed.

Referring to the design parameters of typical OSD, three specimens were designed, including two specimens of traditional single-side welded rib-to-deck joint and one specimen of double-side welded rib-to-deck joint as a contrast, as depicted in Fig. 5. The thicknesses of deck plate and U-rib are 18 mm and 8 mm, and the length and width of specimen are 300 mm and 800 mm, respectively. The penetration rate of both single-side weld seam and double-side weld seam of rib-to-deck joints is 75%. The size of fillet weld ($l = h$) is 7 mm, the size of interior fillet weld is 6 mm, and the specimens are made of Q345qD steel with a nominal yielding strength of 345 MPa. The distance between the center line of the support and the center of the test specimen is 325 mm.

2.3. Test set-up and instrumentation

A rubber bearing is set between the actuator and the specimen with a length of 200 mm, a width of 200 mm, and a height of 40 mm. The transverse center of the loading position is located above the web of U-rib, and the longitudinal center of the rubber bearing overlaps with the longitudinal center of the specimen, as shown in Fig. 6. To investigate the reinforcement effort of interior repair welding and the fatigue behavior of the reinforced joints, the fatigue tests for two single-side welded rib-to-deck joints were carried out in two stages (see Fig. 6): (1)

Table 1
Load Scheme of Test.

Specimens	Welding type	Loading amplitude ΔF (kN)	
		Stage I	Stage II
SRD-I	Single-side weld	45	45
SRD-II	Single-side weld	50	50
DRD-I	Double-side weld	50	—

Stage I: the specimens were loaded until the appearance of fatigue crack at the weld root of rib-to-deck joint; (2) Stage II: the cracked specimens were reinforced by the interior weld repairing method, and the enhanced specimens were reloaded until fatigue failure at the rib-to-deck welded joint. To compare fatigue behavior and failure mechanism of reinforced single-side welded rib-to-deck joint and double-sided welded rib-to-deck joint, the fatigue test of double-sided welded rib-to-deck joint was carried out as well. The loading amplitudes at each stage for different specimens are listed in Table 1.

Moreover, the strain gauges were adopted to monitor the variations of local strains at the weld root and toe under cyclic loading. Fig. 7 shows the locations of the strain gauges which are numbered in accordance with the longitudinal direction. The strain gauges with a distance of 0.4t mm from the exterior weld toe, weld root, and interior weld toe are named as ET, IR, and IT, respectively.

2.4. Result discussions

Firstly, the cyclic loading in Stage I was accomplished, and the monitored strains with the different number of cycles are obtained. Since the root-deck crack cannot be observed under cyclic loading due to its invisibility, it is reasonable that the macroscopic cracks occur at the weld toe or root when the strains of the critical measuring points decrease by 10% according to [2]. To monitor the fatigue crack initiation and propagation, the normalized strain by using a ratio of real-time and initial strain is adopted in this study.

The normalized strains of the measuring points at the weld toe of SRD-I and SRD-II and the weld root of DRD-I in stage I are shown in Fig. 8, where ϵ_0 is initial value of strain, and ϵ is strain value after a certain number of cycles. It can be seen that the normalized strain at the weld root of SRD-I reduces by 10% at the location of -100mm and 50 mm from the center line of specimen after respectively 615,000 cycles and 1000,000 cycles, indicating the appearance of macroscopic cracks at the weld root. Moreover, a reduction of 10% at the weld root of SRD-II can be found at 100 mm and -75 mm away from the center line of specimen after 287,000 cycles and 447,000 cycles, respectively, revealing the potential cracks have occurred at the weld root. Correspondingly, the macroscopic crack may be obtained at the

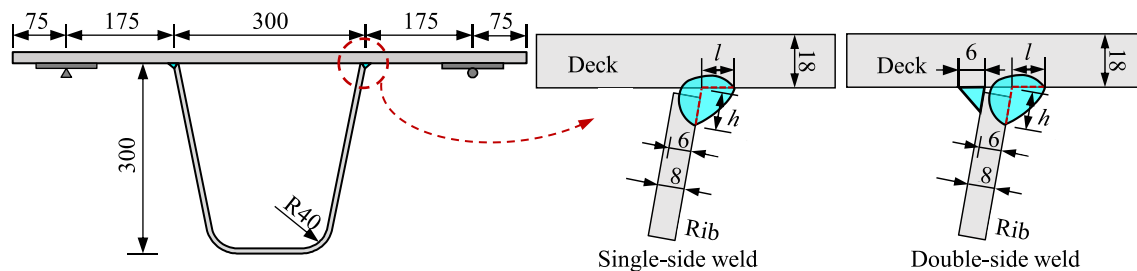


Fig. 5. Dimensions of test specimen (unit: mm).

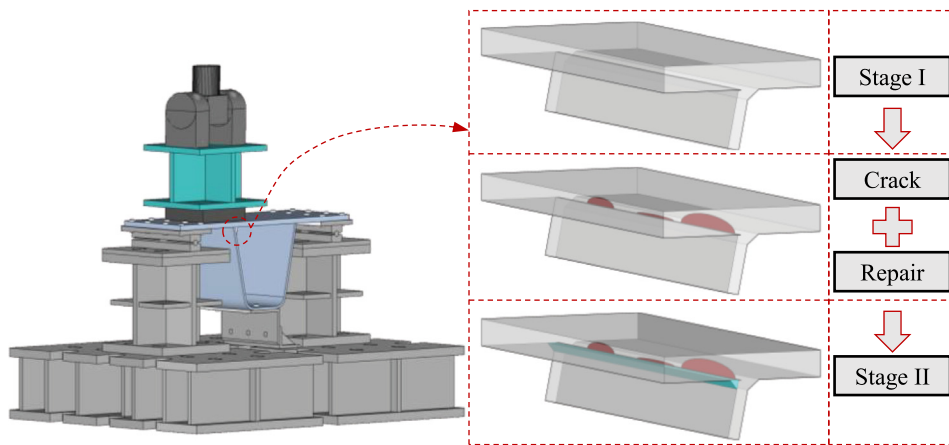


Fig. 6. The stages of test.

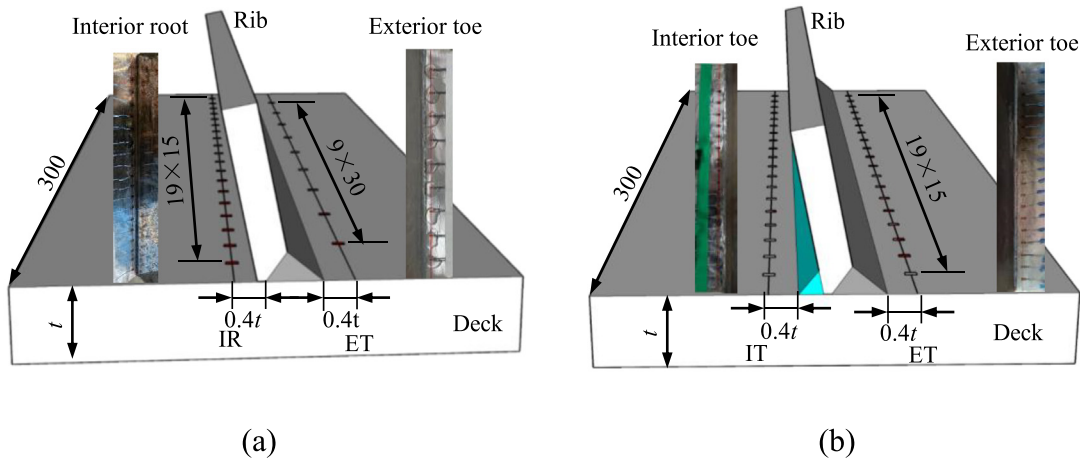


Fig. 7. Arrangement of strain measuring points on (unit: mm): (a) specimen in Stage I; (b) specimen in Stage II.

interior weld toe of DRD-I, where it is about 105 mm away from the center line of specimen after 454,000 cycles with a normalized strain decline of 10%.

Furthermore, the cracked SRD-I and SRD-II were reinforced by the interior repair welding, and the enhanced SRD-I and SRD-II were reloaded until fatigue failure. Fig. 9 shows the nominalized strains of repaired specimens under cyclic loading in Stage II. After 585,000 cycles and 830,000 cycles with a reduction of nominalized strain by 10%, it can be inferred that the macroscopic fatigue cracks may appear at the exterior weld toe of enhanced SRD-I which is respectively -75 mm, and 100 mm away from the centerline of specimen. Similarly, the cracks of reinforced SRD-II respectively propagate at 90 mm and -25 mm from the centerline of specimen after 460,000 cycles and 680,000 cycles.

At last, the cracked specimens were cut by the wire cutter to obtain the microtome sections where the cracks occurred in the different

specimens, as shown in Fig. 10. For SRD-I and SRD-II, it is clear that the cracks have firstly initiated at the interior weld root and propagated to the deck. After interior repair welding, the fatigue cracking has transferred to the exterior weld toe rather than the repaired weld root of SRD-I and SRD-II, indicating the effectivity of interior repair welding for the reinforcement of root-deck crack of the single-side welded joints. Besides, the crack of DRD-I firstly appeared at the interior weld toe, which is similar to the results in [28]. It can be seen that the dominant failure mode of DRD-I (interior toe-deck crack) differs to that of the repaired SRD-I and SRD-II (exterior toe-deck crack). The main reason is that fatigue damage has been accumulated as well at the exterior weld toes of the single-side welded joints under cyclic loading before reinforcement. According to the actual test data, the stress of weld root is greater than that of weld toe for SRD-I and SRD-II, while the stress of interior toe at DRD-I is greater than that of exterior

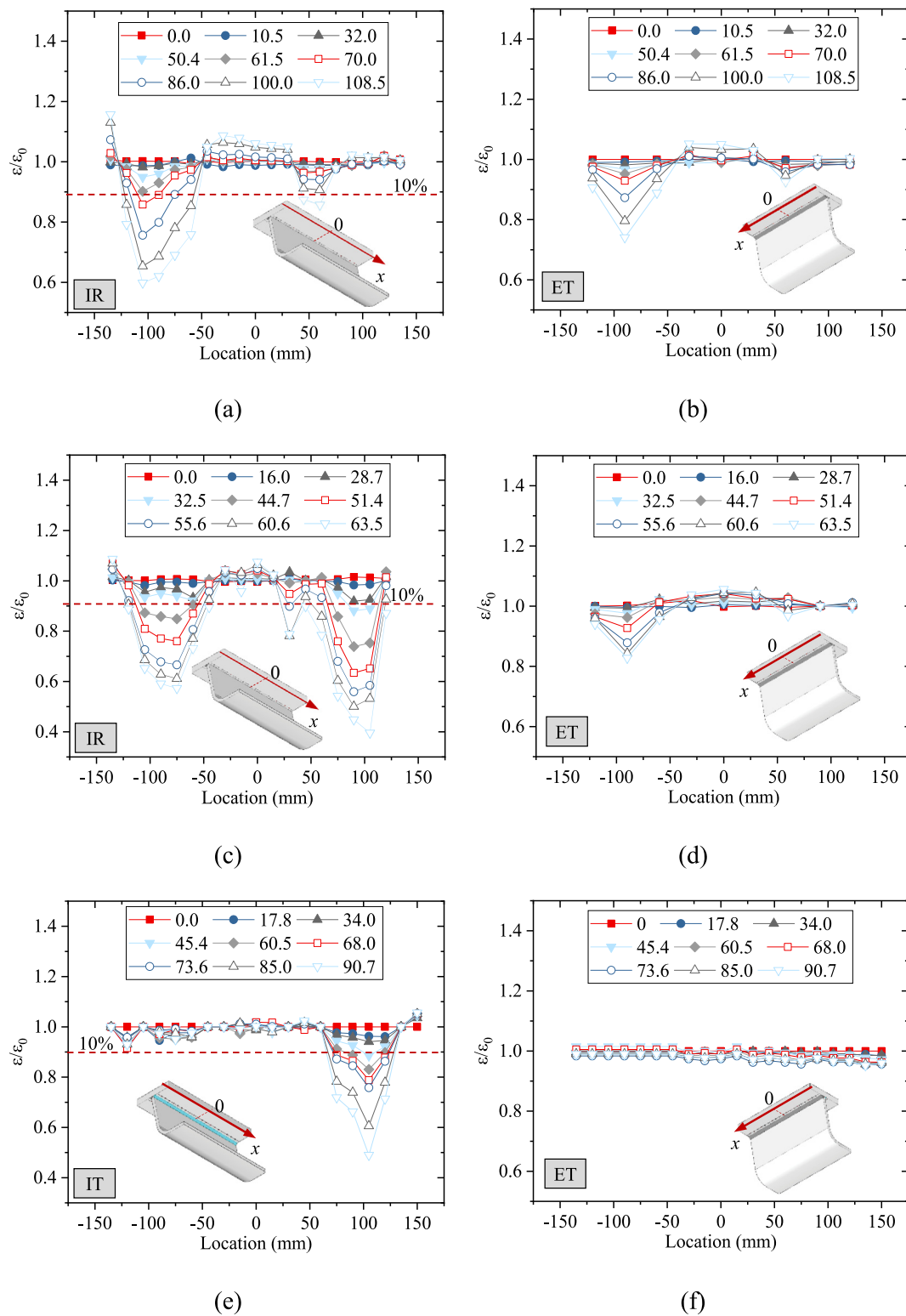


Fig. 8. The variation curves of nominalized strains in Stage I at: (a) interior weld root of SRD-I; (b) exterior weld toe of SRD-I; (c) interior weld root of SRD-II; (d) exterior weld toe of SRD-II; (e) interior weld toe of DRD-I; and (f) exterior weld toe of DRD-I.

weld toe. Therefore, in Stage I, cracks firstly initiate at the weld root of SRD-I and SRD-II, and at the interior weld toe of DRD-I. After the interior welding repair in Stage II, since the newly generated interior weld seams of SRD-I and SRD-II are not subjected to fatigue loading before the interior welding repair, the crack propagation rate of newly generated interior weld toe is less than the intrinsic exterior weld toe. Therefore, the fatigue crack in Stage II firstly appeared at the exterior

weld toe instead of the repaired interior weld toe where there is no fatigue damage accumulation at the beginning of Stage II.

Moreover, the stress ranges of critical measuring points where cracks initiate and grow, and the corresponding number of cycles N_{10} when the nominalized strains decrease by 10% are listed in Table 2. N_e is the corresponding number of cycles at the end of the test. It can be seen that fatigue life can be effectively improved, and the

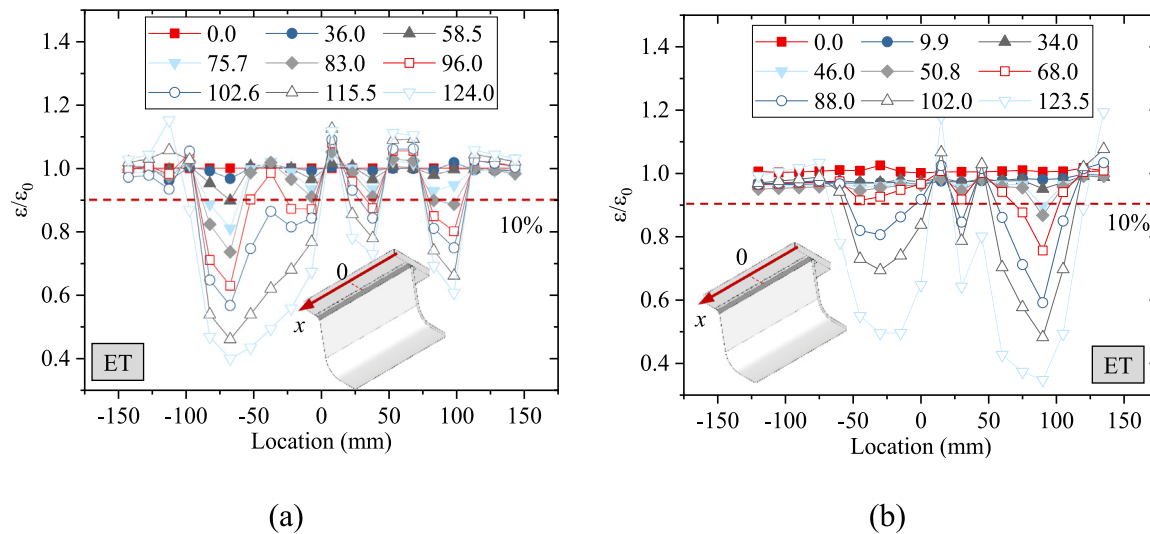


Fig. 9. The variation curves of nominalized strains at the arranged measuring points in Stage II on: (a) SRD-I; and (b) SRD-II.

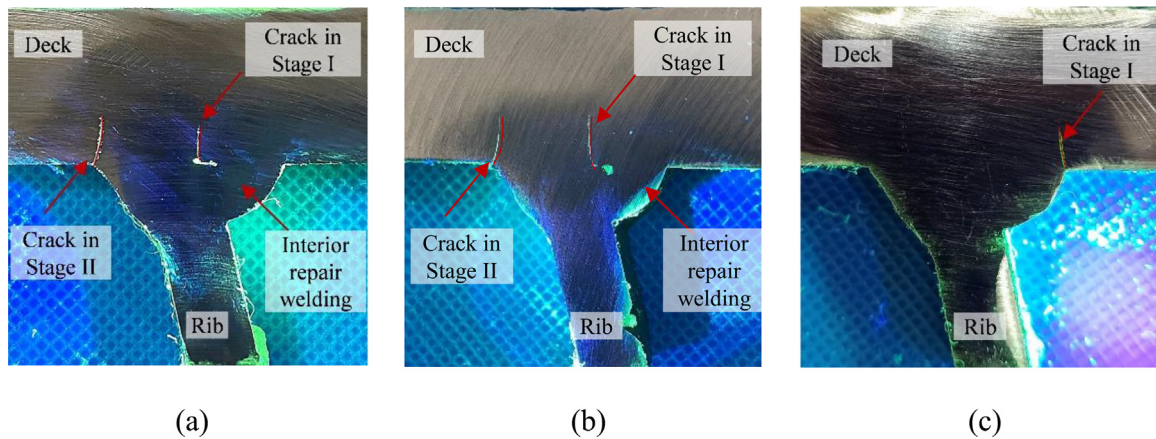


Fig. 10. The fatigue cracks of rib-to-deck after reinforcing: (a) SRD-I; (b) SRD-II; and (c) DRD-I.

Table 2
Fatigue Test Results.

Stage	Specimens	Crack modes	Number of cycles ($\times 10^4$)	
			N_{10}	N_e
Stage I	SRD-I	Root-deck crack	61.5	108.5
	SRD-II	Root-deck crack	28.7	63.5
	DRD-I	Interior toe-deck crack	45.4	90.0
Stage II	SRD-I	Exterior toe-deck crack	58.5	124.0
	SRD-II	Exterior toe-deck crack	41.5	123.5

remaining lives of SRD-I and SRD-II have been improved by 95% and 145%. To analyze the failure mechanism and estimate the remaining life of reinforced single-side welded rib-to-deck joint, the numerical simulation should be further carried out by using fracture mechanics method.

3. Remaining life evaluation

3.1. Linear fracture mechanics method for simulation

Although the types and number of weld defects have been sharply reduced after the application of automation welding techniques, the defect of resemble-crack extremely occurred at the unfused regions of weld root of rib-to-deck joint, as shown in Fig. 11. Similarly, the

defect of resemble-crack can be also observed at the weld toe, where the defect size is smaller than that in weld root. It has been proven in [29] that those resemble-cracks are the potential risk sources leading to cracks initiation and propagation under cyclic loading. Therefore, the fatigue performance of rib-to-deck joints including those resemble-cracks which are regarded as the initial crack can be evaluated by using the linear fracture mechanics method.

The toe-deck cracks and root-deck cracks can be found in SRD-I, SRD-II and DRD-I. Although the root-deck crack is firstly found in SRD-I and SRD-II, the fatigue damage of weld toe in SRD-I and SRD-II is simultaneously accumulated under cyclic loading in Stage I. So it can be assumed that fatigue cracks are synchronous to propagate at both weld root and weld toe with a different of initial crack size at the beginning of cyclic loading. The fatigue life can be obtained by using Paris-Erdogan formula [30,31] as below.

$$\frac{da}{dN} = C (\Delta K_{\text{eff}})^m \quad (1)$$

where C and m are the material parameters to characterize the crack propagation, with values of $5.21 \times 10^{-13} \text{ N mm}^{-3/2}$ and 3 [32], respectively. a is the crack length, and N is the number of cycle. ΔK_{eff} is the amplitude of equivalent stress intensity factor mixed by ΔK_I , ΔK_{II} as below [32,33]. The fatigue crack growth mode of the rib-to-deck joints in OSDs is I-II mixed-mode dominated by mode I [28,34].

$$\Delta K_{\text{eff}} = \sqrt{\Delta K_I^2 + \Delta K_{II}^2} \quad (2)$$

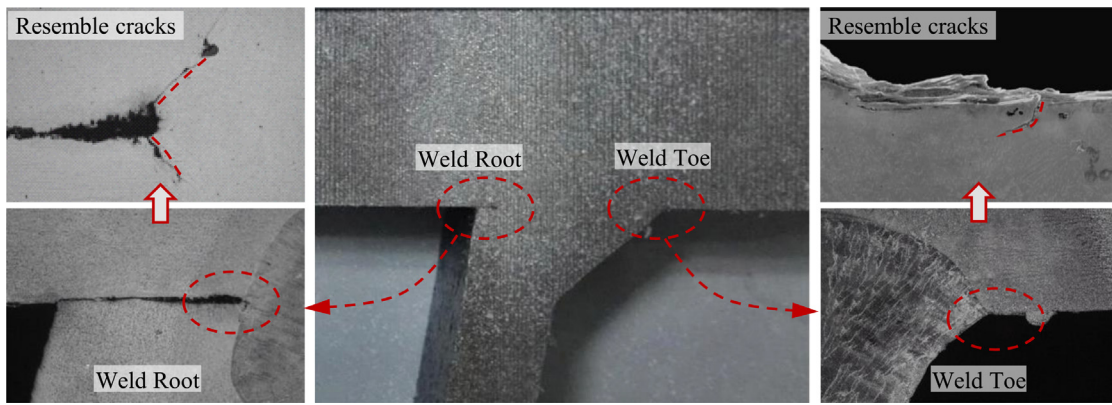


Fig. 11. Resemble-cracks of welded joints.

where ΔK_I and ΔK_{II} are stress intensity factor amplitudes of mode I and II crack, respectively. And the propagation angle θ is

$$\theta = 2 \arctan \left(\frac{1 - \sqrt{1 + 8(K_{II}/K_I)^2}}{4(K_{II}/K_I)} \right) \quad (3)$$

where K_I and K_{II} are stress intensity factor of mode I and II crack, respectively.

To obtain the relationship of crack length and number of cycle, the crack propagation can be numerical simulated by using the finite element method. The resemble-cracks are considered as the initial crack. The propagation increment, Δa_{med} , for median node of the crack front is previously specified (see Fig. 12), and the increments, Δa_{oth} , for other calculation nodes of the crack front are obtained by Eq. (4).

$$\Delta a_{oth} = \Delta a_{med} \left(\frac{\Delta K_{oth}}{\Delta K_{med}} \right)^m \quad (4)$$

where Δa_{med} is the crack propagation increment for the median node of the crack front, and ΔK_{med} is the corresponding stress intensity factor amplitude. Δa_{oth} and ΔK_{oth} are respectively the crack propagation increments and the stress intensity factor amplitudes for other nodes of the crack front.

The crack propagation of the weld root can be directly simulated by using the above equations. Taking the propagation analysis of the root-deck and toe-deck cracks as an example, a_0^{Root} and a_0^{Toe} are the initial crack depths of the weld root and toe, respectively. Assuming that the stress intensity factor amplitude of the root-deck crack, $\Delta K_{i,med}^{Root}$, is greater than, $\Delta K_{i,med}^{Toe}$, of the toe-deck crack, for the i th propagation step, and the propagation increment, $\Delta a_{i,med}^{Root}$, for the median crack front of the root-deck crack is also predefined, the crack propagation increment, $\Delta a_{i,med}^{Toe}$, for the median crack front of the root-toe crack can be determined by Eq. (5).

$$\Delta a_{i,med}^{Toe} = \Delta a_{i,med}^{Root} \left(\frac{\Delta K_{i,med}^{Toe}}{\Delta K_{i,med}^{Root}} \right)^m \quad (5)$$

The final propagation depths of the root-deck and toe-deck cracks can be calculated by Eq. (6).

$$a_{med}^{Toe} = \sum \Delta a_{i,med}^{Toe} \cdot a_{med}^{Root} = \sum \Delta a_{i,med}^{Root} \quad (6)$$

Therefore, the crack propagation life N_p can be calculated by Eq. (7) [35]. For the same weld seam, the number of loading cycles experienced by the weld root N^{Root} and weld toe N^{Toe} should be the same.

$$N_p = N^{Toe} = N^{Root} = \sum \frac{\Delta a_{i,med}^{Root}}{C(\Delta K_{i,med}^{Root})} = \sum \frac{\Delta a_{i,med}^{Toe}}{C(\Delta K_{i,med}^{Toe})} \quad (7)$$

After the cracked joint is repaired, the determination for the initial cracks of repaired joint is of paramount importance. For the cracked

joint reinforced by the interior repair weld, the final propagation depths of the root-deck and toe-deck cracks of the cracked joint before reinforcement can be defined as the initial cracks of the repaired joint. First, the dominant crack of the repaired joint is determined according to the stress intensity factor amplitude. The crack propagation increments of the repaired joint, $\Delta a_{i,med}^{Root}$, $\Delta a_{i,med}^{Toe}$, for the i th propagation step can be obtain by Eq. (5). Then the increments, Δa_{oth} , for other calculation nodes of the crack front are obtained by Eq. (4). Finally, the final propagation depths of the cracks and propagation life for the reinforced joint can be calculated by Eqs. (6) and (7). Therefore, the main framework of the evaluation process of welded joints with multiple failure modes before and after reinforcement is illustrated in Fig. 12. On the basis of the fatigue life analysis of the welded joints before repairing, the influence of multiple failure modes is considered to form a systematic analysis of the reinforced joints.

3.2. Numerical simulation

To simulate the crack propagation and estimate the fatigue life, the finite element models of the specimens were established. Considering the complexity of crack propagation simulation, the sub-model technique is adopted in this study, as shown in Fig. 13. The solid element SOLID45 was used to establish the global model. The solution of nodal displacements in the global model is interpolated onto the relevant parts of the boundary of the sub-model. Note that the meshes at the crack front are refined to fit the singularity of stress field at the crack tip by introducing hexahedron elements SOLID95 in the two outer layers, 15-node wedge singular element in the core layer. The part away from the crack front was transitioned by tetrahedron element SOLID92. The constraints on the both sides of deck are simply supported as same as the real condition, and the constraint on the angle steel of U-rib bottom plate is fixed support. The elastic modulus and Poisson's ratio are 206 GPa and 0.3, respectively.

Sensitivity analysis was performed to investigate the influence of mesh size on stress results. The meshing size of rib-to-deck welded joint is refined from 8 mm to 0.5 mm, and the simulated stress at the weld root under the different meshing sizes were compared in Fig. 14. Considering both the computational efficiency and meshing quality, a mesh size of 2 mm was adopted. To validate the accuracy of finite element model, taking SRD-I as an example, the calculated strains of finite element model at the arranged measuring points are compared to the measured values under a loading of 45 kN, as shown in Fig. 15. An error of less than 5% between the simulated and measured strains demonstrates the accuracy of the established finite element model, which can be further used to investigate the effect of interior repair welding on the improvement of fatigue life.

The statistical analysis of resemble-crack defect size at the single-side and double-side welded rib-to-deck welded joints in [29] were referred in this study. The size of resemble-crack at weld toe is mainly

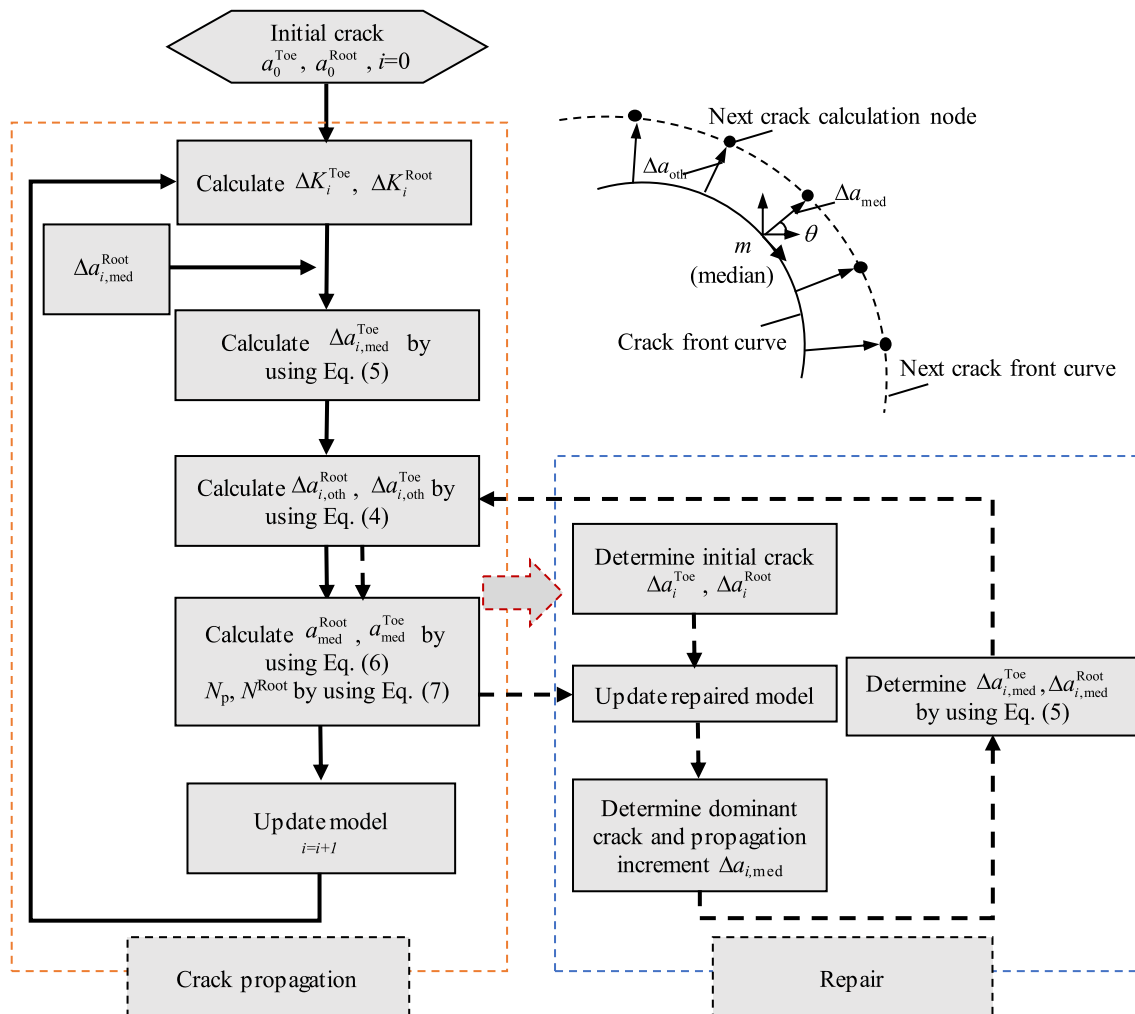


Fig. 12. The evaluation process of fatigue life of welded joints.

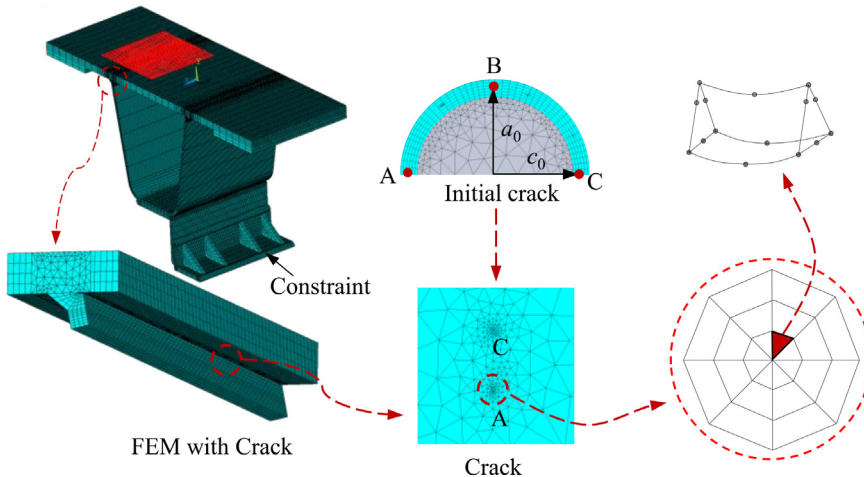


Fig. 13. Finite element model including cracks.

distributed between 20 μm and 40 μm , while the size of resemble-crack at weld root is mainly distributed between 100 μm and 200 μm . In this study, the initial size of crack depth for fracture mechanics at weld toe being determined by the fracture surface of weld toe, is approximately 40 μm , which is in conformity with the value reported in [29]. However, the initial size of crack depth at weld root cannot be determined by

the fracture surface of weld root which has been destructed by the interior repair welding. Therefore, an average value of resemble-crack at weld root investigated in [29] is adopted in this study. Finally, the initial sizes of crack depth at weld root and toe are 40 μm and 150 μm , respectively. Due to the initial crack has strong association in the length direction, it is considered that the initial crack has a

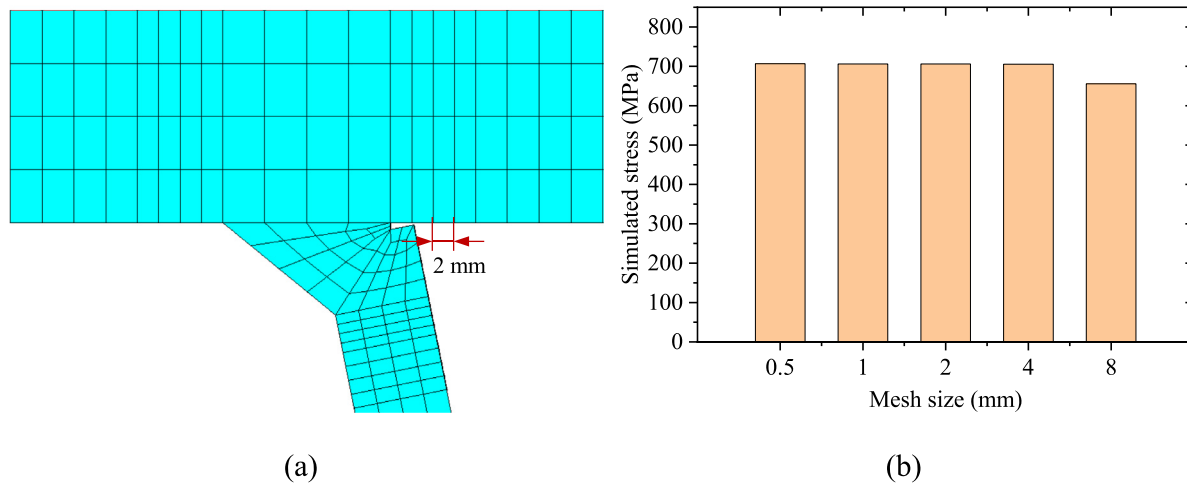


Fig. 14. Mesh size sensitivity analysis: (a) mesh size on the finite element model; (b) simulated stress at the weld root with different mesh sizes.

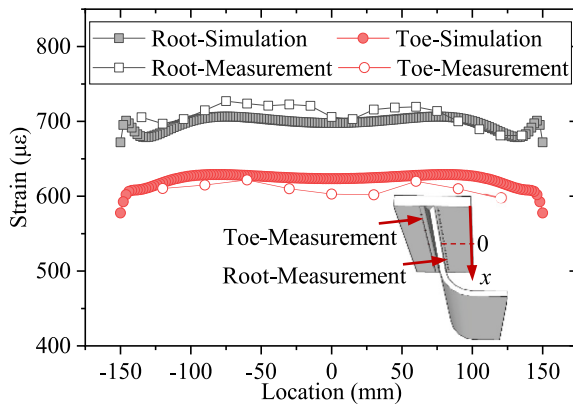


Fig. 15. Comparisons of testing and simulated values.

smaller depth-to-length ratio ($a_0/2c_0$) [29,30,36], and the initial radius of the cracks $a_0/2c_0$ is 0.1 in this study. Besides, the multiple crack propagations at the same seam was observed by the inspection, but they are mutually independent without coalescence. Therefore, the effect of multiple crack propagations at the same seam is ignored in the crack simulation process to facilitate the study of the mutual relationship between multiple failure modes before and after reinforcement.

The numerical simulations of fatigue crack should fully coincide with the fatigue crack initiation and propagation in the specimens (see Fig. 10) as below

(1) When the rib-to-deck joint was subjected to cyclic loading for a period of time, a visible crack was formed at the weld root, and a microcrack was formed at the weld toe as well (see Fig. 16(a)).

(2) After internal repair welding, the root-deck crack was changed into an internal defect, and the finite element model and sub-model were updated. It is assumed that the shape of the intrinsic root-deck crack remains unchanged except that the weld root is welded, as shown in Fig. 16(b).

(3) At last, the toe-deck crack at the exterior weld toe of reinforced joint still grows under cyclic loading, as shown in Fig. 16(c).

The comparison between the measured and simulated cracks of SRD-I in Stage I is shown in Fig. 17. The location and dimensions of the simulated crack are basically consistent with the maximum depth of the actual measured crack.

3.3. Result discussion

The stress intensity factor amplitudes at the crack tip before and after reinforcement are investigated, as shown in Fig. 18. The reduction of stress intensity factor for root-deck crack after repairing is basically 70%. Although the stress intensity factor amplitudes of the root-deck crack in SRD-I after repairing are greater than the propagation threshold $63 \text{ MPa mm}^{1/2}$ [37], a crack propagation of 1 mm along the direction of depth needs 1,545,000 cycles with a stress intensity factor amplitude at the middle crack front (point B) of $107.5 \text{ MPa mm}^{1/2}$. At the same time, the crack growth per millimeter along the direction of length needs 1,217,000 cycles with a stress intensity factor amplitude at the point C of $116.4 \text{ MPa mm}^{1/2}$. Similarly, the stress intensity factor amplitudes of the root-deck crack in SRD-II after repairing are greater than the propagation threshold as well. A crack propagation of 1 mm along the direction of depth in SRD-II needs 1,292,000 cycles with a stress intensity factor range at the point B of $114.1 \text{ MPa mm}^{1/2}$. The crack growth per millimeter along the direction of length needs 1,116,000 cycles with a stress intensity factor amplitude at the point C of $119.8 \text{ MPa mm}^{1/2}$. However, the stress intensity factor amplitude

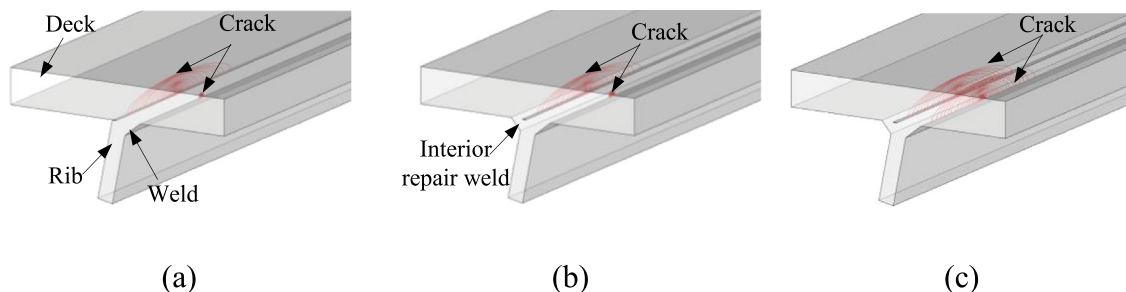


Fig. 16. Numerical simulation of crack propagation: (a) before interior repair welding; (b) interior repair welding; (c) after interior repair welding.

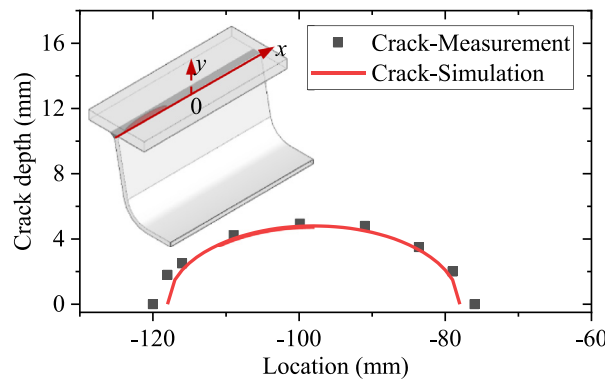


Fig. 17. Numerical simulation of crack shape of SRD-I in Stage I.

at the weld toe keeps increasing in Stage II, and the crack propagation rate continues to accelerate, gradually becoming the dominant crack.

In Stage I, for both SRD-I and SRD-II, the stress intensity factor amplitudes of toe-deck crack increases slowly at first, then increases rapidly and finally increases slowly with the rise of cycles. With the continuous propagation of the root-deck crack, the stresses at the weld toe are continuously reduced (see Figs. 8(b) and (d)), resulting in the decrease of the toe-deck crack propagation rate. Fig. 19 shows the

stress distribution of the exterior weld toe at SRD-I without the root-deck crack, with the root-deck crack, and with the interior repair welding. In Stage II, the stresses at exterior weld toe after reinforcement are redistributed, leading to a jump in the stress intensity factor range of toe-deck crack, and the crack propagation rate of toe-deck crack is faster after repair than before enhancement. Besides, the toe-deck crack propagation rate in the depth direction has a downward tendency after a certain number of cycles, while toe-deck crack propagation rate in the length direction remains an upward tendency under cyclic loading, resulting in a several times difference between depth and length of crack reported in [28,35–37]. Compared with the toe-deck crack, the root-deck crack propagation rate of rib-to-deck joint can be ignored. The interior repair weld seriously retards the propagation of the root crack.

It can be seen that the toe-deck crack propagation becomes the dominant cracking mode after interior repair welding, and considering the damage accumulation before and after reinforcement is necessary for the evaluation of welded joints with multiple failure modes.

3.4. Remaining life

The crack propagations of those specimens at Stage I and II as the number of cycles increases are shown in Fig. 20. The initial crack depths at the weld toe and root in the different specimens with the different crack propagation locations are determined by the monitored strain data. Then, the remaining lives of reinforced SRD-I and SRD-II

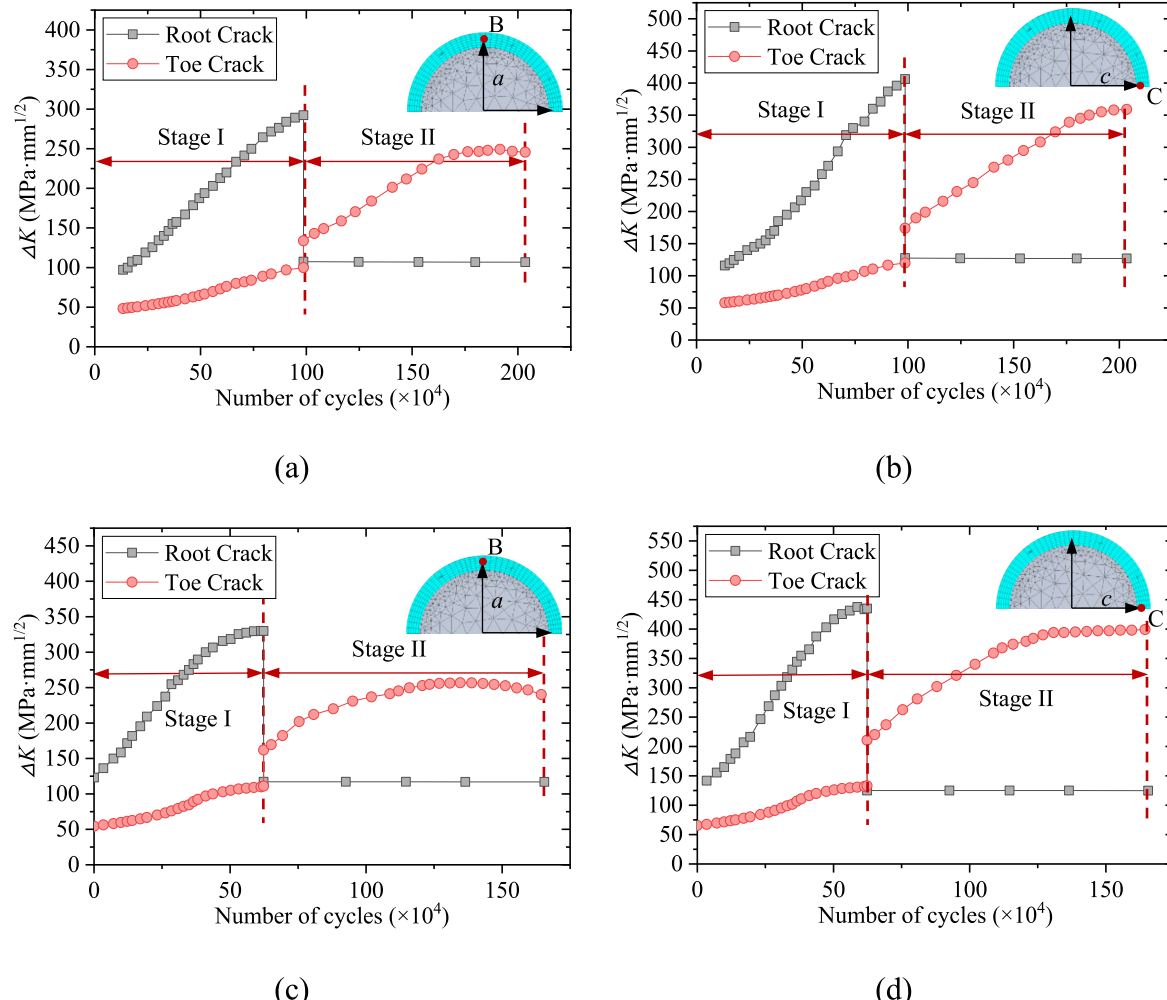


Fig. 18. The amplitude of stress intensity factor versus: (a) the cycles of SRD-I at point B; (b) the cycles of SRD-I at the point C; (c) the cycles of SRD-II at the point B; and (d) the cycles of SRD-II at the point C.

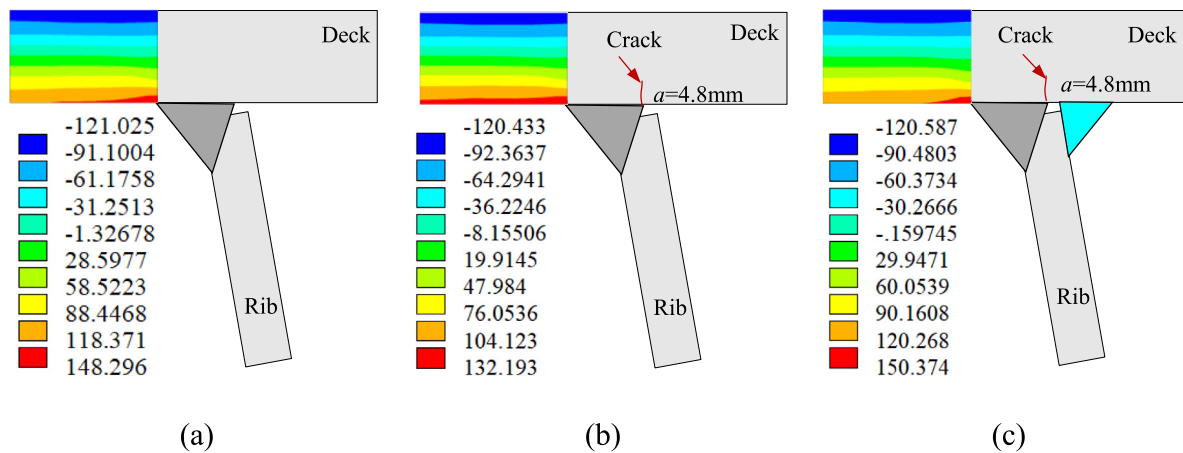


Fig. 19. The stress state of the exterior weld toe at SRD-I: (a) without root-deck crack; (b) with root-deck crack; and (c) after interior repair welding.

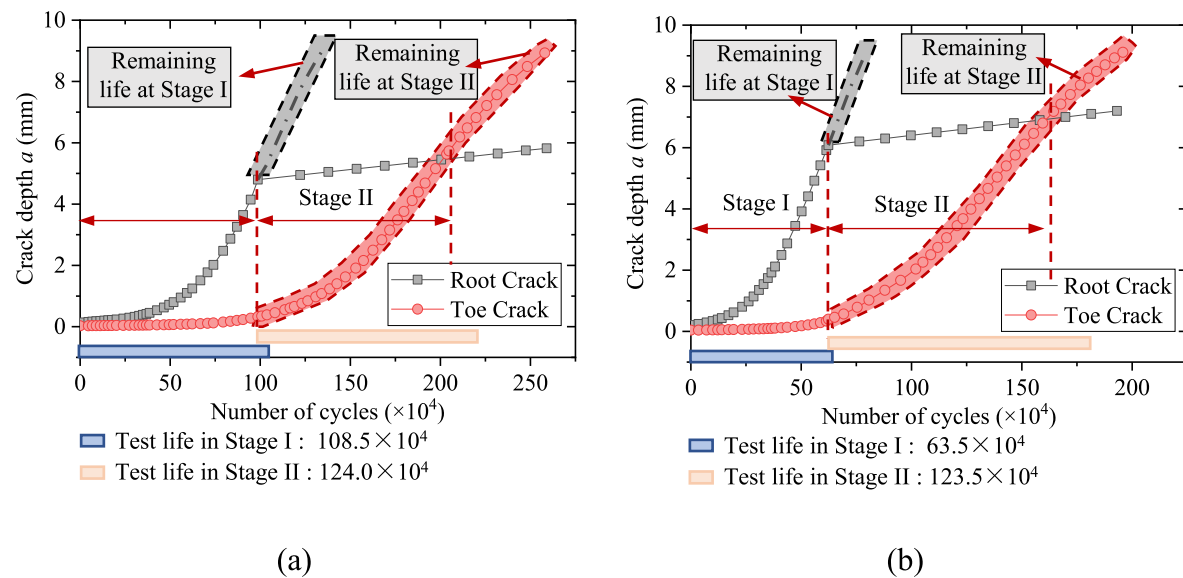


Fig. 20. The crack depth versus cycles curves for: (a) SRD-I; (b) SRD-II.

are simulated using the aforementioned method. The depth of root-deck crack in SRD-I grew to 4.8 mm at the end of Stage I, and the depth of toe-deck crack propagated to 0.32 mm. For SRD-II, the root-deck crack propagated to 6.1 mm at the end of Stage I, while the toe-deck crack extended to 0.4 mm. The depths of root-deck and toe-deck cracks at the end of Stage I are the initial cracks in Stage II. To uniformly evaluate the remaining life of welded joints, the critical crack depth in Stage II for numerical simulation is set as the half thickness of the deck plate in this study. Comparing to the experimental results of fatigue life of SRD-I and SRD-II in Table 2, the deviations of prediction results are 7.8% and 10.2%, respectively. It can be considered that the predicted results are in good agreement with the experimental values, due to the complex influencing factors of the crack propagation.

As a comparison, the crack propagation of those specimens without repairing was also simulated. It can be seen that the interior repair weld considerably prevents the propagation rate of root-deck crack and improves the fatigue life. The fatigue life is decided by the propagation of the exterior toe-deck crack after repairing. The remaining life of SRD-I is about 360,000 without repairing after cyclic loading in stage I. After interior repair welding, the remaining life increases to about 1,780,000, which is about 5 times as long as that without interior repair welding. The remaining life of SRD-II jumps from about 160,000 to more than 1,330,000 after considering the interior repair, resulting in

an increasing of more than 8 times. The fatigue lives of SRD-I and SRD-II are sharply improved by the interior repair welding. The calculated depths of root-deck and toe-deck cracks at the end of Stage I are equivalent to the existing fatigue damages at the weld toe in the calculation of remaining lives. The existing fatigue damage is the main reason for the dominant failure mode transferred from interior root-deck crack to exterior toe-deck crack after the interior repair welding. Considering crack propagation behaviors of each mode before reinforcement is the necessary condition for acceptance of the reinforced design.

4. Conclusions

Based on analytical and experimental studies, the following conclusions are drawn:

- (1) The interior repair weld can effectively prevent the root-deck crack propagation, and the dominant failure mode transferred from interior root-deck crack to exterior toe-deck crack after the interior repair welding. Oppositely, failure mode at the double-sided welded rib-to-deck joint was the interior toe-deck crack.
- (2) The remaining lives of SRD-I and SRD-II with or without the interior repair welding are compared by the association of the fracture mechanics. The remaining lives of SRD-I and SRD-II after interior repair welding are respectively about 5 and 8 times that without the interior

repair welding. The interior repair weld significantly improves the fatigue life of the rib-to-deck joints.

CRediT authorship contribution statement

Ming-zhe Li: Writing – review & editing, Writing – original draft, Validation, Investigation. **Chuang Cui:** Writing – review & editing, Writing – original draft, Validation, Resources, Funding acquisition. **Hao Wang:** Visualization, Validation, Investigation. **Qing-hua Zhang:** Writing – review & editing, Funding acquisition, Conceptualization. **Letian Da:** Visualization, Validation, Investigation. **Yi-zhi Bu:** Writing – review & editing, Project administration.

Declaration of competing interest

The authors declare that they have no known competing financial interests or personal relationships that could have appeared to influence the work reported in this paper.

Data availability

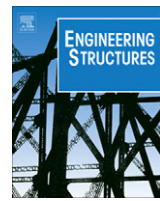
Data will be made available on request.

Acknowledgments

This work was supported by the Research and Development Projects in Key Areas of Guangdong Province, China [grant number 2019B111106002], National Natural Science Foundation of China [grant numbers 52108176, 51978579, 51878561], Sichuan Science and Technology Program, China [grant number 2021YJ0037], the Transportation Science and Technology Project of Sichuan Province [grant number: 2020-B-02] and National Key Research and Development Program of China [2022YFB3706405].

References

- [1] C. Wang, Y. Wang, Effectiveness and durability evaluation of cold reinforcement for Distortion-induced fatigue in steel bridges, *Eng. Fail. Anal.* 135 (2022) 106107.
- [2] M.H. Kolstein, Fatigue Classification of Welded Joints in Orthotropic Steel Bridge Decks, Delft University of Technology, Delft, 2007.
- [3] J. Fisher, J. Barsom, Evaluation of cracking in the rib-to-deck welds of the BronxWhitestone Bridge, *J. Bridge Eng.* 21 (3) (2015) 04015065.
- [4] M. Ahmadivala, J. Berthelemy, O. André, et al., A strategy for rib-to-deck crack propagation analysis and strengthening of orthotropic deck bridges, *Eng. Fail. Anal.* 134 (2022) 106057.
- [5] D.L. Wang, C. Xiang, Y.H. Ma, et al., Experimental study on the root-deck fatigue crack on orthotropic steel decks, *Mater. Des.* 203 (2021) 109601.
- [6] S. Kainuma, M.Y. Yang, Y.S. Jeong, et al., Experiment on fatigue behavior of rib-to-deck weld root in orthotropic steel decks, *J. Construct. Steel Res.* 199 (2016) 113–122.
- [7] Editorial Department of China Journal of Highway and Transport, Review on China's bridge engineering research: 2021, *China J. Highw. Transp.* 34 (02) (2021) 1–97 (in Chinese).
- [8] Z.Q. Fu, Q.D. Wang, B.H. Ji, et al., Rewelding repair effects on fatigue cracks in steel bridge deck welds, *J. Perform. Constr. Facil.* 31 (6) (2017) 04017094.
- [9] J.E. Rodriguez-Sanchez, W.D. Dover, Brennan, Application of short repairs for fatigue life extension, *Int. J. Fatigue* 26 (2004) 413–420.
- [10] Y. Lu, F. Yang, T. Chen, H. Gong, The retardation effect of combined application of stop-hole and overload on sheet steel, *Int. J. Fatigue* 132 (2020) 105414.
- [11] C. Wang, M. Zhai, L. Duan, Y. Wang, Cold reinforcement and evaluation of steel bridges with fatigue cracks, *J. Bridge Eng.* 23 (04) (2018) 04018014.
- [12] Z.Q. Fu, B.H. Ji, X.M. Kong, et al., Grinding treatment effect on rib-to-roof weld fatigue performance of steel bridge decks, *J. Perform. Constr. Facil.* 129 (2017) 163–170.
- [13] K. Yamada, T. Ishikawa, T. Kakiuchi, Rehabilitation and improvement of fatigue life of welded joints by ICR treatment, *Adv. Steel Constr.* 11 (3) (2015) 294–304.
- [14] Q.H. Zhang, Y.M. Liu, Y. Bao, et al., Fatigue performance of orthotropic steel-concrete composite deck with large-size longitudinal U-shaped ribs, *Eng. Struct.* 150 (2017) 864–874.
- [15] S.L. Wang, Z.T. Ke, Y. Gao, et al., Long-term in Situ performance investigation of orthotropic steel bridge deck strengthened by SPS and RPC solutions, *J. Bridge Eng.* 24 (6) (2019) 04019054.
- [16] J. Liu, T. Guo, D. Feng, Z. Liu, Fatigue performance of rib-to-deck joints strengthened with FRP angles, *J. Bridge Eng.* 23 (9) (2018) 04018060.
- [17] Y.Z. Wang, C.S. Wang, L. Duan, Bonding and bolting angle reinforcement for distortion-induced fatigue in steel girder bridges, *Thin-Walled Struct.* 166 (2021) 108027.
- [18] Y. Wang, X.D. Shao, J. Chen, et al., UHPC-based strengthening technique for orthotropic steel decks with significant fatigue cracking issues, *J. Construct. Steel Res.* 176 (2021) 106393.
- [19] F.B.P. DeJong, Renovation Techniques for Fatigue Cracked Orthotropic Steel Bridge Decks, Delft University of Technology, Delft, 2007.
- [20] J. Maljaars, F.V. Dooren, H. Kolstein, Fatigue assessment for deck plates in orthotropic bridge decks, *Steel Constr.* 5 (2) (2012) 93–100.
- [21] S. Teixeira, H. Kolstein, F. Bijlaard, Fatigue assessment of full-scale retrofitted orthotropic bridge decks, *J. Bridge Eng.* 22 (11) (2017) 04017092.
- [22] J.H. Choi, D.H. Kim, Stress characteristics and fatigue crack behaviour of the longitudinal rib-to-cross beam joints in an orthotropic steel deck, *Adv. Struct. Eng.* 11 (2) (2008) 189–198.
- [23] Z.G. Xiao, K. Yamada, S. Ya, et al., Stress analyses and fatigue evaluation of rib-to-deck joints in steel orthotropic decks, *Int. J. Fatigue* 30 (8) (2008) 1387–1397.
- [24] P. Wang, X. Pei, P. Dong, S. Song, Traction structural stress analysis of fatigue behaviors of rib-to-deck joints in orthotropic bridge deck, *Int. J. Fatigue* 125 (2019) 11–12.
- [25] J. Luo, X. Shao, J. Cao, M. Xiong, W. Fan, Transverse bending behavior of the steel-UHPC lightweight composite deck: Orthogonal test and analysis, *J. Construct. Steel Res.* 162 (2019) 105708.
- [26] Y. Liu, F. Chen, N. Lu, L. Wang, B. Wang, Fatigue performance of rib-to-deck double-side welded joints in orthotropic steel decks, *Eng. Fail. Anal.* 105 (2019) 127–142.
- [27] H. Yang, P. Wang, H. Qian, S. Niu, P. Dong, An experimental investigation into fatigue behaviors of single- and double-sided U rib welds in orthotropic bridge decks, *Int. J. Fatigue* 159 (2022) 106827.
- [28] C. Cui, Y. Ma, Q.H. Zhang, L.T. Da, S.H. Han, Fatigue strength and crack growth of double-side welded rib-to-deck joint in orthotropic steel decks, *J. Construct. Steel Res.* 196 (2022) 107444.
- [29] J. Li, Research on Formation Mechanism and Performance Evaluation of Dominant Fatigue Failure Modes of Orthotropic Steel Deck, Southwest Jiaotong University, Chengdu, 2021 (in Chinese).
- [30] K. Pang, H. Yuan, Assessment of three-dimensional multi-crack propagation for fatigue life prediction, *Int. J. Press. Vessels Pip.* 198 (2022) 104660.
- [31] W. Taleb, C. Gardin, C. Sarrazin, 3D predictions of the local effective stress intensity factor as the fatigue crack propagation driving force, *Int. J. Fatigue* 151 (2021) 106365.
- [32] BS 7910: Guide to Methods for Assessing the Acceptability of Flaws in Metallic Structures, BSI Standards Limited, London, 2015.
- [33] R.J. Nuismer, An energy release rate criterion for mixed mode fracture, *Int. J. Fract.* 11 (2) (1975) 245–250.
- [34] C. Cui, Y. Xu, Q. Zhang, Multiscale fatigue damage evolution in orthotropic steel deck of cable-stayed bridges, *Eng. Struct.* 237 (2021) 112144.
- [35] T. Agoda, K. Gowacka, Fatigue life prediction of welded joints from nominal system to fracture mechanics, *Int. J. Fatigue* 137 (2020) 105647.
- [36] Z. Barsoum, I. Barsoum, Residual stress effects on fatigue life of welded structures using LEFM, *Eng. Fail. Anal.* 16 (2019) 449–467.
- [37] B. Wang, W. Nagy, H. De Backer, A. Chen, Fatigue process of rib-to-deck welded joints of orthotropic steel decks, *Theor. Appl. Fract. Mech.* 101 (2019) 113–126.



Fatigue behavior of welded coverplates treated with Ultrasonic Impact Treatment and bolting

Brian Vilhauer^a, Caroline R. Bennett^{b,*}, Adolfo B. Matamoros^{b,1}, Stanley T. Rolfe^b

^a910 Par Ln., Dell Rapids, SD 57022, United States

^bUniversity of Kansas, Civil, Environmental, and Architectural Engineering Department, 1530 W. 15th St., 2150 Learned Hall, Lawrence, KS 66045, United States

ARTICLE INFO

Article history:

Received 6 April 2010

Revised 23 February 2011

Accepted 4 September 2011

Available online 4 November 2011

Keywords:

Fatigue

Bolts

Welds

Cracking

Rehabilitation

Retrofit

Ultrasonic Impact Treatment

Cover plate

Steel bridge

ABSTRACT

Damage due to traffic-induced fatigue is a common problem in welded steel girder bridges. Engineers tasked with the duty of repairing fatigue-damaged bridges face difficult decisions about the choice of repair method to implement. In some instances different repair methods are used in combination, under the assumption that the combined effects of two techniques that have been shown separately to improve fatigue life will result in greater improvement. This study evaluated the interaction that may take place between different repair methods for a particular type of fatigue vulnerable detail. The detail that was chosen for the study was a welded connection between a plate and a coverplate, often used in older bridges. Specifically, this study investigated the fatigue life enhancement afforded by three retrofit methods: post-installation of tensioned bolts behind the weld, application of Ultrasonic Impact Treatment (UIT) to the weld, and a combination of the two techniques.

Results of 15 fatigue tests showed that UIT was a highly effective technique to enhance the fatigue life of coverplate end details. Weld treatment with UIT resulted in an improvement in fatigue life over control specimens by a factor of 25. This translated into an improvement in fatigue life from that of an AASTHO fatigue Category E detail to that of an AASHTO fatigue Category A detail. The bolting procedure, as implemented in this study, had a negligible effect on fatigue life. The combination of the two methods was found to be less effective than using UIT alone due to stresses induced by the bolt on the untreated portion of the weld.

© 2011 Elsevier Ltd. All rights reserved.

1. Introduction

Numerous aging steel highway bridges are currently developing cracks due to traffic-induced fatigue. Many of these bridges were designed at a time when little was known about the causes of fatigue crack initiation and propagation in steel structures. As a result, structural connection details having fatigue-vulnerable combinations of geometric discontinuities and large stress ranges were used in these structures. Many of these details are now recognized as undesirable and are no longer constructed. However, state Departments of Transportation (DOTs) must repair existing fatigue cracks and retrofit susceptible connection details. Due to the escalating costs of bridge replacement coupled with the large number of aging steel bridges with fatigue-susceptible details across the United States, means to efficiently extend the useable life of fatigue-prone steel bridges are critically needed.

Welded connections in steel bridge girders account for a large percentage of fatigue critical details in the national inventory. Welds are particularly susceptible to fatigue cracking because of planar or volumetric discontinuities often present in the weld or base metal, such as porosity, slag inclusions, lack of fusion, and undercut [1]. Additional factors such as geometry-induced stress concentrations, residual stresses, and distortion tend to decrease the fatigue strength of welded connections. This is particularly worthy of consideration given that many common steel bridge girder connections utilize welded connections in a wide range of applications, including cover plates, transverse and longitudinal stiffeners, connection plates, flange transitions, and web-to-flange connections.

Welded cover plates are of especial concern because this is a common detail particularly vulnerable to fatigue damage. Although welded coverplates are no longer commonly used to increase bending resistance of bridges, this was not the case 40 years ago. Many existing bridges were retrofitted with welded coverplates to increase their capacity as traffic loads intensified over time. It has since been found that welded cover plates tend to be particularly susceptible to fatigue crack initiation in the welds at cover plate terminations, and for this reason have been

* Corresponding author. Tel.: +1 (785) 864 3235; fax: +1 (785) 864 5631.

E-mail addresses: crb@ku.edu (C.R. Bennett), abm@ku.edu (A.B. Matamoros), srolfe@ku.edu (S.T. Rolfe).

¹ Tel.: +1 (785) 864 3235; fax: +1 (785) 864 5631.

Nomenclature

Σ_c	stress, MPa (ksi)	A	constant for a particular AASHTO fatigue detail category, MPa ³ (ksi ³)
c	distance from the neutral axis to an extreme fiber on the cross-section, mm (in.)	N	number of fatigue cycles to failure
I	bending moment of inertia, mm ⁴ (in. ⁴)	ΔF_{TH}	stress range corresponding to infinite life of a particular fatigue detail category, MPa (ksi)
δF_n	stress range, MPa (ksi)		

subsequently classified among the worst performing AASHTO fatigue Categories E and E' [2–4].

Improved practices have since emerged for retrofitting susceptible welded coverplates and for installing new cover plates with better performing fatigue details. One mechanism for improving performance of cover plates is to extend the coverplate into a region of compressive stress or to an inflection point, where tensile stress ranges are negligible. Another method is to remove end welds and develop the full moment capacity of the cover plate through a bolted connection. The detail resulting from the latter technique is now classified as an AASHTO fatigue Category B detail [7].

Another accepted method for improving fatigue performance of welded connections that has been successfully applied to coverplates is Ultrasonic Impact Treatment (UIT) [8–10]. Ultrasonic Impact Treatment has been shown to reduce the likelihood of fatigue cracks in weldments by relaxing tensile residual stresses introduced during welding, and by smoothing imperfections on the surface of the weld. Both effects are achieved through application of ultrasonic stress waves at the surface of the weld. The stress waves induce plastic deformations, which leave a residual compressive stresses on the order of the yield strength of the weld metal near the surface of the weld. Because fatigue cracks form primarily at imperfections in regions subjected to high tensile stress ranges, introduction of large compressive stresses and the smoothing of the surface greatly retard and may eliminate formation of fatigue cracks at the location of treatment. Since UIT is generally performed at regions having the greatest tensile stress concentrations, usually weld toes and weld discontinuities, the regions most prone to fatigue crack growth benefit the most from induced compressive stresses. When UIT treatment is performed at the toe of a fillet weld, the change in shape of the zone of plastic deformation also reduces the concentration of stress at the weld toe, as the treated surface has a larger radial shape than does an untreated weld toe.

2. Research significance and objective

The objective of the study was to investigate the effectiveness and interaction of various repair methods on the fatigue life of a commonly used fatigue-vulnerable connection detail. The specific repair methods evaluated were Ultrasonic Impact Treatment (UIT) of the weld, installation of tensioned bolts behind the weld, and the combination of UIT of the weld and installation of tensioned bolts. A cover plate detail was chosen for study because of the prevalence of this detail in aging steel bridges, its simplistic geometric configuration and design, and its poor fatigue performance.

Installation of bolts in an existing welded coverplate as a fatigue strengthening method requires removal of the weld at the coverplate ends so that load transfer can take place through the bolts instead of the weld. Improvements in fatigue life due to post-installation of bolts coupled with weld removal are well documented in studies by Yamada and Albrecht [3] and Simon and Albrecht [4]. In the present study, rather than expand on the fatigue related benefits of post-installing bolts in cover plates, the welds were left in place to study the interaction between post-installed tensioned bolts and welded connections treated

with UIT. For example, fatigue cracks were observed in a bridge in Kansas at connections between gusset plates from cross-bracing and girder flanges [5,6]. These connections developed a prying effect due to deformations imposed by the cross brace on the girder flange that caused fatigue cracks. Bolts were post-installed to counteract the prying effect, but questions remained about the beneficial effects of treating the welds with UIT.

3. Experimental program

Fifteen welded steel specimens, each representative of a girder flange with a welded cover plate, were fabricated using Grade A36 steel. Of those 15 specimens, six were control specimens receiving no treatment (designated CONTROL), three were treated with UIT along the weld toe at the cover plate ends (designated UIT), three had tensioned bolts installed near both ends of the coverplate (designated BOLT), and three had both UIT and tensioned bolts installed near both ends of the coverplate (designated UIT/BOLT). The 15 specimens were fabricated in two batches: the first batch was comprised of 12 steel specimens, after which a second batch comprised of three additional control specimens was fabricated.

3.1. Steel specimen design and testing program

A schematic of the steel specimens is provided in Fig. 1. A bar with dimensions PL 25.4 × 114 × 1270 mm (PL 1.00 × 4.50 × 50.0 in.) was chosen for the plate representing the girder flange, and a bar with dimensions PL 25.4 × 76.2 × 660 mm (PL 1.00 × 3.00 × 26.0 in.) was chosen for the coverplate element. The coverplate element was chosen to be as wide as possible while still allowing ample flange surface on each side to accommodate the fillet weld, while the length was chosen considering shear lag effects and St. Venant's Principle. Shielded metal arc (SMAW) 7.94-mm (0.313 in.) fillet welds were used to connect the coverplates to the flanges, with the weld applied all-around the coverplate element. This weld size and configuration are commonly used for welding bridge coverplates because it is the largest size fillet weld that can be laid in a single pass. The primary purpose of the experimental program was to compare fatigue behavior of treated and untreated specimens. Although not essential to the outcome, AASHTO detail categorization is presented here to provide a frame of reference for the results of the study. To account for the fact that the neutral axis of the cross-section was within the flange plate (rather than far above the weld toe, in the web or top flange), nominal stresses were calculated directly at the weld toe to reflect the normal bending stress at that specific location. Therefore, a stress range reported as 138 MPa (20.0 ksi) implies that this was the nominal tensile bending stress value calculated for a bare steel specimen at the toe of the weld.

After the steel substrate specimens were fabricated, tensioned bolts were post-installed at both ends of the coverplate for six of the specimens. For each coverplate retrofitted with bolts, a 25.4-mm (1.00-in.) diameter ASTM A325 carriage bolt was installed at both coverplate ends. The bolts were tightened using a calibrated pneumatic wrench to have a minimum bolt tension of 227 kN (51.0 kips), the standard minimum bolt tension specified for this

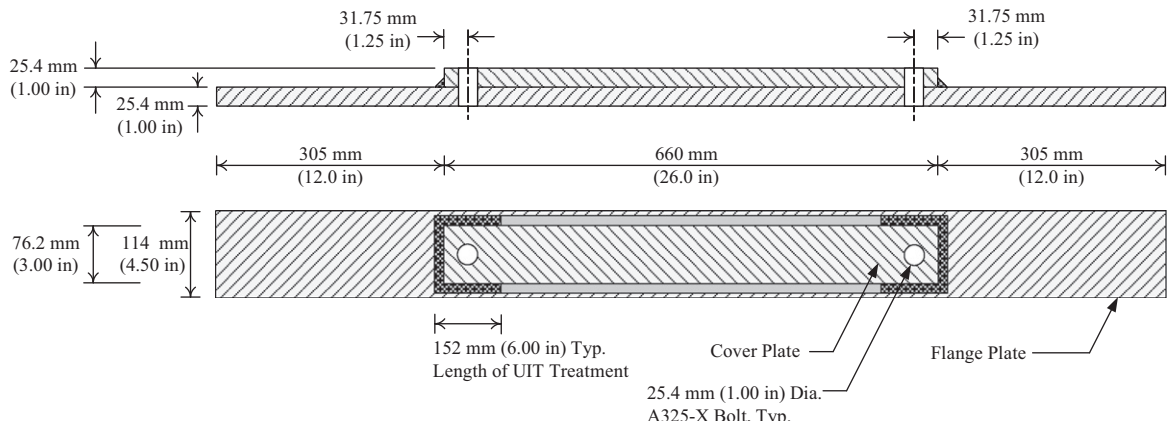


Fig. 1. Schematic of Category E' fatigue specimen.

size and grade of bolt by the American Institute of Steel Construction (AISC) [11]. The bolts were each installed with a standard flat washer on the nut-side of the connection. Because one of the reasons for installing a bolt at the end of a coverplate was to study the influence of bolt tension on the fatigue performance of the weld, the bolts were placed as close as possible to the ends of the coverplates. Therefore, the holes for the bolts were placed at the minimum edge distance of 31.8 mm (1.25 in.), measured from the edge of the coverplate to the center of the hole [11].

Each of the six specimens treated with UIT received treatment at both ends of the coverplate. Treatment was performed across the entire length of the transverse fillet weld and continued along the longitudinal fillet welds on both sides of the coverplate for a distance of 152 mm (6.00 in.), as pictured in Fig. 2. The interior portions of the longitudinal fillet welds did not receive UIT because these segments of the weld were not as prone to fatigue failure as the welds at the coverplate ends (Cat. C as opposed to Cat. E'). At the ends of each treated coverplate, additional UIT treatment was performed at points where stress concentrations were expected to exist, such as weld terminations.

3.2. Stress range

The procedure outlined in the AASHTO LRFD Bridge Design Specification [7] to design bridge members against fatigue failure

is a process that involves selecting a fatigue category for a member or connection detail and then determining the number of load cycles that the member or connection will be subjected to during its design life. Assigning a fatigue category is a method of quantifying the susceptibility of a member or connection to fatigue failure. AASHTO differentiates between eight fatigue categories based primarily on geometry, listed here in order of increasing severity: A, B, B', C, C', D, E, and E'.

After a member or connection has been assigned a fatigue category and the design fatigue life has been determined, a nominal design stress range for that member or connection detail can be calculated using the fatigue life equation in the 2007 AASHTO LRFD Bridge Design Specification [7]:

$$\Delta F_n = \left(\frac{A}{N} \right)^{\frac{1}{3}} \geq \frac{1}{2} (\Delta F)_{TH} \quad (1)$$

where ΔF_n is the stress range, A is a constant for a given detail defined by AASHTO [7], N is the number of fatigue cycles to failure, and $(\Delta F)_{TH}$ is the constant-amplitude fatigue threshold. The equation is an approximation of logarithmic behavior, with the $^{1/3}$ factor defining the slope constant for the $S-N$ curves. The coefficient of $\frac{1}{2}$ on the right hand side of Eq. (1) ensures that when the design stress range is less than half of the constant-amplitude fatigue threshold, the connection detail or member will theoretically have an infinite fatigue life [12].

A literature review was conducted to estimate the increase in fatigue life associated with the retrofit methods evaluated in this study. On this basis a nominal tensile stress range at the transverse weld toe of 59 MPa (8.5 ksi) was initially chosen for the fatigue tests. For reasons discussed later, this stress range was increased gradually to 96.5 MPa (14.0 ksi), 138 MPa (20.0 ksi), and finally to 193 MPa (28.0 ksi). It should be noted that the final stress range was larger than the constant amplitude fatigue threshold for a Category A detail, which meant that the testing program had the ability to detect potential improvements in fatigue categorization up to and including Category A details.

In the course of selecting the final stress range, all three control specimens from the initial fabrication batch were tested at stress ranges lower than 193 MPa (28.0 ksi), leaving no control specimens to be tested at the final stress range. Therefore, three additional control specimens were fabricated by the same fabricator that produced the original 12 specimens. Upon visual inspection, the fillet welds on the second batch of control specimens appeared to be slightly smaller, less consistent, and of lower overall quality than the welds on the 12 original specimens. For this reason, one of the control specimens from the second fabrication batch was tested at a nominal stress range at the weld toe of 138 MPa

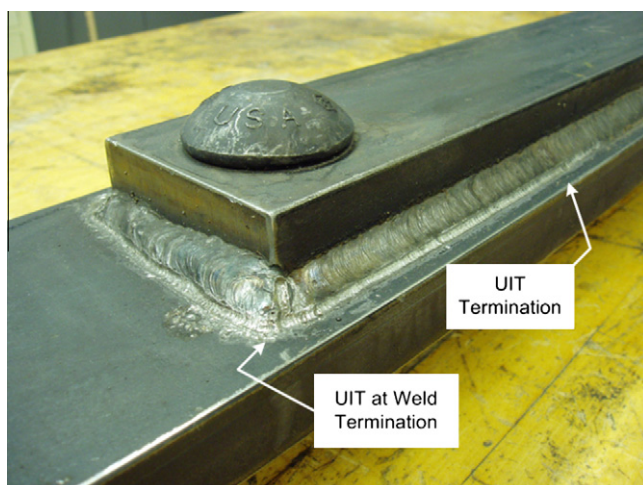


Fig. 2. Weld treated with Ultrasonic Impact Treatment; tensioned bolt installed behind an existing weld at coverplate end.

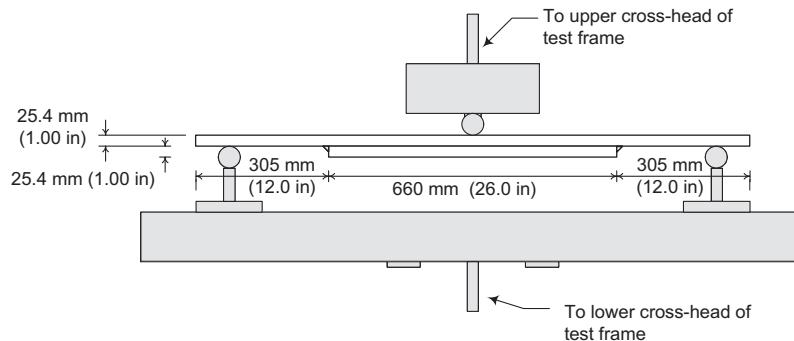


Fig. 3. Experimental three-point bending fatigue test set-up.

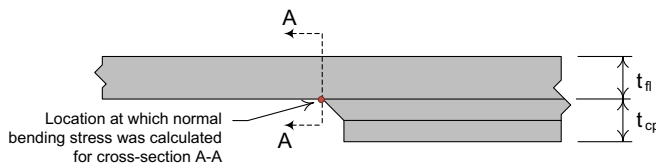


Fig. 4. Location of weld toe stress calculation.

(20.0 ksi), and the results were compared to the fatigue life of a control specimen from the first batch tested at a stress range of 138 MPa (20.0 ksi). This was done to ensure that the control specimens from the first and second fabrication batches had similar fatigue behavior. The other two control specimens from the second fabrication batch were tested at 193 MPa (28.0 ksi), bringing the number of specimens tested at 193 MPa (28 ksi) to 10, and total number of specimens tested to 15.

All stress ranges reported in this study are based on calculations for theoretical stress at the weld toe of the fatigue specimens. The test configuration was such that the specimens were statically determinate, with a load at the center (Fig. 3). Consequently, for an applied force, P , the moment diagram was linear with the maximum moment occurring at the center of the beam. Based on the known geometric cross-section properties of the fatigue specimens, the moment at the weld toe was computed and used to calculate the nominal stress at the weld toe using the familiar expression from beam theory:

$$\sigma = \frac{Mc}{I} \quad (2)$$

The bending moment of inertia, I , was calculated based on dimensions of the flange plate only, because the nominal bending stress being calculated was at the toe of the weld, as shown in Fig. 4. The distance from the neutral axis to the extreme fiber of interest, c , was therefore taken as 12.7 mm (0.50 in.). The bending moment, M , was taken as the moment at the location of the weld toe caused by the applied force (section A-A in Fig. 4). The loads applied to the specimens were chosen to achieve various nominal stress ranges at the location of the weld toe, as reported in Tables 1 and 2.

Differences between the configuration of a plate girder with a coverplate and the specimens evaluated in this study bring about differences in the stress demand on the weld. For example, in a welded connection between a plate girder and a coverplate, the weld is located in an area where the horizontal shear due to bending is likely to be very small. In the specimens used in this study the weld is located near the neutral axis of the specimen, in an area where the shear stresses caused by bending are close to maximum, posing a more stringent fatigue loading condition.

Table 1
Fatigue testing results for ISR specimens.

Specimen ID	Stress range, MPa (ksi)	Cycles to initiation	Cycles to complete propagation failure
CONTROL 1	96.5 (14.0)	2,160,000 ^a	Not achieved
CONTROL 2	58.6 (8.50)	3,850,000 ^a	Not achieved
CONTROL 3	138 (20.0)	500,000	Not achieved
CONTROL 4	138 (20.0)	350,000	Not achieved
UIT 1	138 (20.0)	5,000,000 ^a	Not achieved

^a Achieved run-out.

4. Finite element modeling

Finite element analyses were performed using the commercial software package ABAQUS v.6.6.1 with the primary goal of examining the state of stress at the transverse welds. Two models were developed simulating the behavior of a specimen with a post-installed tensioned bolt: one model was loaded only with the bolt pressure (referred to as the “bolted” model), and the other model simulated behavior of a specimen with a load at midspan, also including the bolt load (referred to as the “bolt/bending” model).

The finite element model geometry was constructed using three-dimensional tetrahedral elements to depict half of the fatigue specimen, taking advantage of the symmetry of the specimen about the center. The mesh was comprised of approximately 50,000 nodes and 250,000 elements. The steel was modeled using an elastic-perfectly-plastic material model. The yield strength was obtained by performing 10 tension tests in accordance with ASTM E8 [13] on coupons obtained from the Gr. A36 steel bars used to fabricate the fatigue specimens.

The entire half-specimen was modeled as a single three-dimensional part instance instead of constructing the model from separate part instances and connecting them using tie constraints or other available connection techniques. Because the physical specimens had an unbonded interface between the flange and the cover plate, a slit measuring 76.2 mm (3.00 in.) wide \times 0.03 mm (0.001 in.) high \times 331 mm (13.0 in.) deep was placed in the center of the model to simulate an initial separation between the surfaces of the flange and coverplate. Because of the very shallow height of the slit, the two surfaces created by this slit came into contact as soon as the center load was applied to the model. Contact properties for the two surfaces of the slit were defined as true surface-to-surface hard contact in the direction normal to the surfaces. Commonly accepted static and dynamic coefficients of friction of 0.74 and 0.57, respectively, for steel-to-steel contact were used to define tangential behavior between the two surfaces.

To simulate contact between the specimen and the middle loading round in the test apparatus, the bottom edge of the flange at the specimen centerline was fixed against translation in three

Table 2

Fatigue testing results for HSR specimens.

Specimen ID	Stress range, MPa (ksi)	Cycles to initiation	Average cycles to initiation	Total cycles to failure
CONTROL 5	193 (28.0)	80,000 ^a	65,000	290,000
CONTROL 6	193 (28.0)	50,000		Not achieved
BOLT 1	193 (28.0)	80,000 ^a	70,000	530,000
BOLT 2	193 (28.0)	50,000		300,000
BOLT 3	193 (28.0)	70,000		400,000
UIT 2	193 (28.0)	1300,000	1700,000	Not achieved
UIT 3	193 (28.0)	2100,000		Not achieved
UIT/BOLT 1	193 (28.0)	550,000	1000,000	2400,000
UIT/BOLT 2	193 (28.0)	1070,000		Not achieved
UIT/BOLT 3	193 (28.0)	1370,000		Not achieved

^a Cycle count to crack initiation determined using stiffness monitoring technique.

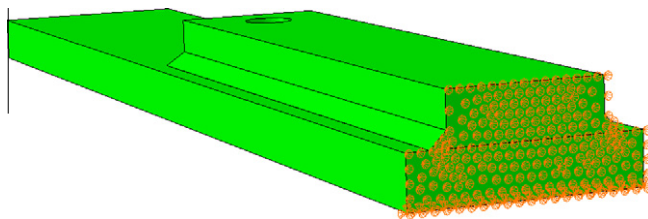


Fig. 5. View of finite element model, showing boundary conditions representing symmetry.

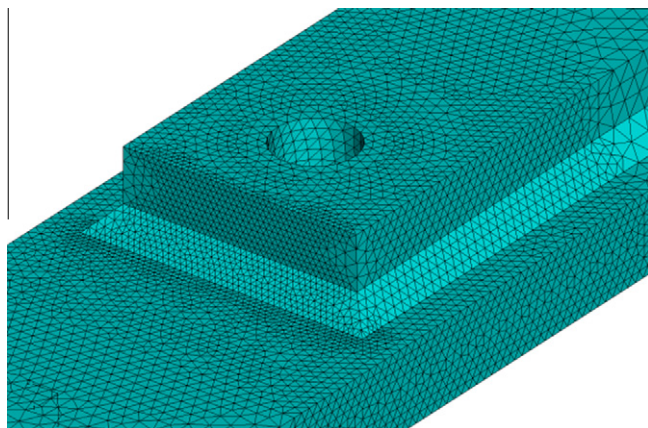


Fig. 6. View of finite element model containing pressures applied from a tensioned bolt.

directions. The boundary conditions at the center of the specimen (axis of symmetry) were defined so the entire cross-sectional surface at the specimen centerline was fixed against translation in the direction parallel to the longitudinal axis, and unrestrained in the other two directions, allowing displacements due to Poisson's effect in the two directions orthogonal to the longitudinal axis. A third boundary condition was applied to simulate the outside two roller supports of the three-point-bending test fixture. Fig. 5 shows the boundary conditions used to represent symmetry within the specimen.

A 25.4-mm (1.00-in.) diameter cylinder of material was removed from the flange and coverplate near the transverse weld (see Fig. 6). Circular pressure loads concentric with the cylindrical bore were applied to the top of the coverplate and the bottom of the flange, simulating forces imposed by a post installed tensioned bolt. As previously indicated, simulations were performed with and without the pressure induced by the bolt with the goal of studying the effect of the bolt tension on the state-of-stress at the weld toe.

While residual stress distributions can readily be implemented into finite element analyses using standardized distributions, the implications of doing so should be carefully weighed with modeling objectives. For this investigation, residual stresses caused by the welding process were not modeled for the following reason. Stress patterns used for modeling residual stresses must always be based off of theoretical distributions that are unlikely to represent the real variations in residual stresses that are likely to exist between specimens, and even between different segments of welds in the same specimen. Rather than compounding errors in the modeling effort, it is believed that capturing changes in load- and bolt- induced stresses presents less complicated, and potentially less erroneous, results.

5. Results and discussion

Five of the 15 total specimens were tested at a nominal weld toe stress ranges of 58.6, 96.5, and 138 MPa (8.50, 14.0, and 20.0 ksi) before a final stress range of 193 MPa (28.0 ksi) was chosen for the remainder of the specimens. All specimens tested at a nominal weld toe stress range less than 193 MPa (28.0 ksi) are henceforth referred to as "Intermediate Stress Range (ISR) specimens". Specimens tested at the final stress range of 193 MPa (28.0 ksi) are referred to as "High Stress Range (HSR) specimens". Experimental and analytical results are presented in the following. Results for ISR and HSR specimens are presented separately for clarity.

5.1. Intermediate stress range (ISR) specimens

Results for intermediate stress range specimens are summarized in Table 1, and are presented on the AASHTO S-N diagram in Fig. 7. As previously mentioned, specimen designations were assigned according to the type of treatment used. For example, the CONTROL designation corresponds to untreated specimens and the UIT designation corresponds to specimens in which the welds were treated with UIT.

The first step of the experimental program was to test several specimens at different stress ranges. This was done to determine fatigue behavior of the untreated specimens and to determine the most appropriate stress range to evaluate the strengthening methods. The first fatigue specimen tested was designated CONTROL 2, and the nominal stress range at the weld toe for this specimen was 58.6 MPa (8.50 ksi). As a reference, the fatigue life for a stress range of 58.6 MPa (8.50 ksi) estimated with Eq. (1) is approximately 635,000 cycles. Fatigue cracks were not observed during the test and the specimen achieved run-out after 3.85 million cycles. The nominal weld toe stress range for the next specimen, designated CONTROL 1, was increased to 96.5 MPa (14.0 ksi). Fatigue cracks were not observed in this specimen either, and the specimen achieved run-out after 2.16 million cycles. The next

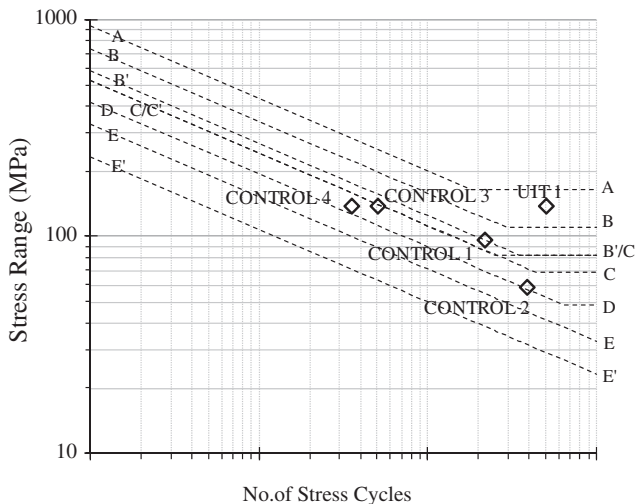


Fig. 7. S-N diagram of ISR specimen results.

specimen, designated CONTROL 3, was tested at a stress range of 138 MPa (20.0 ksi). For the first 930,000 cycles, visual inspection was performed with a dye penetrant following the standard method of inspection recommended by the manufacturer. Because load-deformation data at this point indicated that a reduction in stiffness had taken place, the method of inspection was modified to improve the ability to detect cracks. The modified inspection method differed from the manufacturer's procedure in that a developer was not utilized along with the dye penetrant. Instead, the dye penetrant was applied to the weld surface, allowed to rest briefly, then wiped off. Under the presence of a ultraviolet light, surging of the liquid dye could easily be seen, indicating opening of the crack. The presence of a 6.4 mm (0.25 in.) long crack was detected at the center of the weld toe with the modified inspection method. This rather large crack size clearly showed that crack initiation had indeed taken place prior to 930,000 cycles. In light of this, the initiation life of this specimen was estimated based on observed trends in recorded load and deflection data to be approximately 500,000 cycles. This was one of four specimens for which recorded load and deflection data were used to estimate crack initiation life. The remainder of the specimens were examined for cracks using the improved dye penetrant inspection method, and their corresponding fatigue crack initiation lives were based on the findings of those visual examinations.

The first treated specimen that was tested, UIT 1, was intended to investigate the improvement on fatigue crack initiation life associated with UIT of the welds at a nominal weld toe stress range of 138 MPa (20.0 ksi). Run-out was achieved after specimen UIT 1 reached 5 million cycles without detection of a crack. Although this run-out value was ten times greater than the crack initiation life of CONTROL 3, the goal of the project was to quantify improvement in fatigue life caused by the different treatment methods. Based on the results from these four tests, it was decided that all remaining fatigue tests would be performed at a nominal weld toe stress range of 193 MPa (28.0 ksi) so that as many specimens as possible would develop fatigue cracks instead of achieving run-out. The only exception was specimen CONTROL 4, which was tested at a nominal weld toe stress range of 138 MPa (20.0 ksi) to obtain a point of comparison for the fatigue life of the second batch of specimens.

Specimen CONTROL 4 sustained 350,000 cycles before a fatigue crack was detected. This value was 25% lower than the estimated crack initiation life of specimen CONTROL 3, which was part of the first fabrication batch of specimens and was also tested at a

nominal stress range of 138 MPa (20.0 ksi). The shorter crack initiation life of specimen CONTROL 4 is attributed to the fact that the welds on the three specimens from the second fabrication batch were of lower quality than the welds on the specimens from the first fabrication batch. Although there was a significant difference between the observed fatigue life of these two specimens from the first and second fabrication batches (CONTROL 3 and CONTROL 4), variations of this magnitude are expected in existing bridge structures due to the variability in the quality of welded connections across the national bridge inventory. For this reason, the fatigue lives of the two control specimens from the second fabrication batch tested at a nominal weld toe stress range of 193 MPa (28.0 ksi) were compared with the fatigue lives of the retrofitted specimens (which were part of the first fabrication batch) tested at a stress range of 193 MPa (28.0 ksi) without adjustment.

As evident from the S-N diagram depicted in Fig. 7, the fatigue lives of all intermediate stress range specimens exceeded the fatigue life calculated with the AASHTO fatigue design equation for a Category E' detail by a large margin, with data recorded at the level of Category D or better for each of the five specimens. Of the four ISR control specimens, the two specimens that did not achieve run-out failed after exceeding the AASHTO Category D design curve. Specimens CONTROL 2 and CONTROL 1 achieved the Category D and Category C ranges, respectively, before run-out was achieved. The ISR specimen treated with UIT achieved the AASHTO Category B range in the infinite-life region of the S-N diagram, before run-out.

To place these results into context, it is informative to examine the procedure used to develop the fatigue design equations in the AASHTO Code. Fatigue curves in the AASHTO Code were constructed based on results from numerous fatigue tests performed over a period of several decades, starting in the 1960s, on full-scale bridge girders employing various weld details. For each of the configurations tested, it was found that the presence of gouges and imperfections in a detail decreased the observed fatigue life. Consequently, there is significant variability inherent to the experimental data used to calibrate the AASTHO fatigue design equations. One of the origins of this variability is from details having identical geometric configuration but different size imperfections. For example, in one of the studies the longest fatigue life observed for a specific detail was approximately four times the shortest fatigue life observed for the same detail [1]. To ensure that an adequate margin of safety was incorporated into the design provisions, the AASHTO design equation for each detail category was calibrated so that the calculated fatigue life corresponded to the 95% confidence limit for 95% survival of all details included that category. Consequently, the AASTHO design equation for a given category represents an estimate of the fatigue life of a detail having the worst possible weld quality. The fillet welds tested in this study were determined to be of average quality or better. Given the strong correlation between weld quality and fatigue life, the fact that the specimens outperformed the AASHTO Category E' design curve by a significant margin even though their geometric configuration was similar to that of category E' details may be attributed in part to the high quality of the welds and the conservative nature of the AASHTO design curve.

In addition, different stress concentration factors exist within each fatigue design category as result of each category encompassing details with different geometric configurations. The AASTHO design curve for a given category approximately corresponds to the detail having the most vulnerable geometric configuration within the category, in addition to having the lowest weld quality. Coverplate elements on the specimens tested in the current program were only slightly thicker than the 20 mm (0.80 in.) limit that separates Category E' coverplate details from Category E coverplate details. For this reason, the geometric configuration of

the specimens tested in this study was less susceptible to fatigue damage than other Category E' details with thicker coverplates that were used in the calibration of the Category E' design curve. The combination of relatively high weld quality and less vulnerable geometric configuration accounts for the longer fatigue lives of the specimens.

The authors would like to emphasize that the main goal of this research study was to compare the performance of different strengthening techniques and the interaction between them. Reference to the AASHTO fatigue design categories is presented to provide a basis of comparison with a widely adopted classification. Although the fatigue classification of the specimen evaluated in this study may be the subject of debate, the specific fatigue design category adopted has no bearing on the relative performance of the strengthening techniques evaluated in the study.

5.2. High stress range (HSR) specimens

Results for HSR specimens tested at the stress range of 193 MPa (28 ksi) are provided in Table 2, and are shown superimposed on the AASHTO S-N diagram in Fig. 8.

The average fatigue life for the two control specimens tested at 193 MPa (28.0 ksi) was 65,000 cycles and the difference between their fatigue lives was 38%. It would have been ideal to select a stress range so that all specimens were loaded for at least 100,000 cycles prior to crack initiation, as suggested in the AASHTO [7] LRFD Bridge Design Specification. However, the large improvement in fatigue life displayed by the ISR UIT specimen dictated that the fatigue life of the control specimens had to be very short if the retrofitted specimens were to fail in a finite number of cycles.

The three bolted specimens were tested at a nominal weld toe stress range of 193 MPa (28.0 ksi). The average crack initiation life of the three bolted specimens was 70,000 cycles, and the difference between the least and greatest fatigue lives was 38%. The average crack initiation life for bolted specimens was nearly identical to the average initiation life of control specimens tested at the same weld toe stress range of 193 MPa (28.0 ksi). All control and bolted specimens tested at a weld toe stress range of 193 MPa (28.0 ksi) had an initiation life in the range of AASHTO [7] Category E details. Therefore, it is concluded that post-installing tensioned bolts at the ends of the coverplates without removing the welds had a negligible effect on fatigue life. The fact that fatigue life was unaffected was in part expected because without removal of the weld, load transfer was expected to take place primarily through the weld,

which was not strengthened in any fashion for these specimens. However, what these results have shown is that stresses induced by the post-installed bolts in the area surrounding the weld toe did not have a significant enough effect to improve or reduce the fatigue life of the connection.

All three of the bolted specimens were tested through crack propagation until complete failure of the specimen occurred. Specimen BOLT 1 failed completely at 530,000 cycles, BOLT 2 failed at 300,000 cycles, and BOLT 3 failed at 400,000 cycles, resulting in an average of 410,000 cycles to complete propagation failure. The length of the propagation life of each specimen appeared to be directly proportional to the length of the initiation life of that specimen. Specimens BOLT 1, BOLT 2, and BOLT 3 had propagation lives of 450,000 cycles, 250,000 cycles, and 330,000 cycles, respectively. Although the propagation lives of the three specimens were not equal, all were between 5.7 and 6.7 times longer than their respective initiation lives. These results indicated that a connection with a high-quality weld not only has a longer crack initiation life than a similar connection with a poor-quality weld, but it also has a somewhat slower rate of crack propagation rate. This phenomenon may be attributed to initiation and propagation of cracks at multiple locations in a weld of poor quality as opposed to a smaller number of locations in a weld of high quality. Because the nominal stress range would be identical for the two cases presented, the individual cracks in high-quality and poor-quality welds would be expected to propagate at equal rates after initiation. However, the presence of numerous and intersecting cracks in a weld of poor quality may have an aggregate effect and decrease the overall propagation life of the weld.

Two specimens treated with UIT were tested at a nominal weld toe stress range of 193 MPa (28.0 ksi). The first of these two specimens, designated UIT 2, underwent 1.3 million cycles before a crack was detected with dye penetrant inspection. The second specimen, designated UIT 3, underwent 2.1 million cycles before a crack was detected. The difference between the two was 38%, which coincidentally was the same difference observed between the two control specimens and also between the two bolted specimens tested at a stress range of 193 MPa (28.0 ksi). The average fatigue life of specimens treated with UIT and tested at a nominal weld toe stress range of 193 MPa (28.0 ksi) was approximately 25 times longer than the average fatigue life of untreated control specimens. The crack initiation lives of both control specimens tested at a weld toe stress range of 193 MPa (28.0 ksi) were in the range of AASHTO Category E details. Both UIT-treated specimens tested at the same stress range resulted in AASHTO Category A performance for fatigue crack initiation. Given that specimens treated with UIT in this study experienced an increase in fatigue life equivalent to that of six AASHTO fatigue categories, it was concluded that Ultrasonic Impact Treatment of the transverse weld toes was very effective in extending the fatigue life of the specimens.

Both specimens treated with UIT were tested well past the point of crack initiation to investigate crack propagation behavior. Specimen UIT 2 was loaded for 1.65 million additional cycles after crack initiation and specimen UIT 3 was loaded for 2.29 million cycles after crack initiation. The two specimens treated with UIT displayed significantly lower crack propagation rates than those of control specimens.

All three of the specimens treated with both UIT and with tensioned bolts post-installed at the end of the coverplates, referred to as combination specimens, were tested at a nominal weld toe stress range of 193 MPa (28.0 ksi). The crack initiation life of the first of these specimens, UIT/BOLT 1, was determined using recorded load and deflection data. Examining trends in data, the crack initiation life was estimated to be 550,000 cycles for UIT/BOLT 1. The fatigue lives of the other two combination specimens

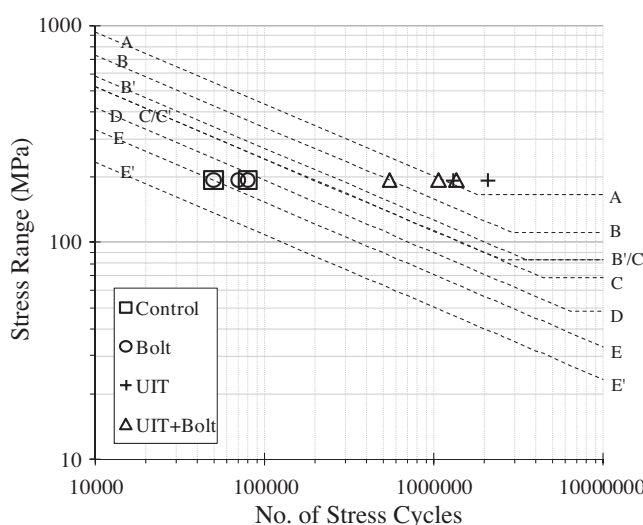


Fig. 8. S-N diagram of HSR specimen results.

were determined by visual inspection using the modified dye penetrant procedure. For specimen UIT/BOLT 2 a fatigue crack was first detected at 1.07 million cycles, while for UIT/BOLT 3 a fatigue crack was first detected at 1.37 million cycles. The average crack initiation life of these three specimens was 1 million cycles. The range of crack initiation lives was 820,000 cycles, and the difference between the specimen with the shortest life and the specimen with the longest life was 60%. Given that the fatigue lives of specimens UIT/BOLT 2 and UIT/BOLT 3 were determined with a more precise method, there was greater confidence in the results of these two specimens. When all three specimens are considered, there was more scatter in the results for the combination specimens than for any of the other three specimen types. It is reasoned that the addition of the post-installed bolt in the combination specimens added an additional state of stress subject to additional variations beyond those present in the UIT specimens, increasing the amount of scatter in the data for those specimens. Additional testing would be beneficial in determining whether this is a contributor to scatter, and would also help to show whether a similar relationship exists between bolted and control specimens.

For specimens tested at a weld toe stress range of 193 MPa (28.0 ksi), the average fatigue life for UIT/BOLT specimens was 41% lower than the average fatigue life for UIT-treated specimens. While all UIT specimens had initiation lives in the AASHTO fatigue Category A range, two of the UIT/BOLT specimens had initiation lives in the AASHTO Category B range, while the third UIT/BOLT had an initiation life in the AASHTO Category A range. Therefore, for the group of specimens tested at a weld toe stress range of 193 MPa (28.0 ksi), the majority of the combination specimens performed the equivalent of one AASHTO fatigue category worse than both UIT-treated specimens. These findings showed that Ultrasonic Impact Treatment of the welds was less effective when tensioned bolts were post-installed at the ends of the coverplates than when UIT was applied without also including post-installed tensioned bolts. Although the installation of tensioned bolts in otherwise untreated specimens was found to have a negligible effect on fatigue life, the installation of tensioned bolts in specimens treated with UIT reduced the improvement in fatigue life caused by the treatment of the welds. Even though the performance of specimens with treated welds and bolts was not as good as the performance of specimens treated only with UIT, the performance was significantly better than that observed in untreated specimens.

It was also observed that specimens treated with UIT experienced a different mode of fatigue cracking and propagation behavior than non-treated specimens. All specimens not treated with UIT (control and bolted specimens) developed fatigue cracks at the toes of the transverse welds, as shown in Figs. 9 and 10. In these specimens, cracks initiated at either the center or one of the ends of the transverse weld toe and propagated into the flange in a direction orthogonal to the longitudinal axis of the specimen. After a crack had initiated, the rate of crack growth increased exponentially until yielding of the reduced flange section caused failure. All specimens treated with UIT (UIT and combination specimens) exhibited surface cracks in the transverse weld throat near one end of the transverse weld, as illustrated in Figs. 11 and 12. On the surface, these cracks propagated along the entire length of the transverse weld throat and into the flange. These specimens displayed crack propagation plateaus, meaning that at some point during propagation the exponential rate of crack growth decreased considerably, and the fatigue crack propagated at a constant rate.

For each UIT-treated specimen, one crack propagation plateau was noted. Interestingly, in the UIT-treated specimens, not only was crack initiation life found to be greater than that for non-UIT treated specimens, but propagation life was also found to be significantly longer than that noted in non-treated specimens. The crack propagation pattern for UIT and UIT/BOLT specimens was as fol-



Fig. 9. Complete propagation of a crack in a non-treated (control) fatigue specimen.



Fig. 10. Complete propagation of a crack in a BOLT treated fatigue specimen.



Fig. 11. Complete propagation of a crack in a UIT-treated fatigue specimen.

lows. On the surface of a weld, a crack initiating at the weld throat near one end of a transverse weld would propagate across the entire length of the transverse weld throat. At each end of the transverse weld, the crack would then propagate around the corner of the fillet weld, moving along the longitudinal weld and toward

the flange at an angle of approximately 45°. The crack would then begin to propagate into the base metal of the flange, advancing in a direction orthogonal to the longitudinal axis of the flange.

For all specimens displaying a propagation plateau, the rate of crack propagation through the flange slowed considerably after cracking in the flange began. Based on this, the authors believe that the crack propagation plateau was reached after the crack propagated through the weld and weld-affected zone, and into good base metal of the flange. In bolted and control specimens, this would not have presented itself, as the crack did not travel through the weld, but rather through the base metal.

5.3. Finite element analysis results

The finite element analysis showed that the tension force in the bolt had the result of inducing tensile stresses in the transverse welds instead of compressive stresses, under no other externally-applied loads. Maximum principal stress and stress direction were used as a metric to quantify the effects of cover plate bolting on fatigue life. The surface of the transverse fillet weld had a tensile principal stress resulting from the tension force in the bolt, as shown in Fig. 13, which shows maximum principal stresses from the “bolted” model. The direction of the maximum principal stress vector from the “bolted” model was approximately parallel to the 3–3 direction (in the through-thickness direction).

According to the analysis with the bolt load, the magnitude of the principal stress at the surface of the specimen, near the middle of the transverse weld, was approximately 55 MPa (8.0 ksi). At the center of the specimen, the stress at the throat of the weld was slightly more highly stressed than the weld toe. The maximum principal tensile stress at the end of the transverse weld was higher than the stress at the middle of the transverse weld. Maximum principal tensile stresses of approximately 82.7 MPa (12.0 ksi) were induced near the ends of the transverse welds by the cover-plate bolts. These results were consistent with the fact that specimens with bolts (BOLT and UIT/BOLT specimens) developed fatigue cracks near the ends of the transverse weld instead of developing cracks near the center of the transverse weld.

The direction of maximum principal stresses under combined bending and bolt tension (“bolt/bending”) was found to be parallel to the face of the weld (at a 45 degree angle with the plane of the plates). The principal stress direction for the scenario with the combined bolt and bending agrees well with the observed crack patterns, which occurred along the length of the transverse weld, with the cracks opening in the same direction as the stress vectors are acting. This can be seen in the photographs of the cracked specimens (Figs. 9–12). The magnitude of maximum tensile principal

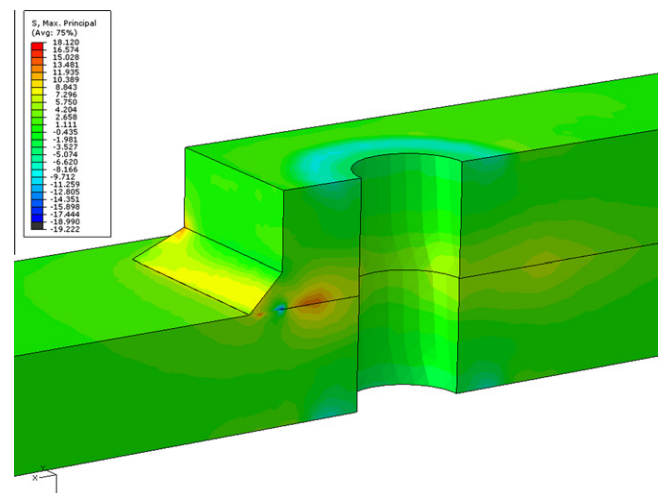


Fig. 13. Fringe plot of finite element modeling results showing sectioned view of maximum principal stress contours in weld region due to application of post-installed tensioned bolt in “bolted” model.

stress range experienced in the “bolt/bending” models was approximately 310 MPa (45 ksi), and occurred directly at the toe of the transverse weld.

Considering the influence of directional stresses, σ_{11} and σ_{33} should have the greatest effect on crack growth at the weld toe, as results from the finite element analyses indicate that it is a combination of these two stress components that drive this mode of crack opening. For clarity, σ_{11} is the directional stress acting in the longitudinal (x -) direction of the specimen, σ_{22} is acting in the transverse (y -) direction, and σ_{33} is in the through-thickness (z -) direction, as shown in Fig. 13. Considering directional stresses from the “bolt/bending” model at the toe of the transverse weld, σ_{11} had a tensile magnitude approximately twice that of σ_{33} , and three times that of σ_{22} . Because σ_{11} was the highest computed tensile stress at the weld toe, it was expected that a crack would open along this direction at the weld toe. This was consistent with the observed crack propagation pattern, in which cracks tended to initiate at the weld toe, except in specimens wherein the weld toe was treated with UIT. The relative magnitude of the computed directional stresses was also consistent with the crack propagation pattern of UI-treated specimens, in that cracking was noted at the throat of the weld, where the inclined surface made it more susceptible to cracking caused by the combined effects of σ_{11} and σ_{33} . It is hypothesized that the UI treatment induced residual stresses that counteracted σ_{11} and σ_{33} at the weld toe, making the weld throat the next most susceptible region. The low magnitude of σ_{22} in the weld toe region relative to σ_{11} and σ_{33} offers explanation as to why cracking along the longitudinal welds was not observed in any of the specimens.

Tests of all specimens that were treated with UIT showed that the residual compressive stresses and the smoothing of the imperfections resulting from the UIT caused a large increase in fatigue life, equivalent to an improvement of at least six AASHTO fatigue categories. The observed crack pattern for specimens treated with UIT (Figs. 11 and 12) shows that failure took place above the treated region of the weld. It was concluded that UIT effectively eliminated the vulnerability of the treated region, shifting the location of the vulnerable area to an untreated region of the weld.

In specimens with treated welds and bolts, the finite element analyses showed that there was an increase in tensile stresses in the transverse welds as a result of coverplate bolting. These specimens also developed cracks above the treated region of the weld, although at a different location along the weld. The increase in tensile stresses observed in the finite element analysis was consistent



Fig. 12. Complete propagation of a crack in a UIT/BOLT treated fatigue specimen.

with the fact that the combination specimens had a shorter average fatigue life than the UIT-treated specimens, and that fatigue cracks developed near the ends of the welds. In these specimens the treatment of the welds was effective in eliminating the vulnerability to fatigue failure at the weld toe, but the initiation life of the untreated region of the weld was reduced due to the increase in tensile stresses induced by the bolts.

In the case of specimens with untreated welds, the crack initiation life was dictated by the vulnerability to fatigue failure of the weld toe. This was evidenced by the fact that for specimens with untreated welds, cracks originated at the weld toe (Figs. 9 and 10). The difference in fatigue lives between specimens with and without bolts was negligible, with the bolted specimens having a slightly higher average fatigue life than the specimens without bolts. Given the range of crack initiation lives observed in the experimental study and the short fatigue lives of these specimens, this difference could not be taken as a certain indication that adding bolts tends to result in a small increase in fatigue life. In fact, the finite element analysis results suggested that a reduction in fatigue life may be expected. The difference in fatigue life between these two types of specimens was not of great significance this study, and could be investigated more precisely by testing additional specimens at a lower stress range.

6. Summary and conclusions

A study of the fatigue behavior of welded coverplate specimens treated with Ultrasonic Impact Treatment, post-installed tensioned bolts, and a combination of UIT and bolting has been presented. Fifteen fatigue specimens were experimentally tested at intermediate and high stress ranges so that differences in fatigue performance could be examined between the three treatment methods, and to investigate interaction effects between them. Computer simulations using a finite element model were performed to gain insight into the effects of the stress field induced by post-installed tensioned bolts behind an existing weld. Results from the study led to the following conclusions:

- UIT was found to be a very effective method of prolonging the fatigue life of the coverplate detail. When fatigue tests were performed at a nominal weld toe stress range of 193 MPa (28 ksi), the welded connection showed improved fatigue performance from that corresponding to an AASHTO fatigue Category E detail to that of a Category A detail.
- UIT-treated specimens exhibited longer crack propagation lives than non-treated specimens, in addition to longer crack-initiation lives.
- Post-installed tensioned bolts had a negligible effect on the fatigue performance of otherwise untreated specimens, indicating that the interaction between the bolt and the weld was negligible. This was not the case when the welds were treated with UIT, where the interaction was found to have a meaningful effect on fatigue life.
- Test results suggested that stresses induced by the post-installed bolt had a significant effect on the fatigue life of the portion of the transverse weld face that was not treated with UIT. This portion of the weld was closer to the point of interaction between the bolt and the coverplate. Conversely, the test results indicated that the stresses induced by the post-installed bolt had a negligible effect on the fatigue life of the treated portion of the weld (the weld toe), which was furthest from the point of interaction between the bolts and the coverplate.
- Finite element analyses showed that post-installing tensioned bolts induced tensile stresses in the untreated region of the weld. This was consistent with an experimentally observed

reduction in the fatigue life of specimens with UIT-treated welds and post installed bolts compared with the fatigue life of specimens treated only with UIT.

On the basis of the results of the fatigue testing program, application of Ultrasonic Impact Treatment to the toes of transverse fillet welds connecting coverplates to girder flanges was found to be very effective as a fatigue life enhancement technique for the fatigue-prone detail studied.

Post-installing tensioned bolts near an existing UIT treated weld was found to be a detriment to fatigue life. It is recommended that if tensioned bolts are to be used in combination with UIT, the placement of the bolts be carefully considered so that any effects of the bolts are dissipated before they reach the weld, so that no unintended interaction may reduce the fatigue life of the treated weld.

This study has illustrated that a “more is better” philosophy may not always result in a longer fatigue life, and that the interaction between retrofit measures may lead to a reduction in the effectiveness of those measures if not considered carefully.

Future work on this topic is warranted. Additional tests at stress ranges utilized in this testing would lend greater statistical significance to the existing data set, while tests performed at other stress ranges would allow new distinctions to be made between the different treatment techniques. Supplementary testing of specimens at low stress ranges would allow greater differentiation to be made between the performances of bolted and control specimens, while tests performed at higher stress ranges would result in additional understanding of the performance of UIT-treated specimens.

Acknowledgements

The authors would like to thank the Kansas Department of Transportation for funding this research and their ongoing cooperative research efforts with the University of Kansas. Additionally, the authors are grateful for donations of supplies and specimen fabrication from Builders Steel in Kansas City, MO. Finally, the authors would like express sincere thanks to Applied Ultrasonics for treating specimens with Ultrasonic Impact Treatment.

References

- [1] Barsom JM, Rolfe ST. Fracture and fatigue control in structures. 3rd ed. West Conshohocken, PA: American Society for Testing and Materials; 1999. p. 237–280.
- [2] Fisher J, Frank K, Hirt M, McNamee B. Effect of weldments on the fatigue strength of steel beams. NCHRP Report No. 102, Washington, D.C.: Highway Research Board, National Academy of Sciences-National Research Council; 1970.
- [3] Yamada K, Albrecht P. Fatigue behavior of two flange details. *J Struct Div* 1977;103(4):781–91.
- [4] Simon S, Albrecht P. Adding fatigue life to cover plate ends. *J Struct Div* 1985;107(5):923–35.
- [5] AASHTO. LRFD bridge design specifications. 4th ed. Washington, D.C.: American Association of State Highway and Transportation Officials; 2007.
- [6] Jones J, Bennett C, Matamoros A, Rolfe S, Roddis K. Fighting fatigue in steel bridges: two case summaries, TR news. Washington D.C.: Transportation Research Board, National Research Council; 2008. p. 25–26, 259.
- [7] Anderson B, Rolfe S, Matamoros A, Bennett C, Bonnelli S. Post retrofit analysis of the tuttle creek bridge br. No. 16-81-2.24, SM Report No. 88. University of Kansas Center for Research; 2007.
- [8] Roy S, Fisher JW, Yen BT. Fatigue resistance of welded details enhanced by ultrasonic impact treatment (UIT). *Int J Fatigue* 2003;25(9–11):1239–47.
- [9] Roy S, Fisher JW. Improving fatigue strength of welded joints by ultrasonic impact treatment. Shanghai, China: IABSE Symposium: Metropolitan Habitats and Infrastructure; 2004.
- [10] Vilhauer, B. Fatigue behavior of welded connections enhanced with UIT and bolting. Thesis, presented to University of Kansas at Lawrence, KS, in partial fulfillment for the degree of Master of Science; 2007.
- [11] AISC. Steel construction manual. 13th ed. American Institute of Steel Construction (AISC); 2005.
- [12] Bennett C, Swanson J, Linzell D. Fatigue resistance of HPS-485W (70W) continuous plate with punched holes. *J Brid Eng* 2007;12(1):98–104.
- [13] ASTM E8-04. Standard test methods for tension testing of metallic materials. West Conshohocken, PA: American Society for Testing Materials; 2007.